Transport and resonant soft x-ray scattering studies of cuprate superconductors under uniaxial stress

Von der Fakultät Mathematik und Physik der Universität Stuttgart zur Erlangung der Würde eines Doktors der Naturwissenschaften (Dr. rer. nat.) genehmigte Abhandlung

Vorgelegt von:

Suguru Nakata

aus Kyoto, Japan

Hauptberichter:	Prof. Dr. Bernhard Keimer
Mitberichter:	Prof. Dr. Laura Na Liu
Prüfungsvorsitzende:	Prof. Dr. Maria Daghofer

Tag der Einreichung:	17. 02. 2022
Tag der mundlichen Prüfung:	24. 03. 2022

Max-Planck-Institut für Festkörperforschung
Universität Stuttgart

Stuttgart, 2022

Abstract

New concepts in condensed matter physics have often been evidenced by macroscopic experiments such as transport and magnetic susceptibility measurements. On the other hand, microscopic spectroscopic experiments have provided energy- and momentum-resolved information related to atomic-scale correlation functions, which directly put constraints to theories describing macroscopic properties from a microscopic Hamiltonian. Therefore the correspondence between macroscopic and microscopic experiments under identical experimental conditions has provided foundations to develop many-body theories.

Since the discovery of high-temperature superconductivity in cuprates, an enormous amount of theoretical and experimental work was carried out to reveal its microscopic origin. While fundamental properties of the superconductivity have been well characterized, a number of aspects in the normal states are still unsolved or only poorly understood to this date. As a consequence of significant electron correlations in this material, various competing orders including superconductivity emerge when physical parameters are progressively tuned. Charge ordering, a leading competitor of superconductivity in cuprates, is significantly modified by uniaxial stress, which simultaneously enables an experimentalist to tune the lattice structure, and thereby the electronic structure, in a continuous fashion and to break point-group symmetries.

In this thesis, I will present charge transport and x-ray scattering experiments on the high-temperature superconductor $YBa_2Cu_3O_{6+x}$ under uniaxial stress to provide the correspondence between macroscopic charge transport and atomic-scale correlation functions and to extend the phase diagram by means of uniaxial stress. This thesis starts with an introduction to cuprates in chapter 1 and a thorough discussion of $YBa_2Cu_3O_{6+x}$, a model system that possesses minimal chemical disorder among the cuprate families in chapter 2, and of the basic principles of the experimental methods I used in chapter 3. The following chapters describe core experimental results.

First, chapter 4 describes charge transport studies under uniaxial stress. The resistivity of $YBa_2Cu_3O_{6+x}$ does not show any anomalies at the charge-density-wave (CDW) onset unlike conventional CDW materials. However, measurements of the normal state resistivity of $YBa_2Cu_3O_{6.67}$ (doping level $\sim$0.12 holes per Cu ion) under uniaxial compression have shown a remarkable correspondence between the differential stress responses of the transport coefficients and charge ordering, which parallels the phenomenology of classical CDW compounds. The sign of the Hall coefficient, the transport probe most sensitive to the Fermi surface of metals, is reversed at $T = T_0$ upon cooling. This phenomenon is often interpreted in terms of a Fermi surface reconstruction induced by the symmetry breaking introduced by the static CDW order. Measurements of the Hall coefficient under uniaxial stress have shown an enhancement of T_0, which is qualitatively in line with this

Fermi surface reconstruction scenario yet quantitatively too small in comparison with the diffraction pattern of the CDW. Therefore we propose that slow fluctuations, rather than the static CDW order, are mostly responsible for the sign reversal of the Hall coefficient. In this way, we reconcile the quantitative discrepancy in the stress effect on Hall coefficient.

Chapter 5 describes resonant soft x-ray scattering studies under uniaxial stress. The three dimensionally correlated (3D) CDW induced by uniaxial stress has been observed only at one particular doping level $YBa_2Cu_3O_{6.67}$ where the quasi-two dimensional (2D) CDW is the strongest. Taking advantage of resonant energy-integrated x-ray scattering experiments, we have expanded the doping range for the investigation of uniaxial stress effects on the CDW. A 3D-CDW similar to the one previously observed in $YBa_2Cu_3O_{6.67}$ was observed at lower doping levels, but not confirmed at higher doping levels up to optimal doping. These doping dependent studies yield insight into the conditions required for stabilizing the 3D-CDW in $YBa_2Cu_3O_{6+x}$. Resonant inelastic x-ray scattering experiments upon cooling in the presence of uniaxial stress have shown different effects on the 2D-CDW from those previously observed when straining only at low temperature. In addition, reciprocal space characters of charge orders and fluctuations and possible effects of uniaxial stress on magnetic excitations were also carefully investigated and discussed.

Zusammenfassung

Neue Konzepte in der Physik der kondensierten Materie wurden häufig durch makroskopische Experimente wie Transport- und magnetische Suszeptibilitätsmessungen nachgewiesen. Andererseits haben spektroskopische Experimente energie- und impulsaufgelöste Informationen über Korrelationsfunktionen auf atomarer Ebene geliefert, und damit Theorien getestet, welche die makroskopischen Eigenschaften mit Hilfe eines mikroskopischen Hamiltonians beschreiben. Die Korrespondenz zwischen makroskopischen und mikroskopischen Experimenten unter identischen Versuchsbedingungen schafft daher die Grundlage für die Entwicklung von Vielteilchentheorien.

Seit der Entdeckung der Hochtemperatur-Supraleitung in Kupraten wurde eine enorme Menge an theoretischen und experimentellen Arbeiten durchgeführt, um ihren mikroskopischen Ursprung aufzudecken. Während die grundlegenden Eigenschaften der Supraleitung gut charakterisiert wurden, sind eine Reihe von Aspekten in den Normalzuständen bis heute ungelöst oder nur unzureichend verstanden. Als Folge signifikanter Elektronenkorrelationen in diesem Material treten verschiedene konkurrierende Ordnungen einschließlich der Supraleitung auf, wenn die physikalischen Parameter progressiv eingestellt werden. Die Ladungsordnung, einer der Hauptkonkurrenten der Supraleitung in Kupraten, wird durch uniaxiale Spannung erheblich verändert, was es dem Experimentator gleichzeitig ermöglicht, die Gitterstruktur und damit die elektronische Struktur kontinuierlich zu verändern und Punktgruppensymmetrien zu brechen.

In dieser Arbeit werde ich Experimente zum Ladungstransport und zur Röntgenstreuung am Hochtemperatursupraleiter $YBa_2Cu_3O_{6+x}$ unter uniaxialer Spannung vorstellen, um die Korrespondenz zwischen makroskopischem Ladungstransport und Korrelationsfunktionen auf atomarer Skala herzustellen und das Phasendiagramm mit Hilfe von uniaxialer Spannung zu erweitern. Diese Arbeit beginnt mit einer Einführung in die Kuprate in Kapitel 1 und einer ausführlichen Diskussion von $YBa_2Cu_3O_{6+x}$, einem Modellsystem, das unter den Kupratfamilien die geringste chemische Unordnung aufweist, in Kapitel 2. Die Grundprinzipien der von mir verwendeten experimentellen Methoden werden in Kapitel 3 zusammengefasst. In den folgenden Kapiteln werden die wichtigsten experimentellen Ergebnisse beschrieben.

Zunächst werden in Kapitel 4 Studien zum Ladungstransport unter einachsiger Belastung beschrieben. Der spezifische Widerstand von $YBa_2Cu_3O_{6+x}$ zeigt im Gegensatz zu konventionellen CDW-Materialien keine Anomalien beim Einsetzen der Ladungsdichtewelle (charge-density-wave, CDW). Messungen des spezifischen Widerstands von $YBa_2Cu_3O_{6,67}$ (Dotierungsgrad $\sim$0,12 Löcher pro Cu-Ion) unter uniaxialer Kompression haben jedoch eine bemerkenswerte Übereinstimmung zwischen den differentiellen Änderungen der Transportkoeffizienten und der Ladungsordnung gezeigt, die der Phänomenologie klassischer

CDW-Verbindungen entspricht. Das Vorzeichen des Hall-Koeffizienten, des Transportkoeffizienten, der am empfindlichsten auf die Fermi-Fläche von Metallen reagiert, kehrt sich beim Abkühlen bei $T = T_0$ um. Dieses Phänomen wird häufig als eine Rekonstruktion der Fermi-Fläche interpretiert, durch die Symmetriebrechung der statischen CDW-Ordnung. Messungen des Hall-Koeffizienten unter uniaxialer Spannung haben eine Erhöhung von T_0 ergeben, die qualitativ mit diesem Szenario der Fermiflächen-Rekonstruktion übereinstimmt, quantitativ jedoch zu klein ist im Vergleich zum Ordnungsparameter der Ladungsdichtewelle, der mit Hilfe von Röntgenstreuung bestimmt wurde. Daher schlagen wir vor, dass langsame Fluktuationen und nicht die statische CDW-Ordnung für die Vorzeichenumkehr des Hall-Koeffizienten verantwortlich sind. Auf diese Weise können wir die quantitative Diskrepanz in der Spannungswirkung auf den Hall-Koeffizienten erklären.

Kapitel 5 beschreibt Studien zur resonanten weichen Röntgenstreuung unter uniaxialer Belastung. Die durch uniaxiale Spannung induzierte dreidimensional korrelierte (3D) CDW wurde bisher nur bei einem bestimmten Dotierungsniveau $YBa_2Cu_3O_{6,67}$ beobachtet, wo die quasi-zwei-dimensionale (2D) CDW am stärksten ist. Unter Ausnutzung der Vorteile von Experimenten mit resonanter energieintegrierter Röntgenstreuung haben wir den Dotierungsbereich für die Untersuchung der Auswirkungen uniaxialer Spannungen auf die CDW erweitert. Eine 3D-CDW, die der zuvor in $YBa_2Cu_3O_{6,67}$ beobachteten ähnelt, wurde bei niedrigeren Dotierungen beobachtet, konnte aber bei höheren Dotierungen bis hin zur optimalen Dotierung nicht bestätigt werden. Diese dotierungsabhängigen Studien geben Aufschluss über die Bedingungen, die für die Stabilisierung der 3D-CDW in $YBa_2Cu_3O_{6+x}$ erforderlich sind. Experimente mit resonanter inelastischer Röntgenstreuung bei Abkühlung in Gegenwart von uniaxialer Spannung haben andere Auswirkungen auf die 2D-CDW gezeigt als diejenigen, die zuvor bei Dehnung nur bei niedriger Temperatur beobachtet wurden. Darüber hinaus wurden die Signatur der Ladungsordnungen und -fluktuationen im reziproken Raum sowie mögliche Auswirkungen der einachsigen Spannung auf magnetische Anregungen sorgfältig untersucht und diskutiert.

Acknowledgements

The scientific work in this thesis represents the study in almost four years, which would have not been achieved without my supervisors, mentors, colleagues, and friends in Stuttgart, Dresden, Berlin, Grenoble, and various other places.

First and foremost, I would like to thank Bernhard Keimer, my PhD supervisor who has kindly accepted me as a PhD student in his department at Max Planck Institute for Solid State Research. I particularly appreciate that he allowed me to work quite independently and gave me time to pursue my ideas. Nevertheless he always made time to discuss our projects in person when I would have liked to and I have been impressed by his sharp and keen insights to interpret experimental results. Thanks to his foresight, I can present both macroscopic and microscopic experiments on cuprates under uniaxial stress in this thesis. I believe that such a combination of two different types of experiments under an extreme condition is quite unusual for a single PhD thesis and, therefore, I have truly enjoyed those mesmerizing projects supervised by him. Alongside my main projects, I have been fortunate to be in charge of providing $YBa_2Cu_3O_{6+x}$ single crystals to a number of collaborators outside of MPI. I appreciate that he has entrusted the work with a lot of responsibilities to me. Throughout communications with the collaborators, I have learned their state-of-the-art experimental techniques and understood the physics of cuprates more deeply.

I am also grateful to my day-to-day supervisor Matteo Minola for his daily supports and guidance. I have learned a lot from him about spectroscopic measurements, in particular RIXS and REXS, and physics of cuprates. He has kindly corrected my drafts a number of times and given me valuable feedbacks, which have improved my academic writing skills a lot. Throughout my PhD study, it was not possible for me to overcome difficult times without him. I am certainly sure that I am still not ready to be a scientific researcher today without his supervision. In addition, I have been particularly impressed by his management skills as a group leader in our group which consists of many individuals who have different cultural perspectives and educational backgrounds. In this respect, I would like to thank current and former members who have made such a circumstance possible. Firstly, I am very thankful to Hun-ho Kim who has achieved pioneering work with uniaxial stress technique in our department and always kindly taught me a number of technical aspects of uniaxial stress experiments. I am also thankful to Katrin Fürsich, Davide Betto, Emilie Lefrançois, Lichen Wang, Zichen Yang, Yiran Liu, and Sajna Hameed for spending times at synchrotron facilities together and having daily conversations with a cup of coffee at the institute. I am also grateful to Hakuto Suzuki, who had shared the office 7C8 for a long time. As his officemate, I have been impressed by his attitude to research, where he has always learned various theoretical concepts to understand experimental results himself.

He has recommended me great textbooks which broadened my perspectives of condensed matter physics. Conversations with the members in inelastic photon scattering group have been always so enjoyable but also intellectual that I have learned various different points of view regarding other material systems such as nickelates, iridates, and ruthenates.

I am very thankful to Clifford Hicks and Andy Mackenzie, who gave me opportunities to work on uniaxial stress experiments in their group at MPI Dresden. I had been quite happy to directly learn Cliff's cutting-edge uniaxial stress techniques, by which I was struck his delicate and ingenious ideas. During my visits he also invited me in his group meetings where I have enjoyed discussing about his ruthenate projects since I have been always interested in the physics of this material because of my personal background in undergraduate studies. That made me feel as if I were his student rather than just one of visitors. I am also grateful to his group members who supported our experiments and made my time in Dresden enjoyable: Mark E. Barber, Hilary Noad, Kent Shirer, Alexander L. Stern, Veronika Sunko, Thomas Lühmann, Po-Ya Yang, and Kousuke Ishida.

Experiments at synchrotron facilities have been achieved by a number of colleagues and beamline scientists. I am thankful to Enrico Schierle and Eugen Weschke at BESSY UE46 PGM-1 in Berlin and Davide Betto, Roberto Sant, Kurt Kummer, and Nicholas Brookes at ESRF ID32 in Grenoble for their close communications with us, which made a number of challenging beamtimes possible.

I would like to thank Juan Porras and Toshinao Loew who taught me methods to prepare $YBa_2Cu_3O_{6+x}$ single crystals. I am also grateful to members in Scientific Facility Crystal Growth, Masahiko Isobe, Christof Busch, and Sabine Lacher, for the self-flux growth of $YBa_2Cu_3O_{6+x}$ single crystals in a number of different conditions. I would like to thank Masahiko Isobe also for being my external supervisor.

To achieve our uniaxial stress experiments and prepare $YBa_2Cu_3O_{6+x}$ single crystals, supports from service groups in MPI Stuttgart were indispensable: Low temperature service, Crystal preparation service, Mechanical workshop, Fine mechanical workshop, Glass workshop, Electronics workshop, and Computer service. In particular, I would like to thank Barbara Baum for polishing a lot of as-grown crystals and Thomas Frey for producing a number of small metal parts. I am also grateful to technicians in our department, Benjamin Bruha, Michael Schulz, and Heiko Uhlig, for maintaining our experimental instruments on a daily basis and assisting me in ordering products with external companies.

During the middle of my PhD, I have worked on growing iridate single crystals with Kentaro Ueda and Mohamed Oudah and a series of Raman scattering measurements with Armin Schulz. I had opportunities to join beamtimes with Matthieu Le Tacon and Michaela Souliou in ESRF and SPring-8. I worked with Chengtian Lin to improve the sample quality of $YBa_2Cu_3O_{6+x}$. Those works are not mentioned in the final cut of this thesis, yet I would like to acknowledge that I have learned various technical aspects of those experiments which it is often difficult to acquire only from publications.

I would like to thank the former and current members in our department: Alexander Boris, Eva Benckiser, Hlynur Gretarsson, Matthias Hepting, Giniyat Khaliullin, Joel Bertinshaw, Martin Bluschke, Robert Dawson, Christopher Dietl, Laura Guasco, Maximilian Krautloher, Elirjete Kryeziu, Humei Liu, Roberto Ortiz, Rebecca Pons, Daniel Putzky, Ksenia Rabinovic, Padma Radhakrishnan, Xiatong Shi, Pablo Sosa Lizama, Cissy Suen, Hiroto Takahashi, Heiko Trepka, Peter Yordanov, and Valentin Zimmermann.

I am grateful to the administration office staffs in MPI Stuttgart in particular Sonja Balkema and Birgit King who have made my life in Germany quite comfortable while it was the first time for me to live abroad. I also thank Amy Wright and Claudia Strohbach in MPI Dresden who have always smoothly arranged my frequent visits at MPI Dresden. I would like to acknowledge financial support from the Max Planck Society.

I am deeply grateful to Laura Na Liu and Maria Daghofer for being examiners of my defense and evaluating my dissertation.

The world wide pandemic COVID-19 has sharply split my four-year PhD life in half. As it has been the case for anyone all over the world, the latter two years have been completely different from the former two years. Nevertheless, I have been fortunate to work at the institute in pretty much the same way as before. In this respect, I would like to appreciate all people, in particular essential workers, who have made my life possible.

Finally but not least, I would like to thank my parents, Satoru Nakata and Yoko Nakata, and my brother, Ryo Nakata, who have always supported my studies and respected my decisions. I owe what I am today to them.

Contents

Chapter 1

Introduction

Reductionism has revealed that everything in the world is made of elementary particles and their motions can be described with fundamental interactions. The law of nature is written in mathematics, yet the system treated in condensed matter physics has usually as many as 10^{24} atoms[1] and thus we have almost no hope to solve the equations of motion of such an enormous number of particles. On the contrary, we are not interested in exact motions of every particle. What we care about is their macroscopic collective properties emerging from microscopic interactions among particles. Therefore one has to properly simplify problems and cleverly extract some statistical aspects from the systems.

The advantages of studying solids as one of many-body problems in physics are that we already know the basic properties of the building blocks, electrons and nuclei, and interactions among them, and that hypotheses can be relatively easily tested by experiments. As a consequence, the study of condensed matter is one of the largest branches in physics of many-body systems and has influenced other fields such as particle physics each other. For instance it is famous that the concept of the gauge symmetry breaking in the BCS theory, the established theory of superconductivity, was transferred to particle physics to describe the Higgs mechanism, which explains the origin of mass [1]. On the other hand, researches on materials are intimately related to potential future applications such as semiconductor technologies which have changed our lives in the last century. Nevertheless, in this thesis, I will confine discussions only to fundamental physic of high temperature superconducting cuprates, a prototypical example of many-body system where several particles act in concert to give rise to a plethora of emerging collective phenomena.

In this thesis, in particular, I will present charge transport and x-ray scattering experiments on the copper oxide material $YBa_2Cu_3O_{6+x}$, known for its high temperature superconductivity. As a consequence of significant electron-electron correlations in this material, various competing orders including superconductivity emerge progressively when tuning various physical parameters. In this respect, I have applied uniaxial stress to this material as external parameter in order to obtain the correspondence between macroscopic charge transport and atomic scale correlation functions and to extend the phase diagram [2, 3]. In this chapter, before moving on to the results of those experiments, I will start with some basic notions about how we describe collective phenomena in solids and

[1] Assuming the size of an atom is 1 Å, the number of atoms in a cubic 1 cm^3 material where the atoms are closely packed is $1cm^3/(1Å)^3 = 10^{24}$.

charge-density-wave phenomena, which will be key concepts to understand the following chapters.

1.1 Electrons in solids

The simplest theoretical treatment of electrons in solids is to assume that they are free electrons in vacuum [4]. Such a treatment is called the free Fermi gas because electrons are fermions. The wave function $\varphi_{\boldsymbol{k}}$ of the free electron whose momentum is $\boldsymbol{k}$ is given by $\varphi_{\boldsymbol{k}} = \exp(i\boldsymbol{k}\cdot\boldsymbol{r})/\sqrt{\Omega}$, where $\Omega = L^3$ is the volume of a cubic structure whose side is L where N ($= 10^{22} \sim 10^{23}$) electrons exist. Assuming the periodic boundary condition, the energy of the electron whose wave number is $\boldsymbol{k}$ is given as $\varepsilon_{\boldsymbol{k}} = \hbar^2\boldsymbol{k}^2/2m = \hbar^2(2\pi\boldsymbol{n}/L)^2/2m$ where $\boldsymbol{n} = (n_x, n_y, n_z)$ is a vector of any integers. One state can be occupied by only one single electron due to the Pauli exclusion principle derived from the antisymmetric character of a many-body wave function of indistinguishable fermions. Therefore the lowest energy state, ground state, at zero temperature is the state that each electron occupies from the lowest eigenstate one by one. The highest energy of one electron in the ground state ε_{F} is called the Fermi energy and the Fermi wave vector $\boldsymbol{k}_{\mathrm{F}}$ is defined as $\varepsilon_{\mathrm{F}} = \hbar^2{\boldsymbol{k}_{\mathrm{F}}}^2/2m$. In realistic metals, the Fermi energy is a few eV or the Fermi temperature $T_{\mathrm{F}} = \varepsilon_{\mathrm{F}}/k_{\mathrm{B}}$ is 10^4 K, which is much higher than room temperature $\sim 10^2$ K (k_{B} is the Boltzmann constant). Therefore at such a "low" temperature, a marjory of electrons do not contribute to kinetic energies and only electrons near the Fermi energy within $\sim k_{\mathrm{B}}T$ can be thermally excited. This is why the electronic specific heat experimentally observed in metals is T-linearly dependent and much lower than the constant value $3Nk_{\mathrm{B}}/2$ expected based on the law of equipartition for the N-electron system. The energy split between different energy levels near the Fermi energy is $\Delta\varepsilon = \varepsilon_{\mathrm{F}}/N = 10^{-22}$ eV. Therefore the excitation energy of electron-hole pair excitations near the Fermi level is infinitely small for most of experimental resolutions and an infinite number of such electron-hole pair excitations exist near the Fermi level.

While the Coulomb interaction between electrons are completely ignored in the Fermi gas model, in reality the interactions between electrons always exist. To treat the normal state of the interacting fermion systems without long range orders, the new concept called a Fermi liquid was introduced by Landau. The fundamental idea of the Fermi liquid is introducing the interactions between electrons into the non-interacting Fermi gas and adiabatically connecting it to the Fermi liquid state. There is one-to-one correspondence between the states before and after introducing the interaction and the new state can be described by quantum numbers of the old state. The state described by the momentum $\boldsymbol{k}$ in the Fermi liquid theory is called a (Landau) quasiparticle. The quasiparticle with the momentum $\boldsymbol{k}$ on the ground state of the Fermi gas model $|0\rangle$ can be written as follows,

$$\begin{aligned} &{Q_{\boldsymbol{k}}}^\dagger |0\rangle \\ &= \sqrt{z_{\boldsymbol{k}}} \left({C_{\boldsymbol{k}}}^\dagger + \sum_{\boldsymbol{k_1},\boldsymbol{k_2},\boldsymbol{k_3}} \Gamma_1 {C_{\boldsymbol{k_1}}}^\dagger {C_{\boldsymbol{k_2}}}^\dagger C_{\boldsymbol{k_3}} + \sum_{\boldsymbol{k_1},\boldsymbol{k_2},\ldots,\boldsymbol{k_5}} \Gamma_2 {C_{\boldsymbol{k_1}}}^\dagger {C_{\boldsymbol{k_2}}}^\dagger {C_{\boldsymbol{k_3}}}^\dagger C_{\boldsymbol{k_4}} C_{\boldsymbol{k_5}} + \ldots \right) |0\rangle , \end{aligned} \tag{1.1}$$

where ${Q_{\boldsymbol{k}}}^\dagger$ (${C_{\boldsymbol{k}}}^\dagger$) is a creation operator of the quasiparticle (bare electron) and $C_{\boldsymbol{k}}$ is an annihilation operator of the bare electron. $z_{\boldsymbol{k}}$ is called the wave-function renormalization

factor. The first term in the right side denotes the single electron state while the higher order terms denote the many-body states, which represent the particle-hole excitations. In the presence of the interactions, $z_{\boldsymbol{k}}$ ($0 \leq z_{\boldsymbol{k}} < 1$) represents the probability that the single-electron state dominates in the many-body states, i.e, ${Q_{\boldsymbol{k}}}^{\dagger} |0\rangle$ corresponds with the non-interacting Fermi gas state when $z_{\boldsymbol{k}} = 1$ and $\Gamma_1, \Gamma_2, ... = 0$. By renormalizing complex excitations of bare electrons and holes to the (almost) non-interacting quasiparticles, physical quantities in the Fermi liquid theory can be expressed by those in the Fermi gas model with a few factors of proportionality: renormalized mass and Landau parameters. Remarkably, the Fermi surface volume is identical between the two models (Luttinger's theorem [5]), therefore one can discuss the Fermi surface in the interacting system by means of the physical quantities related to the Fermi surface volume defined in the non-interacting system, e.g., the Hall number. This fact allowed us to discuss the Fermi surface reconstruction by means of the Hall effect in chapter 4.

Up until here the Landau quasiparticles are introduced to treat correlated electrons in solids. Such a methodology to simplify correlated many-body problems is one of foundations in condensed matter physics. The low energy excited states in the many-body system are interpreted as (almost) non-interacting elementary excitations. It has been known that a variety of elementary excitations emerge in solids and macroscopic properties of solids are explained by means of the statistical characters of those elementary excitations[2] [7]. In some sense, the research of condensed matter physics could be defined as the study of such elementary excitations at energy scales below 100 meV [8]. While no long range order is considered in the Fermi liquid theory, gapless excitations known as Nambu-Goldstone modes emerge when the system undergoes the long range order associated with the spontaneous symmetry breaking. Examples are phonons in crystals (translational symmetry breaking), magnons in magnetic materials (spin rotational symmetry breaking), and so forth.

One of the solid-state systems for which one needs such a sophisticated methodology is a transition metal oxide such as the cuprates studied in this thesis. The energy eigenstate near the Fermi level arises from the d-electrons in the transition metal oxides. The orbital radius of the d-electrons is smaller than that of the p- and s-orbitals. Therefore, the interatomic overlap of the d-electrons is small and, hence, the d-electrons tend to be localized at atomic sites, in particular for the $3d$ series. In such a case, the description of screening effects by the Fermi gas model, which is appropriate for ordinary metals, is no longer a good approximation and the electron correlation between d-electrons becomes significant. Such a system is called the strongly correlated electron system, and the many-body ground states are often nearly degenerate. As a consequence, a variety of collective orders emerge by slightly tuning physical parameters in those compounds, as is evident in rich phase diagrams (Fig. 1.1) [9]. Such a tuning can be made not only by temperature and chemical substitutions but also by external fields.

The collective phenomenon specifically studied in this thesis is called a charge-density wave (CDW). The correspondence between macroscopic transport behaviors and atomic

[2]The usage of terminologies, *quasiparticles*, *collective excitations*, and *elementary excitations*, is extremely diverse depending on contexts. In this thesis, the original individual particle plus a cloud of disturbed neighbors is termed the quasiparticle (e.g., Landau quasiparticles), while the wavelike motion of all the particles in the system which does not center around individual particles is termed the collective excitation (e.g., magnons), following Ref. [6]. Elementary excitations comprise the universal set of quasiparticles and collective excitations.

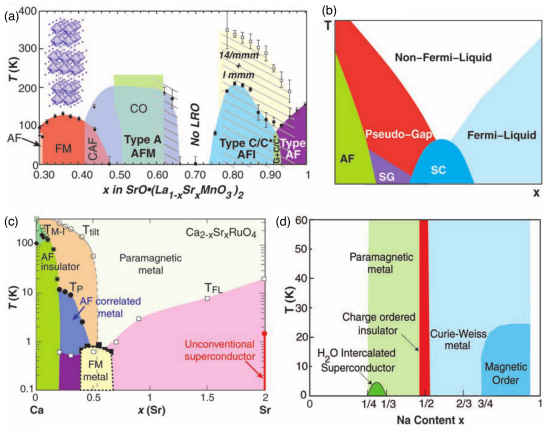

Figure 1.1: **Phase diagrams of the strongly correlated electron systems.** (a) Manganites. (b) Cuprates, studied in this thesis. (c) Ruthenates. (d) Cobaltates. Figures from Ref. [9].

scale correlation functions in classical CDW materials has been well established. The CDW was discovered in the cuprates as a leading competitor of superconductivity, yet a number of the basic properties of the CDW in the cuprates cannot be understood in the conventional theoretical framework.

1.2 Charge-density waves

Let us consider the one-dimensional (1D) metal depicted in Fig. 1.2 to first understand the essence of the CDW as initially proposed by Peierls in the 1930's [10, 11]. In a metal, the valence electron density is uniform and atoms are periodically configured in the real space at high temperature ($T \geq T_{\mathrm{P}}$). In the reciprocal space, the energy dispersion $\varepsilon_k = \hbar^2 k^2/2m$ crosses the Fermi energy ε_{F}. In this system, the charge susceptibility χ, i.e., the response function which indicates the electron density change by a static electric potential, has an instability at $q = 2k_{\mathrm{F}}$ in the reciprocal space. In particular, χ is expressed by the Lindhard function χ_0 in the non-interacting system at zero temperature and χ_0 diverges at $q = 2k_{\mathrm{F}}$. The divergence of the susceptibility implies the infinite response under the infinitesimal external field, thus can be interpreted as a phase transition. As a consequence, the electron density undergoes a transition from the uniform distribution to the modulation with a finite periodicity π/k_{F} at low temperature ($T \leq T_{\mathrm{P}}$). This modulation of the electron density is termed a charge-density wave. The translational symmetry breaking due to the CDW opens a gap in the electronic band dispersion at ε_{F} since $k = \pm k_{\mathrm{F}}$ becomes a boundary of the reconstructed Brillouin zone. As a consequence, the macroscopic charge transport properties transit to an insulator from a metal by the CDW transition. Through the electron-phonon coupling, the phonon dispersion at $q = 2k_{\mathrm{F}}$ is renormalized, which is known as Kohn anomaly. If the renormalized phonon energy reaches zero, the static atomic configurations are also modulated in the real space as seen in Fig. 1.2. To verify this picture experimentally, the electron density modulations can be measured in x-ray diffraction experiments and the metal-to-insulator transition (MIT) can be observed in charge transport measurements.

For higher dimensional materials, some features of the CDW differ from the ones of the 1D case even in Peierls' theory. For instance, only small humps are often observed in the resistivity of the two-dimensional (2D) materials reflecting the partial gap opening on the 2D Fermi surface unlike the complete MIT and full gap opening on the 1D Fermi surface

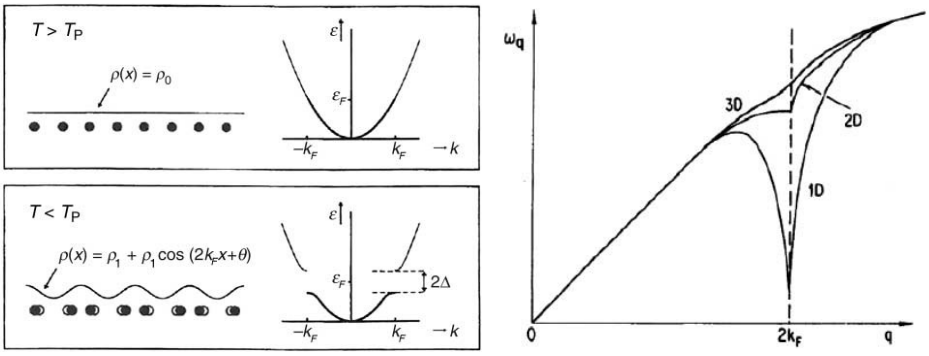

Figure 1.2: **Generic features of CDW.** (Top left) Schematic figure of one dimensional atomic chain (black dots). The electron density as a function of space ($\rho(x)$) is uniform above the Peierls transition temperature T_P. The band dispersion of free electrons cross the Fermi energy. (Bottom left) $T \leq T_\mathrm{P}$. The atomic position is modulated and $\rho(x)$ becomes periodic (the CDW state). The band dispersion near the Fermi level is gapped out. (Right) Kohn anomaly in the phonon dispersion for different dimensions. Figures from Ref. [10].

in the 1D case. On top of that, electrons correlate in real materials, thus the Lindhard function χ_0 is no longer a good approximation to describe the charge susceptibility χ of the strongly correlated systems. Therefore the theoretical treatment of the charge susceptibility χ may need to be more realistic to reconcile the difference between the experimental results and simple theories when they do no agree.

In the case of quasi-2D cuprates, the CDW was first discovered in 1995 in the form of stripes observed in the $La_{2-x}Ba_xCuO_4$ (214) family via neutron diffraction measurements as a leading competitor of superconductivity [12]. The associated transport anomaly in resistivity [13], lattice structural change, and intertwined spin ordering were concomitant in those systems. For a long time the CDW had been evident only in this peculiar $La_{2-x}Ba_xCuO_4$ family, yet in 2012 the CDW was discovered in $YBa_2Cu_3O_{6+x}$ using resonant x-ray scattering [14] and later in all other cuprate families [15]. A number of associated properties in cuprates are, however, different from the conventional Peierls picture. For example, the anomaly in resistivity which indicates the CDW transition is not evident to date, the phonon dispersion is renormalized below the superconducting transition temperature rather than at the CDW onset [16], etc... As is evident from the Kohn anomaly, the CDW is intimately linked with its underlying lattice structure through the electron-phonon coupling. Experiments under isotropic hydrostatic pressure have provided fresh perspectives in this direction, namely the suppression of the charge ordering [17]. In contrast to the hydrostatic pressure, the uniaxial stress enhances the CDW in $YBa_2Cu_3O_{6.67}$ [18]. As in the case of the first discovery of the CDW in $YBa_2Cu_3O_{6+x}$, the uniaxial stress effect on the CDW was studied in microscopic x-ray scattering measurements. Due to technical challenges associated with performing transport measurements at cryogenic temperature under the uniaxial stress in a controlled manner, little was known about complementary macroscopic charge transport coefficients under the same conditions.

In order to fill this void, I will present charge transport and x-ray scattering experiments on $YBa_2Cu_3O_{6+x}$ under the uniaxial stress. These experimental results will be presented

in chapter 4 and chapter 5, respectively. Before moving on to describe the core results, this thesis will continue with the background physics for $YBa_2Cu_3O_{6+x}$ in chapter 2, and explanations about the experimental techniques we have used in chapter 3.

Chapter 2

Background physics for $YBa_2Cu_3O_{6+x}$

2.1 Introduction

Materials with significant electron correlations, known as strongly correlated electron systems, are of particular interest in modern condensed matter physics. Conventional theories often fail to describe the properties of such systems. A representative example is a Mott insulator which is expected to be metallic according to conventional band theory yet is insulating due to electron correlations despite the half-filled electronic configuration. As a consequence of electron correlations, various unconventional orders emerge in such systems when tuning physical parameters, since different many-body ground states are nearly degenerate. A prototypical strongly correlated system is found in the cuprates where high temperature superconductivity emerges in a doped Mott insulator (Fig. 2.1), as was first discovered in $La_{2-x}Ba_xCuO_4$ by Bednorz and Müller in 1986 [19].

Fundamental properties of superconductivity in cuprates, such as the symmetry of the superconducting order parameter, have been relatively well understood within the standard framework of the BCS theory. Also the antiferromagnetic Mott insulating state of parent compounds is well described by the Heisenberg model. What remains under debate in the physics of cuprates are unconventional collective behaviors (e.g., pseudogap, spin orders, charge orders, and various theoretically proposed orders etc..) observed in the intermediate doping regime between undoped and optimal doping, as well as the strange metal phase beyond optimal doping. To get insights into the nature of those collective phenomena, external fields have been utilized on top of temperature and doping to extend the cuprates phase diagram beyond those two parameters.

Applying external fields is a cleaner way to continuously change electronic properties of cuprates than tuning carrier dopings, which inevitablely induces disorders in non-stoichiometric materials. A magnetic field is often used as a tool to suppress superconductivity and is expected to uncover the metallic ground state masked by high temperature superconductivity. Remarkably, high field studies on particularly clean cuprate single crystals have discovered a Fermi surface reconstruction by observing quantum oscillations [20]. Moreover, it was observed in x-ray scattering experiments that the magnetic field stabilizes the CDW introduced in chapter 1 [21, 22]. The quantum mechanical degrees of freedom of electrons (charge and spin) can couple with the lattice, therefore pressure studies have also provided fresh perspectives. To this end, isotropic hydrostatic pressure, which suppresses

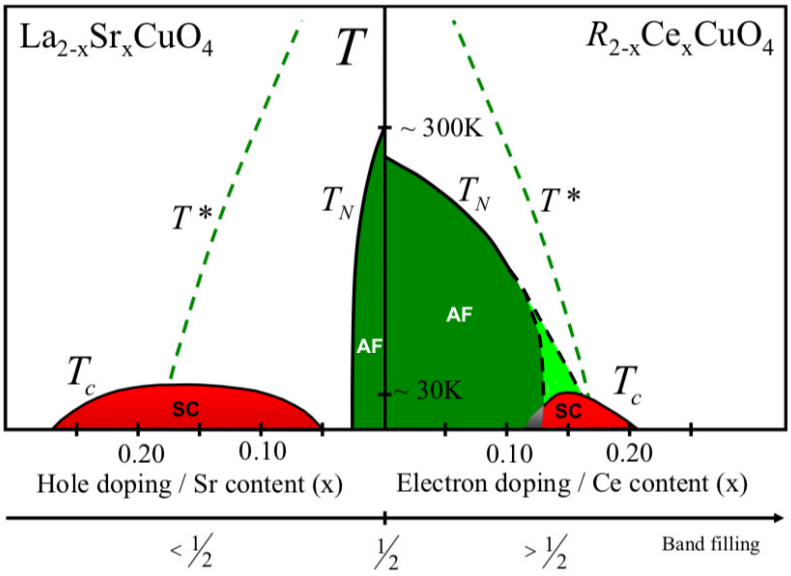

Figure 2.1: **Phase diagram of hole- and electron-doped cuprates.** Superconductivity emerges in a doped antiferromagnetic Mott insulator whose original band filling in the $3d_{x^2-y^2}$ orbital is 1/2 (one electron / hole). The dopant can be holes and electrons. Figure from Ref. [24].

charge order and enhances superconductivity, has been often used [17, 23]. The uniaxial stress, on the other hand, stabilizes charge order and suppresses superconductivity, which is qualitatively opposite to the hydrostatic pressure effects [18]. Lattice vibrations, phonons, are also affected by both hydrostatic and uniaxial pressures, which directly deform the underlying crystal structures. Extending the phase diagram using uniaxial stress as a new axis and providing a correspondence between macroscopic transport coefficients and atomic scale correlation functions under uniaxial stress are among the core motivations of this thesis.

Impacts on theories by cuprates should be also mentioned as a closing topic of the introduction. Broadly speaking, there are two theoretical approaches in condensed matter physics given the impossibility to exactly solve equations of motion of all components of a solid and given that only electrons near the Fermi level contribute to the macroscopic properties as we stressed in chapter 1.1. One approach is to (exactly) solve a simple model Hamiltonian. Those models are believed to contain the essence of the many-body effects although one always has to bear in mind whether the model properly captures all aspects of the real material. The Hubbard model is a representative example. The absence of analytic solutions in the two-dimensional Hubbard model, often used as a model of cuprates, has stimulated numerous computational efforts to obtain the ground and excited states. The other approach is to solve the first-principle Hamiltonian with reasonable approximations, such as density functional theory (DFT). While DFT does not predict Mott insulating states in the cuprate parent compounds, the phonon spectra obtained by DFT and the description of metallic states are reasonably consistent with experimental observations. In the following we discuss several theoretical descriptions which help to understand experimental findings.

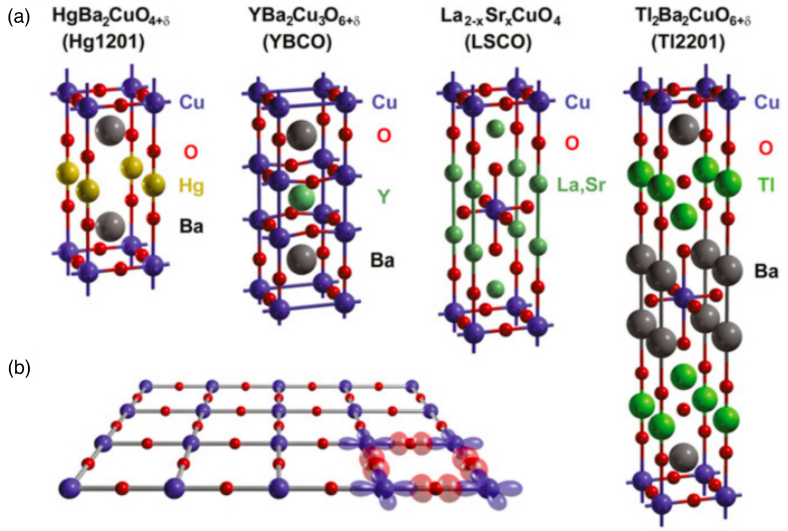

Figure 2.2: **Crystal structure of cuprates.** (a) Unit cells of different cuprate compounds. (b) CuO_2 planes. The hybridization of $3d_{x^2-y^2}$ orbital on the copper site and $2p_x$ and $2p_y$ orbitals on the oxygen sites is illustrated. Figures from Ref. [25].

This chapter will present, describe, and classify the most typical features of cuprates with particular focus on the $YBa_2Cu_3O_{6+x}$ system studied in this thesis. As it is always the case for any material, the information about the crystal structure and electronic structure near the Fermi level is the starting point to understand the origin of the macroscopic properties. For instance, the orbital degrees of freedom in $3d$ orbitals of the cuprates are essentially frozen and, thus, the starting point can be simplified considering this aspect before tackling complex problems. In the following sections, the crystal structure, electronic configuration, Fermi surface, and the phase diagram are discussed and explained in detail in order to understand the physics at the base of $YBa_2Cu_3O_{6+x}$.

2.2 Crystal structure

The common feature among all cuprate compounds is a CuO_2 plane in their layered perovskite structure sandwiched by charge reservoir layers[1] (Fig. 2.2). The CuO_2 plane consists of CuO_4 square-shaped plaquettes whose oxygen corners are shared with adjacent squares. The CuO_4 plaquette is classified into three types depending on the number of apical oxygens out of the CuO_2 plane. CuO_2 planes with zero, one, or two apical oxygens give raise to square, pyramid, or octahedral structure, respectively. In the $La_{2-x}Ba_xCuO_4$ (214) compounds, those classifications correspond to T, T*, and T' structures. The number of CuO_2 planes in a unit cell depends on the compounds. It can be one (La-based 214 compounds, $HgBa_2CuO_{4+\delta}$), two ($Bi_2Sr_2CaCu_2O_{8+\delta}$, $YBa_2Cu_3O_{6+x}$), three ($HgBa_2Ca_2Cu_3O_{8+\delta}$, $Bi_2Sr_2Ca_2Cu_3O_{10}$), and more. The highest T_c at ambient pressure is

[1]Charge reservoir layers are also known as block layers as proposed by Tokura and Arima [26]. Following their classification method, electron doped cuprates were discovered by themselves [27].

found in the three-layer compound, $HgBa_2Ca_2Cu_3O_{8+\delta}$. The role of the other elements in the charge reservoir layers is to supply charges into the the CuO_2 planes. From an ionic viewpoint, one CuO_2 plane consists of Cu^{2+} and O^{2-} therefore the CuO_2 plane is charged -2. In parent compounds, the charge of the charge reservoir layers is +2 to maintain the charge neutrality of the whole crystal. For example in La_2CuO_4, the charge reservoir layer, La_2O_2, is charged +2 as the valence number of the La ion is +3. By substituting La^{3+} with Ba^{2+}, the charge of the charge reservoir layers is reduced by x in $La_{2-x}Ba_xCuO_4$, and the excess charge of $+x$ enters the CuO_2 plane. In this case the effective hole doping charge in the CuO_2 plane equals $+x$. In a similar fashion, it is possible to dope electrons into the CuO_2 plane, e.g., in $Nd_{2-x}Ce_xCuO_4$ by substituting Nd^{3+} with Ce^{4+}. Those two types cuprates are termed hole-doped and electron-doped cuprates, respectively, depending on the dopant type. The comparison between hole-doped and electron-doped cuprates is an important issue in the study of cuprates. Nevertheless, in this thesis we focus on hole-doped samples.

The unit cell of $YBa_2Cu_3O_{6+x}$ is shown in Fig. 2.3. As in other cuprates, the unit cell is a layered structure comprising two CuO_2 planes. There are two different positions for Cu atoms and four different positions for O atoms in the unit cell. The Cu(1) atom and the O(1) atom bond together and they form CuO chain layers. The O(1) site is fully occupied in fully-oxygenated $YBa_2Cu_3O_{6+x}$ ($x = 1$) while the O(1) site is completely empty in the parent compound ($x = 0$). In the intermediate range ($0 < x < 1$), the O(1) sites are partially filled and various oxygen superstructures are formed in the CuO chain layers. The planar Cu(2), O(2), and O(3) atoms and the apical O(4) form the pyramid structure. However the distance between the Cu(2) atom and adjacent oxygen atoms differ quite a bit between in-plane and out-of-plane. The bond length of Cu(2)-O(4) is 2.3 Å while it is 1.9 Å between Cu(2) and O(2)/O(3), which realizes the two-dimensional nature of the CuO_2 plane. The in-plane Cu-O-Cu bond is not flat and characterized by a buckling which makes the Cu-O-Cu bond angle 165° [28, 29, 30]. Bond valence sums studies show that the valences of Y and Ba atoms are nearly unchanged from valence numbers expected from their ionic bonds in the entire hole doping range [29]. It indicates that the Y layer between two CuO_2 plane layers and the BaO layer between the CuO_2 plane and CuO chain layer merely stabilize the crystal structure.

The crystal structure of the parent compound of $YBa_2Cu_3O_{6+x}$ is tetragonal. It undergoes a structural transition to orthorhombic as the oxygen content increases. The in-plane lattice parameter slightly increases upon doping up to $x = 0.35$. Beyond this value, two distinct in-plane lattice parameters are observed and the orthorhombicity monotonically increases upon doping until the chains are fully oxygenated (Fig. 2.4). In the orthorhombic phase, oxygen superstructures are present in the CuO chain layers. The oxygen superstructure orders are characterized by the periodicity of distinct patterns of chains filled with oxygen running along the b-axis (Fig. 2.5 (a)). The periodicity of those oxygen orders along the a-axis depends on the oxygen content x: the roman number in the order name indicates the periodicity, e.g., Ortho-I order has a period of one lattice constant, Ortho-II order has a period of two lattice constants, and so forth. The superstructure stability and correlation length also depend on temperature (Fig. 2.5 (b)). The long-range oxygen order in the CuO chain layers plays an important role for the electron transfer from the CuO_2 planes as one can see from the fact that the T_c of $YBa_2Cu_3O_{6.50}$ is different in the case of Ortho-I and Ortho-II orders [34] (Fig. 2.6 (a)). The electron transfer from the

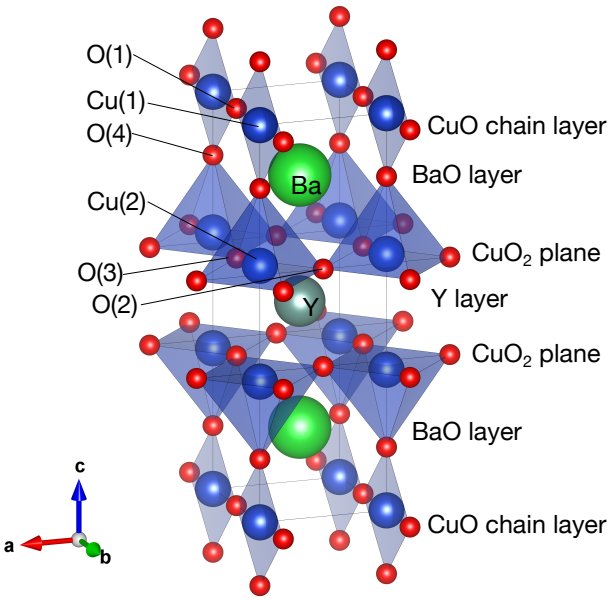

Figure 2.3: **Unit cell of $YBa_2Cu_3O_7$.** The unit cell of $YBa_2Cu_3O_{6+x}$ ($x \neq 1$) is larger than this unit cell shown here because O(1) atoms in the CuO chains are removed when $x \neq 1$. This figure was generated by VESTA [31].

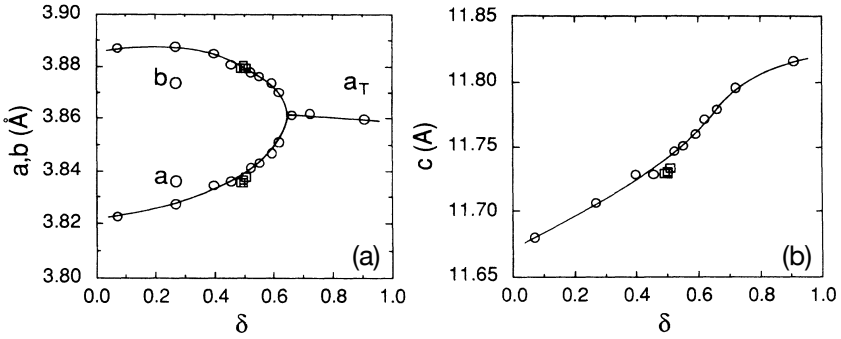

Figure 2.4: **Lattice parameters of $YBa_2Cu_3O_{7-\delta}$ as a function of δ.** (a) In-plane lattcie parameters. (b) Out-of-plane lattice parameter. Figures from Ref. [30]

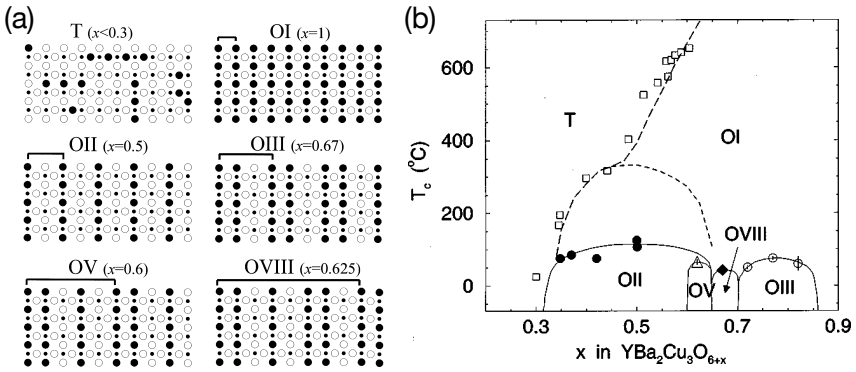

Figure 2.5: **Oxygen orders of $YBa_2Cu_3O_{6+x}$.** (a) Schematic picture of oxygen orders in the CuO chain layer. Small filled circles represent Cu(1) sites and large filled (unfilled) circles represent occupied (unoccupied) O(1) sites. T implies the tetragonal disordered state, and OI, OII, OV, OVIII, and OIII refer Ortho-I, Ortho-II, Ortho-V, Ortho-VIII, and Ortho-III oxygen orders, respectively. x in parenthesis is the optimal oxygen stoichiometry for each oxygen order. Figure from Ref. [32]. (b) Structural phase diagram of oxygen orders obtained in x-ray diffraction measurements. Figure from Ref. [33].

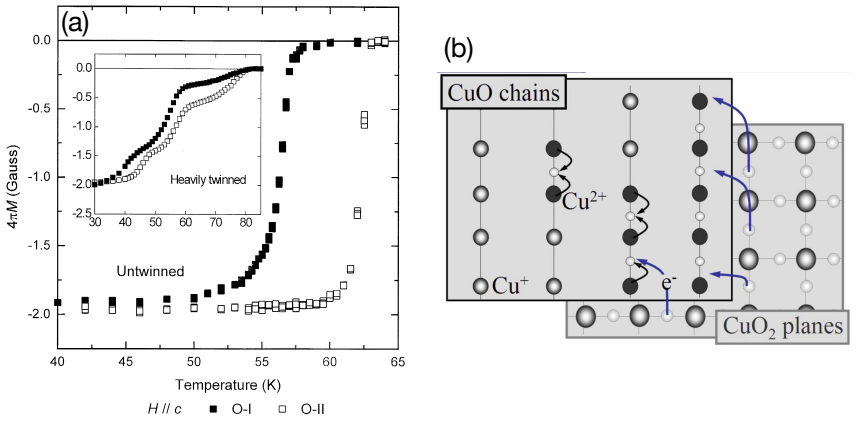

Figure 2.6: **Role of oxygen orders.** (a) Temperature dependence of magnetization for $YBa_2Cu_3O_{6.50}$. Filled (unfilled) points are the data for Ortho-I (Ortho-II) samples. Figures from Ref. [34]. (b) Schematic figure to explain the role of CuO chains for the charge transfer to CuO_2 layers. Figures from Ref. [35].

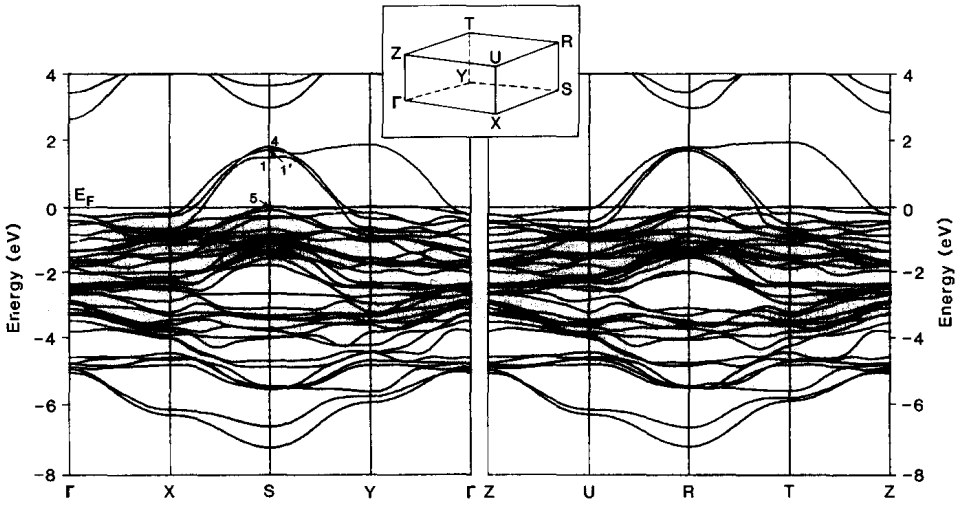

Figure 2.7: **Band structure of $YBa_2Cu_3O_7$ based on DFT.** The reciprocal space is along the high symmetry directions in the $k_z = 0$ (left) and π/c (right) planes of the orthorhomnic Brillouin zone. Nearly identical band structure at $k_z = 0$ and π/c planes reflects the two-dimensional nature of the electronic structure. Figures from Ref. [38].

CuO_2 plane to CuO chain layer is also qualitatively explained in Fig. 2.6 (b). The valence of the Cu(1) ions in a vacant chain is +1. As the oxygen is inserted between two Cu(1) sites, the valence of Cu(1) becomes +2 to keep the charge. At this stage there is no charge transfer between the CuO chain layer and the CuO_2 layers. Therefore x in $YBa_2Cu_3O_{6+x}$ is not equal to the hole doping p (the number of holes per Cu ion in the CuO_2 plane) unlike $La_{2-x}Ba_xCuO_4$ families where holes are doped by heterovalent substitutions. When a chain segment with at least two oxygen atoms is formed around $x > 0.35$, the electron transfers from the CuO_2 planes to the chain layers.

2.3 Electronic configuration and Fermi surface

Density-functional theory (DFT) calculations have shown that a strongly hybridized Cu $3d$-O $2p$ anti-bonding band lies across the Fermi level in lanthanum-based cuprates [36, 37] and $YBa_2Cu_3O_{6+x}$ [38]. As shown in Fig. 2.3, the broad band stemming from Cu $3d$-O $2p$ hybridization is dominant (the band width is $\sim$ 9 eV), whereas the Y $4p$, O $2s$, and Ba $5p$ bands are narrower and located at -21.3 eV, -16.7 eV, and -10.3 eV below E_F, respectively. Therefore those bands other than Cu $3d$ and O $2p$ orbitals do not contribute to the low energy physics. The valence number of Cu can be +1 (d^{10}), +2 (d^9), or +3 (d^8). In fact, photoemission [39, 40] and x-ray absorption [41] studies have shown that the valence of Cu is +2 (d^9). Note that the photoemission studies indicated the existence $d^{10}\underline{L}$ states ($\underline{L}$ is a ligand hole) through the Cu $3d$-O $2p$ covalency [39].

The unit cell has certain symmetries and it is invariant under symmetry operators such as rotation, inversion, and mirror reflection. It is known that those symmetry operators belong to a certain point group and the number of total point groups is 32. For example, the cubic (octahedron type) group is one of them. If the Hamiltonian of the system is

invariant under the group operators, properties of the energy levels of each orbital can be classified by means of the symmetry and, thus, the problems can be simplified. Let us consider that one Hamiltonian $\mathcal{H}$, its energy eigenvalue is E, and the wavefunctions that belong to $\mathcal{H}$ are ϕ_n $(n = 1, 2, ..., d)$, where d is the degeneracy of the eigenstates $(\mathcal{H}\phi_n = E\phi_n)$ and those are orthonormal basis functions. When $\mathcal{H}$ is invariant under an operator R which belongs to one group $\mathcal{G}$, $\mathcal{H}$ and R are commutative, namely $[\mathcal{H}, R] = 0$. In this case,

$$\mathcal{H}(R\phi_n) = R\mathcal{H}\phi_n = RE\phi_n = E(R\phi_n). \tag{2.1}$$

Therefore $R\phi_n$ is also an eigenfunction of $\mathcal{H}$. Since the set of ϕ_n $(n = 1, 2, ..., d)$ forms the orthonormal basis, $R\phi_n$ is equal to the linear combinations of ϕ_n $(n = 1, 2, ..., d)$. If one defines coefficients of the linear combination as $(\phi_m, R\phi_n) = D_{mn}(R)$, then one obtains,

$$R\phi_n = \sum_{m=1}^{d} \phi_m D_{mn}(R). \tag{2.2}$$

Initially ϕ_n are defined as eigenfunctions of $\mathcal{H}$ in terms of quantum mechanics, Eq. (2.2) mathematically indicates that the matrix $D(R)$ is a representation of the group $\mathcal{G}$ and ϕ_n are bases of this representation because one can easily prove that $D(R)$ is a homomorphism[2]. In the representation theory, irreducible representations for all the point groups are algebraically known and one can obtain the number of irreducible representations (i) in a certain representation, such as $D(R)$ in Eq. (2.2), $n^{(i)}$ using the following formula:

$$n^{(i)} = \frac{1}{h} \sum_{R \in \mathcal{G}} \chi_R^{(i)} \chi_R, \tag{2.3}$$

where h is the order of $\mathcal{G}$. $\chi_R^{(i)}$ and χ_R are the characters of the irreducible representations (i) and the representation $D(R)$, respectively. The character of a representation is defined as the trace of the representation, e.g., $\mathrm{Tr}[D(R)]$. Applying this general theory to the $3d$ orbitals whose wave function $\varphi_{nlm}(\boldsymbol{r})$ is given as a product of the radial function $P_{nl}(r)$ and the spherical harmonics $Y_{lm}(\theta, \phi)$ $(\varphi_{nlm}(\boldsymbol{r}) = P_{nl}(r)Y_{lm}(\theta, \phi)$ $(n = 2,\ l = 2,\ m = 0, \pm 1, \pm 2))$ under the cubic (octahedron) group $(\mathcal{G} = O_h)$, one obtains $(n^{(a_{1g})}, n^{(a_{2g})}, n^{(e_g)}, n^{(t_{1g})}, n^{(t_{2g})}) = (0, 0, 1, 0, 1)$. Therefore the five-fold degenerate $3d$ orbitals are split into two-fold degenerate e_g orbitals and three-fold degenerate t_{2g} orbitals (Fig. 2.8). This is called the crystal field splitting. Note that the wave functions of e_g and t_{2g} orbitals are elongated along the main axes (x, y, z) and the diagonal axes (xy, yz, zx) of the cubic crystal system, respectively. Therefore in the octahedron case, the t_{2g} orbitals are the ground states because those are away from the ligands (Fig. 2.8). For the same reason, the e_g orbitals are the ground states in the case of tetrahedron type. Note also that when multiple electrons d^n $(n = 2, 3, ..., 8)$ exist in the $3d$ orbitals, the ground state is not obvious because of Hund's rule originated by the electron-electron Coulomb interaction. The treatment of the multiple electrons[3] is beyond the scope of this thesis, because the valence of Cu is +2 (d^9) in cuprates, thus, hereafter we focus on the single hole case.

[2]For $R_i, R_j, R_k \in \mathcal{G}$ which satisfy $R_iR_j = R_k$, $D(R)$ is called a homomorphism if $D(R_i)D(R_j) = D(R_k)$ is satisfied.

[3]Multiple electrons (or holes) are usually described by multiplet structures. The details of the multiplet structures can be seen anywhere, e.g., in Ref. [42].

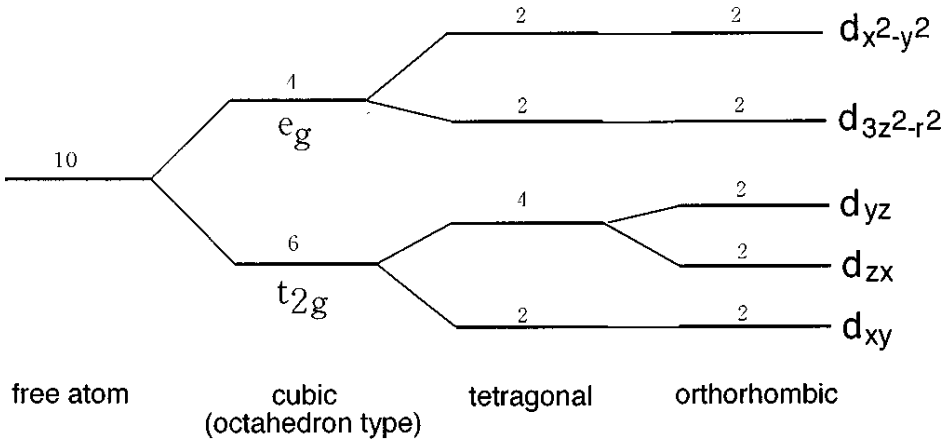

Figure 2.8: **Energy diagram of $3d$ orbitals under the crystal field.** The symmetries of the crystal fields are free atom, cubic, tetragonal, and orthorhombic from the left side. The numbers on each level are the degeneracy including spins. Note that the energy level is opposite if the cubic symmetry is the tetrahedron type. Figure from Ref. [43].

Up until now we have seen that the lowered symmetry by a crystal lattice leads to degeneracy splitting and the energy of the lowest energy state becomes lower. Conversely, the crystal lattice can be spontaneously distorted by degeneracy splitting. Although the lattice distortion requires an elastic energy gain, the total energy of the electron and lattice systems can be further lowered depending on the balance of the two effects. This phenomenon is known as the Jahn-Teller effect. In fact the $e_{\rm g}$ hole in Cu^{2+} is a well known Jahn-Teller ion, which leads to a further tetragonal distortion with the Cu-O bond of out-of-plane which is longer than that of in-plane. This distortion results in a splitting of the partially occupied $e_{\rm g}$ orbital into occupied $d_{3z^2-r^2}$ states and half-filled $d_{x^2-y^2}$ states (Fig. 2.8).

We have seen that the Cu $3d$ orbitals split due to the crystal field and the highest energy state is the $3d_{x^2-y^2}$ state in the atomic picture. In an octahedral crystal field, the six-fold degenerate O $2p$ levels split into two-fold degenerate σ and four-fold degenerate π orbitals, which are parallel and perpendicular to the planar Cu-O direction, respectively (Fig. 2.9). The strong covalency between the $3d_{x^2-y^2}$ orbital and O $2p_\sigma$ orbital results in the strong hybridization between those two orbitals. This hybridization consists of the anti-bonding and bonding bands depending on the relationship of the phase between the two orbitals. This anti-bonding band can be seen as a remarkably simple dispersive feature near the Fermi energy in the band structure calculation shown in Fig. 2.3. The bottom dispersive bands in Fig. 2.3 are the bonding bands. While this hybridization gives the wide band width, the hybridization between the other Cu $3d$ and O $2p_\pi$ orbitals is weak due to the small overlap of the wave functions.

In non-interacting or weakly interacting electron systems, the simple classification between metals and insulators is made based on the filling of the electronic bands. The system whose highest energy band is partially filled is metallic, whereas it is insulating if it is fully filled. In other words, the Fermi level of insulators lies in a band gap, while the one of metals lies in a band. In this description, the half-filled $3d_{x^2-y^2}$ orbital which we consider

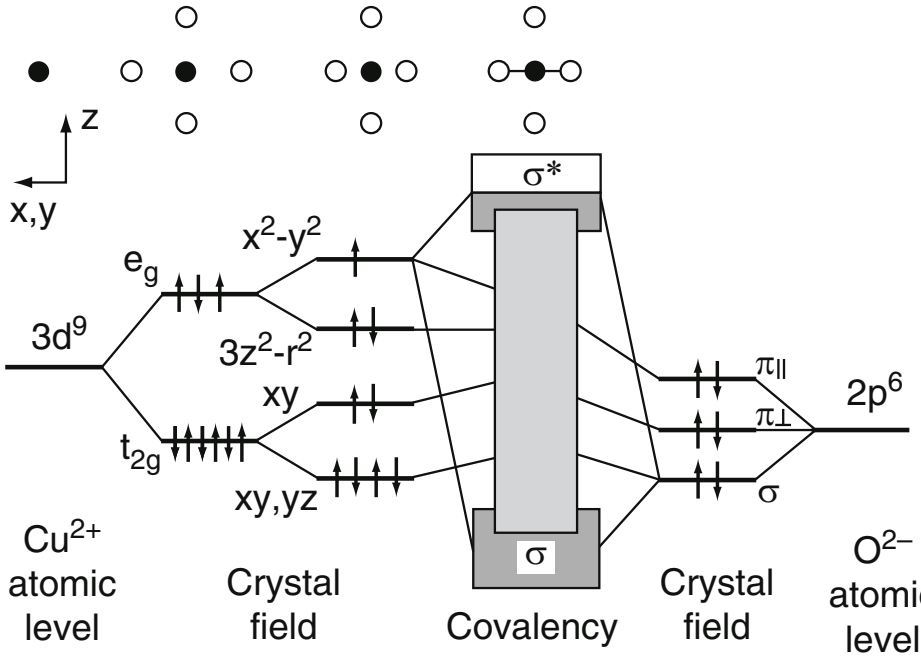

Figure 2.9: **Energy diagram of Cu $3d$ orbitals, O $2p$ orbitals, and their hybridization under the crystal field.** The crystal field splitting in Cu $3d$ orbitals (same as Fig. 2.8) and O $2p$ orbitals are shown. The planar Cu $3d_{x^2-y^2}$ orbital and O $2p_\sigma$ orbitals are hybridized due to their covalency. Figures from Ref. [44].

here is always expected to be a metallic state as one can see the band crossing at the Fermi energy (Fig. 2.3). However, the parent compound of cuprates shows insulating behaviors in transport experiments. The key to understand this discrepancy between the expectation from conventional theories and the reality of experiments is the intra-atomic Coulomb repulsion on the Cu $3d_{x^2-y^2}$ orbital. To treat such a correlation effect, the two-dimensional Hubbard model has been extensively studied as a minimal theoretical model of cuprates.

$$\mathcal{H} = -t \sum_{<ij>\sigma} \left(c^\dagger_{i\sigma} c_{j\sigma} + c_{i\sigma} c^\dagger_{j\sigma} \right) + U \sum_i n_{i\uparrow} n_{i\downarrow}, \tag{2.4}$$

where $c^\dagger_{i\sigma}$ ($c_{i\sigma}$) is a creation (annihilation) operator of an electron on the site i and $n_{i\sigma} = c^\dagger_{i\sigma} c_{i\sigma}$. In this model, the Coulomb-U represents the intra-atomic Coulomb repulsion in the localized Cu $3d$ orbitals. Intuitively, first and second terms in the Hubbard model represent the itinerant and localized nature of correlated metals, respectively. In the limit of $t \gg U$, the correlation effect is ignored and this model is reduced to the single-band tight-binding model. This model describes metallic states (Fig. 2.10 (a)) and, therefore, is often used to phenomenologically describe quasiparticle dispersions near the Fermi level of doped metallic cuprates. When the Coulomb-U is finite, however, the double occupancy on one atomic site costs the Coulomb-U, which prevents inter-atomic motions of electrons. In the presence of the Coulomb-U, the charge transfer process between two atomic sites $d^n d^n \rightarrow d^{n-1} d^{n+1}$ can lower the total energy of the system by opening the single-particle gap U, which splits the $3d$ orbitals into the lower Hubbard band (LHB) and upper Hubbard band (UHB) as depicted in Fig. 2.10 (b-d). By this gap opening,

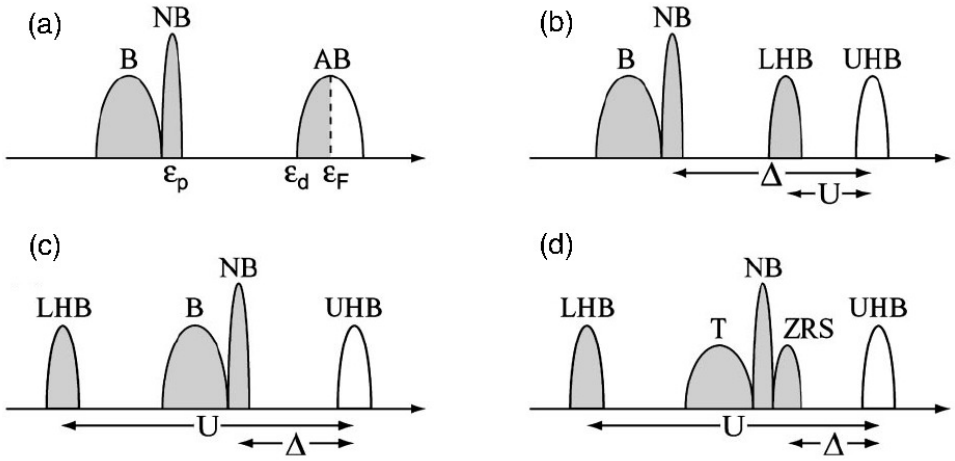

Figure 2.10: **Schematic density of states of half-filled correlated metals.** (a) A band metal without electron correlations. (b) A Mott-Hubbard insulator ($U < \Delta$). (c) A charge-transfer insulator ($U > \Delta$). (d) A charge-transfer insulator with a Zhang-Rice singlet state. It is the case of the cuprates. Abbreviations, B: bonding bands, AB: anti-bonding bands, NB: non-bonding bands, UHB: upper Hubbard band, LHB: lower Hubbard band, ZRS: Zhang-Rice singlet, T: triplets due to the hybridization between the Cu $3d$ and O $2p$ orbitals. Figures from Ref. [47].

the density of states becomes zero around the Fermi level, which is consistent with the insulating behavior in charge transport experiments.

However, this atomic picture where only the Cu $3d$ orbitals are considered is oversimplified to model cuprates because those orbitals are hybridized with the O $2p$ orbitals. Therefore the model should include at least the cluster of Cu and O atoms in the CuO_2 plane. In this case, one needs to consider the charge transfer from the ligand oxygen to the Cu $d^n \rightarrow d^{n+1}\underline{L}$ and the total energy is lowered by the charge transfer energy Δ. The single particle gap of the cluster is given by either U or Δ, whichever is lower [45]. When $U < \Delta$, the system is called a Mott-Hubbard insulator and the low energy physics can be described by the single-band Hubbard model without the O $2p$ orbitals (Fig. 2.10 (b)). On the other hand the system is called a charge-transfer insulator if $U > \Delta$ (Fig. 2.10 (c)). Such a classification was made by Zaanen, Sawatzky, and Allen[4] [45]. Based on the photoemission studies, U and Δ of the various cuprates were estimated to be 6 - 8 eV and 0.3 - 2 eV, respectively [46, 39] and, thus, the parent compounds of the cuprates are categorized as charge-transfer insulators ($U > \Delta$).

To deal with the hybridization between the Cu $3d_{x^2-y^2}$ and O $2p_x$ ($2p_y$) orbitals in the CuO_2 planes, the Emery model (also known as p-d or three band model) was introduced [48].

$$\mathcal{H} = \sum_{i,j,\sigma} \varepsilon_{ij} a^\dagger_{i\sigma} a_{j\sigma} + \frac{1}{2} \sum_{i,j,\sigma,\sigma'} U_{ij} a^\dagger_{i\sigma} a_{i\sigma} a^\dagger_{j\sigma'} a_{j\sigma'}, \tag{2.5}$$

[4]In a solid, electrons form bands at each energy level with the finite band width (e.g., W_d, W_p for the d, p-bands, respectively). Therefore the band gap of a Mott insulator is smaller than the single-particle gap and given by $U - W_d$ for a Mott-Hubbard insulator or $\Delta - (W_d + W_p)/2$ for a charge-transfer insulator.

where i is the lattice site on the CuO_2 planes. $a^{\dagger}_{i\sigma}(a_{i\sigma})$ is a creation (annihilation) operator of a hole with the spin σ in the $3d$, O $2p_x$ and $2p_y$ states at the site i. The site-diagonal terms $(\varepsilon_{ii}, U_{ii})$ are the band levels and on-site Coulomb repulsion, i.e., (ε_d, U_d) and (ε_p, U_p) for the $3d$, O $2p$ states. Finite off-diagonal terms are hopping integrals $\varepsilon_{ij} = \pm t$ and an interaction $U_{ij} = V$ between neighboring sites (Cu and O). The Emery model is the multi-band Hamiltonian yet can be effectively simplified to the single band Hamiltonian called $t - J$ model because of the hybridization between correlated Cu and the non-correlated O orbitals as shown by Zhang and Rice [49]. It suggested that the hybridization between the Cu $3d$ spin and O $2p$ hole forms the singlet (so-called Zhang-Rice singlet), and the band of the Zhang-Rice singlet is the highest energy state below the Fermi energy (Fig. 2.10 (d)). The $t - J$ model is also the effective Hamiltonian of the single-band Hubbard model in the limit of $U \gg t$. In this effective single band Hamiltonian, the Zhang-Rice singlet band effectively plays the role of the LHB in the Mott-Hubbard insulator. Below the hole doping level where the system transits to a metal from an insulator, it is considered that the localized Zhang-Rice singlets are spatially randomly distributed.

So far the electronic configurations of the parent or lightly doped compounds have been described in the localized picture to explain the Mott insulating behaviors due to electron correlations. To explain metallic properties of the doped cuprates in the itinerant picture, the Fermi surface will be discussed in the rest of this section. As shown in Fig. 2.11, the spectral weight of the single-particle spectral function obtained in angle-resolved photoemission spectroscopy (ARPES) measurements appears at the Fermi level upon hole doping while the density of states is completely gapped out in the parent and lightly doped compounds (Fig. 2.10). In the low doping regime, the spectral weight appears only around $\boldsymbol{k} \sim (\pi/2, \pi/2)$. This is known as the Fermi arc whose topology is disconnected in the first Brillouin zone. The absence of spectral weight around $\boldsymbol{k} \sim (\pi, 0),\ (0, \pi)$ is interpreted as the pseudogap formation. Upon further doping, the Fermi arcs become longer and finally they bridge to form the connected Fermi surface [50]. The Fermi surface observed by ARPES on a sample whose hole doping is p is a hole-like Fermi surface whose area is $1+p$ centered at $\boldsymbol{k} \sim (\pi, \pi)$ in the intermediate doping regime and an electron-like Fermi surface whose area is 1-p centered at $\boldsymbol{k} \sim (0, 0)$ in the overdoped regime. In comparison with the Hall number $n_{\rm H}$ based on the high field Hall effect experiments (Fig. 2.11), the carrier density is consistent with ARPES only for $p > p^* = 0.19$ (p^* is the critical doping of the pseudogap) although it is not obvious how the carrier density based on the disconnected Fermi arc is estimated.

Quantum oscillations are another powerful technique to obtain information about the Fermi surfaces of metals. For $p > 0.19$, a large hole-like Fermi surface was observed with quantum oscillations and it is in line with the ARPES and Hall measurements [20]. On the other hand, in the lower doping regime where the magnetic order prevails ($p < 0.08$), the presence of small Hall like Fermi pockets was indicated by quantum oscillations experiments. This could be understood as a small hole Fermi surface reconstructed by the antiferromagnetic order or fluctuation whose propagation vector is $\boldsymbol{Q}_{\rm AF} = (\pi, \pi)$[5] (Fig.

[5]Conventionally, $2\pi/a$ is often used as the unit of scattering vectors $\boldsymbol{Q}$ in scattering experiments while $1/a$ is often used as the unit of momentum $\boldsymbol{k}$ in photoemission experiments, where a is the lattice constant. For instance, $\boldsymbol{Q}_{\rm AF} = (1/2, 1/2)$ in the former unit and (π, π) in the latter unit. In this thesis, we basically follow this convention but $1/a$ is used as a common unit in discussing scattering vectors in relation with the Fermi surface.

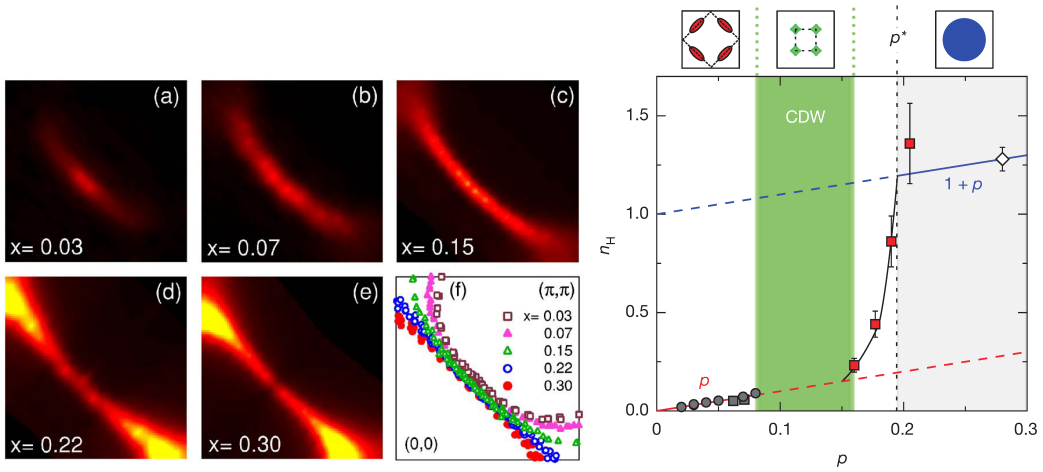

Figure 2.11: **Doping dependence of the Fermi surface and Hall number.** (Left) (a-e) The spectral weight of the single-particle spectral function at the Fermi level in the first quadrant of the first Brillouin zone measured in ARPES on $La_{2-x}Sr_xCuO_4$ ($x = 0.03$, 0.07, 0.15, 0.22, and 0.30). Note x is equal to the hole doping p in these compounds. (f) The peak positions of the momentum-distribution functions in panels (a-e). Figures from Ref. [50]. (Right) The Hall number n_H as a function of the hole doping p measured in the high field Hall effect measurements. The red line indicates $n_H = p$; the blue line indicates $n_H = 1 + p$, which is naively expected based on the single hole Fermi surface shown in the left panels. Data are from $La_{2-x}Sr_xCuO_4$ (gray circles), $YBa_2Cu_3O_{6+x}$ (gray and red squares), and $Tl_2Ba_2CuO_{6+\delta}$ (white diamond). Schematic Fermi surfaces are shown above the graph: Reconstructed small hole pockets below $p = 0.08$, where the magnetism prevails (red), reconstructed small electron pockets between $p = 0.08$ and 0.16, where the CDW prevails (green), and a single large hole Fermi surface centered at (π, π) above $p = 0.19$ (blue). Figures from Ref. [52].

2.11). For a long time, the corresponding Fermi surface was not detected in ARPES yet such a reconstruction was reported in very recent ARPES measurements in multi layered cuprates [51]. Another complication exists at the intermediate doping range where charge orders were observed ($0.08 < p < 0.16$). In this regime, the carriers could be electrons rather than holes based on the negative Hall number at low temperature. Moreover, the quantum oscillation measurements also suggested the presence of the small electron pocket. This is attributed to the Fermi surface reconstruction induced by the static CDW order. Due to the absence of clear ARPES data of $YBa_2Cu_3O_{6+x}$ in this doping regime, with the strongest charge order among cuprates families, some important information about the Fermi surface, e.g., its shape and location in reciprocal space, is still missing.

Overall, the metallic behavior of the doped cuprates can be relatively well understood in the Fermi liquid theory for $p > 0.19$. On the other hand, unconventional non-Fermi liquid like states for $p < 0.19$ have prevented researchers from understanding the metallic properties in terms of conventional Fermi liquid theory and at the same time provided further complications in relation to charge and spin orders, pseudogap, and Mott insulating states. Nevertheless, we have presented an overview of the basic building blocks of cuprates, i.e., the crystal structure and electronic configurations. In the following section, the various

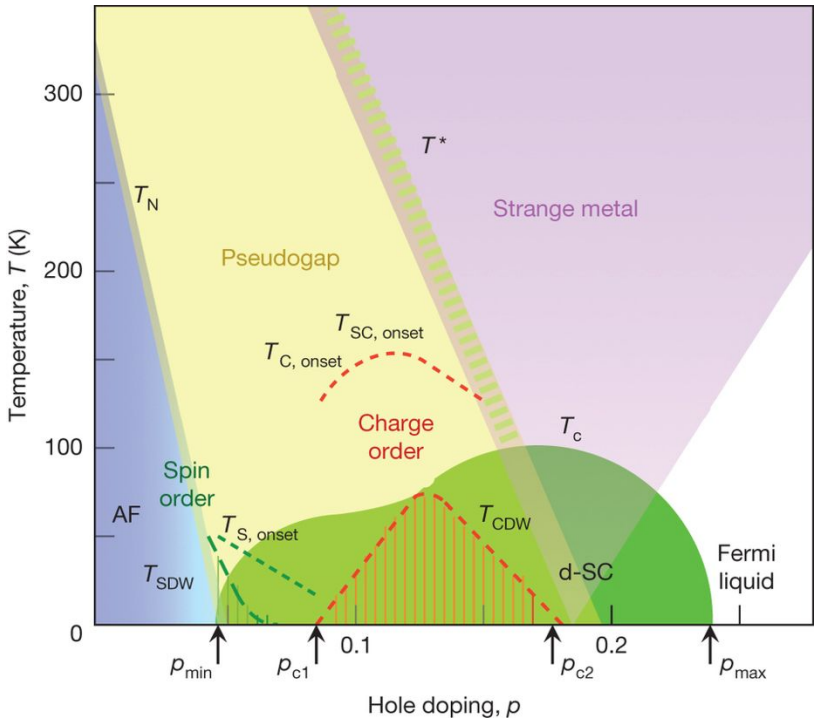

Figure 2.12: **Generic phase diagram of hole-doped cuprates.** Figure from Ref. [53].

collective orders in the cuprate phase diagram are phenomenologically described with a particular focus on the charge ordering.

2.4 Phase diagram and phenomenology

The phase diagram of the hole-doped cuprates is depicted in Fig. 2.12. The undoped parent compound ($p = 0$) is an antiferromagnetic Mott insulator. The long range antiferromagnetic order is rapidly suppressed upon doping holes into the system and completely vanished at $p_{\mathrm{min}} \sim 0.05$. Above p_{min}, the superconductivity sets in and the superconducting critical temperature T_{c} increases as the holes are doped. T_{c} is maximized at $p_{\mathrm{opt}} \sim 0.16$, called optimal doping. In the doping region above p_{opt}, known as overdoped regime, the superconductivity is rapidly suppressed and no longer observed above $p_{\mathrm{max}} \sim 0.30$. On the other hand, the doping region between p_{min} and p_{opt} is called underdoped regime and there diverse ground states reside. A plateau of T_{c} is observed around $p \sim 0.125$ in the middle of the underdoped regime, which has been known as the 1/8 anomaly named after this particular doping $p \sim 0.125$, which is also that of most samples studied in this thesis. The normal state above T_{c} in the underdoped regime is known as the pseudogap state where gap-like signatures are observed in many physical quantities. The origin of the pseudogap is still controversial to date. The presence of charge orders and spin orders in a part of the pseudogap regime also has prevented a full understanding of the pseudogap. The pseudogap is seen up to the characteristic temperature T^* and the strange metallic behavior is observed above T^*. The metallic behavior in this regime, namely the T-linear resistivity, differentiates the strange metal from the ordinary Fermi liquid like metals where

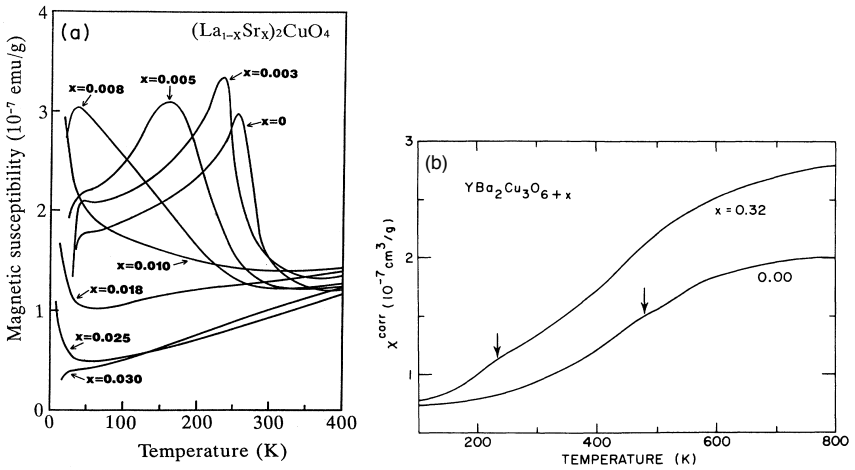

Figure 2.13: **Magnetic susceptibility of lightly doped cuprates.** (a) $(La_{1-x}Sr_x)_2CuO_4$ for various x. Figure from Ref. [54]. (b) $YBa_2Cu_3O_6$ and $YBa_2Cu_3O_{6.3}$. Figure from Ref. [55].

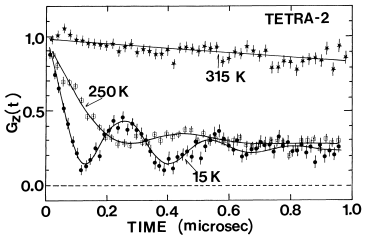

Figure 2.14: **Zero-field μ^+ spin relaxation functions $G_Z(t)$ of $YBa_2Cu_3O_{6.2}$ in μSR measurements.** The oscillation below T_N indicates the presence of a magnetic order. Figure from Ref. [56].

T^2-dependent resistivity is expected. As a consequence, the strange metal phase is the least understood part of the phase diagram.

In the following sections, those phases in the phase diagram will be discussed on the basis of several experimental findings.

Antiferromagnetism

Macroscopic magnetic susceptibility measurements indicate the antiferromagnetic order in the $(La_{1-x}Sr_x)_2CuO_4$ system, up to $x \sim 0.075$ [54]. The susceptibility in this system showed the typical Curie-like temperature dependence, where the Néel temperature T_N can be seen as a local maximum of the magnetic susceptibility (Fig. 2.13). As substituting Sr for La, T_N is lowered and this peak structure finally vanishes, indicative of the suppression of the antiferromagnetic order. The susceptibility in other cuprates including $YBa_2Cu_3O_{6+x}$ showed, however, quite broad temperature dependence, where the only kink like structure appears around T_N [55]. On the other hand, oscillations of asymmetry of muons due to a long range magnetic order were clearly observed below T_N in muon spin rotation (μSR) measurements (Fig. 2.14). The three-dimensional antiferromagnetic order was also observed by neutron diffraction measurements on La_2CuO_4 below the Néel temperature $T_N = 220$ K [57]. The order is commensurate and collinear antiferromagnetic with the ordering vector $\boldsymbol{Q}_{AF} = (1/2, 1/2, 1)$. The static magnetic order persists upon doping holes, yet the ordering vector is shifted away from the commensurate one. The doping

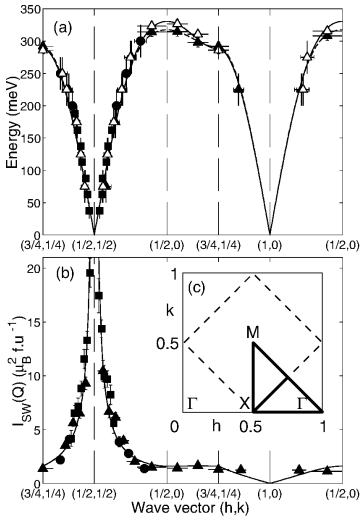

Figure 2.15: **Spin waves observed in La_2CuO_4 by inelastic neutron scattering.** (a) Dispersion relationship along high symmetry directions in the 2D-Brillouin zone shown in panel (c) at $T = 10$ K (open symbols) and 295 K (filled symbols). Squares, circles, and triangles were obtained for the incident neutron energy 250 meV, 600 meV, and 750 meV, respectively. (b) Spin-wave intensity at 295 K. The solid curves show the predictions of linear spin-wave theory. Figures from Ref. [61].

dependence of the incommensurability has been studied by neutron scattering experiments and it monotonically increases as a function of doping [58]. The spin moment orientation depends on the system. For instance, it is along the Cu-O bond direction in $YBa_2Cu_3O_6$ while it is along the diagonal direction (45 degrees away from the Cu-O bond direction) in La_2CuO_4.

The orbital degrees of freedom in $3d$ orbitals of the cuprates are essentially frozen and the charge degrees of freedom are also frozen in the Mott insulating state. Therefore the magnetism in undoped cuprates is well described by the Heisenberg model,

$$\mathcal{H} = -2J \sum_{<i,j>} \boldsymbol{S}_i \cdot \boldsymbol{S}_j, \tag{2.6}$$

where $\boldsymbol{S}_i$ is a total spin moment of electrons localized at i-th ion and J is the exchange interaction between spin moments of i-th and j-th ions. $\Sigma_{<i,j>}$ means the summation for spin moments of neighboring i-th and j-th ions. One obtains the Heisenberg model in the limit of $U \gg t$ in the Hubbard model (Eq. 2.4), where J is given by $J = -2t^2/U$. Antiferromagnetism, the state where spins are aligned anti-parallel, corresponds to the case of $J < 0$ whereas ferromagnetism emerges otherwise to minimize the energy. When the phase transition associated with the spontaneous symmetry breaking takes place, the collective excitation without energy gap called the Nambu-Goldstone mode appears. It is a spin wave (or magnon) in the case of the long range magnetic order, which breaks the spin rotational symmetry. The exchange interaction J in the Heisenberg model can be determined by measuring spin waves. The determination of J was attempted indirectly by Raman scattering measurements through the two-magnon process, i.e., the scattering between two magnons whose momentum magnitude is identical yet opposite in sign, [59, 60] and directly by inelastic neutron scattering measurements where the dispersive relationship of the low energy spin waves was observed (Fig. 2.15) [61]. In later years, the spin wave dispersion was also observed in resonant inelastic x-ray scattering (RIXS) measurements [62].

The long range antiferromagnetic order is completely suppressed at $p \sim 0.05$ yet spin fluctuations persist up to the optimal doping even in the absence of the static magnetic ordering [63]. The spin-wave-like dispersions in paramagnetic metals are termed paramangons. In the doping regime where superconductivity emerges, the spin fluctuations can play

the role of the bosonic glue for Cooper-pairs, i.e. carriers in superconductors. Antiferromagnetic spin fluctuations provide a qualitative explanation of the d-wave superconducting order parameter (see also next section).

Superconductivity

High temperature superconductivity in cuprates is named after its high superconducting transition temperature T_c compared with conventional superconductors known before cuprates. The theory of conventional superconductivity is called the BCS theory named after Bardeen, Cooper, and Schrieffer who first gave microscopic explanations for conventional superconductivity [64]. Thanks to the huge successes of the BCS theory, it has been widely believed that superconductivity could not survive above 30 K from both theoretical and experimental perspectives before Bednorz and Müller discovered high-temperature superconductivity in 1986 [65]. The record of the highest transition temperature has been beaten again and again after the first discovery. Several different experimental approaches to realize higher T_c materials beyond cuprates have been attempted in, e.g., iron-based superconductors [66] and hydrides under extremely large hydrostatic pressure [67]. Nevertheless so far the highest T_c at ambient pressure has been reported in one of cuprate families, i.e., $HgBa_2Ca_2Cu_3O_{8+\delta}$ which has $T_c \sim$130 K [68].

What makes the cuprates different from conventional superconductors? To address this point, it is useful to review the essence of the BCS theory [69]. When the spin-orbit interaction between two electrons is sufficiently weak, the wave function of two electrons $\Psi(\boldsymbol{r_1}, \sigma_1; \boldsymbol{r_2}, \sigma_2)$ can be decomposed into the orbital part $\varphi(\boldsymbol{r_1} - \boldsymbol{r_2})$ and spin part $\chi(\sigma_1, \sigma_2)$, i.e., $\Psi(\boldsymbol{r_1}, \sigma_1; \boldsymbol{r_2}, \sigma_2) = \varphi(\boldsymbol{r_1} - \boldsymbol{r_2})\chi(\sigma_1, \sigma_2)$. When those two electrons are placed onto the Fermi surface and the interaction between two electrons $V(\boldsymbol{r_1} - \boldsymbol{r_2})$ are not spin dependent, the Schrödinger equation to be solved is

$$\left[-\frac{\hbar^2}{2m}(\nabla_1^2 + \nabla_2^2) + V(\boldsymbol{r_1} - \boldsymbol{r_2})\right] \varphi(\boldsymbol{r_1} - \boldsymbol{r_2}) = (E + 2E_{\mathrm{F}})\varphi(\boldsymbol{r_1} - \boldsymbol{r_2}), \tag{2.7}$$

where E_{F} is the Fermi energy and E is the energy of two electrons with respect to E_{F}. The Fourier transformation of this equation is

$$(2\varepsilon_{\boldsymbol{k}} - E)\varphi(\boldsymbol{k}) = -\sum_{\boldsymbol{k'} > \boldsymbol{k}_{\mathrm{F}}} V(\boldsymbol{k}, \boldsymbol{k'})\varphi(\boldsymbol{k'}), \tag{2.8}$$

where $\varepsilon_{\boldsymbol{k}} = \hbar^2\boldsymbol{k}^2/2m - E_{\mathrm{F}}$ is the single particle energy of one electron. If one assumes that the interaction is attractive, $V(\boldsymbol{k}, \boldsymbol{k'}) = -|V_0|$, in the vicinity of the Fermi energy ($|\varepsilon_{\boldsymbol{k}}| < E_c$), one obtains the binding energy E as follows.

$$E \simeq -2E_c \exp(-2/N_0|V_0|) < 0, \tag{2.9}$$

when $N_0|V_0|$ is sufficiently small (weak coupling regime). N_0 is the density of states around the Fermi level. Eq. 2.9 tells that a bound state between two electrons always exists because the energy of two electrons is lowered if the attractive interaction exists. Such a bound state of two electrons is called a Cooper pair. The superconducting state is interpreted as the "Bose-Einstein-condensation-like" phase-coherent state of many Cooper

pairs in a solid, also known as the BCS state[6]. Therefore the central task in research of superconductivity is to reveal what the pairing potential $V(\boldsymbol{k}, \boldsymbol{k'})$ is from various experimental results. Early researchers of cuprates wondered whether Cooper pairings are formed as in conventional superconductors described by the BCS theory. The quantization of magnetic flux in cuprates was studied and the value of the quantum flux was $h/2e$, implying that the carriers in cuprate superconductors are also Cooper pairs [71]. Therefore one can in principle try to understand the superconductivity of cuprates in the framework of the (extended) BCS theory.

To discuss the bound state of two electrons (Eq. 2.9), the attractive interaction $V(\boldsymbol{k}, \boldsymbol{k'})$ was approximated to be constant in a certain energy range for simplicity, yet $V(\boldsymbol{k}, \boldsymbol{k'})$ needs to be clarified by experiments. The attractive interaction is related with the order parameter of superconductivity $\Delta(\boldsymbol{k})$ defined as

$$\Delta(\boldsymbol{k}) = \sum_{\boldsymbol{k'}} V(\boldsymbol{k}, \boldsymbol{k'}) \left\langle c_{-\boldsymbol{k'}\uparrow} c_{\boldsymbol{k}\downarrow} \right\rangle , \tag{2.10}$$

where $c_{\boldsymbol{k}\sigma}$ is an annihilation operator of an electron with the momentum $\boldsymbol{k}$ and spin σ and $\langle \cdots \rangle$ implies the mean field operation. The information of the order parameter is intimately linked with the pairing potential. In the mean field approximation, the order parameter $\Delta(\boldsymbol{k})$ follows the gap equation

$$\Delta(\boldsymbol{k}) = -\sum_{\boldsymbol{k'}} V(\boldsymbol{k}, \boldsymbol{k'}) \frac{\Delta(\boldsymbol{k'})}{2E_{\boldsymbol{k'}}} \tanh\left(\frac{E_{\boldsymbol{k'}}}{2k_{\mathrm{B}}T}\right), \tag{2.11}$$

where $E_{\boldsymbol{k}} = \sqrt{{\varepsilon_{\boldsymbol{k}}}^2 + |\Delta(\boldsymbol{k})|^2}$ is the single particle energy of Bogoliubov quasiparticles, which can be directly observed in ARPES. Obtaining solutions $\Delta(\boldsymbol{k}) \neq 0$ from this self-consistent equation is a necessary condition of the superconducting transition. If one assumes the spherical Fermi surfaces in the normal state, the pairing interaction can be expanded by spherical harmonics $Y_{l,m}(\boldsymbol{k})$,

$$V(\boldsymbol{k}, \boldsymbol{k'}) = -4\pi \sum_{l} V^l \sum_{m} Y_{l,m}(\boldsymbol{k}) Y^*_{l,m}(\boldsymbol{k'}). \tag{2.12}$$

In this case, for each angular momentum l, the superconducting order parameter is also expressed by means of $Y_{l,m}(\boldsymbol{k})$ through Eq. 2.11,

$$\Delta(\boldsymbol{k}) = \Delta^{(l,m)} Y_{l,m}(\boldsymbol{k}). \tag{2.13}$$

The symmetry of superconductivity can be s-wave (l=0), p-wave (l=1), d-wave (l=2), and so forth, based on the angular momentum l of the Cooper pairing[7]. The wave function of a Cooper pair is antisymmetric, therefore the spin part is antisymmetric (termed spin-singlet pairing) for l = 0, 2, ... and symmetric (termed spin-triplet pairing) for l = 1, 3, ...

[6]The attractive interaction in most of solids is not strong enough to actually induce the Bose-Einstein condensation (BEC), therefore this expression is intuitive but inaccurate for describing the BCS state. The BEC state was actually observed in the ultracold atomic systems rather than solid-state systems [70].

[7]In a solid, the assumption of the spherical Fermi surface is no longer valid because of the point group symmetry of the crystal lattice. Therefore the symmetry of $\Delta(\boldsymbol{k})$ should be classified by irreducible representations of the point group. Nevertheless we use this classification based on the angular momentum to intuitively understand the momentum dependence of $\Delta(\boldsymbol{k})$.

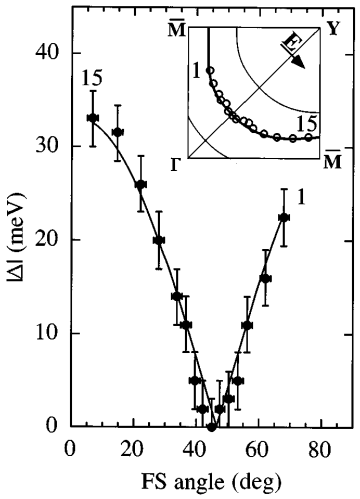

Figure 2.16: **Momentum dependence of the superconducting gap.** The gap amplitude was estimated by ARPES measurements on $Bi_2Sr_2CaCu_2O_{8+\delta}$. The gap amplitude is zero at the nodes ($\boldsymbol{k} \sim (\pi/2, \pi/2)$). Accordingly, the momentum points where the amplitude is maximized ($\boldsymbol{k} \sim (\pi, 0),\ (0, \pi)$) are termed anti-nodes. Inset shows the Fermi surface. Figures from Ref. [72].

The assumption in discussing Eq. 2.9 corresponds to the s-wave symmetry because the pairing interaction was assumed to be spherically symmetric. This simple assumption actually works for most conventional superconductors. The isotropic pairing is mediated by phonons and E_c is given by the Debye frequency $\hbar\omega_{\mathrm{D}}$, the maximum frequency of phonons. In this framework, the BCS theory explains a number of properties of conventional superconductivity such as the isotope effect, universal ratio $\Delta(T=0)/k_{\mathrm{B}}T_{\mathrm{c}} = \pi/e^{\gamma} \simeq 1.76$, and so on[8] [69]. Electrons at the same site tend to form a Cooper pair in the case of s-wave superconductors because $\Delta(\boldsymbol{r_1} - \boldsymbol{r_2})$ is a delta function in the real space if $\Delta(\boldsymbol{k})$ is constant in the $\boldsymbol{k}$-space. However in correlated materials, such a formation is energetically unfavorable because of the strong onsite Coulomb interaction. To avoid the pair formation at the same site ($\Delta(\boldsymbol{r_1} - \boldsymbol{r_2}) = 0$ when $\boldsymbol{r_1} = \boldsymbol{r_2}$), the summation of the superconducting order parameter over the Fermi surface needs to satisfy the following relationship, also known as a modern definition of unconventional superconductivity.

$$\sum_{\boldsymbol{k}} \Delta(\boldsymbol{k}) = 0. \tag{2.14}$$

To meet this criterion, $\Delta(\boldsymbol{k})$ needs to change the sign on the Fermi surface. It is impossible for the s-wave gap function whose amplitude is constant but possible for the higher order gap functions such as the p- and d-wave ones. The momentum points where $\Delta(\boldsymbol{k}) = 0$ are termed nodes, which were observed in a number of experiments.

To model the superconductivity in cuprates, the antiferromagnetic spin fluctuation has been proposed for a pairing potential as follows [73, 74].

$$V(\boldsymbol{k}, \boldsymbol{k'}) \sim \frac{3}{2} U^2 \chi_s(\boldsymbol{k} - \boldsymbol{k'})\ (>0), \tag{2.15}$$

where $\chi_s(\boldsymbol{k} - \boldsymbol{k'})$ is the dynamical spin susceptibility. The antiferromagnetic fluctuations shows a peak feature at $\boldsymbol{Q} = (\pi, \pi)$ in the dynamical spin susceptibility, therefore by

[8] γ is Euler's constant. $\gamma = \lim_{n\to\infty} (\sum_{k=1}^{n} 1/k - \log n)$

assuming χ_s to be $\chi_s(\boldsymbol{q}) = \delta(\boldsymbol{q} - \boldsymbol{Q})$, the gap equation (Eq. 2.11) becomes

$$\begin{aligned}\Delta(\boldsymbol{k}) &\sim -\sum_{\boldsymbol{k'}} \frac{3}{2} U^2 \chi_s(\boldsymbol{k} - \boldsymbol{k'}) \frac{\Delta(\boldsymbol{k'})}{2E_{\boldsymbol{k'}}} \tanh\left(\frac{E_{\boldsymbol{k'}}}{2k_{\mathrm{B}}T}\right) \\ &= -\frac{3}{2} U^2 \frac{\Delta(\boldsymbol{k}+\boldsymbol{Q})}{2E_{\boldsymbol{k}+\boldsymbol{Q}}} \tanh\left(\frac{E_{\boldsymbol{k}+\boldsymbol{Q}}}{2k_{\mathrm{B}}T}\right). \end{aligned} \tag{2.16}$$

Thus the gap equation (Eq. 2.16) has solutions only if

$$\Delta(\boldsymbol{k})\Delta(\boldsymbol{k}+\boldsymbol{Q}) < 0 \tag{2.17}$$

is satisfied. $V(\boldsymbol{k}, \boldsymbol{k'})$ in Eq. 2.15 is a repulsive interaction between two quasiparticles. However it can be effectively interpreted as an attractive interaction by changing the sign of the order parameter between two points connected by $\boldsymbol{Q} = (\pi, \pi)$ on the Fermi surface, i.e., $\boldsymbol{k}_{\mathrm{F}}$ and $\boldsymbol{k}_{\mathrm{F}} + \boldsymbol{Q}$ (Eq. 2.17). In this model, the symmetry of the order parameter is given by $d_{x^2-y^2}$ ($\Delta(\boldsymbol{k}) \propto {k_x}^2 - {k_y}^2$) and such a momentum dependence of the gap amplitude was observed in ARPES measurements (Fig. 2.16) [75, 72]. The d-wave symmetry is also consistent with Josephson junction experiments [76]. In momentum space, the van Hove singularities where the density of states of quasiparticle is large exist near $\boldsymbol{k} = (\pm\pi, 0),\ (0, \pm\pi)$ and those points are connected by $\boldsymbol{Q} = (\pi, \pi)$. Therefore the effectively strong attraction between two quasiparticles could be ascribed to the spin fluctuations, which would explain why T_{c} of cuprates is high. Experimental correspondence between T_{c} and the exchange interaction J in the Heisenberg model also favors this scenario [77].

However the spin fluctuation mechanism concerned here may be too simple to fully catch the nature of the superconductivity in cuprates [78]. The electron-phonon coupling was clearly observed in both electron and phonon single particle spectra [79, 80]. Therefore it is not clear whether the phonon contribution can be completely ruled out in order to quantitatively explain the high T_{c}. Also the BCS theory tells that T_{c} in unconventional superconductors defined by Eq. 2.14 is very sensitive to (nonmagnetic) disorder as demonstrated in Sr_2RuO_4 [81]. Despite the non-stoichiometric nature of cuprates, T_{c} being rather insensitive to disorder has been another topic of research on these materials.

Pseudogap

The pseudogap state is characterized by another gap-like feature which appears in several types of excitation spectra above the superconducting transition temperature T_{c}. It was first pointed out in the spin-lattice relaxation rate in nuclear magnetic resonance (NMR) measurements. A sharp drop in the relaxation rate was observed below 100 K, well above $T_{\mathrm{c}} = 61$ K [82]. Subsequently signatures of the pseudogap were found in the Knight shift in NMR measurements [83] and spin excitations in the inelastic neutron scattering measurements [84]. The pseudogap was also directly observed as suppression of the density of states around Fermi level above T_{c} and below the pseudogap temperature T^* in ARPES measurements [85, 86]. A large energy shift of the energy-distribution curves was observed in the anti-nodal regions ($\boldsymbol{k} \sim (\pi, 0)$) but not in the nodal regions ($\boldsymbol{k} \sim (\pi/2, \pi/2)$) [87]. As a consequence the spectral weight at the Fermi level is observed around the nodal regions as disconnected Fermi arc in the first Brillouin zone (Fig. 2.17). Upon hole doping, the length

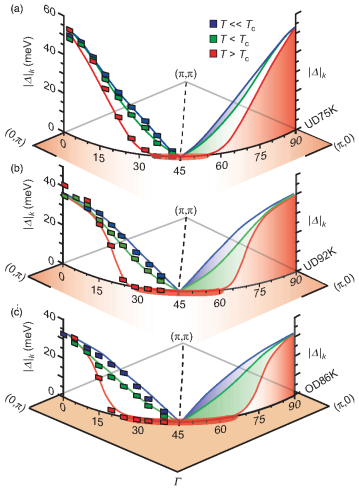

Figure 2.17: **Schematic of the momentum dependence of the superconducting gap and pseudogap.** The gap amplitude was estimated by ARPES measurements on $Bi_2Sr_2CaCu_2O_{8+\delta}$. (a) Underdoped sample with $T_c = 75$ K. (b) Underdoped sample with $T_c = 92$ K. (c) Overdoped sample with $T_c = 86$ K. The Fermi arc (red curves) exists above T_c, reflecting the pseudogap opening only in the anti-nodal regions. Below T_c, the Fermi arc is gapped out except for the nodal point. The superconducting gap amplitude is well described by the *d*-wave symmetry. Figures from Ref. [92].

of the Fermi arcs increases and finally a connected Fermi surface appears. Accordingly, T^* decreases monotonically as a function of the hole doping p and the pseudogap is not observed anymore in the overdoped regime ($p > p^* = 0.19$) (Fig. 2.12).

The qualitative similarity between the momentum dependence of the pseudogap and of the *d*-wave superconducting order parameter had led many to believe that the pseudogap state could be characterized as the precursor of the superconductivity, i.e., preformed Cooper pairs or superconducting fluctuations, which are phase incoherent states [88]. However signatures of the superconducting fluctuations were observed only just above T_c and did not persist up to T^* in a number of experiments, e.g., microwave measurements [89]. Also the node of the *d*-wave superconducting order parameter exists only at one point on the Fermi surface where it crosses with the high symmetry lines ($k_y = \pm k_x$) while the pseudogap is zero on the Fermi arc in ARPES as shown in Fig. 2.17 [90, 91, 92, 93]. Based on this quantitative discrepancy between the superconductivity and pseudogap states, it was proposed that the two states could actually be in competition.

In light of this possible phase competition, another proposal that the pseudogap could be characterized as a distinct thermodynamic phase associated with the spontaneous symmetry breaking has been put forward. As in Peierls' theory of charge-density waves, a finite $\boldsymbol{Q}$ order such as the CDW can potentially open a gap on the Fermi surface. The nesting by the charge order which connects two ends of the Fermi arc was suggested as the Fermi surface instability [94]. The signature of gap opening due to density waves distinct from the superconductivity was also observed in ARPES measurements as a back-bending feature in the quasiparticle band dispersions in the anti-nodal regions [95]. However the quantum critical point for the pseudogap is $p = 0.19$ while it is at $p = 0.16$ for the charge order. Also the T^* is much higher than the onset of the charge order, T_{CO} ~150 K at maximum. On top of that, the pseudogap is ubiquitously observed in all cuprates while the Fermi surface shape is quite material dependent. Therefore it is hard to explain the pseudogap which equally occurs in different materials at high temperature T^* solely as a consequence of the Fermi surface instability associated with the density waves.

While onset of charge density wave order does not coincide with T^*, recently other types of symmetry broken states were reported at T^*: rotational symmetry breaking and time-reversal symmetry breaking. The former is often termed nematicity and was first pointed out by transport measurements of $La_{2-x}Sr_xCuO_4$ and $YBa_2Cu_3O_{6+x}$ [96].

Subsequently the nematicity was reported in a number of experiments, e.g., scanning tunneling spectroscopy [97], ARPES [98, 99], and Raman scattering [100]. The in-plane anisotropic Nernst coefficient and magnetic susceptibility, which behave like an order parameter of the nematicity, were observed below T^* [101, 102, 103]. Furthermore the nematic susceptibility diverges towards T^* [104]. Anisotropic signals in the spin excitations measured by inelastic neutron scattering were observed although the onset of this nematicity originated from the spin sector is much lower than T^* unlike other measurements [105, 58]. As a possible mechanism behind the nematicity, fluctuations of stripe order [106, 107] and the Fermi surface instability (so-called Pomeranchuk instability) [108, 109, 110, 111, 112] have been theoretically proposed, yet the origin of nematicity is still not clear to date. On the other hand, the time-reversal symmetry breaking was reported in polarized Kerr effect measurements [113] and polarized neutron diffraction measurements [114, 115], motivated by the intra-unit cell loop current order theory proposed by Varma *et al.* [116]. It was pointed out that the Kerr effect could be interpreted as the result of the chiral charge ordering [117], thus it is not clear whether the time-reversal symmetry breaking is the only interpretation of this experiment.

The origin of the pseudogap needs to be elucidated by future studies including former theoretical proposals whose experimental verifications are not still clear, e.g., the momentum dependent Mott transition suggested by the dynamical mean field theory (DMFT) [118].

Strange metal

Right after the discovery of superconductivity in the cuprates, the normal-state resistivity was found to be T-linear over a wide temperature range and not saturated up to 1000 K [119]. Such metallic behaviors are in stark contrast to the conventional Fermi liquid theory where the resistivity is expected to be T^2-dependent and saturated at high temperature due to the Mott-Ioffe-Regel criterion [4, 120]. Such a non-Fermi liquid like metallic state was called strange metal and interpreted as a marginal Fermi liquid at the early stage [121]. In the underdoped regime, the T-linear resistivity was observed only above the pseudogap temperature T^* and the temperature dependence deviates from the linear below T^* [122]. The T-linear resistivity persists down to $\sim T_c$ at the optimal doping where the T_c is the highest in the entire hole doping range, thus it was suggested that the pairing mechanism may be closely linked with the strange metal in relation with the quantum criticality [123].

The normal-state resistivity is, however, masked by superconductivity below T_c. In the underdoped cuprates ($p < p^*$), the upturn in the resistivity at low temperature, reminiscent of an insulator, was observed under high magnetic fields which obliterate superconductivity [124]. The relatively low T_c in the 214 families have enabled one to perform similar studies on the optimally doped and overdoped cuprates under a steady field. For $p > p^*$, the upturn in the resistivity was not observed but instead the T-linearity persists down to $T \to 0$, indicative of the quantum critical point of the pseudogap at $p = p^*$ and $T = 0$ [125]. Further studies revealed that the T-linear resistivity as $T \to 0$ is a generic feature of a number of cuprate families for $p > p^*$ [126, 127]. This universality in the T-linear dependence in spite of different Fermi surfaces is explained by means of the Planckian limit, $\hbar/\tau = k_B T$, i.e., the upper boundary of the decay rate of Landau quasiparticles in the Fermi liquid theory [4, 128]. Such a doping dependence of the strange metallicity was

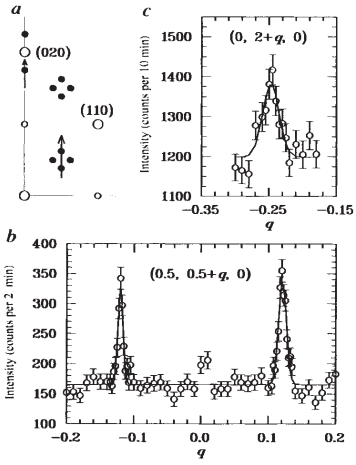

Figure 2.18: **Neutron diffraction measurements on $La_{1.48}Nd_{0.4}Sr_{0.12}CuO_4$.** Measurements were performed at 11 K. (a) Reciprocal space map in the $(H, K, 0)$ plane. White circles indicate Bragg peaks for the LTT structure black points denote the superstructure peaks originated by charge and spin orders. (b) Neutron diffraction scan along (1/2, 1/2+q, 0) indicated in (a). The peaks at $q = \pm 0.125$ are originated from the spin orders. (c) Scan along (0, 2+q, 0) indicated in (a). The peaks at $q = \pm 0.25$ are originated from the charge orders. Figures from Ref. [12].

also obtained in a recent numerical study on the doped Hubbard model [129].

Charge order

Right after the discovery of superconductivity in cuprates, Zaanen and Gunnarsson made theoretical predictions about a charge ordering tendency based on the doped Hubbard model [130]. Subsequently the charge order was first experimentally observed in the 214 compounds by Tranquada *et al.* in neutron diffraction measurements [12]. Below the structural transition temperature from the low temperature orthorhombic (LTO) phase to the low temperature tetragonal (LTT) phase (70 K), a superstructure peak appears at $\boldsymbol{Q} = (0,\ 2 - \delta_{\text{charge}},\ 0)$ where $\delta_{\text{charge}} = 0.25$, which indicates the formation of a charge order whose periodicity in the real space is four times the structural unit cell. Upon further cooling, another superstructure peak appears at $\boldsymbol{Q} = (1/2,\ 1/2 + \delta_{\text{spin}},\ 0)$ where $\delta_{\text{spin}} = 0.125$, which indicates the spin order. The real space periodicity of the spin order is eight times of the unit cell and two times that of the charge sector. These intertwined charge and spin orders form the so-called stripe order[9] (Fig. 2.18). Note that neutron scattering measurements cannot detect the charge correlation because of the charge neutrality of neutrons, therefore the associated lattice distortion was detected indirectly from the electron density modulation. In later years, a direct observation of the density wave modulation in the charge sector was demonstrated by Abbamonte *et al.* with resonant soft x-ray scattering measurements [131].

Anomalies in both in-plane and out-of-plane resistivities at the stripe order onset were noticed even before the discovery of the stripe order [132]. The Hall coefficient is reversed upon cooling [133]. It indicates a Fermi surface reconstruction induced by the stripe order, but the clear effect on the Fermi surface below and above the stripe order onset was not confirmed in ARPES measurements [134, 135]. Recent Hall effect experiments suggested that the sign of the Hall coefficient is reversed for $x < 0.11$ but it does not cross zero for $x = 0.12$ where the stripe order is the most stabilized [136]. It implies that the balance between the original Fermi surface area and the reconstruction may matter in

[9]The term "stripe" is sometimes differently used to emphasize the uniaxial nature of charge and spin orders which are not necessarily intertwined. The biaxial counterpart is often called "checkerboard" accordingly.

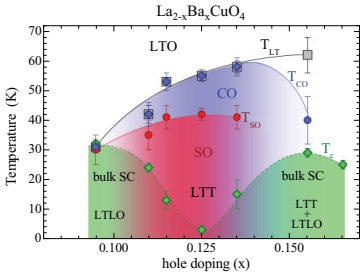

Figure 2.19: **Phase diagram of $La_{2-x}Ba_xCuO_4$ in the vicinity of the 1/8 doping.** Abbreviations, LTO: low temperature orthorhombic phase, LTT: low temperature tetragonal phase, LTLO: low temperature less-orthorhombic phase, CO: charge order, SO: spin order, SC: superconductivity. Figure from Ref. [139].

interpreting the Hall coefficient [137]. Further information regarding the stripe order in the 214 compounds is summarized in the latest review by Tranquada, Dean, and Li [138].

The stripe order is particularly strong at $x \simeq 0.125$, where T_c is hugely suppressed < 5 K in the 214 system (Fig. 2.19). It suggests a clearly competitive relationship between the stripe order and superconductivity. The suppressed T_c dome was called the 1/8 anomaly named after its doping value $x = 0.125 = 1/8$. The reminiscent plateau like behavior in T_c around the 1/8 doping regime was also observed in $YBa_2Cu_3O_{6+x}$ (Fig. 2.12), yet no indication of static orders was known for a long time.

Although the charge orders were considered to be peculiar to the 214 families for a long time, the charge-density waves in $YBa_2Cu_3O_{6+x}$ were first discovered with RIXS by Ghiringhelli *et al.* in 2012 [14]. The periodic structure of the valence electron density modulation is evident as a quasielastic peak in the energy- and momentum-resolved RIXS spectra shown in Fig. 2.20. The peak in the reciprocal space is located at $\boldsymbol{Q} \sim 0.31$ along the Cu-O bond direction, which is close but not identical to the commensurate wave vector $\boldsymbol{Q} = 1/3 \simeq 0.33\cdots$. This incommensurate peak corresponds to the valence electron density modulation with the periodicity of ~ 3.2 in-plane lattice constants, which breaks the translational symmetry of the underlying crystal lattice. It is confirmed that the charge modulation develops in the CuO_2 planes based on its energy dependence, where the quasielastic peak was observed only with the absorption edge of the Cu(2) site and not with that of the Cu(1) site. Although the same compound was investigated in previous resonant energy-integrated x-ray scattering (REXS) measurements [140], the CDW quasielastic peak was not clearly observed at that point. Moreover, based on the polarization dependence of the RIXS cross section, the quasielastic peak was found to be from the charge scattering rather than the spin scattering. The quasielastic peaks are observed along two Cu-O bond directions, namely a- and b-axis in $YBa_2Cu_3O_{6+x}$, at the wave vector $\boldsymbol{Q} = (\delta_a, 0),\ (0, \delta_b)$ in the two-dimensional Brillouin zone. δ_a and δ_b are the incommensurate values. This immediately implies two candidates for the spatial characters of the charge order: a uniaxial CDW with domains where the stripe-like modulation runs along the two different in-plane directions or the checkerboard (biaxial) order. The former picture has been put forward and supported by a number of recent experiments [141, 142]. The out-of-plane correlation length of those CDW domains is much shorter than the in-plane correlation lengths, indicative of their two-dimensional nature. The very broad quasielastic peak along the out-of-plane direction is located at half-integer values in the reciprocal space [22]. It indicates an inter-layer anti-correlation, which is explained by the long-range Coulomb interaction between holes in the adjacent layers [143]. The CDWs discussed so far are called the 2D-CDWs in this thesis to distinguish them from the three-dimensionally correlated CDW introduced below.

At the 1/8 doping, the CDW is observed below 150 K. The intensity and correlation

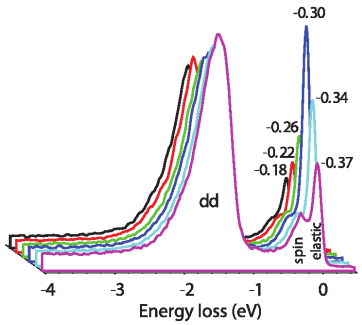

Figure 2.20: **RIXS spectra of $Nd_{1.2}Ba_{1.8}Cu_3O_7$ for various wave vectors.** The elastic peak corresponds to the 2D-CDW. Figure from Ref. [14].

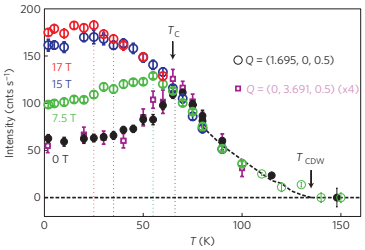

Figure 2.21: **Temperature dependence of the 2D-CDW in $YBa_2Cu_3O_{6.67}$.** Data under magnetic fields are also displayed. Figure from Ref. [22].

length monotonically increase upon cooling, are maximized at the superconducting transition temperature T_c, and monotonically decrease upon further cooling below T_c (Fig. 2.21). This temperature dependence clearly demonstrates the suppression of the CDW by superconductivity. On top of that, the CDW below T_c is enhanced in presence of a magnetic field which weakens superconductivity while the CDW above T_c is barely affected. Once the superconducting long-range order is completely obliterated by a sufficiently high magnetic field, the enhancement of the CDW is saturated and the temperature dependence resembles that of an order parameter. The competition between those two phases is clearly evident based on such temperature and magnetic field dependences.

The CDW in $YBa_2Cu_3O_{6+x}$ has been comprehensively studied thanks to the minimal chemical disorders with defects mainly confined in the CuO chain layers and clean CuO_2 planes, which were also demonstrated by the quantum oscillation measurements which require high-quality samples whose mean-free path needs to be greater than the cyclotron radius [20]. Soon after the discovery, the doping dependence of the 2D-CDW was investigated by Achkar *et al.* [144], Blackburn *et al.* [145], and Blanco-Canosa *et al.* [146]. The CDW in $YBa_2Cu_3O_{6+x}$ is observed in the doping range of $p = 0.08$ - 0.16 on top of the 1/8 plateau of the superconducting dome (Fig. 2.22). The competitive relationship between the CDWs and superconductivity also explains the reason why the 1/8 plateau is present. The onset temperature of the CDW depends on the hole doping and ranges between 100 and 150 K, that is the intermediate range between the superconducting transition temperature T_c and the pseudogap temperature T^*. The highest onset temperature is observed at the 1/8 doping, analogous to the stripe order in the 214 compounds. The doping dependence of the incommensurability (δ_a and δ_b) in $YBa_2Cu_3O_{6+x}$ is, however, quite different from the one deduced from the charge sector of the stripe order in the 214 compounds. The incommensurability in $YBa_2Cu_3O_{6+x}$ linearly decreases upon hole doping, while the one in the 214 compounds increases and is saturated above the 1/8 doping (Fig. 2.23). Also, unlike the stripe order, no static magnetic order intertwined with the CDW was observed in $YBa_2Cu_3O_{6+x}$. The static magnetic order is observed as the spin-density waves only at the low doping levels ($p \leq 0.085$), which barely overlap with the

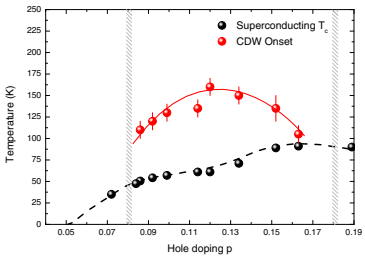

Figure 2.22: **Phase diagram of $YBa_2Cu_3O_{6+x}$ around the 1/8 doping.** The red and black points indicate the onset temperatures of the 2D-CDW and superconductivity, respectively, at various hole doping levels. Figure from Ref. [151].

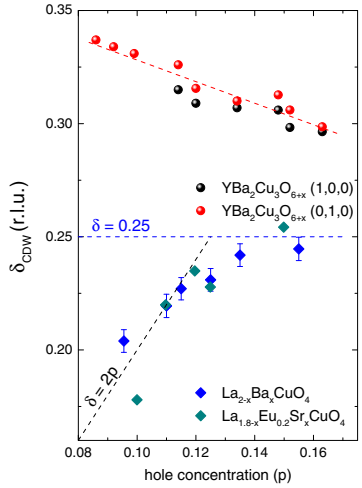

Figure 2.23: **Hole doping dependence of the CDW wave vector.** The black and red circles indicate the incommensurability δ_a and δ_b of $YBa_2Cu_3O_{6+x}$, respectively. The values deduced from the stripe order in the 214 compounds are also shown. Figure from Ref. [151].

doping levels where the CDW is observed [105, 147, 58]. We remark that CDWs were also observed in Bi-based cuprates [94, 148] and Hg-based cuprates [149]. The characters of the CDW are quantitatively material-dependent yet qualitatively similar in all compounds. Another charge order was also observed in the overdoped regime of the Bi-based cuprates [150].

In the presence of the electron-phonon coupling (EPC), the CDW affects the phonons in ordinary CDW materials [10, 11]. The anomaly is observed as the softening of the phonon dispersions at the CDW wave vector, known as the Kohn anomaly. The structural phase transition takes place if the energy of the phonon mode approaches zero by this softening as experimentally observed in quasi one-dimensional (1D) systems. Details and mechanisms of the CDW strongly depends on the dimensionality of the electron system in each material and those of non-1D materials are typically complex. In the case of $YBa_2Cu_3O_{6.6}$, the strong phonon softening was observed in non-resonant hard x-ray scattering (IXS) experiments (Fig. 2.24) [16]. This anomaly is, however, the strongest not at the onset temperature of the CDW but at T_c unlike the typical Kohn anomaly. This aspect also implies the complex and competing nature of the CDW and superconductivity. The phonon dispersions are typically measured by non-resonant IXS measurements whose energy resolution is significantly better than that of the RIXS. Recent advancement of the energy resolution in RIXS enabled the observation of the phonon contributions in the RIXS spectra and the estimation of the EPC strength was attempted taking advantage of the leading phonon term in the RIXS cross section which is different from the one of the non-resonant IXS [152, 153].

A three-dimensional (3D) CDW in $YBa_2Cu_3O_{6.67}$ in x-ray scattering measurements under the high magnetic field was reported [21, 154, 155]. Above the magnetic field exceeding 15 T, a new sharp peak feature in the quasielastic intensity appears at the integer

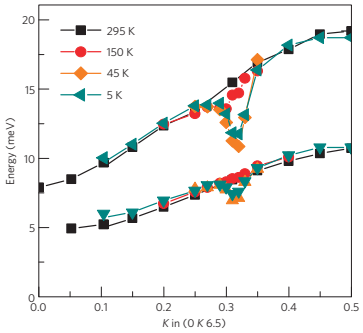

Figure 2.24: **Low-energy phonon dispersions near the CDW wave vector in $YBa_2Cu_3O_{6.6}$.** The anomaly at the CDW wave vector ($K \sim 0.31$) is pronounced below T_c rather than the CDW onset. Figure from Ref. [16].

value along the L direction in the reciprocal space, indicating the in-phase correlations between adjacent CuO_2 layers in contrast to the anti-correlation observed as the broad peak at half-integer L arising from the 2D-CDW. The in-plane incommensurability of the 3D-CDW is the same as the one of the 2D-CDW. The correlation lengths of the 3D-CDW at 30 T (${\xi_b}^{3D} \sim 180$ Å, ${\xi_c}^{3D} \sim 50$ Å) are much greater than those of the 2D-CDW (${\xi_b}^{2D} \sim 40$ Å, ${\xi_c}^{2D} \sim 7$ Å), implying the long-range nature as can be intuitively understood from the much sharper peak in the reciprocal space (Fig. 2.25 (a)). While the 2D-CDW appears along both Cu-O bond directions, the 3D-CDW is observed only along the b-axis. So far the magnetic field induced 3D-CDW was observed below the 1/8 doping with the x-ray scattering measurements [156]. The ultrasound experiments indicated the thermodynamic phase transition into the 3D-CDW in the similar doping range where the 2D-CDW is observed [157]. The magnetic field induced 3D-CDW was also observed in NMR measurements [158, 159]. In any cases the onset temperature of the field-induced 3D-CDW is always below zero-field T_c unlike the one of the 2D-CDW (Fig. 2.26). A similar but different 3D charge order was observed also in $YBa_2Cu_3O_{6+x}$ thin films even in the absence of magnetic field [160]. This 3D charge order persists up to room temperature and arises also from the CuO chain layers unlike the CDWs in bulk materials.

More recently, the 3D-CDW in $YBa_2Cu_3O_{6.67}$ ($p = 0.12$) was induced by the uniaxial stress above and below T_c unlike the magnetic field induced one observed only below T_c [18]. The 3D-CDW was observed only along the b-axis when 1% compressive strain was applied along the a-axis but no 3D-CDW correlation was induced by the strain along b-axis. The correlation lengths of the strain-induced 3D-CDW at 1% (${\xi_b}^{3D} \sim 310$ Å, ${\xi_c}^{3D} \sim 94$ Å) are larger than the values reported under magnetic field. The complete softening of the phonon mode at the wave vector of the 3D-CDW is associated with this CDW transition, in analogy with soft-mode-driven CDW in classical CDW materials such as $NbSe_2$. The uniaxial stress also selectively enhances the 2D-CDW perpendicular to the stress direction [142]. This result suggests that the spatial nature of the 2D-CDW is stripe rather than checkerboard because CDWs along both directions should be simultaneously modified if the spatial character is checkerboard-type. This strain effect on the 2D-CDWs is observed for both a- and b-axis compressions while the 3D-CDW is induced by the compression only along the a-axis. So far the strain-induced 3D-CDW was observed only at this peculiar doping level ($p = 0.12$), therefore the investigation of different doping levels is one of main subjects in this thesis as shown in chapter 5.

The origin and driving force behind charge ordering phenomena are one of the central issues. In fact, the 2D-CDW has been considered to be nucleated around spatially random defects based on the 'central peak' in the IXS measurements [16]. The non-

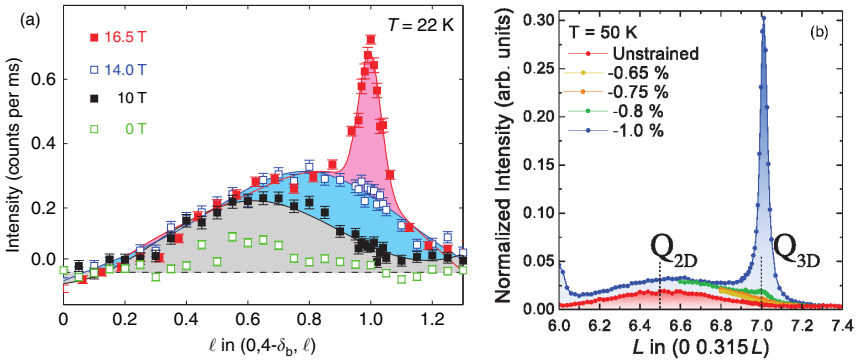

Figure 2.25: **3D-CDW in $YBa_2Cu_3O_{6.67}$.** The reciprocal space scans of the quasielastic intensity along the out-of-plane direction around $\boldsymbol{Q} = (0,\ \delta_b,\ L)$ measured under magnetic field in panel (a) and uniaxial stress in panel (b). Figures from Ref. [155, 18].

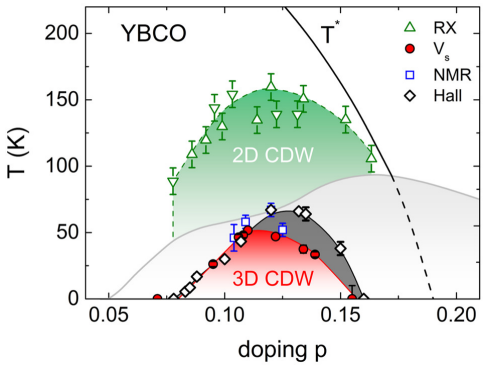

Figure 2.26: **Phase diagram around the 1/8 doping under magnetic field.** Green triangles indicate the onset temperature of the 2D-CDW deduced from the x-ray scattering measurements. The red circles and blue squares indicate the onset of the 3D-CDW deduced from the ultrasound measurements and NMR, respectively. The black diamonds are the temperature where the sign of the Hall coefficient is reversed. Figure from Ref. [157].

stoichiometric CuO chain layers are natural defect sites and thus naively explain the maximum in the 2D-CDW diffraction at the half-integer points along the out-of-plane direction (Fig. 2.25). This picture is also consistent with the lack of thermodynamic signatures at the onset and considerable intensity in the zero-temperature limit, despite the competition with superconductivity. On the other hand, the 3D-CDW are considered to be a genuine electronic phase based on its long range nature and strong competition with superconductivity [142].

Overall it is now well established that the charge ordering is a ubiquitous tendency in all underdoped cuprates. The correspondence with the charge transport properties is, however, not clear and quite different from classical CDW materials, e.g., the absence of any noticeable features in the normal-state resistivity. A number of anomalous transport properties, such as the sign reversal of the Hall coefficient and the presence of the small electron Fermi surface suggested by quantum oscillation measurements, were reported even before the discovery of the CDW in RIXS and have later been attributed to charge ordering [161, 162]. Detailed explanations of the anomalous transport coefficients in relation with the charge ordering will be further provided in the introduction of chapter 4. To provide further information on this issue, we present normal-state transport measurements under uniaxial stress in chapter 4. Extending the phase diagram of the charge orders by uniaxial stress is presented in chapter 5.

Chapter 3

Experimental methods

3.1 Introduction

Many experiments in condensed matter physics can be categorized as observations of the response of materials when they are stimulated by external fields. Examples are the electrical current under the electric field (charge transport experiments), the magnetization under the magnetic field (magnetic susceptibility experiments), and so forth. Such states stimulated by the external fields are in general non-equilibrium states, and the complete theoretical treatment of such states is still one of the most difficult problems in physics to date. Nevertheless, as far as the response is linearly proportional to the external field, the linear response theory through the Kubo formula which calculates various physical quantities from the microscopic Hamiltonian has been well established to deal with the non-equilibrium states [163]. In this framework, the central work for theorists is to derive macroscopic properties by calculating response functions, which can be experimentally constrained by microscopic measurements. In general, assumptions in the linear response theory are not always valid, yet complementary macroscopic and microscopic experimental insights under the same experimental conditions are considered to be valuable to develop solid-state theories.

This chapter continues with elaborations of experimental methods that we have used for the measurements presented in the next two chapters from their principles to practical aspects. First, we explain the uniaxial stress technique used as an external field in all measurements. Subsequently the sample preparation for the strain experiments is illustrated in detail since it is a key step to perform successful strain experiments. In the later two sections, basic principles of the transport experiments and resonant x-ray scattering experiments are described. In particular, the complementarity of those two experiments to elucidate the properties of quantum materials is stressed.

3.2 Uniaxial stress technique

3.2.1 Introduction

In research on quantum materials, the uniaxial stress technique with piezoelectric stacks was utilized by Fisher *et al.* around 2010 [164] while previously it was used mainly in the

field of semiconductors [165]. This technique has been applied in a number of systems to study unconventional phenomena in quantum materials such as nematicity in iron-based superconductors [166], hidden orders in URu_2Si_2 [167], etc... The nematic susceptibility deduced from transport properties under strain was defined to discuss thermodynamic phase transitions by means of Landau theory. Although the accessible strain was limited because samples were directly attached on a piezoelectric stack, the response was large enough to study the nematicity in these compounds. In 2014, Hicks *et al.* have made a newly designed apparatus to apply the uniaxial stress on a sample[1] [169]. The combination of the careful sample preparation into a tiny rectangular shape[2] and the new piezoelectric stack based apparatus has made it possible apply the strain around 1 % routinely. The discovery that T_c of Sr_2RuO_4 under strain becomes more than twice [169, 170] has driven a lot of following studies. Crucially, one of them has provided a fresh perspective on the nature of superconducting order parameter [171]. This strain technique has been applied to the research of cuprates as well [18]. Besides the selection of the material, it was a new attempt in two aspects: i) the piezoelectric stack based apparatus has been integrated in a synchrotron facility to perform x-ray scattering measurements and ii) the strain effect was observed by microscopic energy- and momentum-resolved experiments while this strain technique was previously implemented only in laboratory-based macroscopic measurements. The success in the x-ray scattering experiment has motivated us to perform further strain experiments on cuprates at in-house laboratories and different synchrotron facilities.

In this section, terminologies, stress and strain, will be defined and their fundamental properties are reviewed to better understand our measurements in the next chapters. Subsequently, the piezoelectric stack based apparatus will be elaborated. In the end, we illustrate a new technical contributions to strain experiments, a sample carrier that has made strain measurements more efficient.

3.2.2 Stress and strain

When an elastic material is deformed, one can evaluate this deformation by two kinds of physical quantities: stress and strain. They are intimately related but not identical (Fig. 3.1). The stress is defined as a measure how the force is distributed in the object per unit area and its unit is N/m^2 in the SI system. On the other hand, the strain is defined as a measure of the relative displacement compared with the original length of the deformed object and thus it is a dimensionless quantity by definition.

Generally, the strain ε_{ij} can be defined as a nine component tensor

$$\varepsilon_{ij} = \frac{1}{2}\left(\frac{\partial u_i}{\partial x_j} + \frac{\partial u_j}{\partial x_i}\right), \ (i, j = x, y, z), \tag{3.1}$$

where $\boldsymbol{u}$ and $\boldsymbol{x}$ are a three component displacement vector and coordinate vector in a Cartesian coordinate system, respectively. This representation is called the tensor representation. By definition, $\varepsilon_{ij} = \varepsilon_{ji}$. Considering this symmetry, the engineering

[1] Technical developments about the uniaxial stress technique before the apparatus invented by Hicks *et al.* are well described in chapter 2.4 of Ref. [168].

[2] Hereafter, we call this sample shape a needle shape for simplicity.

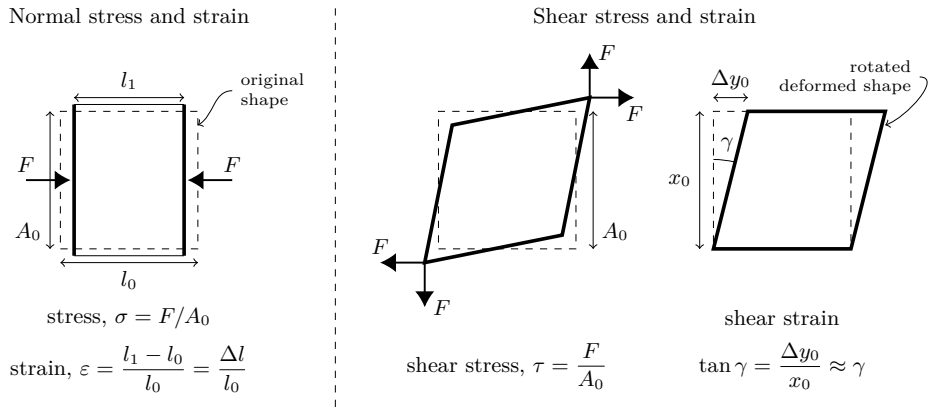

Figure 3.1: **Stress and strain.** Conceptual schematics of normal stress and strain (left) and shear stress and strain (right). Figures from Ref. [168].

representation where the number of strain vector component is six is also used:

$$\boldsymbol{\varepsilon} = \begin{pmatrix} \varepsilon_1 \\ \varepsilon_2 \\ \varepsilon_3 \\ \varepsilon_4 \\ \varepsilon_5 \\ \varepsilon_6 \end{pmatrix} = \begin{pmatrix} \varepsilon_{xx} & \\ \varepsilon_{yy} & \\ \varepsilon_{zz} & \\ 2\varepsilon_{yz} & (= 2\varepsilon_{zy}) \\ 2\varepsilon_{zx} & (= 2\varepsilon_{xz}) \\ 2\varepsilon_{xy} & (= 2\varepsilon_{yx}) \end{pmatrix}. \tag{3.2}$$

Likewise, the stress vector is also defined in the same dimension as that of the strain vector. In the engineering representation, ε_i (σ_i) are normal strain (stress) for $i = 1, 2, 3$ and shear strain (stress) for $i = 4, 5, 6$, respectively as depicted in Fig. 3.1.

One can see the relationship between the stress and strain by a thermodynamic consideration [172]. The first law of thermodynamics is

$$\mathrm{d}U = \mathrm{d}Q - \mathrm{d}W, \tag{3.3}$$

where $\mathrm{d}U$, $\mathrm{d}Q$, and $\mathrm{d}W$ are the change in internal energy, the energy gain as heat, and the work done by the system on its surroundings. In our case the system is an elastic material and the work $\mathrm{d}W$ done by the small strain $\mathrm{d}\varepsilon_{ij}$ per unit area is

$$\mathrm{d}W = -\sigma_{ij}\mathrm{d}\varepsilon_{ij}. \tag{3.4}$$

Since the Helmholtz free energy F is related to the entropy S and temperature T as $F = U - TS$, the total derivative of the Helmholtz free energy $\mathrm{d}F$ is given by

$$\begin{aligned} \mathrm{d}F &= \mathrm{d}U - S\mathrm{d}T - T\mathrm{d}S & (3.5)\\ &= \mathrm{d}Q - \mathrm{d}W - S\mathrm{d}T - T\mathrm{d}S & (3.6)\\ &= -S\mathrm{d}T + \sigma_{ij}\mathrm{d}\varepsilon_{ij}. & (3.7) \end{aligned}$$

Therefore $\sigma_{ij} = (\partial F/\partial\varepsilon_{ij})_T$ and $S = (\partial F/\partial T)_{\varepsilon_{ij}}$. This means that one can capture a thermodynamic phase transition by measuring the stress and strain simultaneously in

a similar manner to entropy measurements that are often experimentally obtained by measuring the heat capacity as a function of temperature.

In an isothermal process, one can expand the free energy to a power series of strain,

$$F(T, \varepsilon_{ij}) = K(T) + b_{ij}\varepsilon_{ij} + \frac{1}{2}C_{ijkl}\varepsilon_{ij}\varepsilon_{kl} + \dots \,. \tag{3.8}$$

To be $\sigma_{ij} = 0$ when $\varepsilon_{ij} = 0$, $b_{ij} = 0$ because $\sigma_{ij} = \partial F/\partial\varepsilon_{ij}$. Using this formula and ignoring higher order terms, one obtains the relationship between σ_{ij} and ε_{ij},

$$\sigma_{ij} = C_{ijkl}\varepsilon_{kl}. \tag{3.9}$$

This is called the generalized Hooke's law. C is called a stiffness tensor. One can easily see the analogy to the Hooke's law for the one dimensional spring: $f = kx$, where f, k, and x are the force, spring constant, and displacement. This relationship can be represented in an inverse way:

$$\varepsilon_{ij} = S_{ijkl}\sigma_{kl}, \tag{3.10}$$

where S is called the shear modulus. By definition, the stiffness tensor C has 81 components in the tensor representation (36 components in the engineering representation), however the number of independent components is reduced to 21 at most due to the symmetries of the stiffness tensor C. For the application to our studies, materials studied in this thesis have a point group symmetry, therefore, the number of the independent components in the stiffness tensor C is further reduced. For instance, the generalized Hooke's law for the orthorhombic lattice structure whose point group symmetry is $D_{2\mathrm{h}}$ in the engineering representation is given as follows:

$$\begin{pmatrix}\sigma_1\\ \sigma_2\\ \sigma_3\\ \sigma_4\\ \sigma_5\\ \sigma_6\end{pmatrix} = \begin{pmatrix}C_{11} & C_{12} & C_{13} & 0 & 0 & 0\\ C_{12} & C_{22} & C_{23} & 0 & 0 & 0\\ C_{13} & C_{23} & C_{33} & 0 & 0 & 0\\ 0 & 0 & 0 & C_{44} & 0 & 0\\ 0 & 0 & 0 & 0 & C_{55} & 0\\ 0 & 0 & 0 & 0 & 0 & C_{66}\end{pmatrix}\begin{pmatrix}\varepsilon_1\\ \varepsilon_2\\ \varepsilon_3\\ \varepsilon_4\\ \varepsilon_5\\ \varepsilon_6\end{pmatrix}. \tag{3.11}$$

The Young's modulus (E_i) is defined as the ratio of the stress to strain along the principal directions: $E_i = \sigma_i/\varepsilon_i$ ($i = 1, 2, 3$). The magnitude of E_i is direction-dependent. In a similar manner, the Poisson's ratio is also defined to described the transverse expansion of an elastic material induced by the longitudinal force, e.g., $\nu_{12} = -\varepsilon_2/\varepsilon_1$ and $\nu_{13} = -\varepsilon_3/\varepsilon_1$. Therefore the transverse expansion (changes in ε_2 and ε_3) is observed on top of the longitudinal expansion (change in ε_1) by uniaxial stress σ_1 due to the off-diagonal components of the stiffness tensor C. This phenomenon is called the Poisson effect. As seen in more details in chapter 5, this is why one observes shifts of Bragg peak along the out-of-plane direction by in-plane uniaxial pressure in x-ray scattering measurements.

3.2.3 Uniaxial stress / strain rig

Experiments presented in this thesis were performed with upgraded versions of the piezoelectric-based strain apparatus developed by Hicks *et al.* [173]. For the x-ray

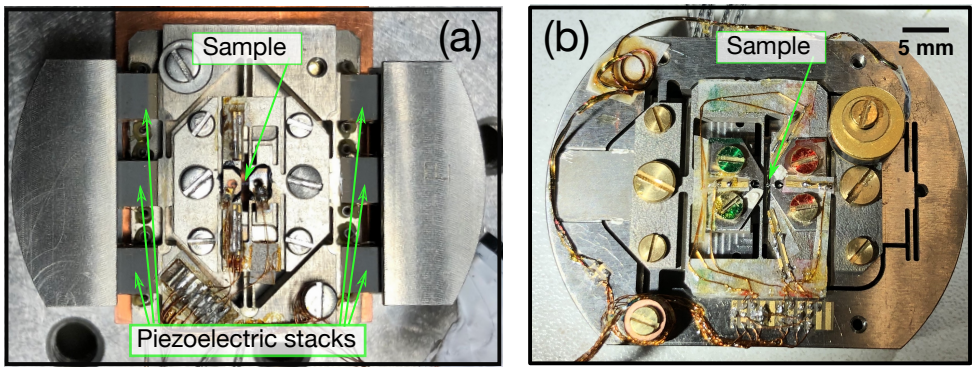

Figure 3.2: **Photographs of uniaxial pressure cells.** (a) Strain rig used for x-ray scattering measurements. The piezoelectric stacks are exposed and thus indicated by arrows. Black bar shaped object at the center is a sample. (b) Stress rig usd for transport experiments. All the piezoelectric stacks are covered by the rig itself thus not visible in this view.

scattering experiments, we have used the same setup used in previous x-ray scattering measurements [18, 142]. In the x-ray diffraction experiments, the nominal strain can be confirmed by Bragg peaks which directly indicate the lattice parameters of crystals. On the other hand, there is no direct indication of the strain in most of in-house measurements such as transport or magnetization measurements. In this regard, it is important to know whether the strain is actually applied or not especially when the physical quantities in the measurements are observed to be strain-independent. Therefore, the device we have used for the transport measurements has an additional function: a force sensor, which allows more accurate measurements. For simplicity, we term the device used for the x-ray scattering measurements the *strain rig* and the new device with the force sensor used for the transport measurements the *stress rig* hereafter. Both rigs are shown in Fig. 3.2.

The central idea of the strain devices is that the uniaxial pressure is produced by the piezoelectric stacks present along the long direction of a sample and the applied strain is monitored by capacitors integrated in the device. Selective application of voltage on each piezoelectric stack enables one to realize both tensile and compressive stress. For the voltage application, it requires electrical connections and they can be easily installed in the cryostat with a sufficient space for the device and feedthrough for vacuum to cool down the system. It allows one to perform *in-situ* control of the strain on a single-crystalline sample at cryogenic temperature. One potential measure of the strain is the voltages applied on the piezoelectric stacks, however it is well known that the displacement of a piezoelectric stack shows a huge hysteresis loop when the voltage is applied and then released (Fig. 3.3). In other words, in general, there is no one-to-one correspondence between the displacement and voltage, therefore the voltage is not an ideal measure of the strain, particularly in this device that possesses multiple piezoelectric stacks.

To overcome this difficulty, two parallel-plate-capacitor-based displacement sensors are integrated in those strain devices. The capacitance value C is related to the dimensions of the capacitor: $C = \epsilon_0 A/d$, where ϵ_0, A, and d are the permittivity of vacuum, the plate area, and the distance between two plates, respectively. Simultaneous measurements of C allows one to monitor the displacement of the sample independently of the voltage on the

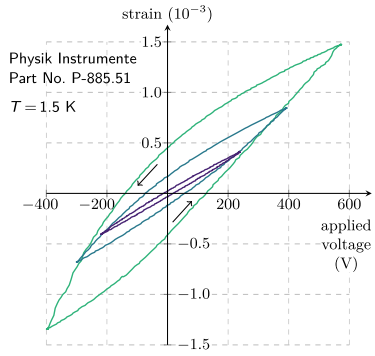

Figure 3.3: **Hysteresis loop of a piezoelectric stack.** The voltage was applied and released three times and three hysteresis curves are displayed. Figure from Ref. [174]

piezoelectric stacks, which has a hysteresis. We measure the capacitance value with the capacitance bridge AH2550A from Andeen-Hagerling whose precision is $\sim 10^{-6}$ pF. For instance, the typical value of the capacitance that we have used for the REXS experiments is ∼1.8 pF before applying the strain and ∼2.5 pF after applying high compressive strain such as -1 %. (Actual values of the capacitance depend on details of the sample preparation such as the sample shape and dimensions.) This method usually gives a sufficient accuracy to estimate the displacement of the strained sample. The displacement produced by the piezoelectric stacks Δd can be estimated by measuring the capacitance before and after applying the strain. Since one can check the sample length under strain L ahead of measurements, the nominal strain is $\Delta d/L$. The typical sample length is set to be $L = 800$ μm, thus the nominal strain is -1 % if the sample is deformed by Δd = -8 μm. In x-ray scattering measurements, the applied strain can be independently verified by measuring the Bragg peaks.

This is the central idea of the *strain rig* and used for a number of previous experiments on cuprates and ruthenates. However there is one assumption in quantitatively analyzing data obtained by the strain rig. The displacement of the capacitor is assumed to be equal to that of the sample but, in reality, this is often not the case because the sample is mounted on titanium sample plates with soft glue, Stycast 2850 FT. Therefore the displacement of the sample is often overestimated and thus some empirical parameters have been used to prevent the overestimation. More crucially, it is hard to notice if the sample slips because of bad gluing only from the capacitance value. To this end, another parallel-plate-capacitor force sensor is integrated in series with the sample in the *stress rig*. The spring constant of this sensor is much greater than that of typical samples, therefore the displacement of the force sensor is not identical to that of the mounted sample anymore. However the force applied on the sample is identical to that on the force sensor, therefore knowing the spring constant of the force sensor, one can estimate the stress, i.e., the force divided by the cross sectional area of the samples in an accurate way. Since the mounted sample is the only object that transmits the force to the force sensor, one does not observe any force by applying the voltage to the piezoelectric stacks if the strain is not applied on the sample for any reasons such as sample buckling or slipping. Also one can determine the zero stress / strain state more accurately by carefully mounting the sample as clearly demonstrated in Fig. 3.4 while this is hard to do with the strain rig.

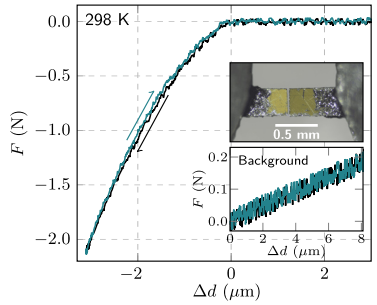

Figure 3.4: **Force-displacement curve for a titanium sample.** Since the sample is separated when the tensile force is applied, a zero-force state is evident from the force sensor while the displacement sensor always measures the displacement generated by piezoelectric stacks. The inset also shows the data when the sample is separated which indicates the coupling between the force sensor and the applied displacement. Figure from Ref. [174]

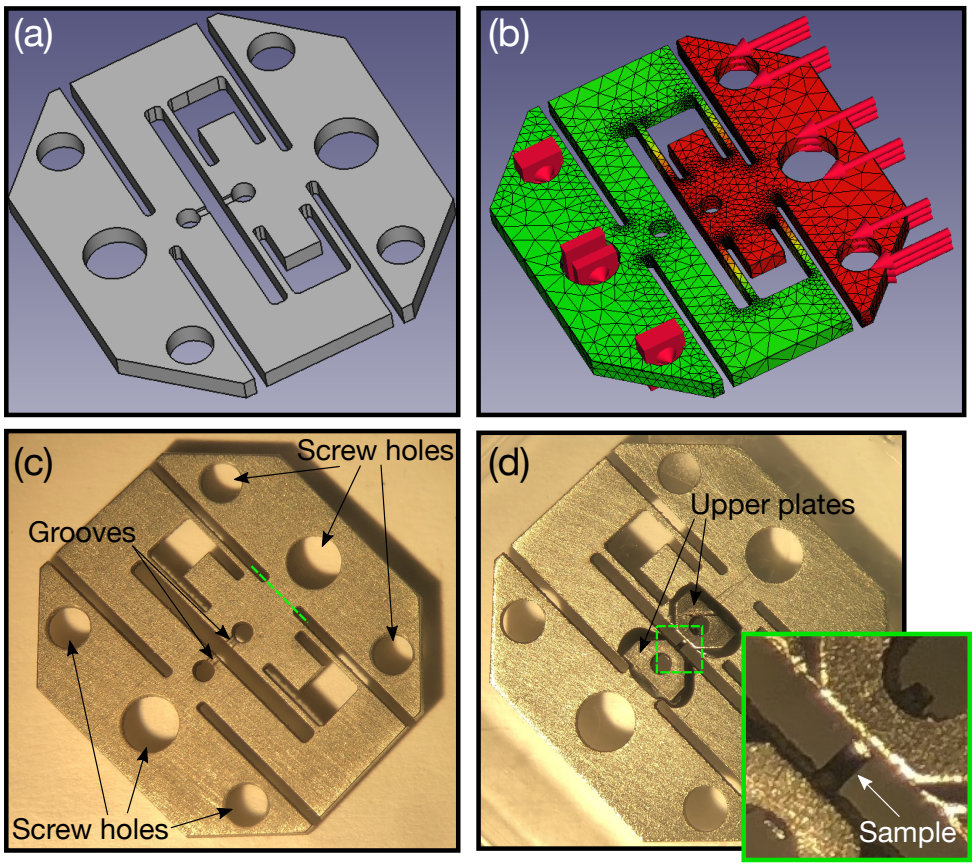

Figure 3.5: **Sample carrier.** (a) Schematic of the sample carrier generated with 3D CAD. (b) Deformed sample carrier in the finite element simulation. The carrier is fixed at the bottom left three screw holes and the force was applied along red arrows at the top right three screw holes. The displacement is represented by red color and the green part is not displaced in this simulation. (c) Picture of a sample carrier made from titanium based on the design shown in (a). It is seen on the strain rig in Fig. 3.2 (a). Screw holes are to fix the carrier on the strain rig. Grooves are for placing a needle shaped sample. Green dashed lines indicates the potential cutting position to determine the zero-stress state with the stress rig. (d) Same as (c) but after mounting a sample. Upper plates are placed on the carrier and those are fixed by glue, Stycast 2850FT. Inset shows a zoom around the sample.

3.2.4 Sample carriers

In the former design for mounting a sample on stress / strain rigs, a sample has been mounted directly on the rig. As seen in the following section, it takes a quite long time to prepare one properly shaped sample, and mounting such a tiny sample on the device always requires extreme precision and concentration. Also one has to break the sample when dismounting it from the rig for example due to internal failures of the device such as bad electrical connections despite a good sample preparation. Therefore, for performing more efficient measurements and improving practical convenience, I have designed a sample carrier so that one can easily mount a sample on the rig. The schematic image of the carrier is shown in Fig. 3.5 (a). The central idea is that one can mount a tiny sample on this carrier first and then mount this carrier on the rig. Since the size of the carrier is a few cm scale, one can easily mount and dismount it on the rig just by tightening screws even without a microscope. Also one does not have to break a sample when dismounting the carrier from the rig. This new method requires only ten minutes or so to exchange from one carrier to another, while it takes at least several hours to mount a sample on the rig directly, including four hours to cure the Stycast 2850 FT. This makes measurements more efficient in many occasions. For example, it is obviously impossible to mount a sample on a rig while another sample mounted on the rig is in the cryostat for transport experiments in the former sample mounting design. However, in the current method, one can attach electrical wires on the sample mounted on the carrier while another sample is being measured in the cryostat. This method is also favorable outside of in-house laboratories in beamtimes at synchrotron facilities. The typical duration of one beamtime is several consecutive days or sometimes a week, therefore several samples are usually measured during one beamtime. The number of samples that can be mounted on a rig before the beamtime was still limited by the number of rigs available (typically only a few), yet one can mount samples on the carriers as much as possible ahead of each beamtime. It significantly reduces the preparation time at beamlines when one has to change a sample. As a consequence, one can focus on experiments at the synchrotron facilities.

The force generated by the piezoelectric stacks is applied not only on the sample but also on the sample carrier in this design, thus it is important to know the mechanical properties of the carrier to apply the strain on the sample efficiently. To this aim, we have simulated the mechanical behavior of the carrier prior to the production. Figure 3.5 (b) shows the deformed carrier under 5 N of uniaxial force for titanium obtained by a finite element simulation. In this simulation, the spring constant of the carrier was estimated to be less than 10 % of the one of typical needle shaped $YBa_2Cu_3O_{6+x}$ samples. Therefore the strain produced by the piezoelectric stacks efficiently transfers to the sample.

Also on this carrier there are grooves of width 400 μm and depth 150 μm where the sample is placed as indicated in Fig. 3.5 (c). In the previous design, the sample was placed on the flat titanium plates with Stycast 2850 FT. Therefore it was sometimes not easy to align the sample along the uniaxial pressure direction. On the other hand in the present case, the sample is naturally aligned by these grooves. After placing the sample buried in the Stycast 2850 FT, upper plates are put on top of the carrier to ensure the homogeneous strain as shown in Fig. 3.5 (d). Since the Stycast 2850FT epoxy includes particles diameters up to 45 μm, the ideal sample thickness is $\sim$ 100 μm predetermined by the depth of the grooves for efficient strain transfer. It is usually quite feasible to obtain needle shaped samples whose thickness is 100 μm since the thickness of the original

$YBa_2Cu_3O_{6+x}$ single crystals before cutting and polishing is much greater than 100 μm. The distance between two grooves is equal to the exposed length L where the strain is applied and can be set in producing the carriers, therefore carriers with shorter gap length can be prepared for materials whose original size is not as large as $YBa_2Cu_3O_{6+x}$.

To determine the zero stress, one could in principle split the sample by the tensile force as explained in Fig. 3.4. However it is not feasible to perform transport experiments under these conditions because the current flow is disrupted. Instead of cutting the sample itself as in the inset picture of Fig. 3.4, the mechanically identical setup can be achieved by cutting a part of the carrier as indicated by the green dashed line in Fig. 3.5 (c). The samples for stress sweep measurements in the transport experiments in the next chapter were prepared in this fashion and the thus zero stress state was determined.

3.3 Sample preparation

3.3.1 Introduction

Single crystals of $YBa_2Cu_3O_{6+x}$ studied in this thesis were grown using the self-flux method [175]. As starting materials, powders of Y_2O_3, $BaCO_3$, and CuO were mixed in a crucible which is made of ZrO_2 stabilized with Y_2O_3. The crucible was placed in the furnace and the flux undergoes a thermal treatment for several days to homogenize the melt and initiate the growth of the crystals. After this thermal treatment, the crucible was decanted inside the furnace into a larger porous material which absorbs the remaining flux. After cooling to room temperature the crystals can be picked from the crucible. The typical dimensions of crystals obtained in this method are $a \times b \times c = 2 \times 2 \times 0.5$ mm^3. However they can be larger or smaller depending on details of each trial. A schematic of the growth process is shown in Fig. 3.6.

As-grown samples have unknown and inhomogeneous oxygen contents and the crystal structure is twinned: multiple domains of orthorhombic structure exist in one crystal because of random distribution of CuO chains. Therefore further annealing treatments are necessary to study $YBa_2Cu_3O_{6+x}$ samples whose oxygen content and crystal structure are well determined.

3.3.2 Annealing: tuning oxygen contents

The properties of cuprates depend on the hole doping of the CuO_2 plane (the number of holes per Cu atoms), therefore it is crucial to accurately control this quantity and obtain homogeneously doped samples for advanced measurements. This is often achieved by heterovalent substitution or tuning the oxygen content. In the case of $YBa_2Cu_3O_{6+x}$, the latter method is routinely used. By annealing crystals under the certain oxygen partial pressure, the amount of oxygen in the CuO chain layers is controlled. Lindemer *et al.* systematically characterized the oxygen stoichiometry x of $YBa_2Cu_3O_{6+x}$ in different conditions of temperature and oxygen partial pressure as shown in Fig. 3.7 [178]. For instance, to obtain $YBa_2Cu_3O_{6.67}$ which we mainly studied in this thesis, one can tune the oxygen content by annealing crystals at 555 °C with 5% O_2. To obtain homogeneously tuned oxygen content, the duration of the annealing process is also important. As illustrated

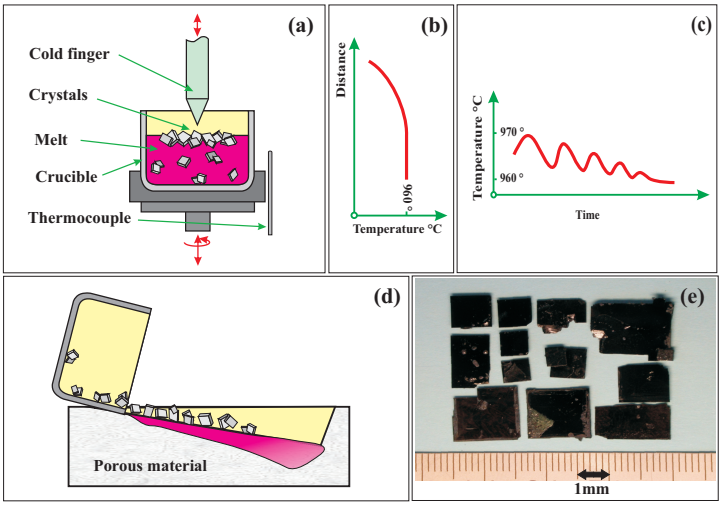

Figure 3.6: **Schematic explanation of $YBa_2Cu_3O_{6+x}$ single crystal growth using the self-flux method.** (a) Schematic of the sample growth apparatus in a furnace. (b) Temperature gradient around the growth interface made by the cold finger. (c) Oscillation of temperature generated by the motion of the cold finger. (d) Schematic of decanting: the crystals are separated from the residual melt absorbed by a porous material.(e) Typical single crystals of $YBa_2Cu_3O_{6+x}$. Figures from Ref. [176].

in Ref. [179], the oxygen diffusion process can be modeled using the following formula:

$$\frac{c(t) - c_e}{c_0 - c_e} = \frac{8}{\pi^2} \exp(-t/\tau), \tag{3.12}$$

where $\tau = b^2/\pi^2 D(T)$ is the relaxation time, $c(t)$ is the oxygen concentration as a function of time, c_0 is the initial concentration, c_e is the saturation concentration, b is the width of the sample (or the thinnest side of the sample), $D(T)$ is the diffusion constant, and T is temperature. The temperature dependence of the diffusion constant is given by $D(T) = D_0 \exp(\Delta E/k_B T)$, where k_B is the Boltzmann constant, D_0 is the diffusion constant and the activation energy ΔE is estimated to be around 0.8 eV for $YBa_2Cu_3O_{6+x}$. Therefore, the relaxation time τ is essentially determined by the annealing temperature T and the thinnest sample dimension b. One has to consider those parameters in annealing samples to estimate τ, yet based on our experiences one week is usually long enough to obtain a homogeneous doping level. It took around five days to reach the equilibrium at 460 °C (Fig. 3.8)[3]. Also the initial oxygen concentrations have little effect on the relaxation time τ as can be seen in Fig. 3.8, thus in practice one can just anneal as-grown samples to tune the oxygen content. In order to stabilize the oxygen content obtained by this annealing process, the samples should be quenched by dropping them into liquid nitrogen right after opening the furnace. The oxygen content becomes inhomogeneous again if they are gradually cooled down to room temperature.

[3]To obtain $YBa_2Cu_3O_7$, i.e., fully oxygenated samples, they should be annealed at 365 °C under 100 % O_2. It is relatively low temperature and therefore the samples are annealed for one month.

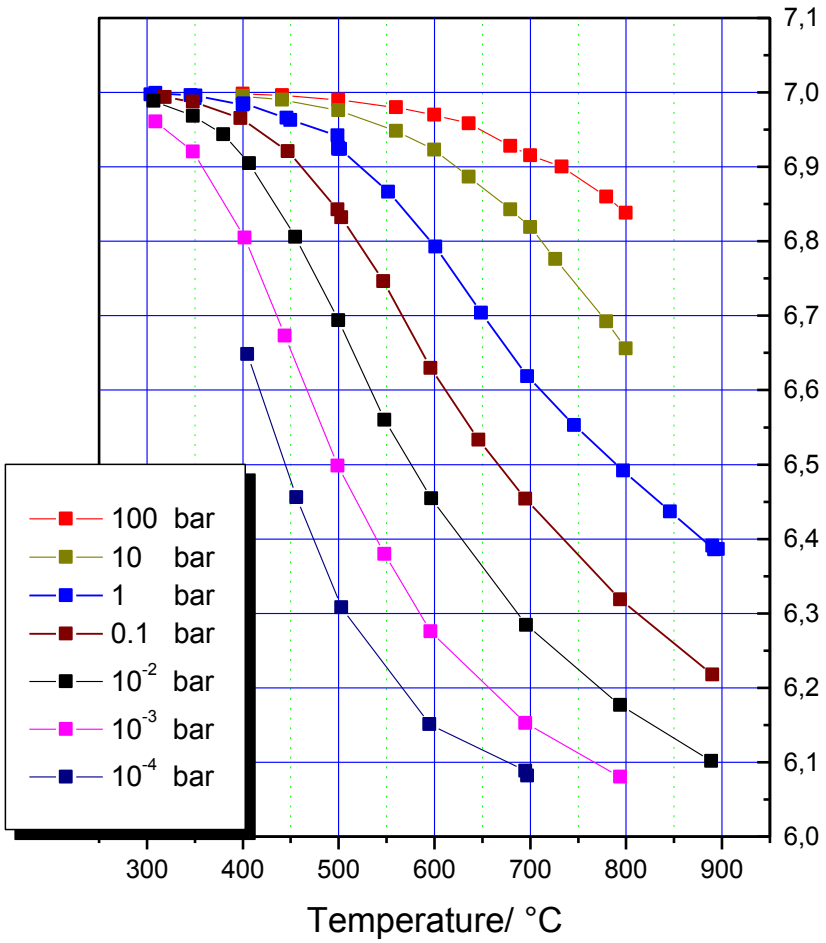

Figure 3.7: **Oxygen content of $YBa_2Cu_3O_{6+x}$ as a function of annealing temperature and the oxygen partial pressure.** The vertical axis indicates $6+x$. Based on the target doping level, one can choose the combination of temperature and partial pressure. The relaxation time τ depends on the temperature and sample dimensions. Figure from Ref. [177].

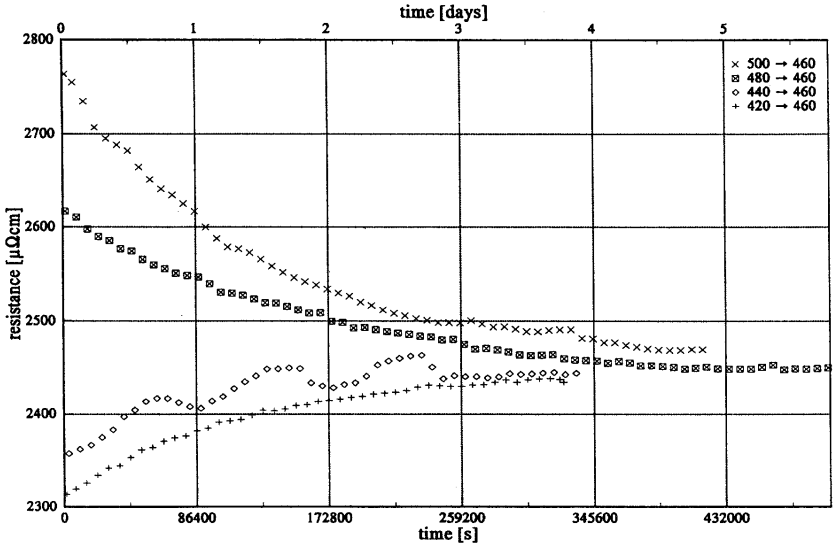

Figure 3.8: **Time dependence of the resistivity in $YBa_2Cu_3O_{6+x}$ annealed at 460 °C.** Each curve shows the resistivity at 460 °C of four different samples obtained after annealing at 500 °C, 480 °C, 440 °C, and 420 °C representing different hole doping levels. The resistivity does not change after the oxygen content reaches the equilibrium value at 460 °C. Figure from Ref. [179].

3.3.3 Detwinning

A distinct feature of $YBa_2Cu_3O_{6+x}$ among cuprate families is the oxygen order in the CuO chain layer. By annealing crystals as described in the previous section, the amount of oxygen in the CuO chain layers becomes homogeneous, however the orientation of the chain is still mixed, i.e., twinned. As described in Ref. [180], to make samples twin-free, samples were mechanically stressed with ∼50 MPa at 400 °C in Ar. The presence of the twin domains can be observed by means of a polarized microscope (Fig. 3.9). The color of each domain on the surface viewed through the microscope is different depending on the relative orientation of the polarization and domain direction. Note that using this method, one can check the twinning only on the surface because the penetration depth of the visible light is limited. Nevertheless, this simple method always gives sufficient accuracy. A more precise check can be made by other techniques too, e.g., phonon spectra obtained in Raman scattering measurements [181].

3.3.4 Low temperature annealing

To maximize the domain size of the oxygen orders in the CuO chain layers, samples should be annealed at a temperature which is a little below the structural transition temperature [32, 182]. This is achieved by annealing the samples in a glass tube sealed with 800 mbar of Ar for one week. Note that the transition temperature of the ortho-VIII order in $YBa_2Cu_3O_{6.67}$ that we have mainly studied in this thesis is 40 °C (Fig. 2.5 (b)), therefore leaving the samples in this doping regime at room temperature is a good condition to maximize the domain size of the oxygen order.

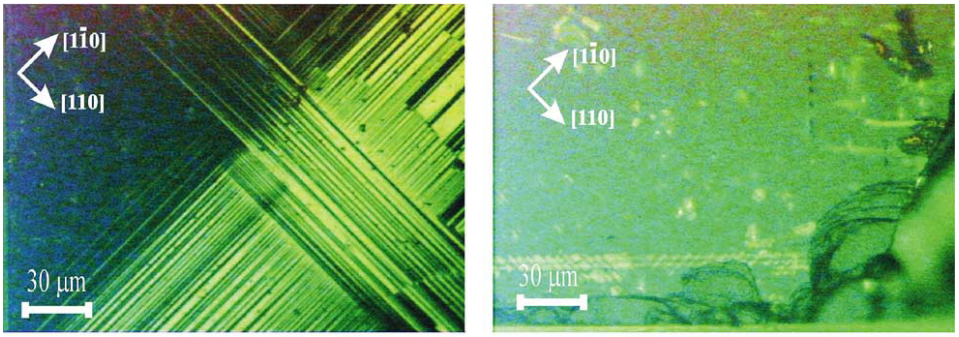

Figure 3.9: **Crystal surface of $YBa_2Cu_3O_7$ through the polarized microscope.** The image was taken under the polarized microscope before detwinning (left) and after detwinning (right) Figures from Ref. [180].

3.3.5 Characterization and selection of high-quality samples

After the three annealing steps (tuning the oxygen content, detwinning, and maximizing the oxygen order), it is important to characterize the crystal quality before moving on to preparing samples for advanced measurements. To this end, we routinely check the superconducting transition temperature T_c and the c-axis lattice parameter c.

As mentioned in chapter 2.2, x in $YBa_2Cu_3O_{6+x}$ is not equal to the hole doping p per Cu ion in the CuO_2 planes unlike the 214 cuprate families. T_c usually gives a reasonable indication of p, yet different T_c's indicate the same oxygen contents particularly for $x < 0.5$ depending on the oxygen orders in the CuO chain layers as shown in Fig. 3.10 (a). Also T_c is easily reduced if samples are contaminated by impurities [183]. Therefore T_c is not an ideal indicator to estimate p. In addition, T_c is not so susceptible to p around the 1/8 doping region, which is well known as the 1/8 plateau, where we have mainly worked in this thesis. On the other hand, T_c *v.s.* c is a more unique relation, thus c has been commonly used for $YBa_2Cu_3O_{6+x}$ to estimate p. The empirical relationship between p and c has been carefully studied in Ref. [182] and is given as follows:

$$p = 11.491y + 5.17 \times 10^9 y^6, \tag{3.13}$$

where $y = 1 - c/c_0$. c is the c-axis lattice parameter and c_0 is 1.18447 nm. The c-axis lattice parameter was determined with x-ray diffraction (XRD) measurements at room temperature. Since the lattice parameter varies only in very narrow range from $c = 11.771$ Å ($YBa_2Cu_3O_{6.40}$, $p = 0.072$) to $c = 11.6835$ Å ($YBa_2Cu_3O_{6.99}$, $p = 0.189$), it is important to accurately estimate c from XRD data. Therefore, the $2\theta - \theta$ scans were measured for multiple Miller indices of the Bragg plane, (0,0,l) ($l = 10, 11, 12, 13, 14$) as shown in Fig. 3.11. To obtain c by the Bragg's law, we used $2\theta_0$ which satisfies the following relationship as explained in Ref. [184],

$$\lim_{\theta \to \theta_0} \frac{\cos^2\theta}{2} \left(\frac{1}{\sin\theta} + \frac{1}{\theta} \right) = 0. \tag{3.14}$$

Based on the c-axis lattice parameter c measured in the XRD measurements, the hole doping p was estimated using Eq. (3.13). In this way, one can see where T_c and p of each

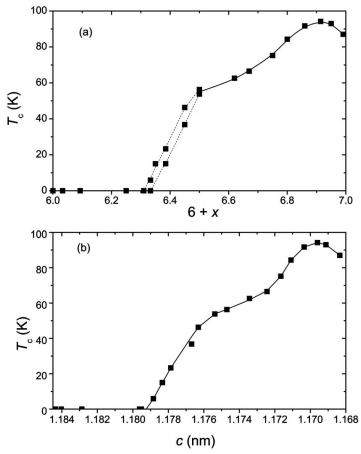

Figure 3.10: T_c **of** $YBa_2Cu_3O_{6+x}$**.** The horizontal axis is the oxygen content (a) and the c-axis lattice parameter (b). T_c *v.s.* c shows more unique relationship, particularly for $x < 0.5$. Figures from Ref. [182].

sample are located in the T_c-p phase diagram. We have compared those physical quantities with the T_c-p phase diagram based on the highest quality samples obtained in previous studies [182, 151]. All the samples studied in this thesis satisfy this highest standard of $YBa_2Cu_3O_{6+x}$.

3.3.6 Preparation for strain experiments

As described in Ref. [169], the strained samples have to have a long bar shape, the so-called "needle" shape. The typical dimensions of a needle shaped sample are $a(b) \times b(a) \times c = 2 \times 0.2 \times 0.1$ (mm^3) for straining along the a-axis (b-axis). The sample length is not an important parameter, because the sample is partially strained and this length is determined by the distance between two clamps. $L = 600$ - 800 μm was used in the present studies. The sample width ω is, however, important and the strain homogeneity has been studied by means of finite element analysis [168]. In our sample mounting method, the strain inhomogeneity is less than 1 % at a distance ω away from the clamp. Therefore L/ω should be greater than 3 to achieve the homogeneous strain at the center of the sample. Therefore, ω =200 μm is a reasonable choice for $L = 600$ - 800 μm. The sample thickness t is another important parameter because the sample can be easily buckled by strain if the thickness is too small. The critical ratio between L and t is estimated to be $L/t = \pi/\sqrt{3\varepsilon}$, where ε is the strain. To achieved 1 % strain, one can see that $t = 100$ μm is thick enough by a back-of-the-envelope calculation.

As mentioned above, the typical dimensions of as-grown samples is $a \times b \times c = 2 \times 2 \times 0.5$ mm^3 and it does not change after the annealing processes. Therefore the sample has to be cut and polished in a controlled way to obtain needle shaped samples. First, the sample was cut using a tungsten wire saw (WS-22 from IBS Fertigungs- und Vertriebs-GmbH). To fix the sample on the sample stage, Technovit®5071 is used. This glue does not have to be heated for curing and can be dissolved by acetone at room temperature. It is ideal for $YBa_2Cu_3O_{6+x}$ since the oxygen content becomes more inhomogeneous when the sample is heated in air. Utilizing a thin wire, the sample loss during the cutting process is less than 100 μm. The cut sample is still too thick for the strain experiments, therefore the sample is polished down to the "needle" shape with the desired 100 μm thickness. Both ab surfaces

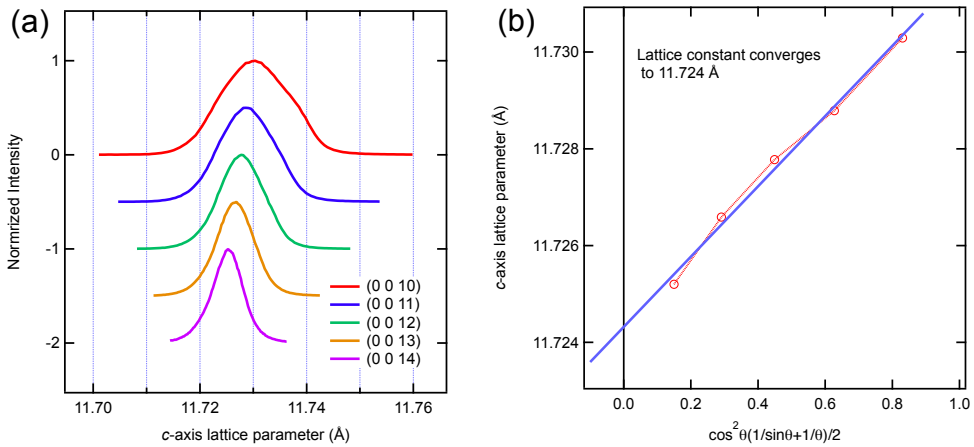

Figure 3.11: **X-ray diffraction measurements.** (a) Normalized $2\theta - \theta$ scans for the Miller indices of the Bragg plane, (0,0,l) ($l = 10, 11, 12, 13, 14$). The horizontal axis is converted to the lattice parameter from θ using the Bragg's law. For clarity, the curves are shown with offsets vertically. (b) c-axis lattice parameter that gives the peak of the $2\theta - \theta$ scans in (a) (red points). Fitting with the linear function (blue line). The extrapolation of the experimental data is defined such that Eq. (3.14) is satisfied. Here the data of sample 3 (R555c1N4) used in the transport experiments are shown as an example.

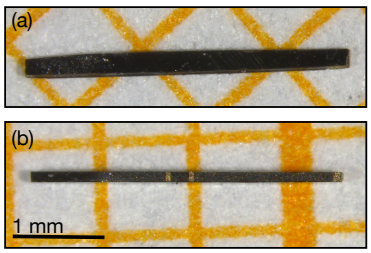

Figure 3.12: **Photographs of a needle shaped sample.** (a) Top view. (b) Side view. Gold patches on the surface are electrical contacts for transport experiments.

were polished for measurements under high strain: any small cracks or indentations on the surface could cause the strain inhomogeneity which results in buckling of the sample even with relatively small strain. For transport experiments, one has to bear in mind that the electrical contacts are placed only on the sides of the sample to observe the in-plane quantities [185, 23]. Therefore the gold was deposited on the sample surfaces before the polishing process and the surface was polished also to get rid of the gold on the *ab*-surface.

3.4 Transport measurements

3.4.1 Introduction

Observations of new transport phenomena in solids are often the first driving forces for condensed matter physicists to start studying new physics. Great examples are the discoveries of zero resistivity in superconductors [186] and the quantized Hall coefficient in the quantum Hall effect systems [187], both of which had significant impact and motivated physicists to elucidate their microscopic origins and to establish a new direction of physics.

In short, transport phenomena can be defined as phenomena where (quasi)particles in solids affected by external fields such as electric or magnetic fields deliver electricity or heat from one place to another. This implies that transport phenomena are in general associated with energy dissipation, which requires us to analyze the phenomena as a problem of non-equilibrium systems. The general theoretical treatment of non-equilibrium states is still one of the most difficult subjects in thermodynamics and statistical mechanics to date. However it was rigorously proven that the dissipation of the response of the physical quantity by the external field in a non-equilibrium state is equal to the its fluctuation in an equilibrium state as long as the response is linearly proportional to the external field. This is known as the fluctuation-dissipation theorem [163]. The linear response theory is a special example, where one can relate the macroscopic transport phenomena and microscopic response functions in a rigorous fashion. In the framework of this theory, establishing quantitative correspondences between macroscopic transport coefficients and atomic scale correlation functions can provide fresh perspectives for solid-state research.

In this section, we explain general theoretical descriptions of electrical transport properties in solids and the experimental setup of our transport measurements.

3.4.2 Theoretical descriptions of transport experiments

In this section, we describe the formalism of transport properties in several ways from a phenomenological classical picture to a general quantum mechanical picture. As the theory develops, it becomes less phenomenological and one can understand the microscopic origin of the various transport properties in relation with microscopic correlation functions.

Ohm's law

Ohm's law was discovered by Henry Cavendish in 1781, but his discovery had not been known until James Clerk Maxwell published "Electrical Researches of Henry Cavendish" in 1879. Since Georg Simon Ohm re-discovered and published this law in 1826, nowadays it is called Ohm's law.

Ohm's law states that a potential difference between two points in an electrical circuit is proportional to the current that flows between the two points. When the potential difference is V and the current is I, the following relationship is established.

$$V = RI. \tag{3.15}$$

The factor of proportionality R is called resistance. R depends on the dimension, material, and temperature of the conductor.

For later explanations, let us derive the differential form of Ohm's law. To this aim, let us consider the infinitesimal cross section of the conductor whose area is ΔS and normal vector is $\boldsymbol{n}$, then the current which flows at the cross section I is expressed as $I = \boldsymbol{j} \cdot \boldsymbol{n} \Delta S$, where $\boldsymbol{j}$ is the current density at this cross section. On the other hand, the potential difference between two infinitesimal points along the normal line with respect to the cross section V is given by $V = \boldsymbol{E} \cdot \boldsymbol{n} \Delta L$, where $\boldsymbol{E}$ is the electrical field at the cross section and ΔL is the distance between the two points. Using the equations, one can derive

$$\boldsymbol{j} = \sigma \boldsymbol{E}, \tag{3.16}$$

where $\sigma(=1/\rho)$ is a conductivity defined as the inverse of $\rho = R\Delta S/\Delta L$ called resistivity, which depends on temperature and material of the conductor. Note that σ (and ρ) is in general a tensor that connects two vectors, $\boldsymbol{j}$ and $\boldsymbol{E}$. This formula expresses Ohm's law in the infinitesimal space, also called the differential form of Ohm's law. In the language of the linear response theory, $\boldsymbol{j}$ and $\boldsymbol{E}$ are the response and external field, and σ is the response function.

Obviously, this formalism is based on a phenomenological classical picture, which does not enable one to understand the microscopic origin of resistivity. Nevertheless we stress that physical quantities measured in experiments are V and I of a sample.

Drude model

The Drude model was proposed by Paul Karl Ludwig Drude in 1905. This model is one of the applications of the kinetic theory of gases. It is assumed that charged particles such as electrons or holes can move around and are scattered by cations fixed at certain space points in a certain relaxation time τ. Note that the scattering of the charged particles is introduced phenomenologically in this model, hence the microscopic mechanism of the scattering is not considered at all. In this model, the classical mechanical equation of motion of one charged particle can be described as

$$m\frac{d}{dt}\boldsymbol{v} = -\frac{m}{\tau}\boldsymbol{v} + q\boldsymbol{E}, \tag{3.17}$$

where $m, \boldsymbol{v}, q$ are the mass, velocity, and charge of a charged particle, respectively. In a steady state ($d\boldsymbol{v}/dt = \boldsymbol{0}$), one can obtain

$$\boldsymbol{j} = qn\boldsymbol{v} = \left(\frac{nq^2\tau}{m}\right)\boldsymbol{E}, \tag{3.18}$$

where n is the carrier density. It is nothing but the differential form of Ohm's law (Eq. 3.16). Under the magnetic field $\boldsymbol{H}$ the equation of motion is modified due to the Lorentz force as follows:

$$m\frac{d}{dt}\boldsymbol{v} = -\frac{m}{\tau}\boldsymbol{v} + q\left(\boldsymbol{E} + \frac{1}{c}\boldsymbol{v}\times\boldsymbol{H}\right). \tag{3.19}$$

The Hall coefficient is defined as $R_{\mathrm{H}} = E_y/H_z j_x$ in a steady state, therefore it turns out that

$$R_{\mathrm{H}} = \frac{1}{nqc}. \tag{3.20}$$

Remarkably by measuring the Hall effect R_{H}, one can identify the type of the carrier from the sign of R_{H} since it depends on the charge q: $+/-$ corresponds to holes/electrons. However, the scope of the Drude law is limited and it is theoretically imperfect for the following reasons. As mentioned above, we treat the charged particles in the framework of classical mechanics while they should be treated quantum mechanically. In fact, the Drude model cannot predict the existence of band insulators for this reason.

Boltzmann transport theory

Here, we describe the Boltzmann equation to treat the transport coefficients of quasiparticles. Since this is a semiclassical picture, one can define $(\boldsymbol{r}, \boldsymbol{k}, t)$ by ignoring the uncertainty principle between $\boldsymbol{r}$ and $\boldsymbol{k}$. The distribution function of particles $f(\boldsymbol{r}, \boldsymbol{k}, t)$ is defined as

$$f(\boldsymbol{r}, \boldsymbol{k}, t) d^3r d^3k = \begin{pmatrix} \text{The number of the particles whose position and wave number} \\ \text{are within } (\boldsymbol{r}, \boldsymbol{r} + d\boldsymbol{r}) \text{ and } (\boldsymbol{k}, \boldsymbol{k} + d\boldsymbol{k}), \text{ respectively} \end{pmatrix}. \tag{3.21}$$

The distribution function obeys the following equation (Boltzmann equation),

$$\frac{\partial}{\partial t} f(\boldsymbol{r}, \boldsymbol{k}, t) + \boldsymbol{v} \cdot \frac{\partial}{\partial \boldsymbol{r}} f(\boldsymbol{r}, \boldsymbol{k}, t) + \frac{\boldsymbol{F}}{\hbar} \cdot \frac{\partial}{\partial \boldsymbol{k}} f(\boldsymbol{r}, \boldsymbol{k}, t) = \left(\frac{\partial f}{\partial t} \right)_{\text{coll}}, \tag{3.22}$$

where $\boldsymbol{v} = \partial \boldsymbol{r} / \partial t$ and $\boldsymbol{F} = \partial (\hbar \boldsymbol{k}) / \partial t = e\boldsymbol{E}$. The right side $(\partial f / \partial t)_{\text{coll}}$ implies the collisions among the particles. Note that this formalism is quite general so that one can apply various physical models to express general flows beyond electrons in solids. To calculate electrical transport properties of electrons in solids, the relaxation time approximation is often used: $(\partial f / \partial t)_{\text{coll}} = -\left(f(\boldsymbol{r}, \boldsymbol{k}, t) - f_0 \right) / \tau(\boldsymbol{k})$, where f_0 is the distribution function in the equilibrium state in the absence of the electric field (the Fermi-Dirac distribution function) and $\tau(\boldsymbol{k})$ is the relaxation time. Assuming the steady state $((\partial f / \partial t) = 0)$, the uniformity in the real space $(\partial f(\boldsymbol{r}, \boldsymbol{k}, t) / \partial \boldsymbol{r} = 0)$, and the relaxation time approximation, the distribution function is given by

$$f(\boldsymbol{k}) = f_0 + e\tau(\boldsymbol{k}) \boldsymbol{E} \cdot \boldsymbol{v} \frac{\partial f(\boldsymbol{k})}{\partial \varepsilon(\boldsymbol{k})}, \tag{3.23}$$

where $\boldsymbol{v} = \partial \varepsilon(\boldsymbol{k}) / \partial (\hbar \boldsymbol{k})$ is the group velocity of the quasiparticles. The current along the i-direction j_i under the electric field along the j-direction E_j $(i, j = x, y, z)$ is given by

$$j_i = -e \sum_{\boldsymbol{k}} v_i f(\boldsymbol{k}) \simeq e^2 \sum_{\boldsymbol{k}} v_i v_j \tau(\boldsymbol{k}) \left(-\frac{\partial f_0(\boldsymbol{k})}{\partial \varepsilon(\boldsymbol{k})} \right) E_j. \tag{3.24}$$

Therefore the conductivity σ_{ij} defined in the Ohm's law (Eq. 3.16) is

$$\sigma_{ij} = e^2 \sum_{\boldsymbol{k}} v_i v_j \tau(\boldsymbol{k}) \left(-\frac{\partial f_0(\boldsymbol{k})}{\partial \varepsilon(\boldsymbol{k})} \right). \tag{3.25}$$

If one assumes isotropic scattering, i.e., a $\boldsymbol{k}$-independent scattering rate τ, for the energy dispersion of free electrons $\varepsilon(\boldsymbol{k}) = \hbar^2 \boldsymbol{k}^2 / 2m$, the conductivity is given by $\sigma_{xx} = ne^2\tau / m$ which reproduces the result of the Drude model. The group velocity of quasiparticles can be derived from the single particle spectra of quasiparticles $\varepsilon(\boldsymbol{k})$, but there are a number of candidate scattering mechanisms which are reflected by $\tau(\boldsymbol{k})$: impurities, phonons, magnons, Coulomb interactions between electrons etc... Those could be in principle decomposed by their temperature dependence of resistivity yet it is often difficult to accurately identify which scattering mechanism plays a dominant role especially when multiple scattering mechanisms are of comparable strength. In this regard, complementary scattering experiments are valuable source of information about possible elementary excitations which scatter with quasiparticles and about the origin of the charge transport properties. We remark that an attempt to relate the resistivity of cuprates with the lifetime of quasiparticles obtained in photoemission experiments was reported [188].

Linear response theory: Kubo formula

To treat transport properties further microscopically beyond the Boltzmann theory, the linear response theory is famously known. In the quantum field theory, the current operator $\boldsymbol{j}(\boldsymbol{r})$ under the electromagnetic fields is given as follows:

$$\boldsymbol{j}(\boldsymbol{r}) = -\frac{ie\hbar}{2m}\left(\psi^\dagger(\boldsymbol{r})\nabla\psi(\boldsymbol{r}) - \nabla\psi^\dagger(\boldsymbol{r})\psi(\boldsymbol{r})\right) - \frac{e^2}{m}\boldsymbol{A}(\boldsymbol{r})\psi^\dagger(\boldsymbol{r})\psi(\boldsymbol{r}), \tag{3.26}$$

where $\psi(\boldsymbol{r})$ is the field operator of the electron and $\boldsymbol{A}(\boldsymbol{r})$ is the vector potential of the electromagnetic field. The first term on the right side of Eq. 3.26 is called the paramagnetic current $\boldsymbol{j}^{\text{para}}(\boldsymbol{r})$ and the second term is called the diamagnetic current $\boldsymbol{j}^{\text{dia}}(\boldsymbol{r})$. The latter quantity plays an important role to interpret the Meissner effect in superconductors theoretically. The diamagnetic current is by definition proportional to the vector potential, therefore it is already a part of the linear response. Let us consider the contribution from the paramagnetic current. The Hamiltonian of the free-electron system under the electromagnetic field in the second quantization formalism is given by

$$\mathcal{H} = \int d\boldsymbol{r}\psi^\dagger(\boldsymbol{r})\left(\frac{1}{2m}(\boldsymbol{p} - e\boldsymbol{A}(\boldsymbol{r}))^2 + e\varphi(\boldsymbol{r})\right)\psi(\boldsymbol{r}), \tag{3.27}$$

where $\boldsymbol{p}$ is the momentum operator and $\varphi(\boldsymbol{r})$ is the electric potential. Thus the perturbative Hamiltonian $\mathcal{H}'$ within the first order of $\boldsymbol{A}(\boldsymbol{r})$ is given as follows:

$$\mathcal{H}' = -\int d\boldsymbol{r}\ \boldsymbol{j}^{\text{para}}(\boldsymbol{r})\cdot\boldsymbol{A}(\boldsymbol{r}). \tag{3.28}$$

Therefore one obtains the expected value of the current operator in the Fourier space as a linear response of the vector potential, by following the general treatments in the linear response theory (the Kubo formula) for the present case [163]:

$$\langle j_\mu(\boldsymbol{q},\omega)\rangle = \sum_{\nu=x,y,z}\left\{\Phi_{\mu\nu}(\boldsymbol{q},\omega) - \frac{ne^2}{m}\delta_{\mu\nu}\right\}A_{\nu,\boldsymbol{q},\omega}, \tag{3.29}$$

where the current-current correlation function $\Phi_{\mu\nu}(\boldsymbol{q},\omega)$ is defined as

$$\Phi_{\mu\nu}(\boldsymbol{q},\omega) = \frac{i}{\hbar}\int_0^\infty dt\ e^{i\omega t-\delta t}\int d\boldsymbol{r}\ e^{-i\boldsymbol{q}\cdot(\boldsymbol{r}-\boldsymbol{r}')}\left\langle[j_\mu^{\text{para}}(\boldsymbol{r},t), j_\nu^{\text{para}}(\boldsymbol{r}',0)]\right\rangle. \tag{3.30}$$

Note $\boldsymbol{j}^{\text{para}}(\boldsymbol{r},t)$ is a current operator in the Heisenberg picture. Therefore one can understand the electrical transport associated with the energy dissipation by means of the current-current correlation function in the equilibrium state. In this scheme, the Hall coefficient for a free electron system in a weak magnetic field was also derived [189].

Theoretically one ends up calculating the correlation function $\Phi_{\mu\nu}(\boldsymbol{q},\omega)$ with realistic interactions to derive the conductivity experimentally observed in solids in some ways such as the Feynman diagram method at zero temperature or the Feynman diagram method through Matsubara Green functions at nonzero temperature [190]. Since the field operator of electrons $\psi(\boldsymbol{r})$ is directly related to the Green function of electrons, one can see how the transport properties are related to such fundamental microscopic correlation functions.

3.4.3 Experimental setup

The resistivity measurement was performed with the typical four-point setup. It is hard to accurately measure the resistance of the sample with a two-point setup because one measures the total voltages arising from the resistance of wires between the sample and voltmeter plus the resistance of the sample which is often much smaller than that of the wires due to only a few hundred μm scale sample size. For the Hall measurements, on top of two contacts for the current, two additional contacts perpendicular to the current flow are indispensable, therefore the geometry has to be four-point. Nevertheless, six contacts were prepared for one sample to obtain a possibility to measure two longitudinal and two transverse potential drops simultaneously. In this method, the current flows through the sample homogeneously and the potential drop between two points of the sample is accurately measured.

Lock-in amplifiers, e.g., SR830 from Stanford Research Systems, have been used for the voltmeter as well as a part of the current source. The output voltage with a certain frequency from the lock-in amplifier with a series resistor acts as the current source. A sophisticated current source which enables one to minimize the common-mode voltage was used in all the measurements (see details in Appendix A of Ref. [168]). The reference voltage from the lock-in amplifier and the series resistor were set to 1-5 V and 1 kΩ, therefore the typical current value was 1-5 mA. A digital lock-in multiplies the reference and sample voltages, thereby rejects all signals whose frequencies are different from the reference frequency. This acts as a low-pass filter. The DC signal of the sample resistance can be obtained from the voltage with the frequency of the current, which is identical to the reference one, therefore the in-phase signal is used for the resistance. Likewise the signal with $\pi/2$ shift is simultaneously obtained using the lock-in amplifier. In the electrical circuit we used for the transport measurements, the in-phase and out-of-phase signals correspond to the resistance and reactance of the complex impedance, respectively. The reference frequencies used for all the experiments were 50-100 Hz, however the actual frequencies strongly depend on the cryostat environment and sample preparation. For instance, bad contacts on the sample can be highly capacitative.

Transport measurements on quantum materials at cryogenic temperature and/or under magnetic field are routinely conducted in PPMS® from Quantum Design. However the sample space of the PPMS® is not large enough to accommodate the stress rig, therefore the variable temperature insert (VTI) from Oxford Instruments was used to realize the simultaneous applications of uniaxial stress and magnetic field at low temperature.

3.5 X-ray scattering measurements

3.5.1 Introduction

In the previous section, we have explained how the macroscopic transport properties are related to the atomic scale correlation functions. The latter physical quantities can be experimentally obtained in microscopic experiments such as photoemission and scattering measurements. The results obtained in microscopic experiments directly constrain theoretical proposals of transport properties. Conversely, studying low energy elementary excitations by scattering experiments provides crucial hints to understand the anomalous

transport properties of quantum materials.

Elementary excitations, quasiparticles and collective modes, can be described by the following three basic quantities [8]. The single particle Green function $G(\boldsymbol{r}, \boldsymbol{r'}, t-t')$ is defined as follows:

$$G(\boldsymbol{r}, \boldsymbol{r'}, t-t') = -i \left\langle \{\psi^\dagger(\boldsymbol{r}, t), \psi(\boldsymbol{r'}, t')\} \right\rangle \theta(t-t'), \tag{3.31}$$

where $\psi(\boldsymbol{r}, t)$ is the field operator of electrons and $\theta(t)$ is a step function. $\langle \cdots \rangle$ indicates the thermal average in the grand canonical ensemble. The single particle Green function represents the probability that one electron placed at a certain place and time $(\boldsymbol{r}, t)$ propagates to another $(\boldsymbol{r'}, t')$. Experimentally this quantity can be measured by ARPES, a "photon-in and electron-out" technique, which measures a single particle spectral function $A(\boldsymbol{k}, \omega) = -\mathrm{Im}(G(\boldsymbol{k}, \omega))/\pi$, where $G(\boldsymbol{k}, \omega)$ is the Fourier transform of $G(\boldsymbol{r}, \boldsymbol{r'}, t-t')$ [47]. The charge density response function $\chi_{\rho\rho}(\boldsymbol{r}, \boldsymbol{r'}, t-t')$ is defined as

$$\chi_{\rho\rho}(\boldsymbol{r}, \boldsymbol{r'}, t-t') = -i \langle [\rho(\boldsymbol{r}, t), \rho(\boldsymbol{r'}, t')] \rangle \theta(t-t'), \tag{3.32}$$

where $\rho(\boldsymbol{r}, t)$ is the charge density operator. $\chi_{\rho\rho}(\boldsymbol{r}, \boldsymbol{r'}, t-t')$ represents the probability that the charge density at $(\boldsymbol{r}, t)$ propagates to $(\boldsymbol{r'}, t')$. This quantity characterizes charge collective modes such as plasmons. The electron energy-loss spectroscopy (EELS), an "electron-in and electron-out" technique, measures the dielectric loss function $-\mathrm{Im}[1/\epsilon(\boldsymbol{Q}, \omega)] \propto \mathrm{Im}[\chi_{\rho\rho}(\boldsymbol{Q}, \omega)]$. Likewise, for spin operators $S(\boldsymbol{r}, t)$ instead of the charge counterparts $\rho(\boldsymbol{r}, t)$, the spin response function $\chi_{SS}(\boldsymbol{r}, \boldsymbol{r'}, t-t')$ is defined as

$$\chi_{SS}(\boldsymbol{r}, \boldsymbol{r'}, t-t') = -i \langle [S(\boldsymbol{r}, t), S(\boldsymbol{r'}, t')] \rangle \theta(t-t'). \tag{3.33}$$

Inelastic neutron scattering (INS), a "neutron-in and neutron-out" technique, measures $\mathrm{Im}[\chi_{SS}(\boldsymbol{Q}, \omega)]$ and characterizes spin collective modes such as magnons [191, 176]. Those are the three basic quantities that describe the elementary excitations. On the other hand, inelastic x-ray scattering (or light scattering in general), a "photon-in and photon-out" technique, measures $\mathrm{Im}[\chi_{nn}(\boldsymbol{Q}, \omega)]$, i.e., the Fourier transformation of the electron density response function,

$$\chi_{nn}(\boldsymbol{r}, \boldsymbol{r'}, t-t') = -i \langle [n(\boldsymbol{r}, t), n(\boldsymbol{r'}, t')] \rangle \theta(t-t'), \tag{3.34}$$

where $n(\boldsymbol{r}, t)$ is the electron density operator. Technically speaking, this quantity is different from the charge density response function $\chi_{\rho\rho}$ and, therefore, its sensitivity to the type of excitations is different. For instance, the dominant contributions in χ_{nn} are phonons since most of the electrons in a solid reside in core states, while valence excitations, such as plasmons, are dominant contributions in $\chi_{\rho\rho}$. In this sense inelastic x-ray scattering (χ_{nn}) is an essentially good probe of phonons. However, as stressed in chapter 2, x-ray scattering has played an important role to observe not only phonons but also spin excitations and charge-density waves in the research of cuprates. In next section, we will explain the scattering cross section of the inelastic x-ray scattering process more explicitly with a particular focus on the resonant condition.

3.5.2 Inelastic x-ray scattering

Here we will explain the basic principle of the non-resonant inelastic x-ray scattering measurements (IXS) and resonant inelastic x-ray scattering measurements (RIXS) [192].

The system in a light scattering experiment comprises a matter and a photon. To describe the cross section of the light scattering, let us consider the non-relativistic Hamiltonian $\mathcal{H}$ of the system:

$$\mathcal{H} = \sum_j \frac{1}{2m}\left(\boldsymbol{p}_j - e\boldsymbol{A}(\boldsymbol{r}_j,t)\right)^2 + \sum_{j\neq k}\frac{e^2}{|\boldsymbol{r}_j-\boldsymbol{r}_k|} + \sum_{\boldsymbol{q},\omega}\left(a_\omega^\dagger(\boldsymbol{q})a_\omega(\boldsymbol{q})+\frac{1}{2}\right), \tag{3.35}$$

where $m, e, \boldsymbol{p}_j$, and $\boldsymbol{r}_j$ are the mass, charge, momentum operator, and position operator of the electron j in a solid, respectively. $\boldsymbol{A}(\boldsymbol{r},t)$, and $a_\omega^\dagger(\boldsymbol{q})(a_\omega(\boldsymbol{q}))$ are the vector potential and the creation (annihilation) operator of the photon whose energy and momentum are ω and $\boldsymbol{q}$, respectively. The initial and final states of the scattering process are $|\Phi_\mathrm{i}\rangle = |\mathrm{i}\rangle\otimes|\boldsymbol{k}_0,\omega_0\rangle$ and $|\Phi_\mathrm{f}\rangle = |\mathrm{f}\rangle\otimes|\boldsymbol{k}_1,\omega_1\rangle$, respectively ($|\mathrm{i}\rangle$, $|\mathrm{f}\rangle$ and $|\boldsymbol{k}_0,\omega_0\rangle$, $|\boldsymbol{k}_1,\omega_1\rangle$ denote eigenstates of electrons and photons, respectively). The eigenenergies of $|\mathrm{i}\rangle$ and $|\mathrm{f}\rangle$ are E_i and E_f, respectively. The characteristic energies in solids ($\sim$ 0.1 - 1 eV) are much lower than x-rays ($\sim$ 1 keV) and, hence, the Born approximation is valid (Fig. 3.13). Thus the transition rate from $|\Phi_\mathrm{i}\rangle$ to $|\Phi_\mathrm{f}\rangle$ ($R_{\mathrm{i}\to\mathrm{f}}$) is given by Fermi's golden rule.

$$R_{\mathrm{i}\to\mathrm{f}} = 2\pi\left|\left\langle\Phi_\mathrm{f}\middle|\mathcal{H}^{(2)}\middle|\Phi_\mathrm{i}\right\rangle + \sum_\mathrm{m}\frac{\left\langle\Phi_\mathrm{f}\middle|\mathcal{H}^{(1)}\middle|\Phi_\mathrm{m}\right\rangle\left\langle\Phi_\mathrm{m}\middle|\mathcal{H}^{(1)}\middle|\Phi_\mathrm{i}\right\rangle}{E_\mathrm{i}+\omega_0-E_\mathrm{m}}\right|^2\delta\left((E_\mathrm{i}+\omega_0)-(E_\mathrm{f}+\omega_1)\right), \tag{3.36}$$

where $|\Phi_\mathrm{m}\rangle = |\mathrm{m}\rangle\otimes|0,0\rangle$ whose eigenenergy is $E_\mathrm{m}+0$ and

$$\mathcal{H}^{(1)} = -\frac{e}{2m}\sum_j(\boldsymbol{p}_j\cdot\boldsymbol{A}(\boldsymbol{r}_j,t)+\boldsymbol{A}(\boldsymbol{r}_j,t)\cdot\boldsymbol{p}_j), \tag{3.37}$$

$$\mathcal{H}^{(2)} = \frac{e^2}{2m}\sum_j\boldsymbol{A}(\boldsymbol{r}_j,t)^2. \tag{3.38}$$

Non-resonant condition

Since the energy of the x-ray ω_0, ω_1 is much higher than the excitation energy in solids $|E_\mathrm{i}-E_\mathrm{m}|$, the dominant contribution in $R_{\mathrm{i}\to\mathrm{f}}$ is from the first term of the right side in Eq. 3.36. In this case,

$$R_{\mathrm{i}\to\mathrm{f}}(\boldsymbol{Q},\omega) = 2\pi\left(\frac{2\pi}{\Omega_t}\frac{e^2}{m}\frac{\boldsymbol{\epsilon}_1\cdot\boldsymbol{\epsilon}_0}{\sqrt{\omega_1\omega_0}}\right)^2\left|\left\langle\mathrm{f}\middle|{n_{\boldsymbol{Q}}}^\dagger\middle|\mathrm{i}\right\rangle\right|^2\delta\left(E_\mathrm{i}+\omega-E_\mathrm{f}\right), \tag{3.39}$$

where Ω_t is the sample volume and $\boldsymbol{\epsilon}_1$ and $\boldsymbol{\epsilon}_0$ are the polarization of the scattered photons. ${n_{\boldsymbol{Q}}}^\dagger$ is the Fourier transformation of the electron density operator $n(\boldsymbol{r},t)$. In experiments, one observes the statistical average over the initial states of the sum over the final states of this transition rate,

$$R(\boldsymbol{Q},\omega) = \sum_\mathrm{i}e^{\beta(\Omega-E_\mathrm{i})}\sum_\mathrm{f}R_{\mathrm{i}\to\mathrm{f}}(\boldsymbol{Q},\omega) = 2\pi\left(\frac{2\pi}{\Omega_t}\frac{e^2}{m}\frac{\boldsymbol{\epsilon}_1\cdot\boldsymbol{\epsilon}_0}{\sqrt{\omega_1\omega_0}}\right)^2 S(\boldsymbol{Q},\omega), \tag{3.40}$$

where β is the inverse temperature, Ω is the grand potential of the grand canonical ensemble, and $S(\boldsymbol{Q},\omega)$ is called the dynamical structure factor (i.e., the electron density correlation function) and given by

$$S(\boldsymbol{Q},\omega) = \int_{-\infty}^{\infty}\frac{\mathrm{d}t}{2\pi}e^{i\omega t}\int\mathrm{d}\boldsymbol{r}\;e^{-i\boldsymbol{Q}\cdot\boldsymbol{r}}\int\mathrm{d}\boldsymbol{r'}\;e^{-i\boldsymbol{Q}\cdot\boldsymbol{r'}}\sum_\mathrm{i}e^{\beta(\Omega-E_\mathrm{i})}\left\langle\mathrm{i}\middle|n(\boldsymbol{r},t)n(\boldsymbol{r'},0)\middle|\mathrm{i}\right\rangle. \tag{3.41}$$

Experimentally one counts the number of photons δN whose energy is between ω_1 and $\omega_1 + \mathrm{d}\omega_1$ within the differential solid angle $\mathrm{d}\Omega$.

$$\delta N = \Omega_t R(\boldsymbol{Q}, \omega) \frac{\Omega_t \mathrm{d}^3 \boldsymbol{k}_1}{(2\pi)^3} = \Omega_t R(\boldsymbol{Q}, \omega) \frac{\Omega_t \omega_1^2 |\mathrm{d}\omega_1| \mathrm{d}\Omega}{(2\pi)^3}. \tag{3.42}$$

The differential cross section of this scattering is defined by δN, $\mathrm{d}\omega_1$, and $\mathrm{d}\Omega$ as follows and thus is described by means of $S(\boldsymbol{Q}, \omega)$:

$$\frac{\mathrm{d}^2\sigma}{\mathrm{d}\Omega \mathrm{d}\omega} = \frac{\delta N}{|\mathrm{d}\omega_1| \mathrm{d}\Omega} = \frac{e^4}{m^2} \frac{\omega_1}{\omega_0} (\boldsymbol{\epsilon}_1 \cdot \boldsymbol{\epsilon}_0)^2 S(\boldsymbol{Q}, \omega). \tag{3.43}$$

It is the cross section of the non-resonant inelastic x-ray scattering. It is the same formula for the light scattering with free electrons in vacuum, known as Thomson scattering. This is because the energy scale of incoming and outgoing photons is much higher than that of the elementary excitations in solids. Using the fluctuation-dissipation theorem generally proven in the linear response theory, the relationship between the electron density response function $\chi_{nn}(\boldsymbol{Q}, \omega)$ and the dynamical structure factor $S(\boldsymbol{Q}, \omega)$ is given by

$$\mathrm{Im}[\chi_{nn}(\boldsymbol{Q}, \omega)] = -\pi(1 - e^{-\beta\omega}) S(\boldsymbol{Q}, \omega). \tag{3.44}$$

This is what "the inelastic x-ray scattering measures the electron density response function." stated above means. Note that the Raman scattering is also classified in this scattering process yet the momentum range is limited only in the vicinity of zero [193]. Since the charge-density wave is the modulation of electron density, the CDW can be detected in non-resonant x-ray scattering. For instance, the reciprocal space dependence of the dynamical structure factor of the CDW in $YBa_2Cu_3O_{6.54}$ has been well studied by means of the non-resonant x-ray diffraction measurements [194]. Also, the uniaxial stress effects on the CDW in $YBa_2Cu_3O_{6.67}$ were also pointed out by the non-resonant x-ray scattering experiments [18].

Resonant condition

On the other hand, the second term of the right side in Eq. 3.36 is dominant if the energy of the incoming photon is tuned to be $\omega_0 = E_\mathrm{m} - E_\mathrm{i}$. The resonant condition enables one to obtain stronger intensity in spectra as one can imagine from the dominator which is almost zero. Moreover, the spectra becomes element-specific, and the intermediate state $|\Phi_\mathrm{m}\rangle$ plays a crucial role unlike the non-resonant process. To calculate the resonant contribution and compare with experimental RIXS spectra for their interpretations, one ends up approximating the formula in some ways, such as the dipole approximation: $e^{i\boldsymbol{k}\cdot\boldsymbol{r}} = 1 + i\boldsymbol{k}\cdot\boldsymbol{r} + \cdots \sim 1$. Therefore here we explain unique features in RIXS by intuitively explaining elementary excitations experimentally observed in cuprates and other materials instead of explaining approximation methods to calculate RIXS spectra from theoretical perspectives.

The first example is orbital excitations, specifically so called *dd*-excitations. As in the case of other Mott insulators, the orbital physics in cuprates is governed by the crystal field. The energy levels of the orbitally active ion are split and the orbital ground state is uniquely determined by local single-ion considerations. The orbital excitations from

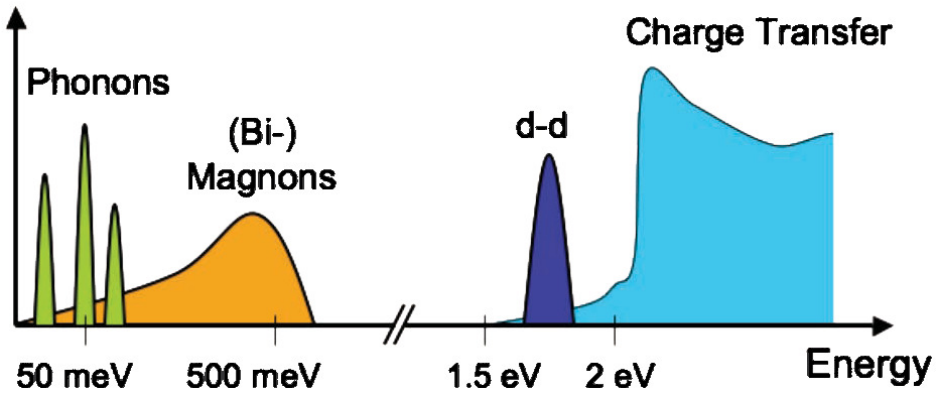

Figure 3.13: **Elementary excitations accessible by RIXS.** The approximate energy scales of each excitation in correlated electron materials such as transition-metal oxides are also indicated. Figure from Ref. [195].

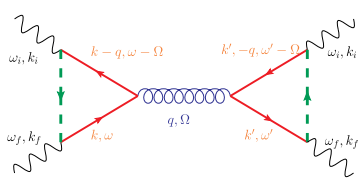

Figure 3.14: **Feynman diagram of the leading one phonon contribution to RIXS.** The dotted lines denote the Cu $2p$ core hole, solid lines denote the $3d$ conduction electrons, and the circular line denotes the phonon. Figure from Ref. [152].

the ground state are transitions between the different crystal-field levels. Crystal-field transitions between different d orbitals are called dd-excitations. In optical spectroscopy local dd-transitions in which the angular momentum does not change are forbidden by the dipole selection rule ($\Delta l = 0$) while they are clearly observed in RIXS spectra (Fig. 3.13) because this process is two dipole-allowed transitions (d-to-p and p-to-d) ($\Delta l = \pm 1$). Despite the low energy resolution at the early stage of the RIXS studies, RIXS has provided complementary information about the dd-excitations that cannot be measured by optical spectroscopy. We remark that a many-body approach is essential to be more general beyond the single ion treatment.

IXS and INS[4] are often used to measure phonons whose energy scale in solids is typically below 100 meV (Fig. 3.13). Because of the typical energy resolution, RIXS is currently not a routine technique to detect phonons. On the other hand, the theoretical studies have shown that the leading term of RIXS phonon cross sections is fundamentally different from the one of the non-resonant IXS (Fig. 3.14) [152, 196], and therefore the electron-phonon coupling can be extracted from the RIXS phonon spectra [197]. Experimentally it has been recently attempted to extract the electron-phonon coupling from the phonon contribution in cuprates by RIXS experiments [153].

Other features which can be accessible by L-edge RIXS are magnetic excitations, also known as magnons. When the long range magnetic orders set in, the global spin rotational symmetry in solids is broken. As a consequence, characteristic collective magnetic excitations emerge. The magnons have been dominantly measured by INS where

[4]We stressed only spin excitations in neutron scattering experiments early on yet phonons are also observable because neutrons are also scattered by nuclei.

neutrons with spin 1/2 can change the spin of valence electrons. On the other hand the photon spin couples only very weakly with the valence electron spins. Thus the spins are changed by other interactions such as the spin-orbit interactions. For valence electrons, the spin-orbit coupling is usually weak but electrons in core levels possess the very large spin-orbit coupling up to tens of electron volts. In RIXS processes, the core-hole in the intermediate state can play this role: the core-hole can induce the large spin-orbit coupling between the orbital moment generated by a photon and the spin moment of the valence electrons. This explains why the magnon dispersions are not observed in the O K-edge RIXS where the angular momentum of the core hole is 0 ($L = 0$). In cuprates, the magnon dispersions were first detected in RIXS by Braicovich *et al.* in 2010 [62]. Note that the accessible parameter space in RIXS is limited compared with other scattering techniques because of the strong constraint of the incoming energy which has to be one specific absorption energy. For instance, the wave vectors accessible by the Cu-L_3 edge energy are not as long as the (π, π) in the reciprocal space where the magnetic Bragg peak of the antiferromagnetic order is located. As mentioned in the previous sections, INS has been dominantly used to study magnons. However this method typically requires a massive number of samples to compensate small cross sections of magnetic scattering. In this regard, RIXS has a huge advantage where only a single piece of sample is required to obtain spectra and this has been indeed demonstrated by the recent Ru-L edge RIXS experiments where the clear magnon was observed from the sample whose size was only around 50 μm [198]. This is desirable for our strain experiments where one needs to make a sample into the needle shape for the application of homogeneous strain.

We end the discussion of the RIXS features by explaining the CDW. The CDW, i.e., electron-density modulation, can be detected in the non-resonant x-ray diffraction measurements as demonstrated in previous studies [22, 155, 16]. However the diffraction intensity of the CDW originating from valence electrons is in general not strong in the non-resonant condition and is enhanced significantly in the resonant condition. This has been experimentally demonstrated in the previous resonant x-ray scattering experiments for a variety of cuprate families: $YBa_2Cu_3O_{6+x}$ [146], $La_{2-x}Ba_xCuO_4$ [131], $Nd_{2-x}Ce_xCuO_4$ [199], and $La_{1.8-x}Eu_{0.2}Sr_xCuO_4$ [200, 201]. Using the resonant feature of RIXS spectra, one can also investigate the chemical nature of the scattering spectra in comparison with the x-ray absorption spectra [160]. Also for the strain experiments, one has to consider the sample mounting method and the complicated design of the strain rig for the transmission geometry in the hard x-ray scattering measurements, while it is relatively easier in the soft x-ray measurements where the back scattering geometry is used to detect the CDWs in cuprates.

3.5.3 Cu-L_3 edge REXS and RIXS

We have seen that the cross section of RIXS is given as a function of $(\boldsymbol{Q}, \omega)$,

$$\boldsymbol{Q} = \boldsymbol{q}_{\rm in} - \boldsymbol{q}_{\rm out} \quad \text{and} \quad \omega = \omega_{\rm in} - \omega_{\rm out}, \tag{3.45}$$

where $\boldsymbol{q}_{\rm in}$ ($\boldsymbol{q}_{\rm out}$) and $\omega_{\rm in}$ ($\omega_{\rm out}$) are the wave vector and energy of the incoming (outgoing) photons, respectively. From the typical scattering geometry shown in Fig. 3.15, the norm of the wave vector of the elementary excitations is

$$|\boldsymbol{Q}| = 2|\boldsymbol{q}_{\rm in}| \sin(2\theta/2). \tag{3.46}$$

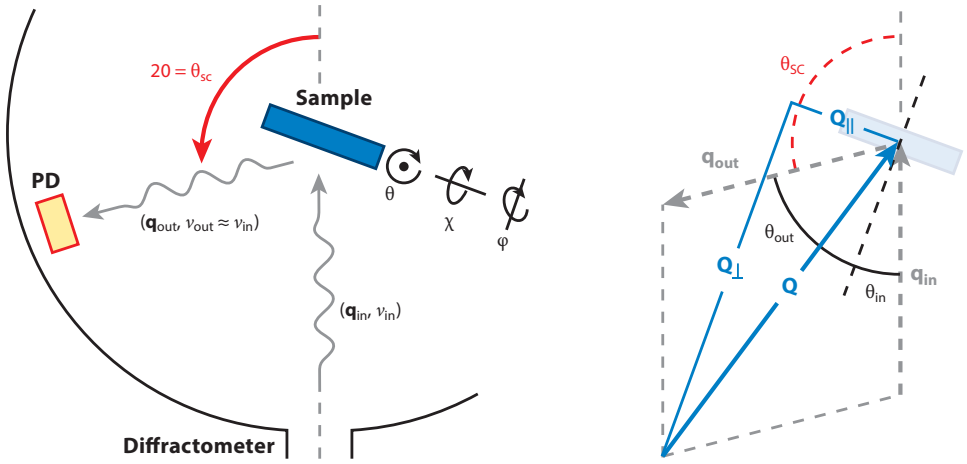

Figure 3.15: **Schematics of a typical diffractometer and kinematics for the scattering process.** ν is used to express the photon energy here instead of ω written in the main text. Abbreviations, PD: photon detector, SC: scattering. Figures from Ref. [192].

Note here the "2θ" is the scattering angle and not necessary twice of the sample angle θ. Also $|\boldsymbol{q}_{\text{in}}| \simeq |\boldsymbol{q}_{\text{out}}|$ is assumed because the difference of photon energy ω is typically at most a few electron volt while the incident energy ω_{in} for the Cu L_3 edge is $\sim$ 932 eV, thus the difference in the wave vector norm is negligibly small. $\boldsymbol{Q}$ can be further decomposed into

$$\boldsymbol{Q} = \boldsymbol{Q}_{||} + \boldsymbol{Q}_{\perp}. \tag{3.47}$$

For practical reasons, 2θ (and as a result $|\boldsymbol{Q}|$) is often fixed in RIXS experiments. However it is not a big issue when one measures the two dimensional materials such as layered cuprates where our region of interest is only $\boldsymbol{Q}_{||}$ and one can assume the physical properties do not strongly depend on $\boldsymbol{Q}_{\perp}$.

In summary, simultaneous measurements of the scattering angle, sample angles, and scattered photon intensities correspond to the RIXS cross section.

The data obtained in synchrotron facilities and presented in this thesis were measured at two different facilities: the UE46-PGM1 beamline at the BESSY II synchrotron of the Helmholtz-Zentrum-Berlin for REXS experiments and the beamline ID32 of the European Synchrotron Radiation Facility, Grenoble, France (ESRF) for RIXS experiments.

REXS at UE46-PGM1 in BESSY II

The UE46-PGM1 beamline in BESSY II is a soft x-ray spectroscopy beamline, which has an XUV diffractometer and high-filed diffractometer [202, 203]. The energy range of the soft x-ray provided by the beamline is between 120 eV and 2000 eV, which includes the $L_{2,3}$-edges of the $3d$ transition metals. The polarization of the incident photons is tunable: linear or circular. In this setup, the photodiode counts the intensity of the scattered photons over a wide energy range including both elastic and inelastic scattering processes. This is why this experiment is called resonant energy-integrated x-ray scattering (REXS) in contrast with RIXS. In REXS spectra the dominant contribution over the entire energy

range arises from the elastic component, therefore the inelastic signals which reside in the REXS intensity are usually interpreted as the background of the elastic signal. On the other hand, the photodiode in the XUV diffractometer (2θ) can be rotated during the measurements as well as the sample (θ). This capability of rotating the photodiode allows one to vary the norm of the scattering vector $\boldsymbol{Q}$ during the measurements, and therefore vary only one component of $\boldsymbol{Q}$ (K, for instance) while fixing the other two components of $\boldsymbol{Q}$ (H and L, in this example). In principle, the same type of measurements can be carried out in the RIXS setup but it is not practical because the huge spectrometer has to be moved for this purpose and realistically this is too time consuming.

RIXS at ID32 in ESRF

The ID32 beamline in the ESRF is a soft x-ray spectroscopy beamline, one of whose end-stations possess the ERIXS spectrometer dedicated to RIXS experiments [204]. The energy range of the incoming photons provided by the beamline is 0.3 - 1.6 keV, which includes the $L_{2,3}$-edges of the $3d$ transition metals and $M_{4,5}$-edges of the $4f$ rare-earth elements. The medium energy resolution in usual operations is around 60 meV at the Cu-L_3 edge which we used for our experiments. According to the estimation by the beamline after the upgrade in 2020, the highest resolution at the Cu-L_3 edge is 25 meV. Before the x-rays are scattered by a sample, a plane grating monochromator is used with variable line spacing (VLS) to obtain a beam whose band width is very narrow. RIXS experiments are performed under the ultra-high vacuum because the x-rays are strongly attenuated in the ambient condition. An in-vacuum four-circle manipulator is available in the sample chamber. This allows one to investigate most of the first Brillouin zone of the cuprates and in particular to explore the azimuthal angle dependence of the RIXS spectra. The ERIXS spectrometer has a 11 m-long arm that moves in the range $2\theta = 50$ - 150° (Fig. 3.16). After the photons are scattered by the sample, they are collimated by an elliptical horizontal mirror and dispersed in energy by a spherical VLS grating analyzer. The photons go thorough the 11 m distance and are detected by the charge-coupled device (CCD) detector. Photons with different energies can be distinguished by isoenergetic lines in the CCD image. This is how one obtains the inelastic signals.

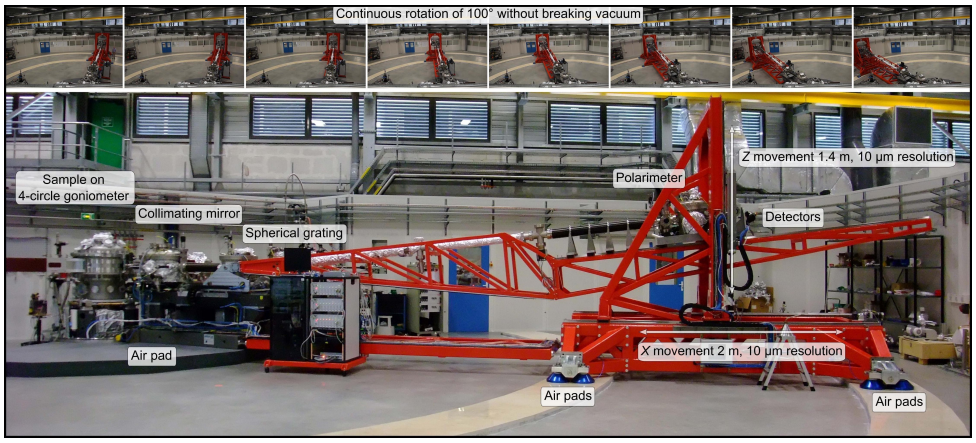

Figure 3.16: **High-resolution ERIXS spectrometer at the beamline ID32.** Figure from the website of ESRF ID32.

Chapter 4

Normal-state charge transport of $YBa_2Cu_3O_{6.67}$ under uniaxial stress

4.1 Introduction

The anomalous normal-state transport properties of the cuprate superconductors challenge the fundamental tenets of solid-state theory, and have thus become emblematic of analogous phenomena in a much larger class of quantum materials [2]. Recent NMR and x-ray scattering experiments have identified charge-density wave (CDW) as a ubiquitous feature of the cuprates families, and as the leading competitor of high-temperature superconductivity at moderate doping levels [159, 14, 15]. However, the gradual "freezing" of the charge correlations upon cooling and the absence of sharp anomalies in transport properties have made it difficult to establish a correspondence between both sets of observables.

To see how anomalous the correspondence in the cuprates is, it is useful to review macroscopic transport behaviors of classical CDW materials. The concept of CDW was theoretically proposed by Peierls for an atomic one-dimensional (1D) chain. Because of the specialty of the Lindhard function for the 1D case, a 1D free-electron system has a generic instability that results in a softening of its phonon dispersion, known as Kohn anomaly, and in the opening of a gap around the Fermi level in the free-electron band due to the periodic potential of the CDW at low temperature that offers the chance of Fermi surface nesting (FSN). The gap opening drives a metal-insulator transition that can be and was observed in resistivity measurements on quasi-1D materials such as TTF-TCNQ as shown in Fig. 4.1 (a) [205, 206]. For higher dimensions, the origin of the CDW and the resulting transport properties usually depend on details of the material. For example, in one of the most prominent 2D materials $NbSe_2$, it is widely considered that the electron-phonon coupling (EPC) plays a key role for the CDW formation [207] and a small hump in resistivity is observed near the onset temperature of the CDW due to the partial gap opening in the 2D Fermi surface (Fig. 4.1 (c)) [208]. As a consequence, the resistivity is usually a good (and often first experimental) indicator of the CDW formation in such materials.

However, it is not clear whether EPC and FSN drive the formation of CDW in quasi-2D cuprates [209] and interestingly, there are no obvious signatures in the resistivity at the onset temperature of the CDW as shown in Fig. 4.2 (a,b) [210], whereas it is well known that the temperature dependence of the resistivity changes at the pseudogap temperature T^* (Fig. 4.2 (c)) [122]. Only a very recent work has suggested a more intimate connection between the onset of the CDW and the departure from T-linear resistivity in underdoped

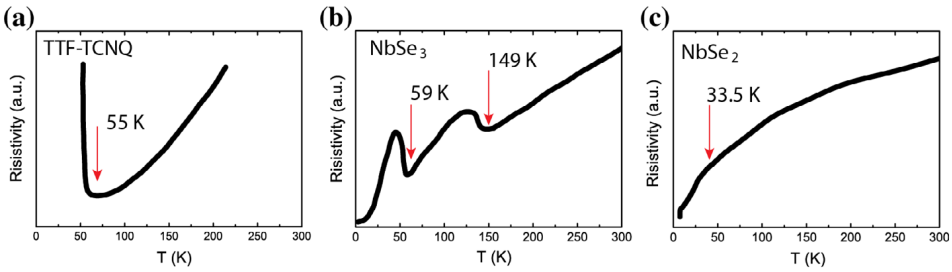

Figure 4.1: **Temperature dependence of the resistivity in classical CDW materials.** (a) One dimensional chain TTF-TCNQ. The clear metal-insulator transition is observed at the onset temperature of the CDW. (b) One dimensional chain $NbSe_3$ (c) Two dimensional layered $NbSe_2$. The hump-like features were observed at the onset temperatures. Figures from Ref. [11].

cuprates showing that the T-linear resistivity of $YBa_2Cu_3O_{6+x}$ is extended and restored when the CDW is suppressed in strained thin films [211]. Recently, experimental efforts under external fields have opened up fresh perspectives on the correspondence between the macroscopic transport and the charge ordering phenomena in the cuprates. Specifically, the application of external magnetic fields of order 100 T has revealed new information about quantum transport phenomena at the lowest temperature where one cannot acquire the transport signals due to zero resistivity of superconductivity [20, 161, 212, 162, 213, 214], but the application of complementary scattering probes under these extreme conditions remains a major technical challenge to date [155, 21, 156, 196].

One of the most remarkable transport features was observed in the Hall effect, which is a powerful transport probe to extract the information of Fermi surfaces in metals. In a certain hole doping regime in the underdoped $YBa_2Cu_3O_{6+x}$, the sign of the Hall coefficient R_H changes from positive to negative, suggesting that the conductive carriers change from hole-like quasiparticles to electron-like ones, upon cooling (Fig. 4.3) [161, 215, 52]. Since the electronic structure of cuprates is essentially a single band, the sign reversal is attributed to the reconstruction of the Fermi surface: from hole-like pocket centered at (π, π) in the Brillouin zone proposed by the first-principle calculations to the electron pocket of the 2D Fermi surface. The small pocket is consistent with the Fermi surface area estimated by quantum oscillation experiments under extremely high magnetic field [20, 162, 216]. In the same doping region where the Fermi surface reconstruction is suggested by the macroscopic transport experiments, the charge orders were observed as the 2D-CDW, which breaks the translational symmetry of the crystal lattice [217, 218, 219, 14, 22, 146, 220, 221, 222]. In fact, those two anomalous transport properties sensitive to the Fermi surface had already suggested the possible presence of the density waves as a trigger of the Fermi surface reconstruction, before the CDW was directly observed as Bragg peaks in the x-ray scattering measurements [14]. Therefore it has been widely accepted that the Fermi surface reconstruction is triggered by this symmetry breaking [214]. However the Fermi surface in the underdoped $YBa_2Cu_3O_{6+x}$ has not been fully known due to a lack of direct observations in photoemission experiments. Therefore the direct information about the reconstructed Fermi surface, e.g., its shape and location in the reciprocal space and more

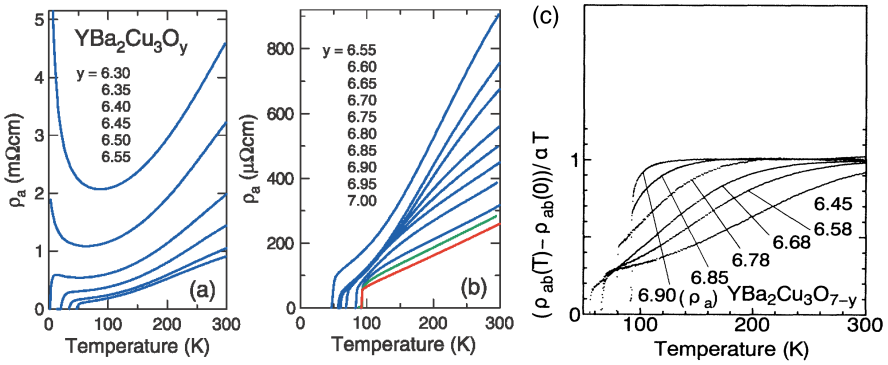

Figure 4.2: **Temperature dependence of the in-plane resistivity in $YBa_2Cu_3O_y$.** (a) $y = 6.30 - 6.55$ (b) $y = 6.55 - 7.00$. The CDW emerges between $y = 6.45 - 6.93$ according to the x-ray scattering experiments [151], yet no anomalies are noticeable around the onset temperatures of the CDW, $T_{\rm CDW} = 100 - 150$ K. (c) The temperature dependence of $(\rho_{ab}(T) - \rho_{ab}(0)/\alpha T)$ to emphasize the anomaly at pseudogap temperature T^*. α is the slope of the T-linear region of the in-plane resistivity. The temperature where the resistivity deviates from the T-linear region coincides with the pseudogap temperature T^* determined by other experiments. Figures from Ref. [210, 122].

crucially the relation with the CDW, are not clear yet.

The propagation vectors of the bidirectional 2D-CDWs are $\boldsymbol{Q}_{\rm 2D-CDW}\sim(0, 0.3, 0.5)$ and $(0.3, 0, 0.5)$. Therefore it is straightforward to explain the Fermi surface reconstruction by this bi-axial nature of the 2D-CDW as shown in Fig. 4.4 (a) [223]. In this case the electron pocket is located around the nodal region of the d-wave superconducting order parameter. However it was pointed out that the correlation length of the short range 2D-CDW was not large enough to explain the transport properties, in particular the quantum oscillations, because the cyclotron radius was estimated to be greater than the correlation length of the short range 2D-CDW [223]. Because of the high superconducting transition temperature $T_{\rm c}$, quantum oscillation measurements at very low temperature have been performed under the high magnetic field, which is known to induce a 3D-CDW whose correction length is much greater than the 2D-CDW, albeit only along the b-axis of $YBa_2Cu_3O_{6+x}$ [158, 155, 21]. Thus the Fermi surface reconstruction could be due to the 3D-CDW: a unidirectional charge order could create an electron pocket in the presence of nematic order, that is, an electronic state characterized by rotational symmetry breaking (Fig. 4.4 (b)) [224]. Nevertheless, the sign of the Hall coefficient changes even in the low magnetic field that is not enough to induce the 3D-CDW (≤ 5 T) (Fig. 4.5). Therefore the static 3D-CDW is less likely to be responsible for at least the sign reversal of the Hall coefficient. Moreover, the sign reversal of the Hall coefficient could be explained by completely different theories unrelated to density waves such as vertex corrections proposed for electron-doped cuprates [225]. Overall, it is not clear whether the static charge orders are responsible for the unusual temperature dependence of the Hall coefficient and the proposed Fermi surface reconstruction.

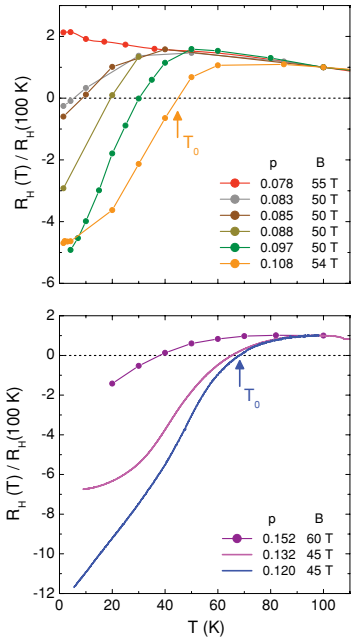

Figure 4.3: **Temperature evolution of the Hall coefficient R_{H} of $YBa_2Cu_3O_y$.** The value of R_{H} is normalized to its value at 100 K. T_0 is the sign change temperature of R_{H}. p and B indicate the doping levels and the magnetic fields used in the measurements, respectively. Figures from Ref. [215].

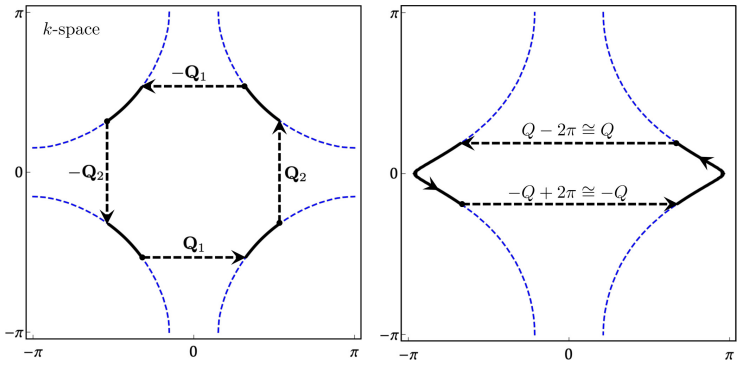

Figure 4.4: **Proposed Fermi surface reconstruction by density waves.** Reconstruction by bidirectional orders (left) and by unidirectional order with nematic distortion of the underlying Fermi surface (right). The underlying Fermi surface is obtained from the tight binding Hamiltonian. The correspondence with the real material is that Q_1 and Q_2 are the propagation vectors of the 2D-CDW and Q is the one of the 3D-CDW of $YBa_2Cu_3O_y$. Figures from Ref. [223].

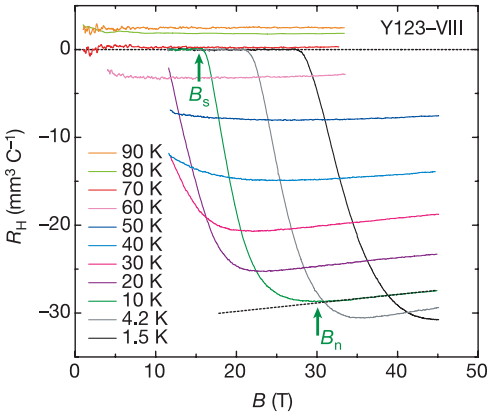

Figure 4.5: **Magnetic field dependence of R_H in $YBa_2Cu_3O_{6.67}$.** The sign change of R_H is observed below 5 T although the signal at lower field is not observable due to the zero resistivity. The sign reversal temperature $T_0 \sim 70$ K dose not depend on the magnetic field. Figure from Ref. [161].

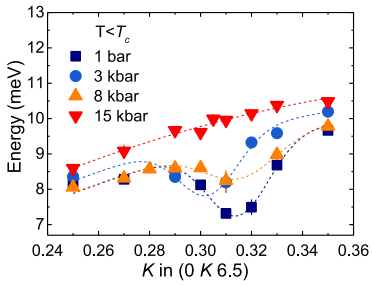

Figure 4.6: **Phonon dispersions in $YBa_2Cu_3O_{6.6}$ under hydrostatic pressure.** The phonon anomaly at the propagation vector of the CDW $\sim$ (0,0.31,6.5) is vanished by the hydrostatic pressure. Figure from Ref. [17].

Hydrostatic pressure is another continuously tunable parameter, by which T_c is enhanced [226]. The anomaly in the phonon dispersion, one of the signatures of 2D-CDW, is completely suppressed by hydrostatic pressure as small as 1 GPa (Fig. 4.6) [17, 227]. Moreover hydrostatic pressure greatly reduces the magnitude of both resistivity and Hall coefficient [228], thereby suggesting the suppression of the CDW by hydrostatic pressure. Since the superconductivity and CDW compete in the underdoped cuprates, the suppression of the CDW by pressure is qualitatively consistent with the enhanced T_c, yet T_c continuously increases even above the critical pressure at which the CDW vanishes completely. Therefore, the hydrostatic pressure effects on different physical quantities are quantitatively contradictory. Moreover the magnitude of the effect is also highly debated in comparison with other probes: pressure of 1.9 GPa has only a modest effect on the CDW measured in NMR [229] and the Hall coefficient at a specific doping level almost does not change up to 2.6 GPa [23]. One key aspect to be considered is the doping change induced by pressure as well as the intrinsic pressure effect on the charge order. Moreover, the measurements were carried out on different samples, and the strong dependence of the doping level on hydrostatic pressure has so far precluded firm conclusions.

Recent experimental advances have enabled the application of highly homogeneous uniaxial stress to complex quantum materials, thereby opening up additional perspectives for *in situ* experiments with a continuously tunable parameter, which were particularly demonstrated

in Sr_2RuO_4 [173, 170]. The application of uniaxial stress in x-ray scattering experiments has already uncovered substantial modifications of the charge-ordered state of the cuprates [18, 142]. Specifically, the 2D-CDWs in $YBa_2Cu_3O_{6.67}$ were selectively enhanced by the uniaxial stress in contrast to the isotropic hydrostatic pressure. Moreover the 3D-CDW was induced in the absence of the magnetic field at high temperature compared with the one uncovered by the magnetic field. However, complementary transport measurements under high stress are difficult because even small cracks can disrupt the current flow, so that little is known about the stress response of the transport coefficients [230]. Despite technical challenges in experiments, it is important to elucidate macroscopic properties, in particular transport properties, corresponding to those underlying ground states confirmed by the microscopic measurements to provide foundations for developments of many-body theories.

To this end, in this chapter, we present measurements of the stress dependence of the normal-state resistivity and Hall coefficient of twin-free single crystals of the underdoped high-T_c superconductor $YBa_2Cu_3O_{6+x}$, which is particularly suitable for such experiments because of its low degree of lattice disorder, which is also evident from a number of quantum oscillation experiments in this compound [20, 162]. We chose the doping level of ~ 0.12 holes per copper ion ($x = 0.67$) where charge ordering is most pronounced [151]. A substantial stress-induced enhancement of the charge order was recently observed on crystals identical to those investigated here, using a nearly identical experimental setup in Ref. [18, 142] and the next chapter. We find remarkable parallels in the stress responses of the transport coefficients and the diffraction signal from static charge-ordering, especially with regard to their temperature evolution and in-plane anisotropy. This correspondence allows us to conclude that the condensation of collective charge fluctuations reduces the resistivity, similar to classical CDW materials with quasi-two-dimensional electron systems, where this effect has been attributed to a loss of inelastic scattering channels in the CDW state [10, 11]. However, we also conclude that the impact of static charge order is too weak to explain the sign reversal of the Hall coefficient as a function of temperature [212]. We argue that in $YBa_2Cu_3O_{6.67}$, liquid-like collective fluctuations of the electron system take on the role of static order in the classical CDW compounds, and we point out the need to develop a theoretical framework to describe the underlying mechanisms [231].

4.2 Experimental methods

The $YBa_2Cu_3O_{6.67}$ samples for the strain experiments have been prepared as explained in section 3.3 of the previous chapter. The oxygen content was controlled by annealing samples at 555 °C in the mixture of 5 % O_2 and 95 % Ar for one week to obtain this specific doping level homogeneously [178]. Subsequently the samples were detwinned with a standard mechanical method [180]. T_c was determined with standard SQUID measurements and the hole doping p was estimated from the c-axis lattice constant

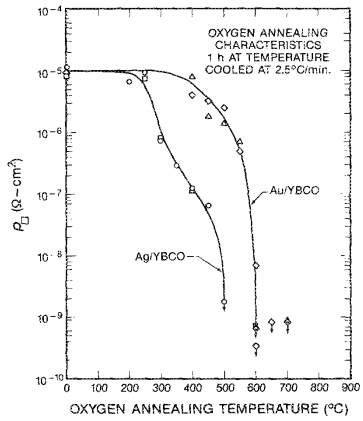

Figure 4.7: **Annealing temperature dependence of the contact resistance.** Silver and gold are used as contacts of $YBa_2Cu_3O_y$ samples. Figure from [232].

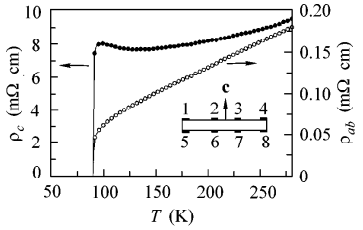

Figure 4.8: **Temperature evolution of the resistivity in optimally doped $YBa_2Cu_3O_{6+x}$.** Both in-plane resistivity ρ_{ab} and out-of-plane resistivity ρ_c are shown. Figure from Ref. [233].

measured with x-ray diffraction measurements at room temperature [182]. The typical sample dimensions are $\sim$ 2.5 mm $\times$ 0.2 mm $\times$ 0.1 mm as illustrated in section 3.3. After shaping the sample, electrical contacts were prepared by sputtering Au on the surface [232]. This is because the surface of $YBa_2Cu_3O_{6+x}$ reacts with CO_2 in air and, therefore, the insulating material $BaCO_3$ forms on the surfaces, which prevents ones from obtaining good contacts for transport experiments [185]. To obtain the good contacts with the bulk $YBa_2Cu_3O_{6+x}$, the sample has to be annealed after the deposition so that the gold can diffuse into the bulk material. Desirable temperature to obtain low resistive contacts has been systematically studied as shown in Fig. 4.7 [232]. In many cases, this process to obtain good contacts is simultaneously done when the samples are annealed to tune their oxygen contents. However this routine method is not feasible in our case because we have to cut and polish samples after tuning the oxygen contents and detwinning samples[1]. Therefore, instead of this routine method, we annealed the needle-shaped samples with gold at 500 °C for one hour in 100 % Ar to make the contact resistance lower and to keep the homogeneity of the oxygen content and detwinned structure as much as possible. In this way, we obtained the contact resistance of the order of 1-10 Ω, which enabled us to perform decent transport experiments. In order to accurately measure the in-plane resistivity, one must be careful not to deposit Au on the *ab* plane of the rectangular shape sample for the driving current. Inhomogeneous currents along the *c*-axis would turn the resistivity signal into a mixture of the in-plane and out-of-plane components which are very different in $YBa_2Cu_3O_{6+x}$ due to its high anisotropy. As one expects from the anisotropic

[1]One may come up with a possibility to control the oxygen contents of needle-shaped samples with gold in an opposite fashion to our steps. This would mean that the samples have to be dropped into the liquid nitrogen when they are quenched, and it is not ideal for quite fragile needle-shaped samples. Also, even if this process were possible, the sample would have to be detwinned afterwards with the pressure of 50 MPa along the long direction of the needle. There is almost no hope to apply such a pressure on the sample in a controlled way with our detwinning setup, where two ends of a sample are just pressed mechanically.

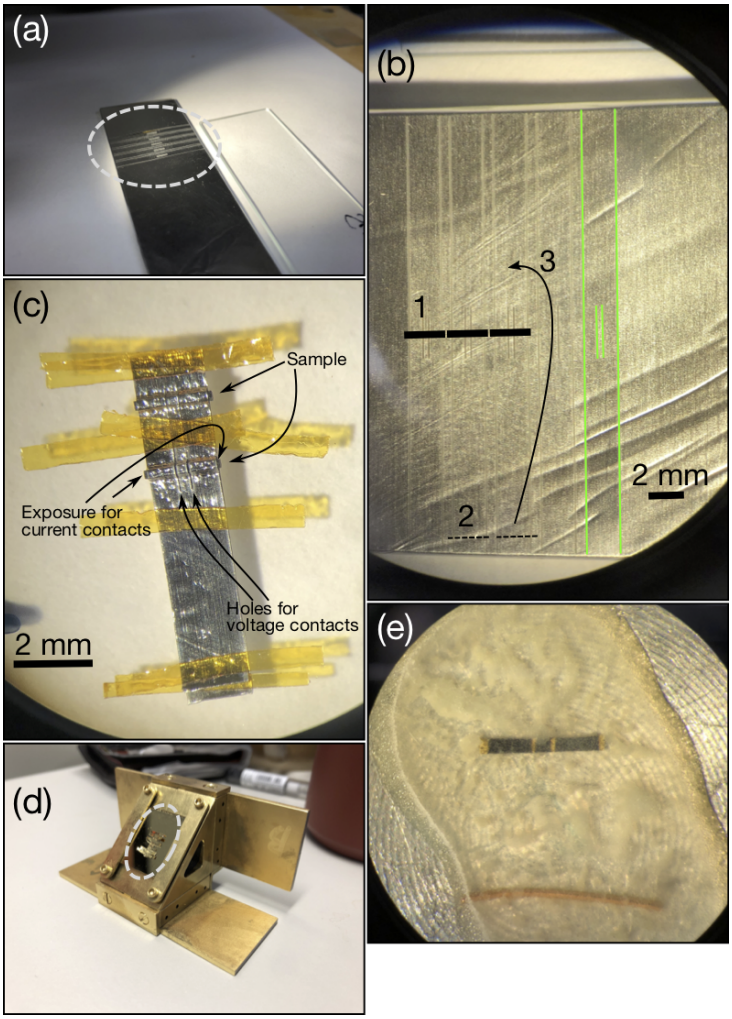

Figure 4.9: **Masking methods.** (a) Aluminum foil mask on a glass plate carefully prepared by the laser cutter, which enables one to make holes whose width is only 30 μm. The dotted circle indicates the zoomed region in panel (b). (b) Expanded picture of the aluminum foil masks. Green lines indicate traces made by the laser cutter for better visibility. Here, five sets of masks including the one indicated by green lines are present. On the left side, a method to mount a sample is shown: 1. place a needle shaped sample, 2. cut the end of the mask, and 3. fold the mask to wrap the sample. (c) Samples wrapped by the mask on the small glass plate. The holes at the center of the sample are for voltage contacts and exposed parts at the ends of the sample are for current contacts. (d) Sample stage for spattering Au. The dashed circle indicates the mask on the small glass plate shown in panel (c). The sample is tilted by 45 degrees and the stage keeps rotating while the deposition, thereby, Au is spattered homogeneously on the surfaces except for the bottom and masked region of the sample. (e) *ab*-surface of the sample after the deposition. The sample is buried in glue for polishing. By polishing the top *ab*-surface, one obtains the sample with gold only on *ac*- and *bc*-surfaces.

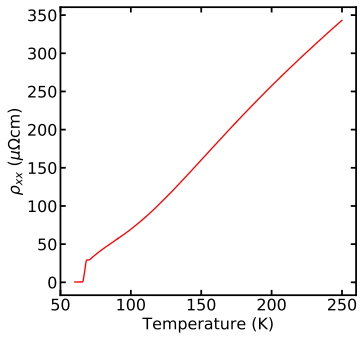

Figure 4.10: **Typical temperature dependence of the in-plane resistivity of $YBa_2Cu_3O_{6.67}$.** As an example, the data on the sample 1 is shown here.

crystal structure, the anisotropy of the resistivity ρ_c/ρ_{ab} is 100-1000 and their temperature dependence is very distinct (Fig. 4.8) [233]. Therefore it is easily noticeable if the c-axis component contaminates the resistivity signal. To meet those geometrical demands of the electrical contacts, a masking method has been used [185]. The detailed procedure to make the gold contacts with the masking method is summarized in Fig. 4.9. Keeping those facts about the electrical contacts in mind, the gold was carefully deposited only on the ac and bc planes. An example of the resistivity curve prepared in this method is shown in Fig. 4.10 and it is in excellent agreement with previous studies [210]. The longitudinal resistivity ρ_{xx} (ρ_{yy}) was measured only along the uniaxial stress σ_{xx} (σ_{yy}) direction. In particular uniaxial pressure was applied along the a-axis for samples 1 and 3 and along the b-axis for sample 2, to measure ρ_{xx} and ρ_{yy}, respectively. The Hall effect was measured with the magnetic field applied along the c-axis for all the samples. The measurements were performed with both positive and negative fields, thereby the contribution of the longitudinal magnetoresistivity was eliminated. Since the transverse contact resistance for the sample 1 was not great enough to perform the Hall effect experiment, the results of only samples 2 and 3 are presented. The characterizations of the three samples are summarized in Table 4.1. The measurements were carried out by a standard ac lock-in method with the driving current with frequency ∼80 Hz. The stress rig has been used and the contact geometry of the sample is seen in Fig. 4.11. Note that in this chapter, we discuss the pressure effect by means of stress rather than strain because the stress was measured more directly in this setup.

Sample name	c (Å)	p	T_c (K)	Dimensions ($a\times b\times c$) (mm^3)
Sample 1 (R555c2N12)	11.721	0.1267	64.8	$2.6 \times 0.23 \times 0.15$
Sample 2 (R555e1N1)	11.723	0.1241	64.7	$0.26 \times 2.1 \times 0.12$
Sample 3 (R555c1N4)	11.724	0.1229	64.2	$3.2 \times 0.23 \times 0.10$

Table 4.1: List of the $YBa_2Cu_3O_{6.67}$ crystals measured in the resistivity experiments. All samples were used for the resistivity measurements and the samples 2 and 3 were used for the Hall effect measurements. The c-axis lattice parameter c is determined with XRD measurements at room temperature and the doping p is estimated using Eq. (3.13). T_c was determined by magnetometry as a midpoint of the diamagnetic response.

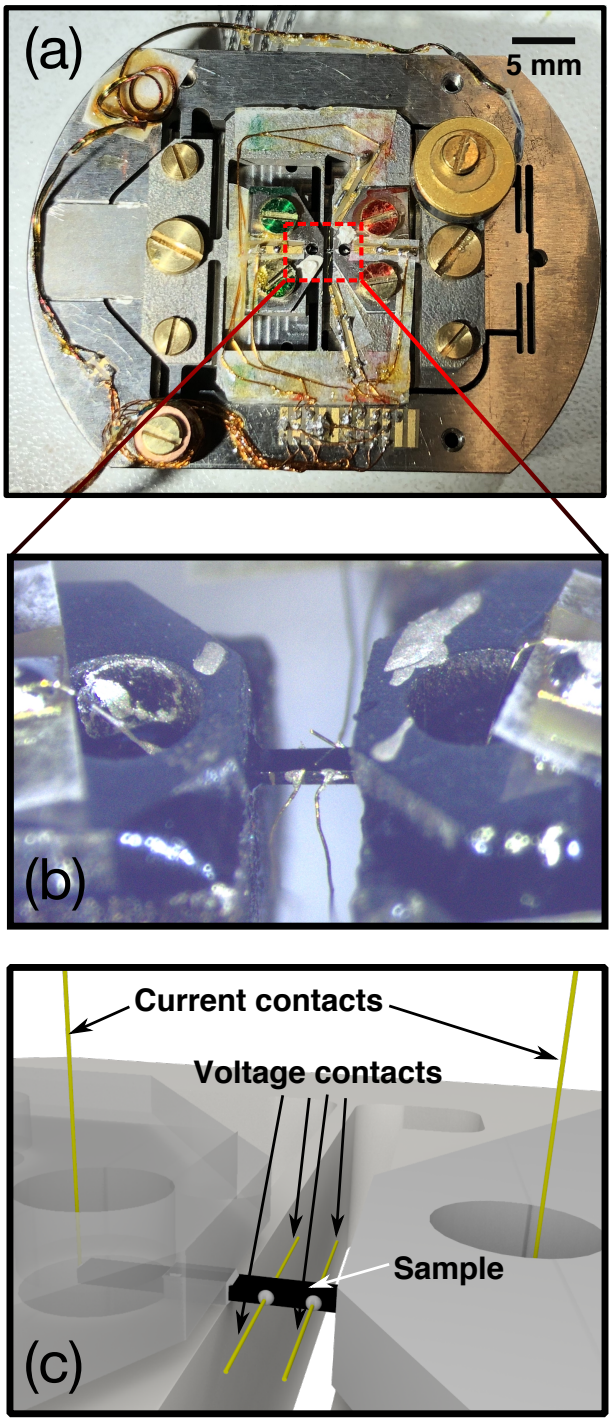

Figure 4.11: **Mounted sample on the stress rig.** (a) Top view of the stress rig. (b) Zoomed side view of the sample. Gold wires were attached on gold pads deposited on the sample with silver epoxy. (c) Schematic figure of panel (b). The longitudinal and transverse voltage contacts were used for the resistivity and Hall effect measurements, respectively. The current flows along the long direction in both measurements.

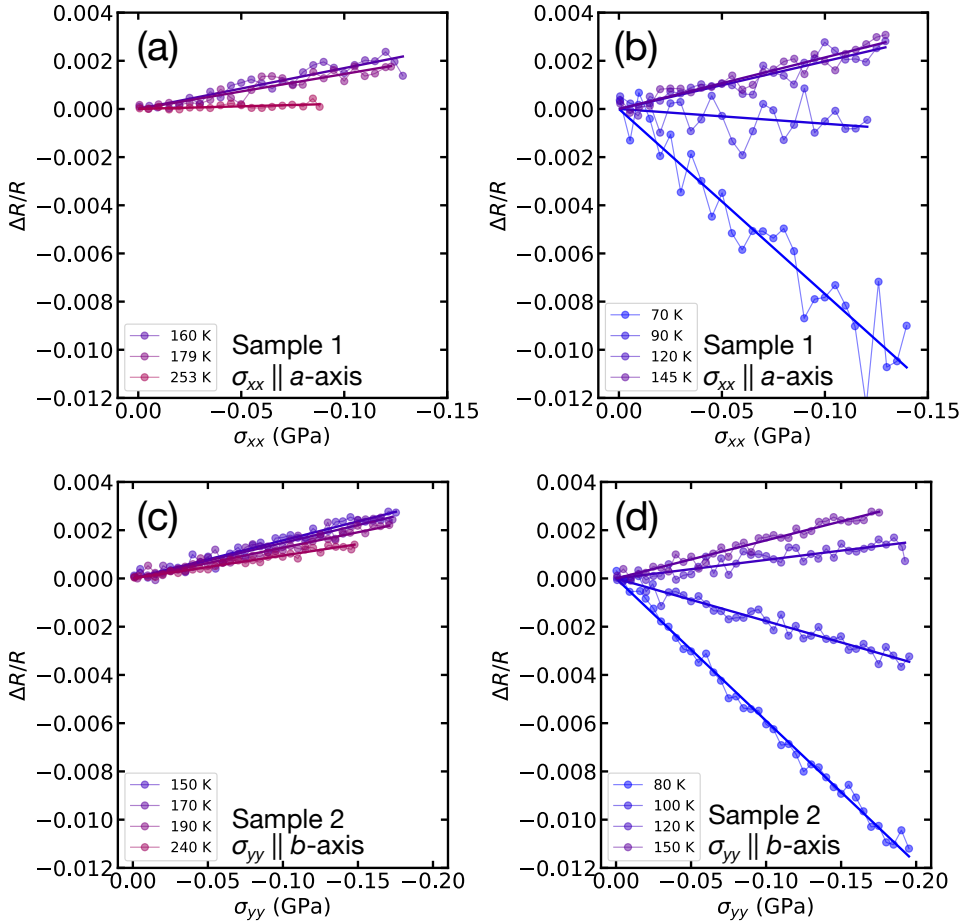

Figure 4.12: **Stress sweep experiments of the normalized electrical resistance at fixed temperatures.** (a) Change of the normalized resistance $\Delta R/R$ *vs.* uniaxial pressure σ_{xx} for different temperatures above 150 K. Resistance R was measured and the uniaxial pressure σ_{xx} was applied along the a-axis. Solid lines are liner fits. (b) Same as (a) with $\leq$ 150 K. (c,d) Same as (d,e) with R and σ_{yy} parallel to the b-axis.

4.3 Results and discussion

4.3.1 Resistivity

Figure 4.12 shows the stress dependence of the normalized electrical resistance for different temperatures. In the stress sweep measurements, samples were mounted on the carrier which can be split by tensile stress as described in section 3.2.4 so that we were able to determine zero force accurately. When the stress was applied and released, no hysteretic behavior was observed. It indicates that the samples were elastically deformed below the plastic limit. At each temperature, within the small noise the resistance shows a linear dependence *vs.* uniaxial pressure. At relatively high temperature, the resistance R increases under the uniaxial compression as shown in Fig. 4.12 (a). This behavior cannot be explained in terms of a mere geometric effect as discussed in detail later. On the other hand, upon cooling this pressure response is gradually weakened and finally below 100

K it changes direction and the resistance R decreases under the uniaxial compression as shown in Fig. 4.12 (b). One may think that the uniaxial pressure dependence along the a-axis is caused by the enhanced a-b crystal anisotropy because the resistivity gets more anisotropic as the crystal anisotropy is increased, e.g., by changing the hole doping [96]. If this were the case one would then expect the qualitatively opposite behavior by the b-axis compression which makes the sample less orthorhombic and less anisotropic. However this possibility is clearly excluded since the stress response along the b-axis shows qualitatively the same behavior as observed along the a-axis as shown in Fig. 4.12 (c,d). We therefore attribute the stress dependence of the in-plane electrical resistance to electrons in the CuO_2 planes rather than the CuO chains which run along the b-axis.

The temperature dependence of the uniaxial pressure responses is summarized in Fig. 4.13 (a) as the pressure derivative $-\mathrm{d}(\Delta R/R)/\mathrm{d}\sigma$ deduced from the linear fits of $\Delta R/R$ *vs.* σ in Fig. 4.12. (Note that we take the negative sign for the compressive stress σ as conventional notation, and then we multiply $\mathrm{d}(\Delta R/R)/\mathrm{d}\sigma$ by -1 so that the positive and negative response in $-\mathrm{d}(\Delta R/R)/\mathrm{d}\sigma$ correspond to more resistive and conductive changes, respectively.) $\Delta R/R$ measured on sample 3 with the a-axis compression in temperature sweep experiments is also plotted to ensure the reproducibility of our observation.

In interpreting our observation, we first considered the impact on the sample geometry, which was deformed by the external stress. In particular, with the aim of being more quantitative, one can derive the Gauge factor $\mathrm{d}(\Delta R/R)/\mathrm{d}\varepsilon$ as

$$\frac{\mathrm{d}(\Delta R/R)}{\mathrm{d}\varepsilon} = \frac{\mathrm{d}(\Delta\rho/\rho)}{\mathrm{d}\varepsilon} + (1+2\nu), \tag{4.1}$$

where ρ, ε, and ν are the resistivity, applied strain, and the Poisson's ratio of an elastic material, respectively. It is derived from the relationship between the resistance and resistivity, $R = \rho l/A$, where l and A are the sample length and cross section, respectively. The second term on the right side of Eq. (4.1), $1+2\nu$, is the geometric factor. Suppose the uniaxial pressure dependence is only due to the geometric factor, i.e., $\Delta\rho = 0$, one obtains $-\mathrm{d}(\Delta R/R)/\mathrm{d}\sigma = -(1+2\nu)/E$, which is a negative constant at all temperature. Using $\nu \simeq 0.25$ [18] and the Young's modulus $E \simeq 150$ GPa [234] for $YBa_2Cu_3O_{6.67}$, the geometric factor $-(1+2\nu)/E$ is only -0.01 GPa^{-1}. It is clear that this simple model based on the geometric factor does not reproduce our experimental results at all. Therefore most of the uniaxial pressure response in the electrical resistance ($-\mathrm{d}(\Delta R/R)/\mathrm{d}\sigma$) is due to the first term on the right side of Eq. (4.1), i.e., resistivity, whose changes depend on the electronic structure and/or scattering rate. Likewise, the resistivity simulated in the non-interacting tight-binding model is expected to monotonically decrease under uniaxial compressive stress and thus does not explain the experimental data (see details in Appendix A).

The strong, non-monotonic temperature dependence of the stress response indicates many-body correlations of the electron system. In view of the recent observation of strongly T-dependent incommensurate charge order by x-ray diffraction on samples of identical composition [144], we compare our transport data to the amplitude of the diffraction signal arising from charge order, which is displayed in Fig. 4.13 (b). We note that the temperature onset of this signal at $T_{CO} \sim 150$ K coincides approximately with the onset of the downturn in $-\mathrm{d}(\Delta R/R)/\mathrm{d}\sigma$ (Fig. 4.13 (a)). It was shown by the recent RIXS measurements that the 2D-CDW orthogonal to the uniaxial stress direction is always

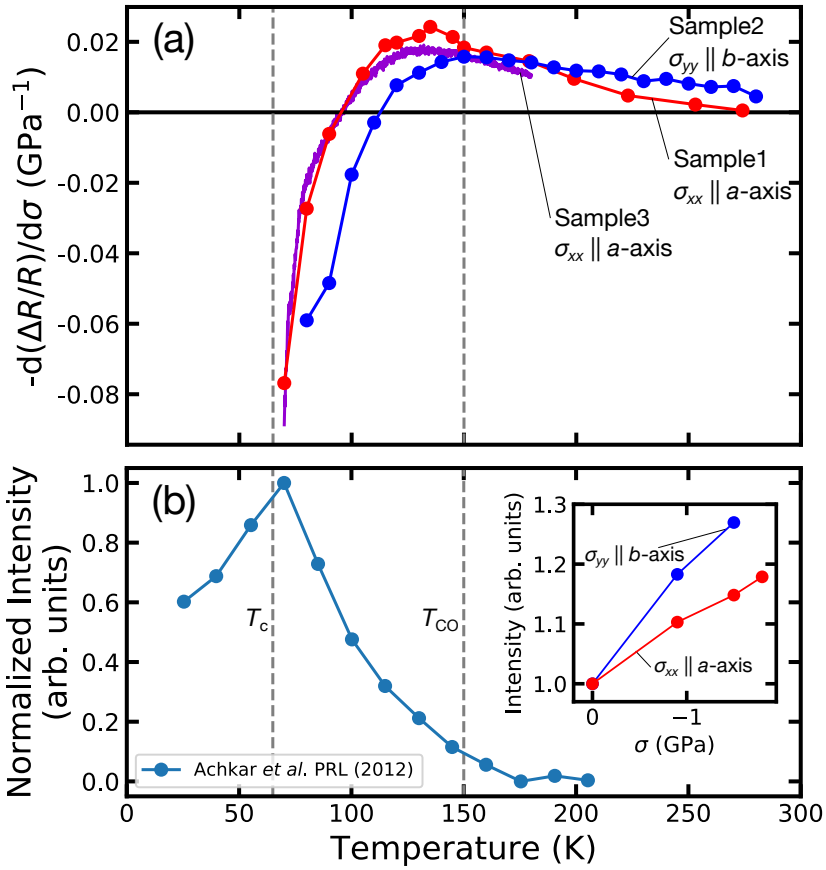

Figure 4.13: **Comparison of transport and diffraction signatures of 2D-CDW.** (a) $-\mathrm{d}(\Delta R/R)/\mathrm{d}\sigma$ *vs.* temperature deduced from Fig. 4.12. One of $\Delta R/R$ of sample 3 obtained in temperature sweep measurements is also shown. The magnitude of $\Delta R/R$ was scaled by -1 GPa to convert to $-\mathrm{d}(\Delta R/R)/\mathrm{d}\sigma$. (b) Temperature dependence of the normalized intensity of the 2D-CDW measured in resonant x-ray scattering experiments. Reproduced from Ref. [144]. Inset: Uniaxial stress dependence of integrated peak intensity of the 2D-CDW (normalized to zero stress) is shown. It was estimated based on the RIXS data in Ref. [142] and details can be seen in Appendix B.

enhanced for both uniaxial pressure directions [142]. The qualitatively symmetric response of $-\mathrm{d}(\Delta R/R)/\mathrm{d}\sigma$ along both a- and b-directions and its close coincidence between T_{CO} and the temperature at which $-\mathrm{d}(\Delta R/R)/\mathrm{d}\sigma$ shows the downturn indicate the signature of the static 2D-CDW in the resistivity which was not apparent in the normal resistivity curves (Fig. 4.2 (a,b) and Fig. 4.10). On top of those qualitative isotropies, the quantitative in-plane anisotropies of the stress response of both quantities also exhibit striking similarities. Specifically, stress along both principal in-plane axes enhances the charge-ordering signal with an amplitude that is larger along b-axis than along a-axis (Inset of Fig. 4.13 (b) and Appendix B) [142], mirroring the amplitude and anisotropy of the stress response of the resistivity where $-\mathrm{d}(\Delta R/R)/\mathrm{d}\sigma$ crosses zero at $\sim$ 110 K and 100 K with the b- and a-axis compression, respectively (Fig. 4.13 (a)). These parallels suggest that the electrical resistivity is reduced by the onset of charge order. A similar effect has been observed in classical CDW compounds with two-dimensional electron systems, where the CDW gap partially reconstructs the Fermi surface such that the impact of the reduced carrier density on the resistivity is over-compensated by the reduced scattering probability of the residual carriers [10, 11].

4.3.2 Hall effect

In light of these considerations, we now discuss measurements of the Hall coefficient R_H, which are displayed in Fig. 4.14. In agreement with prior work in the absence of pressure also shown in Figs. 4.3 and 4.5, the Hall coefficient, R_H, is positive at high temperatures and exhibits a maximum on cooling below $T \sim 150$ K, followed by a zero-crossing at $T_0 \sim 70$ K[2] [161, 215]. Based in part on quantum oscillation measurements at high magnetic fields, these phenomena have been ascribed to the formation of electron pockets via a Fermi surface reconstruction induced by charge ordering (Fig. 4.4) [20, 214, 213, 223]. In qualitative agreement with this scenario, the application of stress amplifies the downturn of R_H upon cooling as is evident from ΔR_H, consistent with the stress-induced enhancement of the charge ordering amplitude inferred from x-ray diffraction [142]. The effect is again larger for stress along b-axis than along a-axis (Fig. 4.14 (c)), mirroring the in-plane anisotropies of the longitudinal resistivity (Fig. 4.13 (a)) and charge-ordering amplitude (Inset of Fig. 4.13 (b)). On a qualitative level, our data thus support the notion of a Fermi-surface reconstruction induced by the experimentally observed charge correlations which are enhanced by the uniaxial stress.

However, we note a large quantitative disparity in the stress responses of the charge ordering amplitude and the transport coefficients. In particular, the intensity of the x-ray reflections increases by $\sim 100\%$ for a-axis compression by 1 GPa [142], whereas only a small modification of R_H and a ~ 1 K shift of T_0 are observed under the same conditions (Fig. 4.14 (d)). A related discrepancy was noted for hydrostatic pressure (Fig. 4.15) [23, 228], which appears to affect the manifestations of charge order in scattering experiments much more strongly than the corresponding transport features [17]. In the latter case, however, the association is complicated by the influence of hydrostatic pressure on the doping level, which varies strongly as a function of doping and may obscure the comparison of

[2]The magnitude of the magnetic field was not high enough to completely obliterate superconductivity, therefore the signal below 40 K turns up towards zero in Fig. 4.14 (a) due to the zero resistivity. The similar upturn is seen around 30 K in Fig. 4.14 (b).

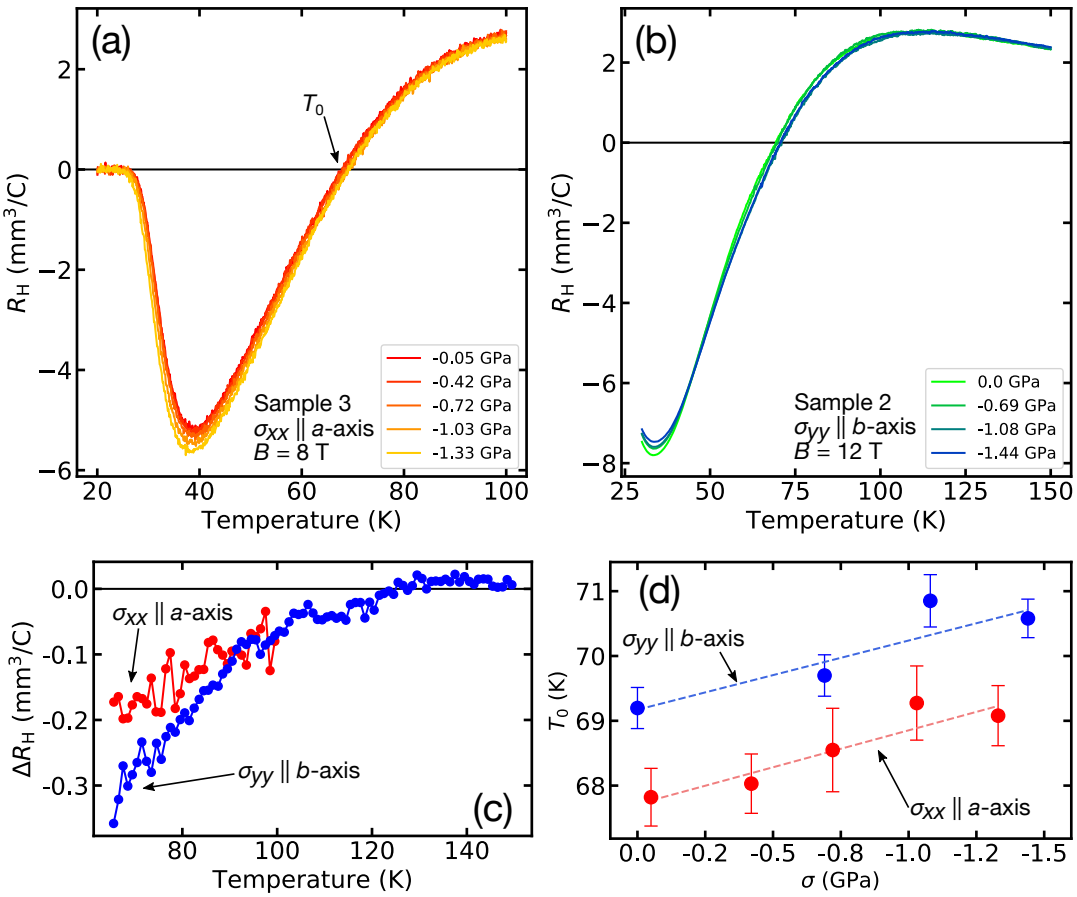

Figure 4.14: **Hall effect under uniaxial stress.** (a) The uniaxial pressure σ_{xx} is parallel to the a-axis and the magnetic field is 8 T along the c-axis. (b) The uniaxial pressure σ_{yy} is parallel to the b-axis and the magnetic field is 12 T. (c) The difference in the Hall coefficient ΔR_{H} between $\sigma \sim$ -1 GPa and $\sigma = 0$. (d) The sign reversal temperature T_0 as a function of stress.

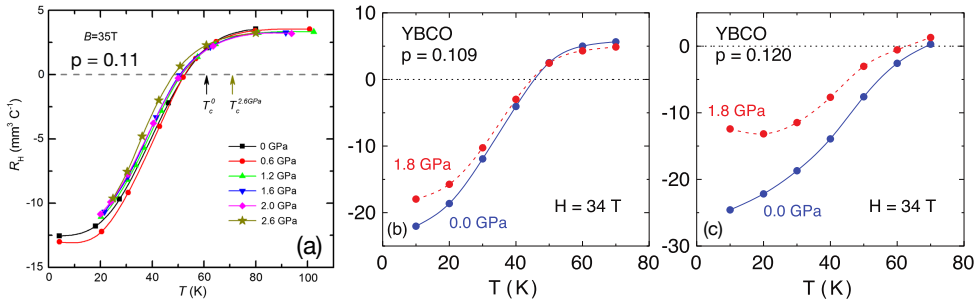

Figure 4.15: **Hall effect under hydrostatic pressure.** The measurements were performed under the high magnetic fields unlike our experiments. (a) Figure from Ref. [23]. (b,c) Figures from Ref. [228].

data on different samples [229]. Uniaxial stress, on the other hand, does not affect the doping level. If the uniaxial stress primarily affects the doping, one would then expect the supression of the CDW, which was never observed in diffraction experiments. Moreover, our measurements were taken on samples prepared in an identical fashion and can thus be compared without any ambiguity. The quantitative disparity between diffraction and transport signatures of charge order is therefore an intrinsic feature of $YBa_2Cu_3O_{6.67}$. We remark that little change in R_H is not because the uniaxial stress response is prohibitted by the symmetry of the system (see details in Appendix C). A possible solution to this conundrum is spatial inhomogeneity of the static charge order, which is indicated by the nonzero width of the diffraction features. X-ray scattering experiments with high energy resolution [16] indicate that the x-ray reflections originate predominantly from charge ordered domains nucleated by residual disorder – a finding that is also supported by NMR results [235]. Conversely, the current flow detected in transport experiments may predominantly originate from regions with weak or absent static charge order, thus explaining the quantitative disparity between the stress responses of static charge order and transport properties.

However, these considerations also show that static charge order is not responsible for the most prominent anomalous transport features of $YBa_2Cu_3O_{6.67}$, including particularly the maximum and sign reversal of the Hall coefficient which only depend weakly on stress (Fig. 4.14). In exploring alternative explanations, we can also rule out a Fermi-surface reconstruction by magnetic order, because static magnetism is not present in the $YBa_2Cu_3O_{6+x}$ system in the doping and magnetic-field range probed by our experiments. In principle, the unusual behavior of the Hall coefficient may arise from electronic correlations unrelated to density-wave orders, including flux-flow phenomena in a phase-incoherent superconducting state that precedes superconducting long-range order. This scenario was invoked early on to explain the sign reversal of R_H [236], but subsequent experiments have called this interpretation into question, based in part on the observed magnetic field independence of T_0 (Fig. 4.5), and on the continuous evolution of the low-field Hall coefficient into the quantum-oscillation regime that indicates a reconstructed Fermi surface in high magnetic fields [215]. Moreover, recent theoretical work indicates that phase-incoherent Cooper pairing does not reverse the sign of R_H [237].

Conventional static CDW order can thus be ruled out as the main origin of the transport

anomalies, and one may ask whether slowly fluctuating, dynamical charge correlations recently uncovered by RIXS with the high-energy resolution [15, 238, 239, 240, 241] offer an alternative explanation. Two factors argue in favor of such a scenario. First, the temperature evolution of the dynamical correlations is closely similar to the one of the static order. Indeed, the diffraction features in elastic x-ray scattering can be understood as a "central peak" resulting from pinning of low-energy collective charge fluctuations by defects [16]. The analogy between the T-evolution of charge order and transport coefficients pointed out above therefore also holds for dynamical correlations. Second, in contrast to the (slightly broadened) Bragg reflections manifesting static order, the dynamical charge correlations exhibit a ring-like pattern in reciprocal space [242], akin to analogous patterns in quantum spin liquids and superfluid helium. Such liquid-like correlations are expected to be less susceptible to stress along particular lattice directions than the static order. Therefore the present results suggest that such ring-like correlations might be present in $YBa_2Cu_3O_{6+x}$ as well.

4.4 Conclusions

In summary, our investigation of the stress dependence of the resistivity and Hall coefficient of $YBa_2Cu_3O_{6.67}$ has demonstrated surprising qualitative analogies to classical CDW materials with two-dimensional electron systems, where the loss of scattering channels in the CDW state lowers the resistivity. One can link the observed resistance under uniaxial pressure to the 2D-CDW via three observations: i) the temperature dependence of the differential resistance peaks and changes trend at a temperature coincident with the onset of the 2D-CDW, ii) a- and b-axis pressures have qualitatively the same effect, and iii) the effect of b-axis pressure is quantitatively larger, in agreement with the RIXS experiments [142]. Our data are compatible with recent experiments on $YBa_2Cu_3O_{6+x}$ thin films, which found that a suppression of charge order by biaxial strain restores the linear-in-T behavior of the resistivity usually observed at higher doping levels [211]. In contrast to our *in-situ* study, however, modification of the biaxial-strain state requires preparation of different thin-film samples, so that the resistivities are difficult to compare on an absolute scale. Interestingly, the long-range-ordered "striped" state in the $La_{2-x}Ba_xCuO_4$ family leads to an increase of the resistivity [13], possibly due to the influence of concomitant magnetic and lattice instabilities.

Quantitatively we found that the uniaxial pressure has very little effect on the Hall coefficient R_H. The sign reversal temperature T_0 changed only by ~ 1 K under the highest stress that we achieved. This observation is in stark contrast to the picture of Fermi surface reconstructed by the static charge orders which are strongly affected by the uniaxial stress demonstrated in the previous x-ray scattering measurements. To ultimately test the Fermi surface reconstruction picture, quantum oscillation measurements under uniaxial stress is desirable. Due to the absence of the magnetism in the sample presently studied, the possibility of the reconstruction by the static magnetic order is firmly excluded. Therefore we inferred the role of slowly fluctuating charge or spin orders should play an important role to reconcile the apparent contradiction.

More importantly, our data suggest a key role of liquid-like, nearly critical charge correlations for fermionic transport, in contrast to the electron-phonon-interaction driven static charge order in the classical systems. There has been a number of theoretical proposals

along these lines, but few explicit calculations of transport coefficients. Calculations of the Hall coefficient in the framework of models with slowly fluctuating charge [231] or spin [243] order indicate a subtle downturn at low temperatures, but a sign reversal has not been predicted to the best of our knowledge. The concrete link between transport and scattering probes of charge correlations uncovered in our parametric study should motivate further progress in the development of this theoretical framework, for instance by including the interplay with pairing fluctuations.

Chapter 5

Resonant soft x-ray scattering of $YBa_2Cu_3O_{6+x}$ under uniaxial stress

5.1 Introduction

X-ray scattering techniques have played an important role to reveal the nature of charge ordering phenomena in $YBa_2Cu_3O_{6+x}$ and other cuprate families [15]. This was the case also for studies of the CDW response to uniaxial stress, which was reported before any transport measurements. Indeed non-resonant inelastic x-ray scattering measurements under uniaxial stress showed that the strong softening of a phonon mode drives the formation of the 3D-CDW [18]. The results provided a new perspective to control competing phases and indicated that uniaxial stress can become a new interesting axis orthogonal to those of temperature and hole doping in the phase diagram. However, the limited counting rate in energy-resolved x-ray experiments has prevented systematic strain studies of CDWs as a function of hole doping. We addressed this issue by using the strain rig at the beamline UE46-PGM1 at BESSY-II to perform much faster Cu-L_3 resonant energy-integrated x-ray scattering (REXS) measurements on $YBa_2Cu_3O_{6+x}$ single crystals with different doping levels under large uniaxial stress.

Interestingly, the intrinsic instability towards uniaxial CDW in cuprates can result in the observed biaxial, short-ranged 2D-CDW in the presence of quenched defects according to theoretical studies [244]. Indeed, many aspects of the previous resonant inelastic x-ray scattering (RIXS) data under uniaxial pressure can be described by this scenario [142]. This manifests itself in the observed symmetric response to compressive strain applied either to the a- or b-axis which alternatively favours the b- or a-CDW[1] domains, respectively, which are already pinned by defects at the onset temperature of the CDW. We carried out further Cu-L_3 RIXS measurements on $YBa_2Cu_3O_{6.67}$ under uniaxial pressure at the beamline ID32 at the ESRF to investigate the defect-pinned 2D-CDW scenario by comparing the intensity of a- and b-CDW upon cooling with and without applied stress.

[1]For simplicity, in this chapter, the 2D-CDW with the propagation vectors $\boldsymbol{Q}_a \simeq (0.305, 0, 0.5)$ and $\boldsymbol{Q}_b \simeq (0, 0315, 0.5)$ are termed a-CDW and b-CDW, respectively.

5.2 REXS measurements

5.2.1 Introduction

It has been well established that the 2D-CDW is a ubiquitous feature in the underdoped region of $YBa_2Cu_3O_{6+x}$ and all other cuprates, which was initially found only in the 214 systems as the stripe order where the charge and spin sectors are intertwined. On the other hand, the 3D-CDW has been to date observed only in $YBa_2Cu_3O_{6+x}$ bulk crystals under external fields (magnetic field [21] and strain [18]) and thin films [160]. While the nucleation around random defects is proposed as the mechanism of development and stabilization of 2D-CDWs, the mechanism of the 3D-CDW is considered to be purely electronic [142]. Therefore the observation of the strain-induced 3D-CDW at the 1/8 doping does not immediately imply how the charge orders, in particular the 3D-CDW, should be affected by strain in other doping regions of the phase diagram of $YBa_2Cu_3O_{6+x}$. To investigate the uniaxial stress effects on the CDWs in $YBa_2Cu_3O_{6.67}$, energy-resolved techniques, namely IXS and RIXS, have been very insightful so far [18, 142]. Thanks to the high energy resolution of hard x-ray scattering measurements ($\sim$ 3 meV), it was revealed that the strong softening of a phonon mode drives the formation of the 3D-CDW induced by strain and observed as quasielastic peak in the IXS spectra. However, from a practical point of view, energy-resolved spectroscopies require a long acquisition time to obtain spectra with a sufficient signal-to-noise ratio. This aspect in RIXS and IXS has prevented researchers from investigating the nature of the strain-induced 3D-CDW systematically, in particular as a function of hole doping of $YBa_2Cu_3O_{6+x}$. Indeed, for this reason, only one particular doping level $YBa_2Cu_3O_{6.67}$ ($p = 0.12$) where the CDW is the strongest has been investigated so far to study the effect of uniaxial stress on the CDWs in $YBa_2Cu_3O_{6+x}$. Taking advantage of the faster acquisition time of REXS measurements, we carried out a systematic doping dependence of the uniaxial stress effects on the CDWs of $YBa_2Cu_3O_{6+x}$.

5.2.2 Experimental methods

The high-quality $YBa_2Cu_3O_{6+x}$ crystals ($x = 0.5, 0.8$, and 0.93) have been prepared as explained in the previous chapters. The oxygen content was controlled by annealing samples at 614 °C ($x = 0.5$) in the mixture of 5 % O_2 and 95 % Ar and 597 °C ($x = 0.8$) and 494 °C ($x = 0.93$) in 100 % O_2 for one week to obtain the specific doping levels [178]. All the samples were detwinned with a standard mechanical method (chapter 3.3.3) [180]. The samples were shaped for the application of strain in the same manner as the transport experiments, yet without the electrical contacts. The detailed information of each sample can be found in Table 5.1. REXS measurements were performed at the UE46-PGM1 beamline of the BESSY II synchrotron (chapter 3.5.3) [202]. The incident energy was set to the Cu-L_3 edge, 932 eV and the σ-polarization (perpendicular to the scattering plane) was used to maximize the charge scattering contribution [63]. The energy and polarization of scattered photons were not resolved, therefore the intensity detected by the photodiode represents an integration over all elastic and inelastic scattering processes with both σ- and π-polarizations. In order to reach the structural Bragg peak (0,0,2), an incident energy of 1100 eV was used. For all doping levels, the compressive stress was

applied along the a-axis of the sample and the measurements were performed at first at the superconducting transition temperature T_c where the CDW intensity is maximized and then at various temperatures to collect a temperature dependence. The strain rig, described in chapter 3.2.3, was used to apply uniaxial stress during the REXS experiments: therefore the strain inferred from the capacitance change is used as a measure of the deformation of the samples and the negative values in strain indicate compression. The strain was monitored in all measurements by looking at the shift of a structural Bragg peak. Due to the scattering geometry, so far only CDWs along the b-axis were observed as a function of the a-axis stress.

Sample name	c (Å)	p	T_c (K)	$a \times b \times c$ (mm^3)	Structure
$YBa_2Cu_3O_{6.5}$ (R614C5N3)	11.739	0.1051	56	$2.6 \times 0.20 \times 0.09$	O-II
$YBa_2Cu_3O_{6.8}$ (R597R1N3)	11.708	0.1448	80	$1.9 \times 0.20 \times 0.13$	O-III
$YBa_2Cu_3O_{6.93}$ (R494L1N4)	11.694	0.1681	93	$3.2 \times 0.20 \times 0.10$	O-I

Table 5.1: **List of the $YBa_2Cu_3O_{6+x}$ crystals measured in the REXS experiments.** The c-axis lattice parameter c is determined with XRD measurements at room temperature and the doping p is estimated based on c using Eq. (3.13). T_c was determined by magnetometry as the midpoint of the diamagnetic response. The structure indicates the oxygen orders in the CuO layers (see details in chapter 2.2 and Ref. [33]).

5.2.3 Results

$YBa_2Cu_3O_{6.5}$ (T_c = 56 K)

We first present the REXS results of $YBa_2Cu_3O_{6.5}$ whose doping is lower than that of $YBa_2Cu_3O_{6.67}$, and thus T_c is slightly lower as well. The strain application was well confirmed by the progressive shift of the Bragg peak (0,0,2) (Fig. 5.1 (a)) as in the case of previous studies. Note that it is not the in-plane Bragg peak but one can observe the elongation along the c-axis, as seen in the Bragg peak shift towards smaller 2θ values, as induced by the uniaxial stress along the a-axis and due to Poisson's effect (see chapter 3.2.2). The intensity of the 2D-CDW is enhanced by strain as shown in Fig. 5.1 (b). It is a similar behavior to the one previously observed in $YBa_2Cu_3O_{6.67}$. Our central observation on $YBa_2Cu_3O_{6.5}$ under uniaxial stress is summarized in the reciprocal space mapping in Fig. 5.2. In the absence of strain, the quasi-two dimensional nature of the CDW without correlations along the crystallographic c direction is evident as a rod extending along the L direction in the K-L map (Fig. 5.2 (a)). The closer to the half integer point L= 1.5 the wave vector is, the stronger the intensity is before applying the strain as already observed in a number of previous studies. At the intermediate strain level (-0.7 %), the intensity distribution in the rod along the L direction changes and the intensity near the integer point $L = 1$ becomes stronger (Fig. 5.2 (b)). Figure 5.2 (c) shows the data at the highest strain level (-1.2 %) where a new peak-like feature is now emerging in at (K, L) = (0.327, 1.025). This is the indication of the three dimensional correlation of the CDW as similarly observed in the recent RIXS experiments on $YBa_2Cu_3O_{6.67}$. Comparing the data displayed in Fig. 5.2 (d) and (e) whose color scale is identical to that in Fig. 5.2 (c),

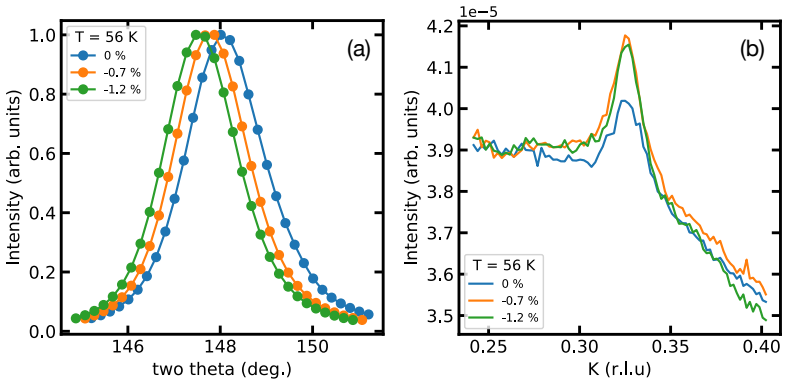

Figure 5.1: **REXS data of $YBa_2Cu_3O_{6.5}$.** (a) Bragg peak (0,0,2) shifts due to Poisson's effect by the in-plain uniaxial stress. (b) REXS intensity around $Q_{\text{2D-CDW}}$ along the K direction at $T = T_c$ for different strain levels.

one can confirm how intense the feature of the 3D-CDW is. The intensity of this peak is not as intense as the one obtained in the IXS measurements where the feature of the 3D-CDW was observed at $(K, L) \simeq (0.3, 7)$ to maximize the structure factor [194]. This change in intensity from IXS to REXS is considered to be due to the weaker structure factor at the accessible momentum space positions confined by the limited photon energy at the Cu-L_3 edge combined with the fact that REXS probes valence charges rather than the core electrons probed by IXS which follow the small atomic displacements associated with the CDW. Also, as shown in Fig. 5.2 (g), the intensity scan along the L direction is strongly distorted and as a consequence the peak position ($L \sim 1.025$) is slightly greater than the integer value 1 where one expects to observe the peak from the three dimensional correlation. This is likely because of self-absorption effects caused by the grazing conditions for outgoing photons which were discussed in the supplementary material of the recent RIXS study. The 3D-CDW REXS peak in the present study in fact completely agrees with the 3D-CDW from the previous RIXS data collected in a similar scattering geometry [142].

To investigate the relationship with superconductivity, the temperature dependence of the strain-induced 3D-CDW was also measured. Figure 5.3 shows the temperature dependence of the REXS scans along the L direction around $Q_{\text{3D-CDW}} = (0, 0.327, 1.025)$. The intensity is maximized at T_c, which implies a strong competition with superconductivity. The 3D-CDW remains intense and visible above T_c at least up to 80 K while the onset temperature of the 2D-CDW at this doping level is 125 K [151]. Essentially the same temperature dependence is evident from complementary measurements along the K direction shown in Fig. 5.4. The sharpness of the 3D-CDW along the K direction enables us to analyze the peak intensities and widths at various temperatures. The temperature dependence of the fitting parameters obtained by the Lorentzian fits are displayed in Fig. 5.5. The competition between the 3D-CDW and superconductivity is clear from the fitting results as well.

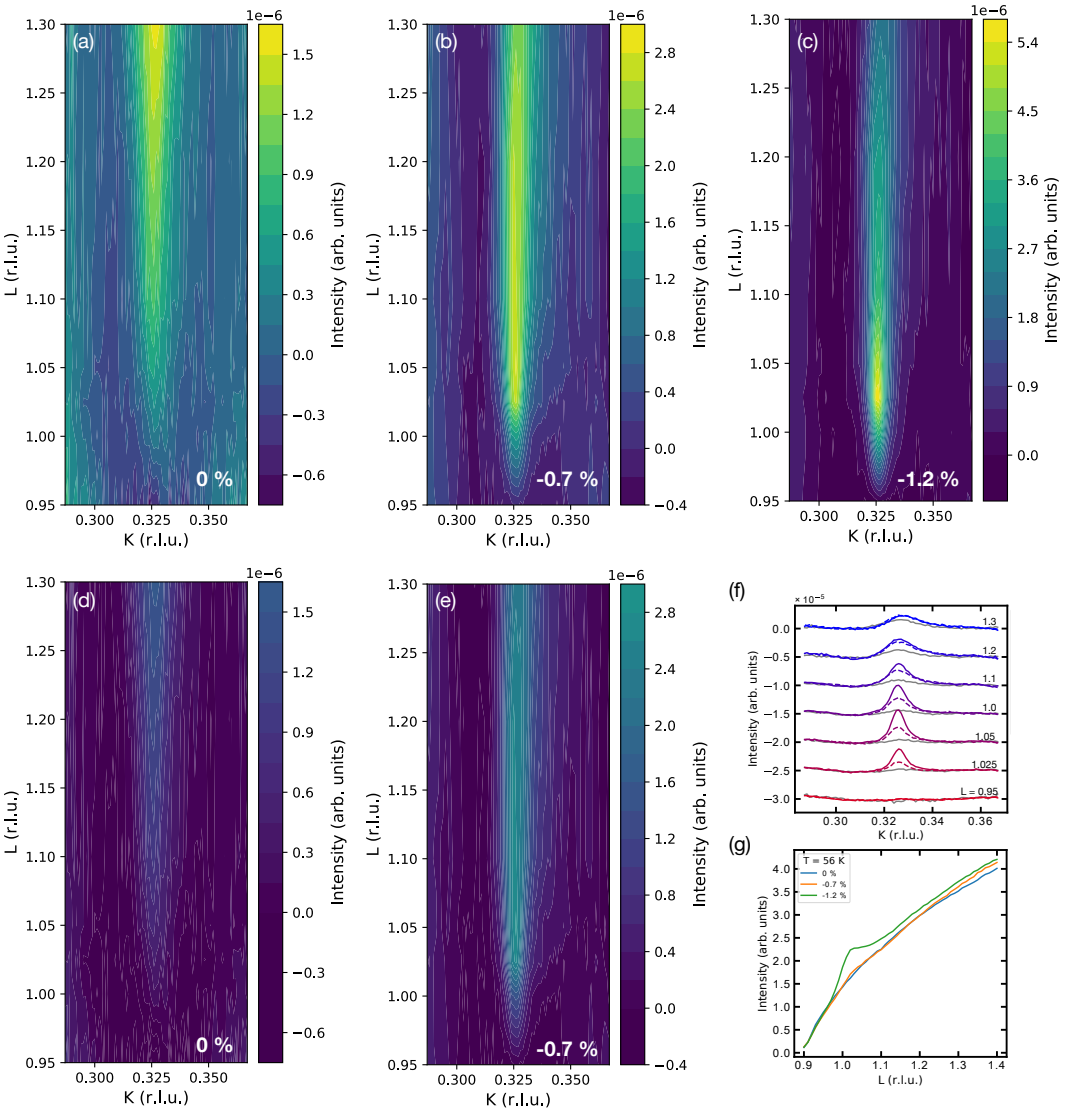

Figure 5.2: **REXS reciprocal space mapping of $YBa_2Cu_3O_{6.5}$ at $T = T_c$ under different strain levels.** The strain direction is parallel to the a-axis. (a-c) REXS intensity color map in the K-L plane under strain of 0 %, -0.7 % and -1.2 %, respectively. (d,e) Same as (a,b) but the color scale of (c) is used to compare their intensities. (f) Original data of (a-e). The solid, dashed, and gray solid curves are data under uniaxial strain of 0 %, -0.7 %, and -1.2 %, respectively. The linear background was subtracted from the raw data and the curves are shown with vertical offsets for clarity. (g) REXS scans at (0,0.327,L) along the L direction for different strain levels.

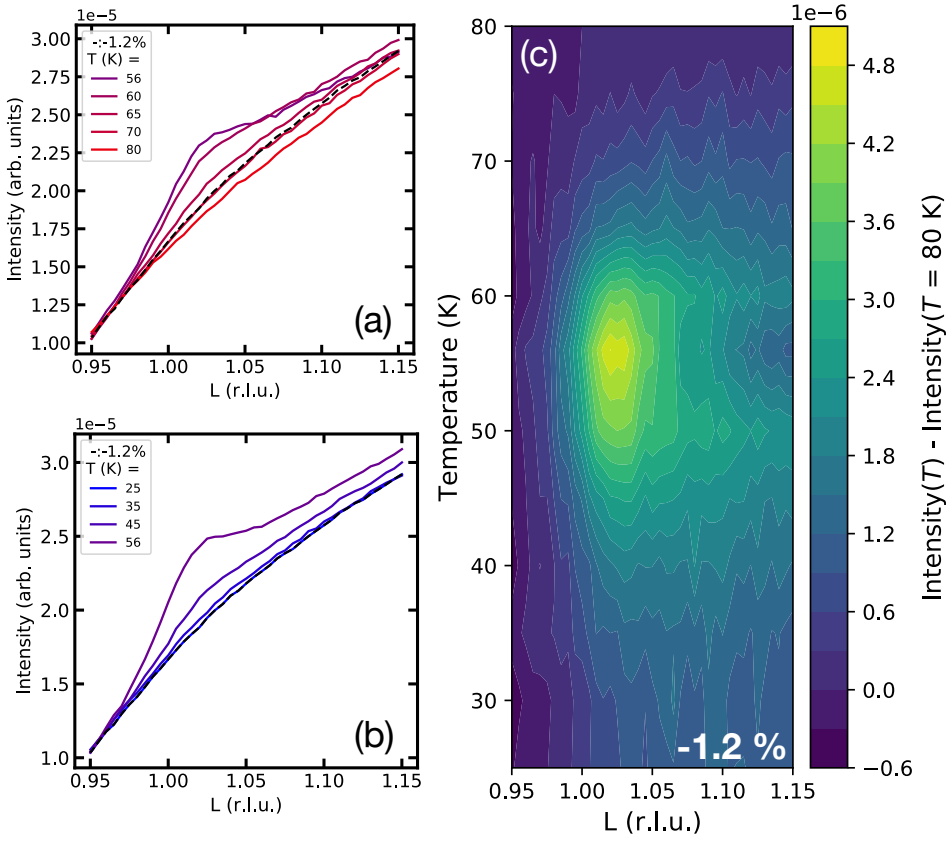

Figure 5.3: **Temperature dependence of the strain-induced 3D-CDW in $YBa_2Cu_3O_{6.5}$ along the L direction around the $Q_{\text{3D-CDW}} = (0, 0.327, 1.025)$.** (a) REXS scan along the L direction measured at $T \geq T_c$. The black dashed curve is the unstrained curve at $T = T_c$. (b) Same as (a) but measured at $T \leq T_c$. (c) REXS intensity map at (0,0.327,L) obtained from (a,b). Intensity at 80 K is subtracted from that at each temperature for clarity.

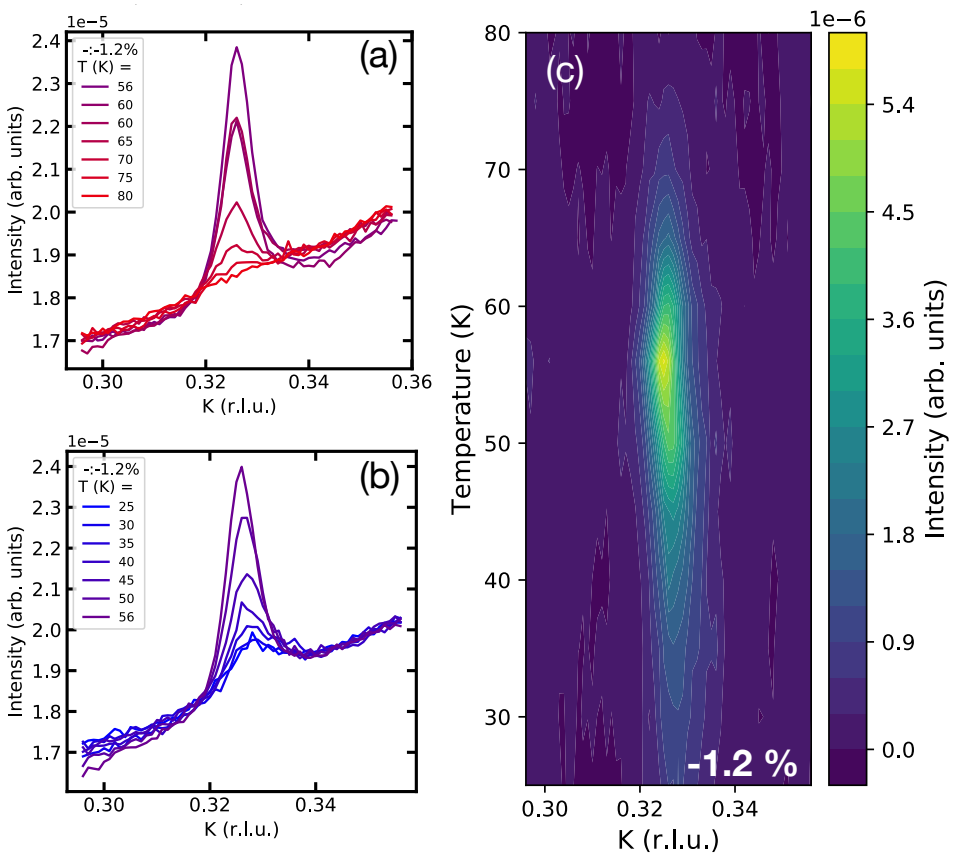

Figure 5.4: **Temperature dependence of the strain-induced 3D-CDW in $YBa_2Cu_3O_{6.5}$ along the K direction around the $Q_{\text{3D-CDW}} = (0, 0.327, 1.025)$.** (a) REXS scan along the K direction measured at $T \geq T_c$. (b) Same as (a) but measured at $T \leq T_c$. (c) REXS intensity map at (0,K,1.025) obtained from (a,b). The linear background is subtracted from that at each temperature for clarity.

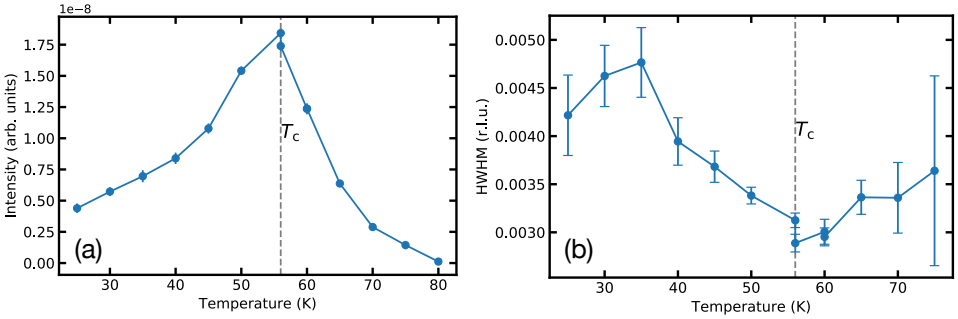

Figure 5.5: **Temperature dependence of the fitting parameters obtained by Lorentzian fits of the K scans around $Q_{\text{3D-CDW}}$ shown in Fig. 5.4.** (a) Area of the Lorentzian. (b) HWHM of the Lorentzian. The error bars are the standard deviations.

$YBa_2Cu_3O_{6.8}$ (T_c = 80 K)

Figure 5.6 shows the REXS data of $YBa_2Cu_3O_{6.8}$ whose doping is higher than that of the extensively studied $YBa_2Cu_3O_{6.67}$. As in the previous cases, the strain application is well confirmed from the shift of the Bragg peak (0,0,2). As shown in Fig. 5.6 (b), the 2D-CDW along the *b*-axis was enhanced by uniaxial stress along the *a*-axis. This is also evident in the *K*-*L* mappings where the rod extending along the *L* direction became more intense (Fig. 5.6 (c,d)). However no clear indication of the peak near *L*=1 was observed even at the highest strain level which induces the 3D-CDW in $YBa_2Cu_3O_{6.5}$ and $YBa_2Cu_3O_{6.67}$.

$YBa_2Cu_3O_{6.93}$ (T_c = 93 K)

Figure 5.7 shows the REXS data of the optimally doped sample $YBa_2Cu_3O_{6.93}$ where the superconductivity is the strongest in the phase diagram. Despite of the strain application confirmed by the Bragg peak (0,0,2) shifts, the very weak and broad 2D-CDW peak seen at this doping does not seem to be affected by the strain at all.

5.2.4 Discussion

Sample (hole doping)	Enhancement of 2D-CDW	Emergence of 3D-CDW
$YBa_2Cu_3O_{6.5}$ ($p = 0.105$)	Yes	Yes ($T_{\text{3D-CDW}} \simeq 80$ K)
$YBa_2Cu_3O_{6.67}$ ($p = 0.12$)*	Yes	Yes ($T_{\text{3D-CDW}} \simeq 75$ K)
$YBa_2Cu_3O_{6.8}$ ($p = 0.145$)	Yes	No
$YBa_2Cu_3O_{6.93}$ ($p = 0.168$)	No	No

Table 5.2: Summary of the observations of the CDWs under compressive strain along the *a*-axis ($\sim$ - 1 %). The results for $YBa_2Cu_3O_{6.67}$ are taken from Ref. [18, 142].

The results regarding the 2D-CDW and 3D-CDW under uniaxial stress are summarized in Table 5.2. Let us first discuss the strain-induced 3D-CDW, which was observed only in $YBa_2Cu_3O_{6.5}$ in the present study. It is reminiscent of the one observed in $YBa_2Cu_3O_{6.67}$ in the previous studies. Considering the proposals of a Fermi surface reconstruction due to charge orders whose correlation length is shorter than that of the oxygen orders in the CuO chain layers [214], it is reasonable to consider that the valence electrons in the CuO_2 planes might be affected by the periodic structure of the CuO chains. However the observation of the same 3D-CDW at both doping levels despite the different oxygen orders in the CuO chain layers (Ortho-II and Ortho-VIII in $YBa_2Cu_3O_{6.5}$ and $YBa_2Cu_3O_{6.67}$, respectively) seems to indicate that the CuO chains (or at least their periodicity) are not crucial for the formation of the 3D-CDW. Indeed the 3D-CDW resonates only at the energy of planar Cu atoms in the CuO_2 planes. Notice that this is at odds with the 3D charge order observed in $YBa_2Cu_3O_{6+x}$ thin films, whose energy dependence also shows a contribution from the Cu atoms in the CuO chain layers [160].

On the other hand, three aspects of the 3D-CDW temperature dependence can differ for these two doping levels, namely, i) the onset temperature, ii) the temperature at which the 3D-CDW is maximized, and iii) the intensity in the zero-temperature limit. First of all, the onset temperature of the strain-induced 3D-CDW in $YBa_2Cu_3O_{6.5}$ is

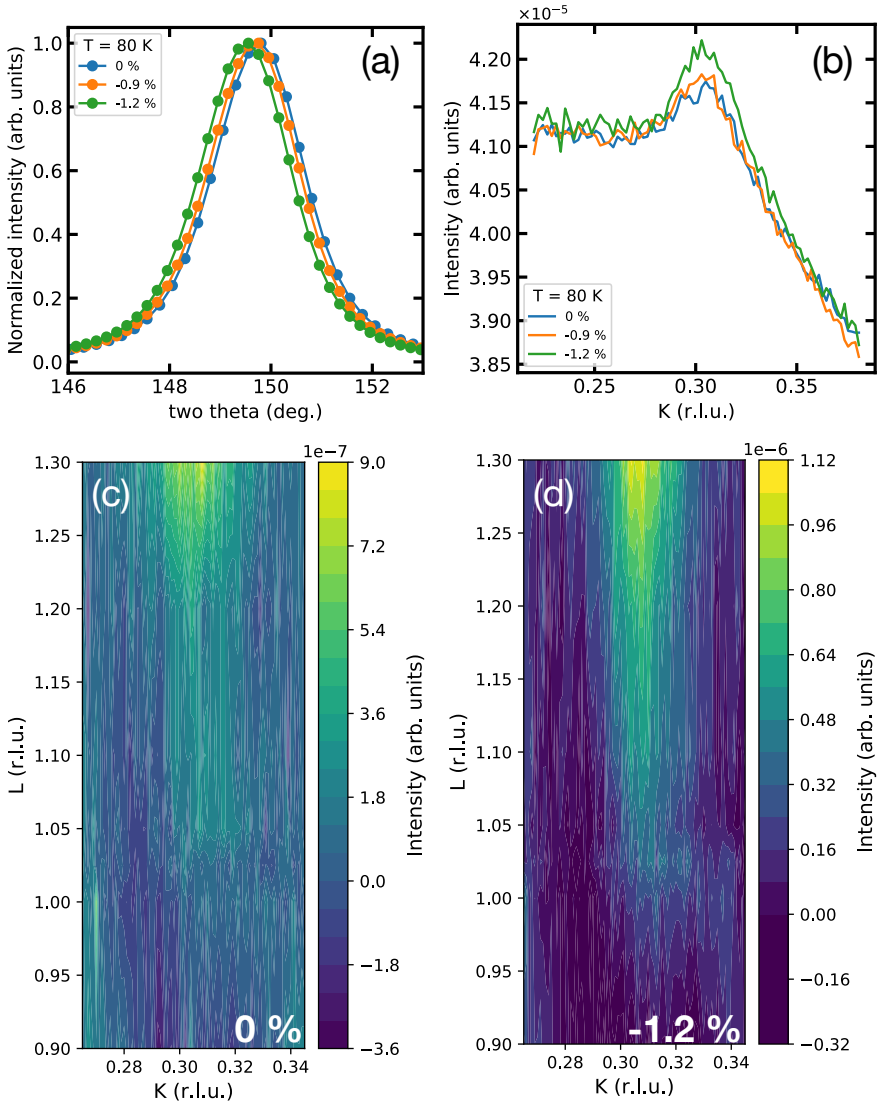

Figure 5.6: **REXS data on $YBa_2Cu_3O_{6.8}$.** The strain direction is parallel to the a-axis. Data were taken at $T = T_c$. (a) Bragg peak (0,0,2) shifts. (b) REXS intensity around $Q_{2D\text{-}CDW}$ along the K direction. (c) Reciprocal space mapping in the K-L plane without strain. (d) Same as (c) but with the strain of -1.2 %.

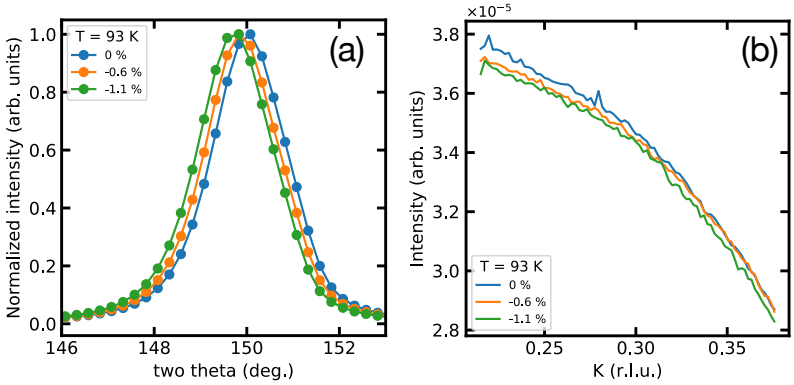

Figure 5.7: **REXS data on $YBa_2Cu_3O_{6.93}$.** The strain direction is parallel to the a-axis. Data were taken at $T = T_c$. (a) Bragg peak (0,0,2) shifts. (b) REXS intensity around $Q_{\text{2D-CDW}}$ along the K direction.

around 80 K (Fig. 5.5 (a)), which is comparable to or even slightly higher than that of $YBa_2Cu_3O_{6.67}$ ($\sim$ 75 K, reported in Ref. [142]). If the 3D-CDW arises as the development of the three-dimensional phase coherence of the 2D-CDW between adjacent layers, in a similar manner to the 3D antiferromagnetic order formation in undoped cuprates [245], one would expect the onset temperature of the 3D-CDW formation in $YBa_2Cu_3O_{6.5}$ to be lower than that of $YBa_2Cu_3O_{6.67}$ because the onset temperature of the 2D-CDW in $YBa_2Cu_3O_{6.5}$ is 125 K *v.s.* 150 K in $YBa_2Cu_3O_{6.67}$. Our result supports the scenario that the 3D-CDW is an electronically driven phase with a distinct mechanism from the one of the 2D-CDWs. The 3D-CDW signal of $YBa_2Cu_3O_{6.5}$ is maximized at the original unstrained T_c (= 56 K) while the 3D-CDW in $YBa_2Cu_3O_{6.67}$ is the most enhanced at the suppressed T_c by uniaxial stress. Note that at present the precise strain dependence of T_c in $YBa_2Cu_3O_{6.5}$ is not clear. However T_c is expected to be lowered by the compression along the a-axis because the suppression of T_c of $YBa_2Cu_3O_{6+x}$ whose unstrained T_c is 59 K is reported in supplementary materials of Ref. [18]. Considerable intensity of the 3D-CDW persists at the lowest temperature in the present study as shown in Fig. 5.5 (a). At first sight, this feature looks different from the first observation of the 3D-CDW investigated by the temperature-dependent non-resonant IXS measurements [18], where more than 90 % of the intensity was already lost at 40 K compared to the maximum intensity at 50 K. Indeed the IXS data supported a much more rapid suppression of the 3D-CDW than the 2D-CDW. However, according to more recent RIXS measurements performed at the same doping level and strain conditions as in the IXS measurements [142], more than 40 % of the intensity at 55 K is still present at 35 K, while the onset and peak temperature of the 3D-CDW are identical in both IXS and RIXS experiments. Therefore it would be better to restrain comparisons of the zero-temperature limit intensity between different doping levels measured in the same setup or at the very least at the same incoming energy, as that considerably affects the structure factor, as previously discussed. It is remarkable that our REXS data shows a considerable intensity of the 3D-CDW at the lowest temperature. Nevertheless, comparing with the 2D-CDW in $YBa_2Cu_3O_{6.51}$ previously studied in the same setup [151], half of the maximum intensity

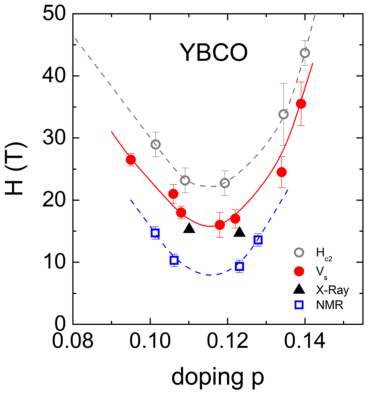

Figure 5.8: **Magnetic field-doping (H-p) phase diagram of $YBa_2Cu_3O_{6+x}$ at $T \to 0$.** H_{c2} indicates the upper critical filed. Other points indicate the onset magnetic field of the field induced 3D-CDW estimated by the ultrasound measurements (red circle), x-ray scattering (black triangle), and NMR (blue square). Figure from Ref. [157].

at T_c persists at the lowest temperature. Therefore it is plausible to conclude that the strain-induced 3D-CDW is more competitive with superconductivity than the 2D-CDW as in the case of $YBa_2Cu_3O_{6.67}$. These three specific differences between two doping levels, i.e., the temperatures at which the strain-induced 3D-CDW sets in, is maximized, and is completely suppressed by superconductivity call for further studies looking for possible trends of strain-induced 3D-CDW, if any, in samples with even lower doping levels, i.e., more underdoped, investigated in the identical setup. Such a measurement are at the time of writing already planned. In this respect, note that ultrasound measurements indicated that 25 T is required to induce the 3D-CDW in the lower doped sample $YBa_2Cu_3O_{6.48}$ despite the weaker superconductivity, whereas 15 T suffices to induce the 3D-CDW in $YBa_2Cu_3O_{6.67}$ [157]. It is thus possible that one may need to apply higher strain to induce the 3D-CDW at lower doping levels. While the temperature dependence of the strain-induced 3D-CDW between the two doping levels in the present study may be slightly different, the temperature range in which the strain-induced 3D-CDW was observed is clearly different from that of the 3D-CDW induced by the strong magnetic field (> 15 T), which was observed only below 50 K in the entire doping region [21, 155]. Therefore, the suppression of superconductivity is not a necessary condition for stabilizing the 3D-CDW at those two doping levels although the strain-induced 3D-CDW does not persist up to higher temperatures such as the pseudogap temperature T^* or room temperature as in the case of the 3D charge order in the thin films [160].

The enhancement of the 2D-CDW by strain was observed in $YBa_2Cu_3O_{6.8}$ as well as $YBa_2Cu_3O_{6.5}$ and $YBa_2Cu_3O_{6.67}$. Such a symmetric response with respect to the 1/8 doping is generally anticipated from the rather symmetric 2D-CDW dome on top of the 1/8 anomaly of the superconducting dome in the phase diagram if the strain directly affects the 2D-CDW. On the other hand, the indication of the strain-induced 3D-CDW was not confirmed in $YBa_2Cu_3O_{6.8}$. So far the magnetic field induced 3D-CDW was reported only in the limited doping range between $YBa_2Cu_3O_{6.5}$ and $YBa_2Cu_3O_{6.67}$ by x-ray scattering [21, 154, 155] and between $YBa_2Cu_3O_{6.45}$ and $YBa_2Cu_3O_{6.67}$ by NMR [235, 246]. The ultrasound measurements indicated the thermodynamic phase transition into the 3D-CDW induced by field also at higher doping[2] levels such as $YBa_2Cu_3O_{6.75}$ and $YBa_2Cu_3O_{6.79}$, which however require larger magnetic fields of 25 and 35 T, respectively (Fig. 5.8) [157]. Therefore, one plausible reason why the strain-induced 3D-CDW was not observed in

[2]Let us clarify that the "higher doping" here always implies the doping region which is higher than the 1/8 doping. It does not necessarily mean the overdoped region.

$YBa_2Cu_3O_{6.8}$ is just because the maximum strain that we achieved is smaller than the onset strain for the 3D-CDW. Such an application of huge stress was recently achieved by F. Jerzembeck *el al.* on Sr_2RuO_4 where the uniaxial stress of -3.2 GPa (which corresponds to the strain of $\sim$ -2 % for $YBa_2Cu_3O_{6+x}$) was obtained using a more sophisticated sample shaping method [247]. Note that even at low temperature, the sample could be plastically deformed (e.g., -2 % at 5 K and -0.2 % at room temperature in Sr_2RuO_4 [174]). The plastic limit which is the nature of any elastic materials restricts the experimentally accessible strain. Therefore as a more realistic and alternative experimental proposal, REXS measurements under simultaneous application of uniaxial strain of -1 % routinely achievable with our current setup and magnetic field which weakens superconductivity could give crucial insights to reveal whether the absence of the strain-induced 3D-CDW is due to the stronger superconductivity or not.

Unlike underdoped samples, essentially no strain effects were observed in the optimally doped sample $YBa_2Cu_3O_{6.93}$. Considering the fact that the 2D-CDW and the strain-induced 3D-CDW always compete with superconductivity, the absence of the strain effects at this doping level can be understood as a result of the strong competition with superconductivity: the superconducting state is more stable than the charge order in general, even at the highest strain level. Such a robustness of superconductivity in the optimally doped sample can be understood from the highest T_c among all the doping levels.

The in-plane crystal anisotropy of $YBa_2Cu_3O_{6+x}$ monotonically increases as a function of the hole doping as shown in Fig. 2.4. In this sense the "built-in" compressive strain along the *a*-axis is stronger in the more highly doped samples before applying the external strain. Nevertheless the 3D-CDW was observed only in $YBa_2Cu_3O_{6.5}$ and $YBa_2Cu_3O_{6.67}$ whose in-plane crystal structure is less anisotropic. It indicates that the built-in anisotropy has a marginal role, if any, for the 3D-CDW formation. Although one may associate the 3D-CDW unidirectionally observed only along the *b*-axis with nematicity, the lack of the 3D-CDW on the higher doping side is in stark contrast to the nematicity which is generally greater in the higher doped compounds in $YBa_2Cu_3O_{6+x}$ [102] and even in other tetragonal cuprates such as $Bi_2Sr_2CaCu_2O_{8+\delta}$ [100, 104]. Unlike a majority of reports on the nematicity from charge sectors, the nematic spin fluctuations have been reported only in the very underdoped samples, namely, $YBa_2Cu_3O_{6.3}$, $YBa_2Cu_3O_{6.35}$, and $YBa_2Cu_3O_{6.45}$ below 150 K [105, 58]. Such a decoupling between the nematicity and charge order was also pointed out by the qualitatively symmetric nematic response of the 2D-CDW to uniaxial compression along both *a*- and *b*-axes and is also evident from the ubiquity of the CDW phenomena observed at much lower temperature than the pseudogap temperature T^* where the nematicity sets in among cuprate families [148, 94, 199, 222, 149]. Although the relationship between the charge and spin sectors is not so trivial, such observations call for future x-ray scattering measurements on $YBa_2Cu_3O_{6.45}$ whose nematicity in the spin sector is the greatest and charge order under the uniaxial stress has not been studied yet.

The electron-phonon coupling (EPC) has been widely considered to be a driving mechanism of the CDW formation in ordinary two-dimensional CDW materials [248, 249, 250] except for one-dimensional CDW materials in which the CDW is well explained solely by the simple Peierls mechanism in terms of the Fermi surface nesting [11]. While a theoretical study has suggested that neither Fermi surface nesting nor EPC can be a simple source for the CDW formation in the case of $Bi_2Sr_2CaCu_2O_{8+\delta}$ [209], the interplay between

the CDW and EPC in the cuprates has been revisited and demonstrated through anomalies in phonon dispersions in a number of recent experiments [16, 153, 251, 252, 253, 254]. Therefore we can speculate that the anisotropic EPC deduced from high-energy phonons [255, 256] can be one of reasons for which the 3D-CDW is stabilized only along the *b*-axis as mentioned above.

5.2.5 Conclusions

In conclusion, taking advantage of the high detection efficiency of REXS measurements, we have investigated the nature of the CDWs at doping levels that were not studied in the previous IXS and RIXS experiments. In $YBa_2Cu_3O_{6.5}$ ($p = 0.105$), the strain-induced 3D-CDW was observed in a similar manner to that of $YBa_2Cu_3O_{6.67}$ ($p = 0.12$) with minor quantitative differences. On the other hand, there was no clear indication of the 3D-CDW even at the highest strain level we could reach in $YBa_2Cu_3O_{6.8}$ ($p = 0.145$) while the 2D-CDW was enhanced. No strain effects on the CDW were observed in the optimally doped sample $YBa_2Cu_3O_{6.93}$ ($p = 0.168$). The fact that the 3D-CDW was not induced in the higher doping regime implies that the superconducting state is a more stable ground state than the CDW even under the high strain condition. To test this interpretation, REXS experiments under larger uniaxial stress or simultaneous application of uniaxial stress and magnetic field could give crucial insights. The lack of the 3D-CDW at the higher doping levels also suggests that the larger built-in strain is not a primary source of the 3D-CDW in $YBa_2Cu_3O_{6.5}$ and $YBa_2Cu_3O_{6.67}$ whose anisotropy is smaller before applying the external strain. This further motivates future experiments on $YBa_2Cu_3O_{6.67}$ under the larger uniaxial compressive stress along the *b*-axis which makes the system less anisotropic or on different cuprate families whose crystal structure is tetragonal such as Hg- or Bi-based ones under uniaxial pressure. We remark that it was recently reported in REXS measurements that the stripe order in $La_{1.475}Nd_{0.4}Sr_{0.125}CuO_4$ was suppressed by small tensile stress around 0.1 GPa [257]. Based on the spectroscopic observations here, thermodynamic investigations such as stress-strain measurements utilizing the stress rigs will make the nature of the strain-induced 3D-CDW clearer.

5.3 RIXS measurements

5.3.1 Introduction

One of the long-standing debates on 2D-CDWs in cuprates regards their spatial character, i.e., uniaxial or biaxial (also termed stripes or checkerboard as seen in Fig. 5.9). Their spatial character is crucial since the translational symmetry breaking due to the CDWs is one of candidates to interpret the Fermi surface reconstruction. This is based on the coincident doping regime where the 2D-CDWs and anomalous transport properties, such as the sign reversal of the Hall coefficient and small electron pockets detected by quantum oscillations, were observed. In $YBa_2Cu_3O_{6+x}$, Comin *et al.* were the first trying to directly answer the question about the spatial character based on the peak shape of the elastic intensity in the reciprocal space obtained by the resonant x-ray scattering [141]. Their findings support a stripe-like uniaxial CDW and this picture was later well established by the differential growth of the 2D-CDWs under uniaxial stress (Fig. 5.10) [142]. In

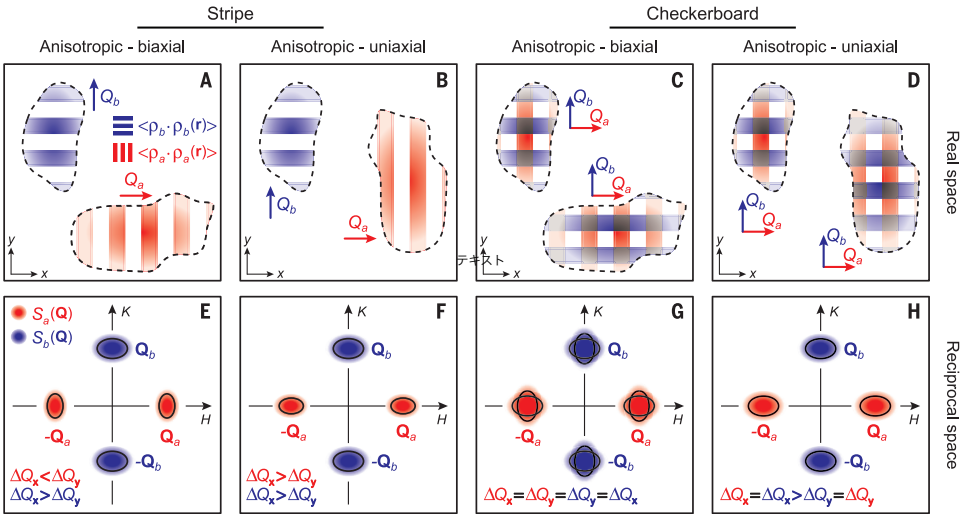

Figure 5.9: **Possible spatial characters of 2D-CDW.** (Top) Schematic electron density modulations in the real space. (Bottom) Peak shapes of the elastic intensities in x-ray scattering experiments in the reciprocal space corresponding to the real space character shown in top panels. Figures from Ref. [141].

diffraction experiments, the intrinsic instability towards uniaxial CDW can result in the observed biaxial, short-ranged 2D-CDW in the presence of quenched defects according to theoretical studies [244]. This defect-pinned 2D-CDW scenario is supported by a number of experimental evidences such as the broad transition, the finite CDW intensity in the zero-temperature limit, and the lack of thermodynamic signatures for a 2D-CDW transition to date. This manifests itself in the observed symmetric response to compressive strain applied either to the *a*- or *b*-axis which alternatively favours the *b*- or *a*-CDW domains, respectively, which are initially pinned by defects. In the non-resonant scattering experiments, it is hard to detect the *a*-CDW because of the CuO chains developing along the *b*-axis and shadowing with their Bragg reflection that of the CDW. Also the capability of rotating the azimuthal angle of the sample in the vacuum chamber is indispensable to study both *a*- or *b*-CDWs in the same experimental conditions. In order to get more insights into the character and strain response of the CDW, we carried out high-resolution Cu-L_3 RIXS measurements on $YBa_2Cu_3O_{6.67}$ under uniaxial pressure at the beamline ID32 at the ESRF to investigate the defect-pinned 2D-CDW scenario by comparing the intensity and correlation lengths of *a*- and *b*-CDW upon cooling with and without applied stress. In Fig. 5.11, the straining and cooling processes and hypothesis expected from the defect-pinned 2D-CDW scenario are summarized. Alongside the main purpose of the measurements, the ring-like signal of dynamical charge fluctuations in the reciprocal space recently observed in other cuprate compounds [258, 242] and the strain effect on the magnetic excitations were also investigated and discussed.

5.3.2 Experimental methods

The $YBa_2Cu_3O_{6.67}$ samples have been prepared as explained in the previous chapters. The oxygen content was controlled by annealing samples at 555 °C in the mixture of 5 %

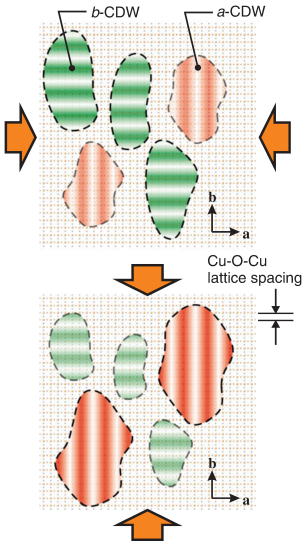

Figure 5.10: **Real-space pictures of 2D-CDW domains in the CuO_2 plane under uniaxial stress.** The CDW perpendicular to the uniaxial stress direction is selectively enhanced, mirroring the stripe nature in the 2D-CDW. Figures from Ref. [142].

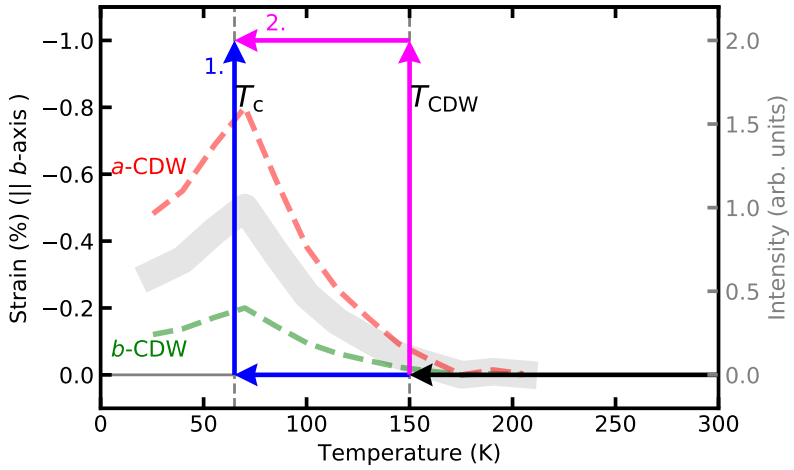

Figure 5.11: **Two cooling processes and hypothesis of the strained cooling effects on 2D-CDWs.** In the previous studies, the process 1. namely, first cooling down to T_c and applying the strain, was used. In the present study, we used the process 2.: applying the strain at T_{CDW} first and cooling down to T_c. We call this process strained cooling. The solid gray curves are typical temperature dependence of the CDW intensity without strain. The red and green dashed curves indicate hypothetical temperature dependence of the *a*- and *b*-CDW upon strained cooling along the *b*-axis. The left and right scale indicate the strain and CDW intensity, respectively. Data (gray curve) are reproduced from Ref. [144].

O_2 and 95 % Ar for one week to obtain this specific doping level [178]. All the samples were detwinned with a standard mechanical method [180]. The samples were shaped for the stress application in the same manner as the transport experiments, yet without the electrical contacts. RIXS measurements were performed on the ERIXS spectrometer at the beamline ID32 at the ESRF [204]. The incident energy was set to be the Cu-L_3 edge, 932 eV. σ-polarization for most of the measurements and the π-polarization for measurements of magnons were used. The polarization of scattered photons was not resolved, therefore both σ- and π-polarized photons were detected. The in-vacuum four-circle diffractometer manipulator of ERIXS enables one to rotate the sample along all three axes. Therefore one can measure both a- and b-CDWs from one sample by rotating the azimuthal angle by 90 degrees without breaking the vacuum, which was not possible in the REXS measurements presented in the previous section. In the previous RIXS experiments under uniaxial stress, the strain was always applied at T_c, where the CDW intensity and correlation length are maximized, indicated as process 1. in Fig. 5.11. On the other hand, in the present study, we followed process 2.: the strain was applied at T_{CDW} and the temperature was cooled down to T_c. We call this process strained cooling. Those two different cooling processes are reminiscent of zero field cooling and field cooling when studying magnetic materials or superconductors. The strain rig without force sensor was used for the RIXS experiments, therefore the strain gauged by the displacement capacitor is used as a measure of the deformation of the samples. The negative values in strain indicate compression.

5.3.3 Results and discussion

We compared intensities of the 2D-CDW peaks along H and K directions as the crystals are cooled down from high ($\sim$ 150 K) to low temperature ($T_c \sim$ 60 K), where the static CDW domains are established, with and without applied uniaxial stress. All the quasielastic data here are the integrated intensity between $\pm$100 meV of the quasielastic energy contribution to the spectra. All the inelastic data are the integrated intensity between -100 and -700 meV in the energy loss. Also all the spectra were normalized by the *dd*-excitation area, which is defined as the area of each RIXS spectrum integrated between -2400 and -1200 meV in the energy loss (see details about *dd*-excitation in chapter 3.5.2).

Strained cooling process

Figure 5.12 shows the quasielastic intensity scans of the 2D-CDWs of $YBa_2Cu_3O_{6.67}$ under the a-axis compression. To show the background of the main intensity of the 2D-CDW, the data at 150 K, where the static 2D-CDWs start to set in, are also displayed. The strain (-1 %) was applied at 150 K, which is the onset temperature of the 2D-CDW, and the temperature was decreased to 60 K (the process 2. in Fig. 5.11). To emphasize the strain effect, the data after releasing the strain at 60 K are also displayed in Fig. 5.12. Upon strained cooling, the b-CDW grows more and the a-CDW is slightly suppressed under a-axis compression applied already at high temperature, compared with the normal cooling case. This feature, the differential growth of the 2D-CDWs upon strained cooling, was even more clearly observed under the b-axis compression as shown in Fig. 5.13. Note that the lineshape of the peaks is not symmetric in Fig. 5.12 (a) and Fig. 5.13 (a). This is likely due to the oxygen ortho-VIII order and the corresponding modulation along the

a-axis generated by the CuO chains developing along the b-axis. One of the peaks is expected to be located at $H = 0.375$ (= 3/8), which is consistent with our observations.

In the previous RIXS study, the stripe character of the 2D-CDWs was concluded based on the differential response of the CDW, where the uniaxial stress enhanced the CDW perpendicular to the stress. The differential growth of the CDWs upon strained cooling in the present study further supports this scenario for the order parameter of the 2D-CDWs since the differential growth of the intensities at (H_{CDW}, 0) and (0, K_{CDW}) cannot be explained by the checkerboard type order parameter. While straining only after cooling down to T_{c} did not affect the CDWs parallel to the strain, as demonstrated in the previous study, in the present case the strained cooling prevented the CDW parallel to the strain from growing. This is particularly evident in Fig. 5.13 (c,d). Phenomenologically one can summarize these observations as follows: the 2D-CDW tends to develop along the direction orthogonal to the external compressive stress upon cooling, but it is hard to suppress the CDW already developed at low temperature by the external uniaxial stress when this is applied only after cooling. Since the oxygen atoms in the CuO chain layers have higher activation energy at T_{CDW} than T_{c}, one may think that the b-axis compression at T_{CDW} made the crystal structure effectively retwinned, i.e., stabilize multi domains of the orthorhombic structure. However the anisotropic scattering intensities at (H_{CDW}, 0) and (0, K_{CDW}) are not expected from the retwinned sample. Also the shoulder peak originating from the O-VIII chain structure apparent only in Fig. 5.12 (a) and Fig. 5.13 (a) allows us to discard the retwinning scenario. Crucially the CDW intensity of intentionally disordered system is reduced by a factor of ~ 2 [259], therefore it is hard to explain the observed differential growth in terms of the disorders in CuO chain layers possibly induced by strain along the direction unfavorable for CuO chains at high temperature. A very recent RIXS study on $YBa_2Cu_3O_{6+x}$ thin films with tensile strain along the b-axis generated by the substrate also shows the differential growth of the a-CDW and b-CDW, qualitatively consistent with our findings [260]. Assuming the tensile stress has at least qualitatively opposite effect to the compressive stress, the suppressed growth of a-CDW under the b-axis tension is in fact consistent with our observation, i.e., the suppressed growth of b-CDW under the b-axis compression. The unidirectional CDW in the thin films has been discussed in the context of nematicity [224]. The differential growth in the present case can be in line with the interpretation for the films.

Search for isotropic ring-like charge orders / fluctuations

Figure 5.14 and 5.15 show H-K reciprocal space maps of the quasielastic and inelastic intensity, respectively. The data were taken by rotating the azimuthal angle of the sample. We have measured those intensities in four different conditions, nevertheless none of the quasielastic intensity maps has shown the peak at $|\boldsymbol{Q}| \sim 0.3$ along the radial direction except for along the H and K axes (Fig. 5.14). In the previous study, quasielastic scans only along the high-symmetry directions, namely, the CuO bond direction and its diagonal direction were investigated in $YBa_2Cu_3O_{6+x}$ and $NdBa_2Cu_3O_{6+x}$ films [261]. It was already pointed out that the diagonal scans were featureless, however a weaker feature along the diagonal direction is generally expected compared to that along the CuO bond direction, even if the circular feature of the charge orders is present as in the case of $Bi_2Sr_2CaCu_2O_{8+\delta}$ [242]. Therefore the detailed azimuthal angle dependent measurements in the present case first seems to demonstrate the absence of the ring-like feature in

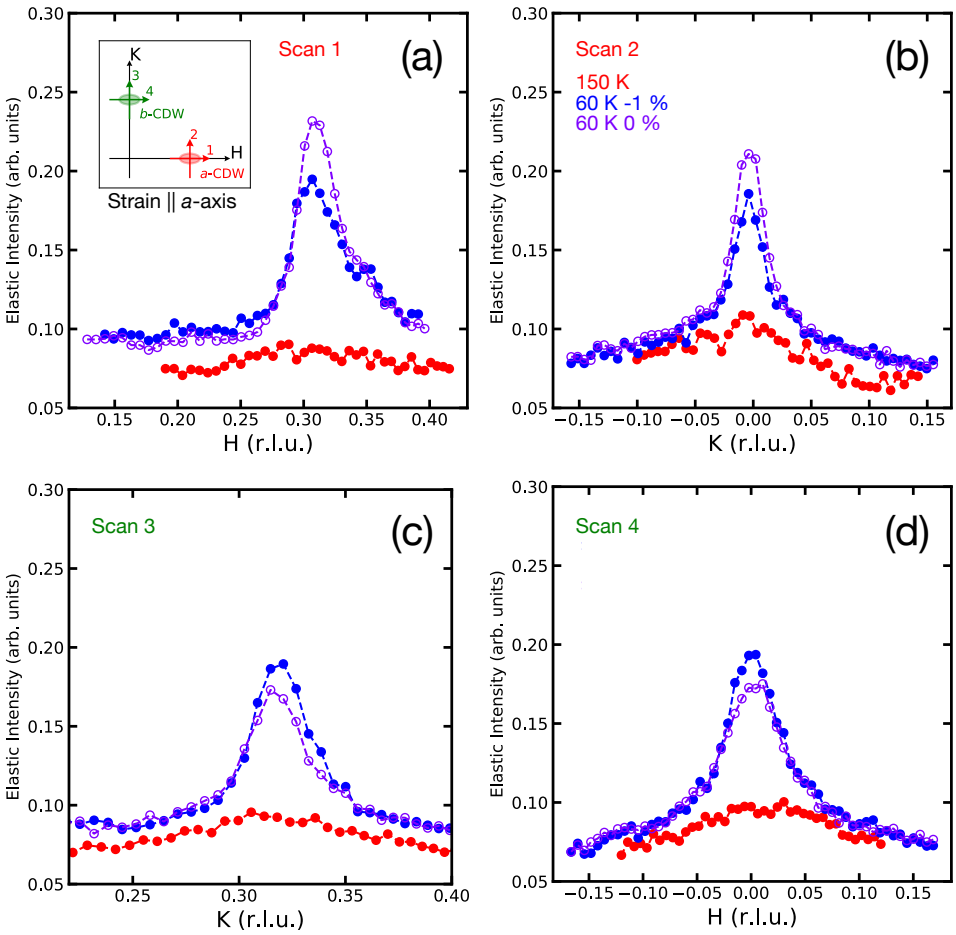

Figure 5.12: **Quasielastic intensity scans of the 2D-CDW of $YBa_2Cu_3O_{6.67}$ under a-axis compression.** The strain (-1 %) was applied at 150 K and the temperature was decreased to 60 K (process 2. in Fig. 5.11). The strain direction is along the a-axis. To indicate the background of the data at low temperature, data of the unstrained material at T_{CDW} (= 150 K) are also shown. Note that the data at 150 K are from a different sample. Inset of (a) shows scans of (a-d) in the reciprocal space.

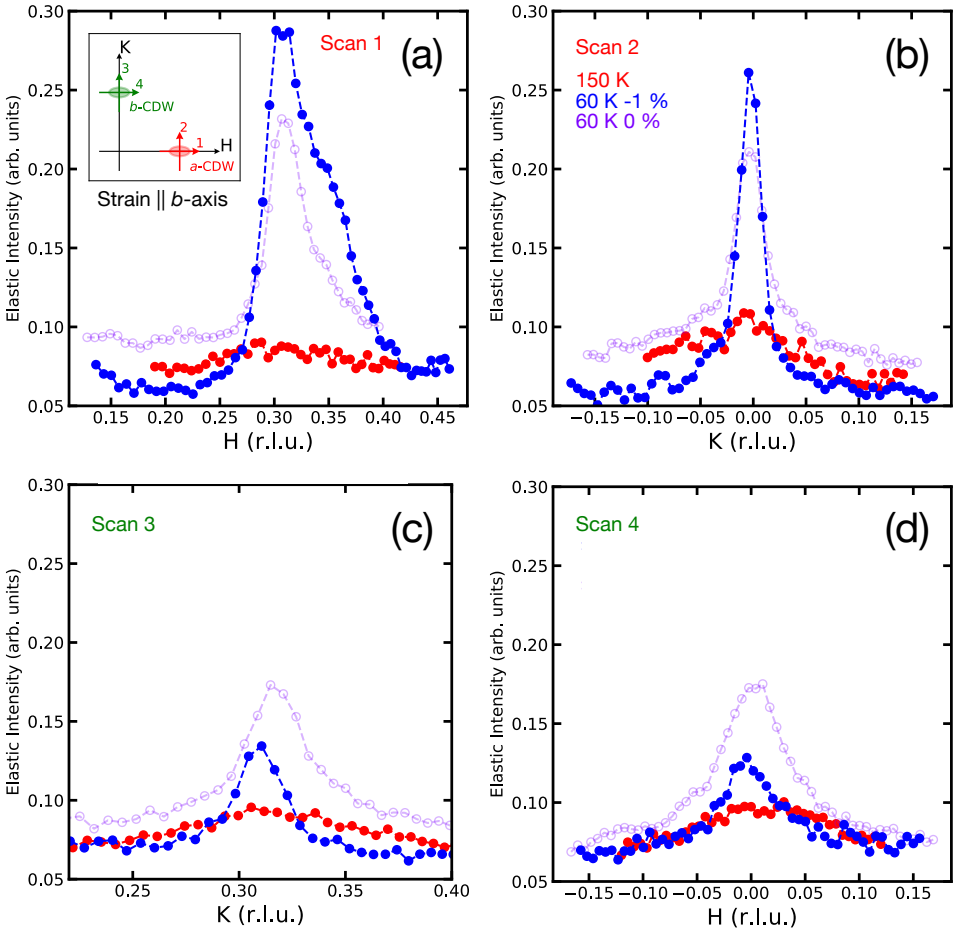

Figure 5.13: **Quasielastic intensity scans of the 2D-CDW of $YBa_2Cu_3O_{6.67}$ under *b*-axis compression.** Same as Fig. 5.12 except for the strain direction, which is along the *b*-axis. Note that the data at 60 K without strain are from Fig. 5.12.

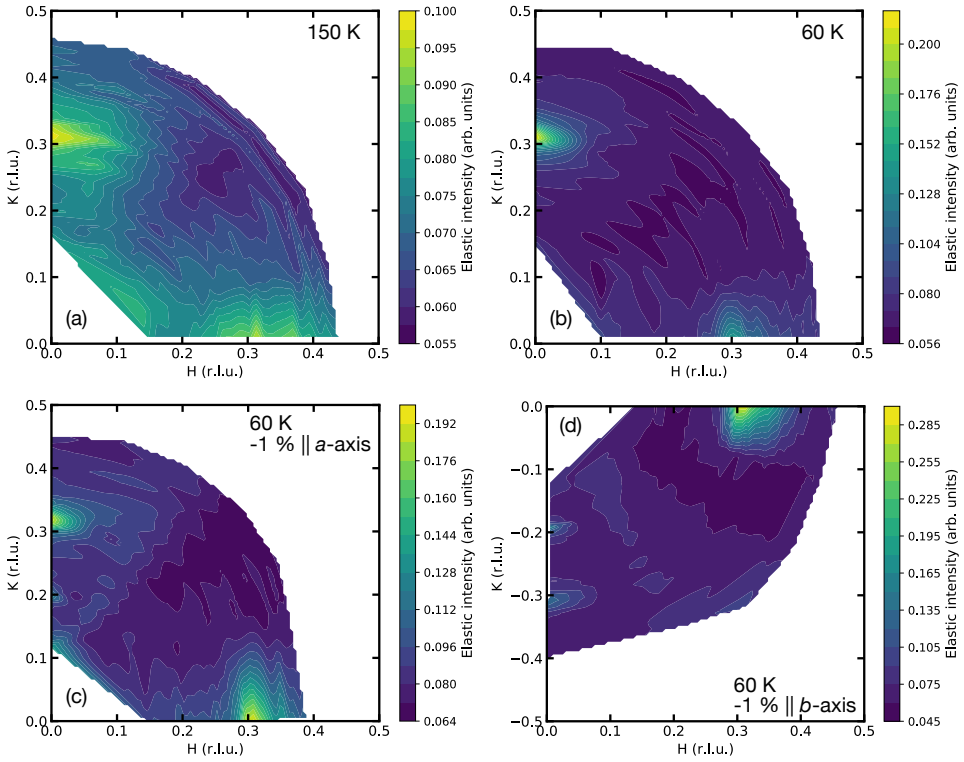

Figure 5.14: ***H*-*K* reciprocal space map of the quasielastic intensity in four different conditions.** (a) $T = 150$ K. (b) $T = 60$ K. (c) $T = 60$ K with -1 % of uniaxial strain along the *a*-axis applied at 150 K. (d) $T = 60$ K with -1 % of uniaxial strain along the *b*-axis applied at 150 K. The energy integration range is between ±100 meV of the quasielastic energy.

$YBa_2Cu_3O_{6+x}$ at quasielastic energies. Specifically at 150 K, at which the contribution from the static CDW is not present in the quasielastic intensity yet the contribution from the charge density fluctuation is still present, the quasielastic intensity does not show a circular character as shown in Fig. 5.14 (a).

On the other hand, the intensity are weakly present at $|\boldsymbol{Q}| \sim 0.3$ along the radial direction in the inelastic intensity maps (Fig. 5.15). The dynamical charge density fluctuation persist towards higher energies in other cuprate families, $Bi_2Sr_2CaCu_2O_{8+\delta}$ (500 - 900 meV) [242] and $La_{2-x}Ba_xCuO_4$ (200 - 350 meV) [239]. Therefore it is possible that these dynamical charge fluctuations appear in the similar energy range (100 - 700 meV, in the present case). Further careful studies are necessary to reveal more precise dispersive features of the dynamical features observed in the inelastic intensity in $YBa_2Cu_3O_{6+x}$, including possible circular ones, by future RIXS experiments with significantly better energy resolution.

No clear effect of uniaxial stress on paramagnons

We have also investigated the strain effects on the low energy excitations. This has been already systematically discussed in the previous RIXS study under uniaxial stress [142], yet

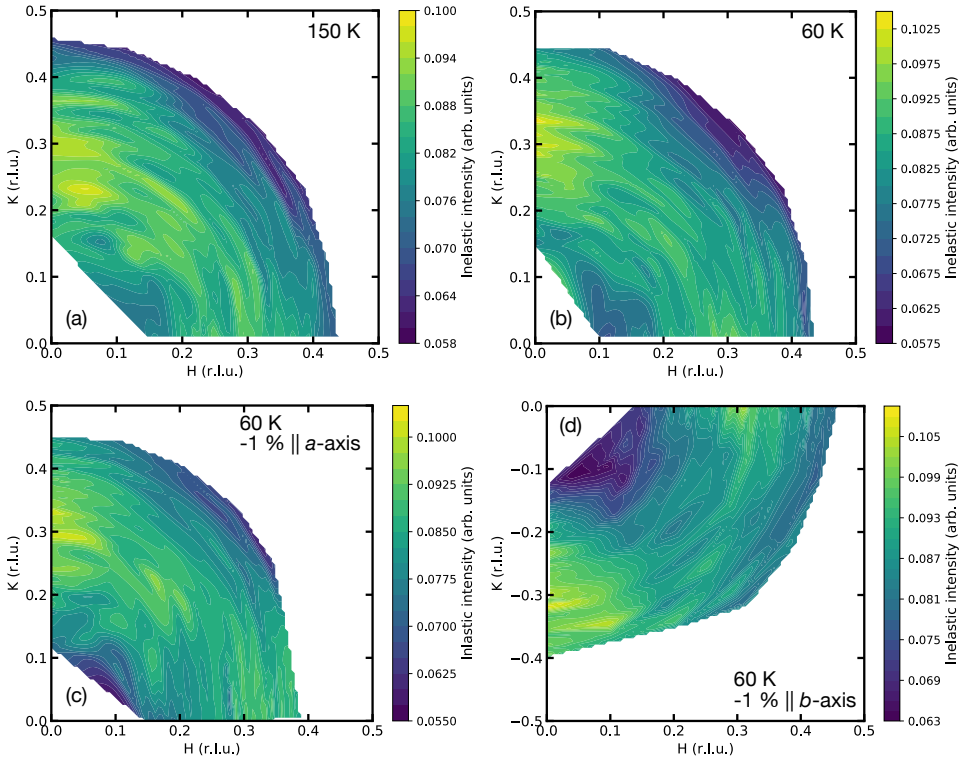

Figure 5.15: H-K **reciprocal space map of the inelastic intensity in four different conditions.** (a-d) The same conditions as those in panels (a-d) of Fig. 5.14. The energy integration range is between -100 and -700 meV in the energy loss.

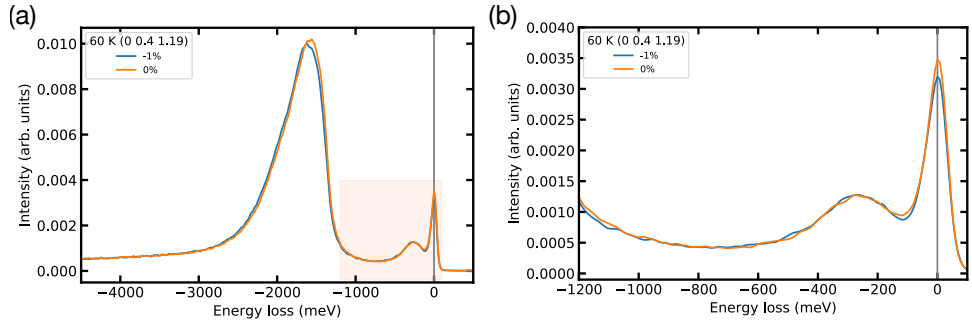

Figure 5.16: **RIXS spectra taken at 60 K at (0 0.4 1.19) with and without uniaxial stress.** The strain was applied along the a-axis. To access the magnetic excitation, the π scattering geometry was used for this measurement. The spectra are shown in a wide energy range (a) and narrow energy range (b).

the strained data were taken mostly with the σ scattering geometry where the contribution from magnetic excitations is minimized. Here, therefore, the π scattering geometry, known to enhance the magnetic scattering signal, was used for this measurement unlike those in Fig. 5.12, Fig. 5.13, and Fig. 5.14 to potentially discuss the magnetic excitations too. Figure 5.16 shows the RIXS spectra at (0, 0.4, 1.19) where the CDW is not affecting the spectra. The strain (-1 %) along the a-axis is applied at 150 K and the spectra were obtained at 60 K. The data without strain was taken after releasing the strain at 60 K. As in the case of the σ polarization [142], there is no appreciable strain effect on the dynamical part of the RIXS spectra.

The magnetostriction effect, i.e., distortions of the crystal structure by a magnetic field which flips the spin orientation of the antiferromagnetic order, is known in the parent compound of $YBa_2Cu_3O_{6+x}$ [262]. Therefore, as a future perspective, it can be interesting to measure the RIXS spectra by applying compressive stress along the b-axis, which makes the crystal structure more tetragonal and may therefore affect the spin orientation of the antiferromagnetic order, although the magnetic long range order no longer develops in the doping regions we have studied.

5.3.4 Conclusions

In conclusion, we have obtained three main findings from the RIXS experiments on $YBa_2Cu_3O_{6.67}$ under uniaxial stress. i) The application of stress before cooling favours the formation of CDW domains perpendicular to the applied stress and conversely suppresses the domains parallel to it. ii) The ring-like charge density fluctuations were not clearly observed at very low energy but possibly exists at higher energy in the first systematic azimuthal angle dependent RIXS measurement. Further measurements with significantly better energy resolution are necessary to investigate low energy dynamical charge fluctuations. iii) No noticeable strain effect on the magnetic excitations ($\sim$ 200 meV) was observed in the present study.

5.4 Conclusions

In this chapter, we have presented the microscopic properties of $YBa_2Cu_3O_{6+x}$ under uniaxial stress, while the macroscopic properties were investigated in the previous chapter.

In the first part, the doping dependence of the CDWs under the uniaxial stress was studied performing REXS measurements in the doping regime that was not investigated previously with energy resolved experiments, namely, IXS and RIXS. While the strain-induced 3D-CDW was observed in the sample with doping lower than 1/8, no indication of the 3D-CDW was confirmed in the more highly doped samples. The 2D-CDW was enhanced in both higher and lower doping regimes, yet no strain effect was observed in the optimally doped sample. Overall the strain responses of the CDWs can be understood in terms of the strong competition between the CDWs and superconductivity. As a next step, the simultaneous application of magnetic field and uniaxial stress will provide additional insights regarding the competition of those phases.

In the second part, a RIXS study with a new cooling method was presented. As one often compares field cooling and zero field cooling for studying magnetic materials, we first carried out the strained cooling process. The suppressed growth of the 2D-CDW parallel to the stress direction was observed, while the 2D-CDW perpendicular to the stress grows more rapidly upon cooling similarly to the case of normal cooling and straining at low temperature. As recently revisited in other cuprate compounds, the in-plane reciprocal space character of the 2D-CDW was also carefully investigated. The absence of ring-like quasielastic intensity implies that the static 2D-CDW in $YBa_2Cu_3O_{6.67}$ is pinned along the crystallographic axes. However the ring-like charge fluctuations possibly exist at higher energy. The dynamical part was also carefully studied yet the strain effect on the magnetic excitations was not as strong as the one on the static CDWs.

Chapter 6

Conclusions and outlook

The work presented in this thesis demonstrated the power of uniaxial-stress experiments in the long-standing quest to establish correspondences between atomic-scale correlations and macroscopic transport in high-T_c cuprate superconductors.

In chapter 4, we presented measurements of the stress dependence of the normal-state resistivity and Hall coefficient of $YBa_2Cu_3O_{6.67}$. We found remarkable parallels in the stress responses of the transport coefficients and the diffraction signal from static charge-ordering. This correspondence allows us to conclude that the condensation of collective charge fluctuations reduces the resistivity, similar to classical CDW materials with quasi-two-dimensional electron systems. However, we also conclude that the impact of static charge order is too weak to explain the sign reversal of the Hall coefficient. We argue that in $YBa_2Cu_3O_{6.67}$, liquid-like collective fluctuations of the electron system take on the role of static order in the classical CDW compounds, and we point out the need to develop a theoretical framework to describe the underlying mechanisms.

In chapter 5, we have presented resonant soft x-ray scattering measurements of $YBa_2Cu_3O_{6+x}$ under uniaxial stress. In the first part, the doping dependence of the CDWs under uniaxial stress was studied performing REXS measurements at doping levels not previously investigated. While the strain induced 3D-CDW was observed in the samples with doping lower than 1/8, no indication of the 3D-CDW was confirmed in the more highly doped samples. The 2D-CDW was enhanced in both higher and lower doping regimes, yet no strain effect was observed in the optimally doped sample. Overall the strain responses of the CDWs can be understood in terms of the strong competition between the CDWs and superconductivity. In the second part, a RIXS study with a new cooling method, strained cooling, was presented. The suppressed growth of the 2D-CDW with modulation parallel to the stress direction was observed, whereas the 2D-CDW perpendicular to the stress grows more rapidly upon cooling, similarly to the case of normal cooling and straining at low temperature. As recently revisited in other cuprate compounds, the in-plane reciprocal space character of the 2D-CDW was also carefully investigated. The absence of ring-like quasielastic intensity is consistent with the notion that the 2D-CDW in $YBa_2Cu_3O_{6.67}$ is pinned along the crystallographic axes. However ring-like charge fluctuations possibly exist at higher energy. The dynamical part was also carefully studied yet the strain effect on the magnetic excitations is negligible in stark contrast with the marked effect on the static CDWs.

As in the case of the initial discovery of the CDW in $YBa_2Cu_3O_{6+x}$ [14], the uniaxial stress effect on CDWs first became evident in the x-ray scattering experiments at synchrotron facilities [18]. Motivated by the previous work, I have started studying macroscopic charge transport under uniaxial stress at in-house laboratories for this thesis. Actually, the uniaxial stress devices based on piezoelectric stacks used in this thesis were first employed in laboratory-based T_c measurements of Sr_2RuO_4 [173]. After this experiment, facility-based microscopic measurements such as ARPES [263] and μSR [264] were carried out to reveal the nature of the strain-induced Lifshitz transition. The bridge established by the uniaxial stress method between macroscopic and microscopic experiments from a theoretical point of view, and between laboratory-based and facility-based experiments from a technical point of view, will stimulate future research on quantum materials.

By carrying out the experiments presented in this thesis, I found that the sample preparation for the transport experiments requires much more careful steps than that for the x-ray scattering measurements. On the other hand, one has more opportunities to test immature ideas in laboratory-based experiments while the experiments at synchrotron facilities tend to be more strategic and less serendipitous because of limited beamtimes. In this respect, I find that laboratory-based spectroscopy techniques, such as Raman scattering, can provide several insights. On top of the efficiency of experiments, the uniaxial stress directly deforms the lattice of a sample, therefore measurements of phonons which are sensitive to the point group symmetries of the crystal lattice are potentially interesting subjects for any kinds of crystals in principle. Magnetic excitations have been dominantly studied by inelastic neutron scattering, which requires a big amount of materials and thereby is not suitable for strain applications. Thanks to the resonant nature of RIXS, magnetic excitations in tiny crystals and a few unit cell thick films can be routinely measured these days. Recent developments of RIXS with the incident photon energy at the L-edge of $4d$ transition metal elements will expand the range of material that can be studied under strain. For instance, one could aim for the direct comparison between RIXS data under strain and a number of previous experimental results and theoretical proposals on Sr_2RuO_4.

The uniaxial stress techniques should not be dedicated only to cuprates and ruthenates. There are a number of materials to be studied under uniaxial stress. In Fe-based superconductors, nematicity, the spontaneous rotational symmetry breaking, has been widely discussed [265]. At the early stage, nematic susceptibilities were studied only by small strain. A larger strain was applied to FeSe only in a recent study [266] and this could extend the knowledge about the nematicity in other Fe-based superconductors as well. Superconducting order parameters in a certain class of materials, namely doped topological insulators, are known to be nematic [267]. Researchers tried to align the domain structure of the nematic superconducting order parameter by uniaxial stress [268]. Such a real space domain control is one fresh way to utilize the uniaxial stress. Superconductivity in nickelates has been realized only in thin films to date [269]. Single crystals were synthesized only recently and strain experiments may reveal what plays a key role for superconductivity in nickelates, e.g., the strain effects and the interface effects by substrates [270]. A Kitaev spin liquid system has been reported only in the presence of an external magnetic field [271] even in the leading candidate material α-$RuCl_3$ [272]. It has been widely considered that the spin-orbit interaction is a key, thus $4d$ and $5d$ compounds

have been mainly discussed as solid-state candidates. Recently one $3d$ compound was theoretically proposed as a new candidate under a crystal field distorted by external strain [273] and, thus, experimental verifications are expected. Of course, applying the strain technique to other cuprate families is also desirable. In this thesis, we have particularly focused on the charge ordering phenomena in the cuprates, but the uniaxial stress can also be utilized to reveal other issues in cuprates such as the pseudogap, strange metallicity, quantum criticality, etc...

Overall we have just started working on a limited number of experimental studies with the uniaxial stress technique and still have a number of potential subjects for many other materials and experimental probes. On the one hand, extending this approach to other collective phenomena will open up new perspectives for quantum materials research, on the other hand this methodology may shed light on controversial issues in a variety of quantum materials as it has been demonstrated in Sr_2RuO_4 where a twenty years old result was overturned [171]. I hope that the work presented in this thesis will be useful for those who would like to study the nature of cuprates and other quantum materials and plan to dig deeper into these subjects.

Appendices

Appendix

A

Tight-binding model calculation

We calculated the strain dependence of the resistivity with a semiclassical approach for the tight-binding model to demonstrate the geometric effects on the electron hopping parameters. Under the relaxation time approximation in a range of the linear response from the Boltzmann equation, the current along the i-direction j_i is given under the electric field along the j-direction E_j $(i, j = x, y, z)$,

$$j_i = -\sum_{\boldsymbol{k},\sigma} e^2 v_{\boldsymbol{k},i} v_{\boldsymbol{k},j} \tau_{\boldsymbol{k}} \left(\frac{\mathrm{d}f(\varepsilon(\boldsymbol{k}))}{\mathrm{d}\varepsilon(\boldsymbol{k})} \right) E_j, \tag{A.1}$$

where e is an elementary charge, $\tau_{\boldsymbol{k}}$ is the relaxation time, $f(\varepsilon(\boldsymbol{k}))$ is the Fermi-Dirac distribution function, $\varepsilon(\boldsymbol{k})$ is the energy dispersion of quasiparticles, and $\boldsymbol{v}_{\boldsymbol{k}}$ is the group velocity of the quasiparticles defined as

$$v_{\boldsymbol{k},i} = \frac{1}{\hbar} \frac{\partial \varepsilon(\boldsymbol{k})}{\partial k_i}. \tag{A.2}$$

In our experiments the longitudinal conductivity σ_{xx} which reads

$$\sigma_{xx} = \sum_{\boldsymbol{k},\sigma} e^2 v_{\boldsymbol{k},x}^2 \tau_{\boldsymbol{k}} \frac{1}{|\nabla_{\boldsymbol{k}} \varepsilon(\boldsymbol{k})|} \delta(\boldsymbol{k} - \boldsymbol{k}_{\mathrm{F}}). \tag{A.3}$$

Here we assumed $\mathrm{d}f(\varepsilon(\boldsymbol{k}))/\mathrm{d}\varepsilon(\boldsymbol{k}) = -\delta(\varepsilon(\boldsymbol{k}) - \mu)$ because the temperature in our experiments is much lower then the Fermi energy. To carry out the calculation further from the general formula to apply the real system, one needs information of the electronic structure $\varepsilon(\boldsymbol{k})$ and the scattering rate $1/\tau_{\boldsymbol{k}}$ of the material. The latter really depends on the microscopic origin of the scattering process [274, 275], let us assume it does not depend on $\boldsymbol{k}$, and to have isotropic scattering, as the simplest approximation. As for the electronic structure, we use the tight-binding model whose Hamiltonian is

$$H = \sum_{i,j,\sigma} t_{i,j} c_{i,\sigma}^{\dagger} c_{j,\sigma}, \tag{A.4}$$

which describes phenomenologically well the quasiparticle band dispersion near the Fermi level of cuprates [276]. Considering up to the second nearest neighbor hopping, the energy eigenvalue in a case of a orthorhombic lattice is given as follows:

$$\varepsilon(k_x, k_y) = \mu - 2t(\cos(k_x a) + \cos(k_y b)) - 4t' \cos(k_x a) \cos(k_y b), \tag{A.5}$$

where a and b, μ, t, and t' are the in-plane lattice parameters, the chemical potential, the nearest, and second nearest hopping integral, respectively. $t = 0.38$ eV and $t'/t = -0.32$ are used in the simulation [276]. Strictly speaking, in $YBa_2Cu_3O_{6.67}$ which is a bilayer system, the band dispersion splits into the anti-bonding and bonding bands due to the interlayer hopping between two CuO_2 planes. However we used only the single band here instead of those two bands for simplicity. Following prior work in Ref. [230], we model the strain effect in the lattice parameters and the hopping integrals as follows:

$$\begin{aligned} &a(\varepsilon_{xx}) = a(1+\varepsilon_{xx}), \quad b(\varepsilon_{xx}) = b(1-\nu_{xy}\varepsilon_{xx}) \\ &t_x(\varepsilon_{xx}) = t(1-\alpha\varepsilon_{xx}), \quad t_y(\varepsilon_{xx}) = t(1+\nu_{xy}\alpha\varepsilon_{xx}) \\ &t'(\varepsilon_{xx}) = t'(1+(1-\nu_{xy})\alpha\varepsilon_{xx}/2) \end{aligned}$$

where ν_{xy} is the Poisson's ratio and α is a parameter that scales the strain effect in the hopping integrals: $\alpha = 7$ was chosen here because the relationship of the Slater-Koster parameter $(pd\mu)$ and the distance between the p and d orbitals d is known as $(pd\mu) \propto d^{-3.5}$ [277]. Thus the group velocity of the quasiparticles along the x direction is given by

$$v_{\boldsymbol{k},x} = \frac{a(1+\varepsilon_{xx})}{\hbar}(2t(1-\alpha\varepsilon_{xx})\sin(k_x a) + 4t'(1+(1-\nu_{xy})\alpha\varepsilon_{xx}/2)\sin(k_x a)\cos(k_y b)). \tag{A.6}$$

Using Eq. (A.3, A.6) , the strain dependence of the electronic structure and the conductivity is estimated up to $\varepsilon_{xx} = -1.5\%$ as shown in Fig. A.1 (a). To compare with the experimental results, the change in the resistivity $\rho_{xx} = 1/\sigma_{xx}$ is plotted instead of the conductivity. In this framework, we find that the resistivity decreases monotonically as a function of compressive strain. It is consistent with an intuition that electrons gain additional kinetic energy along the compressive strain which enhances the overlap of electron wavefunctions between the nearest-neighbor sites. However, in reality, one has to consider also the Coulomb interaction and in fact our simulation based on the tight-binding model does not reproduce our experimental data at relatively high temperature ($T > 100$ K). The Coulomb potential enhanced by the compression can inhibit the hopping of electrons. Therefore the potential energy term could significantly contribute to the resistivity such that it increases as a function of compressive strain. Therefore we expect that a numerical analysis on the transport properties based on the Hubbard model under uniaxial strain would provide closer agreement to our experimental results than our tight-binding model. The disagreement between the experiments and our simple simulation here suggests the importance of many-body correlations already at relatively higher temperature. In addition, as noted we neglected the anisotropy of the scattering rate for simplicity. That also may differentiate the simulation from our experimental results although it is not trivial how we should assume the form of the scattering rate of the underdoped cuprates particularly because of the pseudogap while the knowledge regarding optimally and overdoped cuprates has been accumulated [274, 275]. Thus it is less intuitive to expect what can be improved by adding the anisotropy of the scattering rate[1].

[1]The analysis here with the Boltzmann equation is, as noted, semiclassical so that one may need to consider the Kubo-formula even in the framework of the linear response theory to fully take into account quantum mechanical effects. In addition, it is also not trivial how to take into account the effects of the CDW and reconstructed Fermi surface at relatively low temperature. This has been recently attempted to explain magnetoresistivity in Ref. [278].

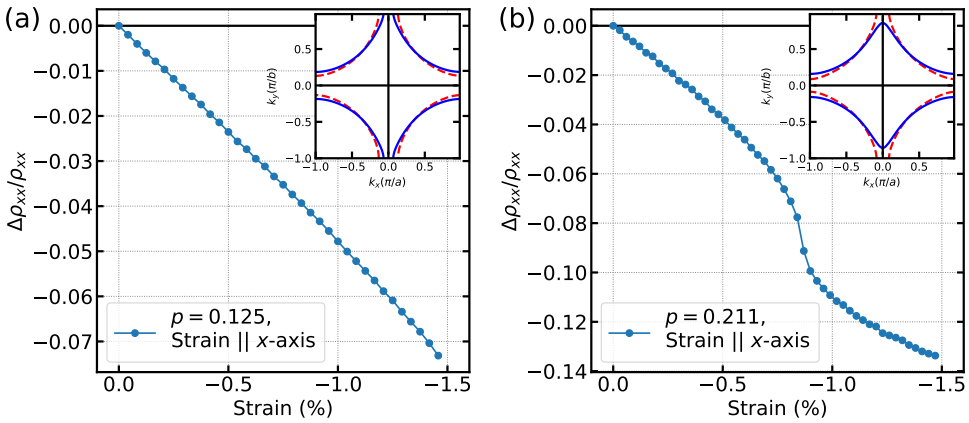

Figure A.1: **Strain dependence of the longitudinal resistivity estimated within the Boltzmann equation framework.** The strain $\varepsilon_{xx}||$ the a-axis. When the summation over the entire Fermi surface is performed, the contribution from the Fermi energy (E_{F}) - 1 meV to E_{F} + 1 meV is integrated. The hole doping was estimated to be 12.5 % (a) and 21.1 % (b) based on the unstrained Fermi surface area through Luttinger's theorem. Inset shows the Fermi surface derived from the tight-binding model on the orthogonal lattice. The dotted red and solid blue curves indicate the Fermi surface which is unstrained and strained by 1.5 %, respectively.

We simulated the same quantity for a different doping level of 21.1 %. The steep change in the strain-dependent resistivity at a certain strain level was found (Fig. A.1 (b)). It is likely because of the Lifsitz transition, i.e., the Fermi surface topology changed by the external strain. Therefore, the resistivity experiments under uniaxial stress in the overdoped regime can be an interesting subject to be studied.

Appendix

B Integrated peak intensity of charge orders

Here we explain how we estimated the integrated peak intensity of 2D-CDW shown in the inset of Fig. 4.13 (b) of the main text. We refer to CDW domains with charge modulation directions along the a- and b-axis as a-CDW and b-CDW, respectively. Likewise, the strain along the i-axis is termed i-strain ($i = a, b$). The integrated peak intensity of j-CDW domain under i-strain $I_{j-\mathrm{CDW}}(\varepsilon_i)$ ($i, j = a, b$) is defined as

$$I_{j-\mathrm{CDW}}(\varepsilon_i) = (I_{j,H}(\varepsilon_i) + I_{j,K}(\varepsilon_i))/2, \tag{B.1}$$

where $I_{j,X}(\varepsilon_i)$ ($X = H, K$) is the integrated peak intensity of the j-CDW estimated from the quasielastic intensity in the scan along the X direction for each i-strain level ε_i (Fig. B.1). Note that only unstrained data are available for a-CDW under a-strain in the scan along the (H_{CDW}, K) (Fig. B.1 (b)) and b-CDW under b-strain in the scan along the (H, K_{CDW}) (Fig. B.1 (g)) due to the technical limitations of the RIXS experiments. However the i-CDW is not affected by the i-strain (Fig. B.1 (a,h)), therefore we use those unstrained data to estimate $I_{i-\mathrm{CDW}}(\varepsilon_i)$ as follows,

$$I_{a-\mathrm{CDW}}(\varepsilon_a) = (I_{a,H}(\varepsilon_a) + I_{a,K}(0))/2, \tag{B.2}$$
$$I_{b-\mathrm{CDW}}(\varepsilon_b) = (I_{b,H}(0) + I_{a,K}(\varepsilon_b))/2. \tag{B.3}$$

$I_{j-\mathrm{CDW}}(\varepsilon_i)$ is summarized in Fig. B.2 (a). Since the unstrained intensity of a-CDW in a particular sample under b-strain (Fig. B.1 (e,f)) is stronger than that of another sample under a-strain (Fig. B.1 (a,b)), the normalized integrated peak intensity ($I_{j-\mathrm{CDW}}(\varepsilon_i)/I_{j-\mathrm{CDW}}(0)$) is shown in Fig. B.2 (b) to extract the relative strain effects on the CDW. We assume that the transport properties are affected by both a- and b-CDWs, therefore the total integrated peak intensity $I_{\mathrm{tot}}(\varepsilon_i)$ is plotted in Fig. B.2 (c).

$$I_{\mathrm{tot}}(\varepsilon_i) = \frac{1}{2}\left(\frac{I_{a-\mathrm{CDW}}(\varepsilon_i)}{I_{a-\mathrm{CDW}}(0)} + \frac{I_{b-\mathrm{CDW}}(\varepsilon_i)}{I_{b-\mathrm{CDW}}(0)}\right). \tag{B.4}$$

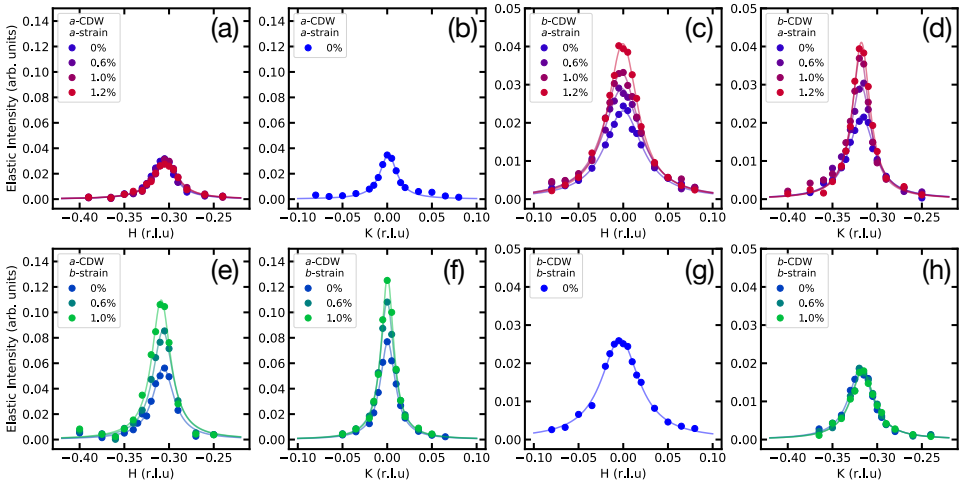

Figure B.1: **Quasielastic intensity measured at 55 K in RIXS experiments.** Solid curves are the Lorentzian fits. (a,b) a-CDW under the a-strain along the H- and K-directions, respectively. (c,d) b-CDW under the a-strain along the H- and K-directions, respectively. (e,f) a-CDW under the b-strain along the H- and K-directions, respectively. (g,h) b-CDW under the a-strain along the H- and K-directions, respectively. Note that quasielastic signals under uniaxial pressure were not measured in configurations of (b) and (g) due to technical limitations of RIXS experiments. Data are reproduced from Ref. [142].

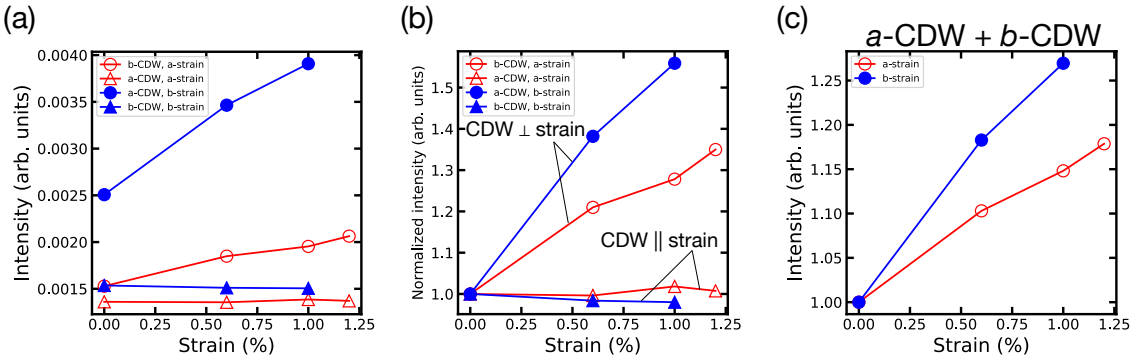

Figure B.2: **Strain dependence of the integrated peak intensity of the 2D-CDW.** (a) $I_{j-\mathrm{CDW}}(\varepsilon_i)$ for $i, j = a, b$. (b) $I_{j-\mathrm{CDW}}(\varepsilon_i)/I_{j-\mathrm{CDW}}(0)$ for $i, j = a, b$. (c) $I_{\mathrm{tot}}(\varepsilon_i)$ defined in Eq. B.4 for $i = a, b$. This figure is identical to the inset of Fig. 4.13 (b) in the main text whose horizontal axis is converted into stress.

Appendix C

Elastoresistivity tensor

The effect of uniaxial stress was little as shown Fig. 4.14. Therefore one may think that the change of R_{H} by uniaxial stress is forbidden by the symmetry of the system. However it is allowed in terms of the symmetry as we show in the following way. To discuss such a property of the symmetry it is convenient to define so-called elastoresistivity tensor, that is a physical response function between the relative change of resistivity and strain. As described in Ref. [279], the elastoresistivity tensor is defined as

$$m_{ij,kl} = \left.\frac{\partial(\Delta\rho/\rho)_{ij}(\boldsymbol{H})}{\partial\varepsilon_{kl}}\right|_{\varepsilon=0}, \tag{C.1}$$

where

$$(\Delta\rho/\rho)_{ij}(\boldsymbol{H}) = \begin{pmatrix} (\Delta\rho/\rho)_{xx}(\boldsymbol{H}) \\ (\Delta\rho/\rho)_{yy}(\boldsymbol{H}) \\ (\Delta\rho/\rho)_{zz}(\boldsymbol{H}) \\ (\Delta\rho/\rho)_{yz}(\boldsymbol{H}) \\ (\Delta\rho/\rho)_{zy}(\boldsymbol{H}) \\ (\Delta\rho/\rho)_{zx}(\boldsymbol{H}) \\ (\Delta\rho/\rho)_{xz}(\boldsymbol{H}) \\ (\Delta\rho/\rho)_{xy}(\boldsymbol{H}) \\ (\Delta\rho/\rho)_{yx}(\boldsymbol{H}) \end{pmatrix} \text{ and } \varepsilon_{ij} = \begin{pmatrix} \varepsilon_{xx} \\ \varepsilon_{yy} \\ \varepsilon_{zz} \\ \varepsilon_{yz} \\ \varepsilon_{zy} \\ \varepsilon_{zx} \\ \varepsilon_{xz} \\ \varepsilon_{xy} \\ \varepsilon_{yx} \end{pmatrix}. \tag{C.2}$$

$(\Delta\rho/\rho)_{ij}(\boldsymbol{H})$ and ε_{ij} are the relative change in the resistivity under the fixed magnetic field $\boldsymbol{H}$ and strain, respectively. It is assumed that the magnetic field is applied along the c-axis. By definition, the tensor in this representation has 81 components but some of components are not independent because physical response functions such as the elastoresistivity tensor must be invariant under the symmetry operations of the system, the crystal point group symmetry and the Onsager relationship in the present case. In the same manner where the elastoresistivity tensor for the D_{4h} symmetry was derived [279], one can derive it for the D_{2h} symmetry which is the crystal point group symmetry of $YBa_2Cu_3O_{6.67}$ as follows.

$$m_{ij,kl}^{D_{2h}} =$$

$$\begin{pmatrix}
m_{xx,xx} & m_{xx,yy} & m_{xx,zz} & 0 & 0 & 0 & 0 & 0 & 0 \\
m_{yy,xx} & m_{yy,yy} & m_{yy,zz} & 0 & 0 & 0 & 0 & 0 & 0 \\
m_{zz,xx} & m_{zz,yy} & m_{zz,zz} & 0 & 0 & 0 & 0 & 0 & 0 \\
0 & 0 & 0 & m_{yz,yz} & m_{yz,yz} & m_{yz,zx} & m_{yz,zx} & 0 & 0 \\
0 & 0 & 0 & m_{yz,yz} & m_{yz,yz} & -m_{yz,zx} & -m_{yz,zx} & 0 & 0 \\
0 & 0 & 0 & m_{zx,yz} & m_{zx,yz} & m_{zx,zx} & m_{zx,zx} & 0 & 0 \\
0 & 0 & 0 & -m_{zx,yz} & -m_{zx,yz} & m_{zx,zx} & m_{zx,zx} & 0 & 0 \\
m_{xy,xx} & m_{xy,yy} & m_{xy,zz} & 0 & 0 & 0 & 0 & m_{xy,xy} & m_{xy,xy} \\
-m_{xy,xx} & -m_{xy,yy} & -m_{xy,zz} & 0 & 0 & 0 & 0 & m_{xy,xy} & m_{xy,xy}
\end{pmatrix}. \tag{C.3}$$

As can be seen, some of components in the tensor must be zero due to the symmetry constraints and the number of independent components is 14 in this case. Since the uniaxial stress $\sigma^\top = (\sigma_{xx}, 0, 0, 0, 0, 0, 0, 0, 0)^\top$ was applied in our experiments, the corresponding strain is $\varepsilon^\top = (\varepsilon_{xx}, \varepsilon_{yy}, \varepsilon_{zz}, 0, 0, 0, 0, 0, 0)^\top$. (Poisson's effect explained in chapter 3.2.2). It is thus allowed that the Hall resistivity $\rho_{xy}(\boldsymbol{H})$ changes under uniaxial stress in our experimental configuration because $m_{xy,xx}$, $m_{xy,yy}$, and $m_{xy,zz}$ can be finite according to this symmetry analysis. Likewise, the longitudinal resistivity $\rho_{xx}(\boldsymbol{H})$ can also be changed by the uniaxial stress.

Bibliography

[1] Philip W. Anderson, *Nature Physics* **11**, 93 (2015). ..... on page 1.

[2] B. Keimer and J. E. Moore, *Nat. Phys.* **13**, 1045 (2017). ..... on pages 1, 63.

[3] D. N. Basov, R. D. Averitt, and D. Hsieh, *Nature Materials* **16**, 1077 (2017). .. on page 1.

[4] K. Yamada, *Electron Correlation in Metals* (Cambridge University Press, 2004). on pages 2, 28, 28.

[5] J. M. Luttinger, *Phys. Rev.* **119**, 1153 (1960). ..... on page 3.

[6] Richard D. Mattuck, *A Guide to Feynman Diagrams in the Many-Body Problem: Second Edition* (Dover Publications, 1992). ..... on page 3.

[7] Liesbeth Venema, Bart Verberck, Iulia Georgescu, Giacomo Prando, Elsa Couderc, Silvia Milana, Maria Maragkou, Lina Persechini, Giulia Pacchioni, and Luke Fleet, *Nature Physics* **12**, 1085 (2016). ..... on page 3.

[8] Sean Vig, Anshul Kogar, Matteo Mitrano, Ali A. Husain, Vivek Mishra, Melinda S. Rak, Luc Venema, Peter D. Johnson, Genda D. Gu, Eduardo Fradkin, Michael R. Norman, and Peter Abbamonte, *SciPost Phys.* **3**, 026 (2017). ..... on pages 3, 55.

[9] Elbio Dagotto, *Science* **309**, 257 (2005). ..... on pages 3, 4.

[10] Pierre Monceau, *Adv. Phys.* **61**, 325 (2012). ..... on pages 4, 5, 32, 68, 76.

[11] Xuetao Zhu, Jiandong Guo, Jiandi Zhang, and E. W. Plummer, *Adv. Phys.: X* **2**, 622 (2017). ..... on pages 4, 32, 64, 68, 76, 92.

[12] J. M. Tranquada, B. J. Sternlieb, J. D. Axe, Y. Nakamura, and S. Uchida, *Nature* **375**, 561 (1995). ..... on pages 5, 29, 29.

[13] Q. Li, M. Hücker, G. D. Gu, A. M. Tsvelik, and J. M. Tranquada, *Phys. Rev. Lett.* **99**, 067001 (2007). ..... on pages 5, 79.

[14] G. Ghiringhelli, M. Le Tacon, M. Minola, S. Blanco-Canosa, C. Mazzoli, N. B. Brookes, G. M. De Luca, A. Frano, D. G. Hawthorn, F. He, T. Loew, M. Moretti Sala, D. C. Peets, M. Salluzzo, E. Schierle, R. Sutarto, G. A. Sawatzky, E. Weschke, B. Keimer, and L. Braicovich, *Science* **337**, 821 (2012). on pages 5, 30, 31, 63, 64, 64, 106.

[15] Alex Frano, Santiago Blanco-Canosa, Bernhard Keimer, and Robert J Birgeneau, *J. Phys.: Condens. Matter* **32**, 374005 (2020). ..... on pages 5, 63, 79, 81.

[16] M. Le Tacon, A. Bosak, S. M. Souliou, G. Dellea, T. Loew, R. Heid, K-P. Bohnen, G. Ghiringhelli, M. Krisch, and B. Keimer, *Nat. Phys.* **10**, 52 (2014). . on pages 5, 32, 33, 33, 59, 78, 79, 93.

[17] S. M. Souliou, H. Gretarsson, G. Garbarino, A. Bosak, J. Porras, T. Loew, B. Keimer, and M. Le Tacon, *Phys. Rev. B* **97**, 020503 (2018). ..... on pages 5, 8, 67, 67, 76.

[18] H.-H. Kim, S. M. Souliou, M. E. Barber, E. Lefrançois, M. Minola, M. Tortora, R. Heid, N. Nandi, R. A. Borzi, G. Garbarino, A. Bosak, J. Porras, T. Loew, M. König, P. M. Moll, A. P. Mackenzie, B. Keimer, C. W. Hicks, and M. Le Tacon, *Science* **362**, 1040 (2018). on pages 5, 8, 33, 34, 36, 39, 57, 68, 68, 74, 81, 82, 82, 88, 90, 90, 106.

[19] J. G. Bednorz and K. A. Müller, *Zeitschrift für Physik B Condensed Matter* **64**, 189 (1986). ..... on page 7.

[20] Nicolas Doiron-Leyraud, Cyril Proust, David LeBoeuf, Julien Levallois, Jean-Baptiste Bonnemaison, Ruixing Liang, D. A. Bonn, W. N. Hardy, and Louis Taillefer, *Nature* **447**, 565 (2007). ..... on pages 7, 18, 31, 64, 64, 68, 76.

[21] S. Gerber, H. Jang, H. Nojiri, S. Matsuzawa, H. Yasumura, D. A. Bonn, R. Liang, W. N. Hardy, Z. Islam, A. Mehta, S. Song, M. Sikorski, D. Stefanescu, Y. Feng, S. A. Kivelson, T. P. Devereaux, Z.-X. Shen, C.-C. Kao, W.-S. Lee, D. Zhu, and J.-S. Lee, *Science* **350**, 949 (2015). ..... on pages 7, 32, 64, 65, 82, 91, 91.

[22] J. Chang, E. Blackburn, A. T. Holmes, N. B. Christensen, J. Larsen, J. Mesot, Ruixing Liang, D. A. Bonn, W. N. Hardy, A. Watenphul, M. v. Zimmermann, E. M. Forgan, and S. M. Hayden, *Nat. Phys.* **8**, 871 (2012). ... on pages 7, 30, 31, 59, 64.

[23] Carsten Putzke, Jake Ayres, Jonathan Buhot, Salvatore Licciardello, Nigel E. Hussey, Sven Friedemann, and Antony Carrington, *Phys. Rev. Lett.* **120**, 117002 (2018). on pages 8, 49, 67, 76, 78.

[24] N. P. Armitage, P. Fournier, and R. L. Greene, *Rev. Mod. Phys.* **82**, 2421 (2010). on page 8.

[25] Neven Barišić, Mun K. Chan, Yuan Li, Guichuan Yu, Xudong Zhao, Martin Dressel, Ana Smontara, and Martin Greven, *Proceedings of the National Academy of Sciences* **110**, 12235 (2013). ..... on page 9.

[26] Yoshinori Tokura and Takahisa Arima, *Japanese Journal of Applied Physics* **29**, 2388 (1990). ..... on page 9.

[27] Y. Tokura, H. Takagi, and S. Uchida, *Nature* **337**, 345 EP (1989). ..... on page 9.

[28] G. Calestani and C. Rizzoli, *Nature* **328**, 606 (1987). ..... on page 10.

[29] R.J. Cava, A.W. Hewat, E.A. Hewat, B. Batlogg, M. Marezio, K.M. Rabe, J.J. Krajewski, W.F. Peck, and L.W. Rupp, *Physica C: Superconductivity* **165**, 419 (1990). ..... on page 10, 10.

[30] J. D. Jorgensen, B. W. Veal, A. P. Paulikas, L. J. Nowicki, G. W. Crabtree, H. Claus, and W. K. Kwok, *Phys. Rev. B* **41**, 1863 (1990). ..... on pages 10, 11.

[31] Koichi Momma and Fujio Izumi, *J. Appl. Crystallogr.* **44**, 1272 (2011). on page 11.

[32] N.H Andersen, M von Zimmermann, T Frello, M Käll, D Mønster, P.-A Lindgård, J Madsen, T Niemöller, H.F Poulsen, O Schmidt, J.R Schneider, Th Wolf, P Dosanjh, R Liang, and W.N Hardy, *Physica C: Superconductivity* **317-318**, 259 (1999). . on pages 12, 46.

[33] M. v. Zimmermann, J. R. Schneider, T. Frello, N. H. Andersen, J. Madsen, M. Käll, H. F. Poulsen, R. Liang, P. Dosanjh, and W. N. Hardy, *Phys. Rev. B* **68**, 104515 (2003). ..... on pages 12, 83.

[34] Ruixing Liang, D.A Bonn, and Walter N Hardy, *Physica C: Superconductivity* **336**, 57 (2000). ..... on pages 10, 12.

[35] H. Alloul, J. Bobroff, M. Gabay, and P. J. Hirschfeld, *Rev. Mod. Phys.* **81**, 45 (2009). on page 12.

[36] L. F. Mattheiss, *Phys. Rev. Lett.* **58**, 1028 (1987). ..... on page 13.

[37] Jaejun Yu, A. J. Freeman, and J. H. Xu, *Phys. Rev. Lett.* **58**, 1035 (1987). on page 13.

[38] S. Massidda, Jaejun Yu, A.J. Freeman, and D.D. Koelling, *Physics Letters A* **122**, 198 (1987). ..... on page 13, 13.

[39] A. Fujimori, E. Takayama-Muromachi, Y. Uchida, and B. Okai, *Phys. Rev. B* **35**, 8814 (1987). ..... on pages 13, 13, 17.

[40] A. Bianconi, A. Congiu Castellano, M. De Santis, P. Delogu, A. Gargano, and R. Giorgi, *Solid State Communications* **63**, 1135 (1987). ..... on page 13.

[41] J. M. Tranquada, S. M. Heald, A. Moodenbaugh, and M. Suenaga, *Phys. Rev. B* **35**, 7187 (1987). ..... on page 13.

[42] C. J. Ballhausen, *Introduction to Ligand Field Theory* (McGraw-Hill, New York, 1962). ..... on page 14.

[43] Masatoshi Imada, Atsushi Fujimori, and Yoshinori Tokura, *Rev. Mod. Phys.* **70**, 1039 (1998). ..... on page 15.

[44] J. Fink, N. Nucker, H. A. Romberg, and J. C. Fuggle, *IBM Journal of Research and Development* **33**, 372 (1989). ..... on page 16.

[45] J. Zaanen, G. A. Sawatzky, and J. W. Allen, *Phys. Rev. Lett.* **55**, 418 (1985). . on page 17, 17.

[46] Zhi-xun Shen, J. W. Allen, J. J. Yeh, J. S. Kang, W. Ellis, W. Spicer, I. Lindau, M. B. Maple, Y. D. Dalichaouch, M. S. Torikachvili, J. Z. Sun, and T. H. Geballe, *Phys. Rev. B* **36**, 8414 (1987). ..... on page 17.

[47] Andrea Damascelli, Zahid Hussain, and Zhi-Xun Shen, *Rev. Mod. Phys.* **75**, 473 (2003). ..... on pages 17, 55.

[48] V. J. Emery, *Phys. Rev. Lett.* **58**, 2794 (1987). ..... on page 17.

[49] F. C. Zhang and T. M. Rice, *Phys. Rev. B* **37**, 3759 (1988). ..... on page 18.

[50] T. Yoshida, X. J. Zhou, K. Tanaka, W. L. Yang, Z. Hussain, Z.-X. Shen, A. Fujimori, S. Sahrakorpi, M. Lindroos, R. S. Markiewicz, A. Bansil, Seiki Komiya, Yoichi Ando, H. Eisaki, T. Kakeshita, and S. Uchida, *Phys. Rev. B* **74**, 224510 (2006). on pages 18, 19.

[51] So Kunisada, Shunsuke Isono, Yoshimitsu Kohama, Shiro Sakai, Cédric Bareille, Shunsuke Sakuragi, Ryo Noguchi, Kifu Kurokawa, Kenta Kuroda, Yukiaki Ishida, Shintaro Adachi, Ryotaro Sekine, Timur K. Kim, Cephise Cacho, Shik Shin, Takami Tohyama, Kazuyasu Tokiwa, and Takeshi Kondo, *Science* **369**, 833 (2020). on page 19.

[52] S. Badoux, W. Tabis, F. Laliberté, G. Grissonnanche, B. Vignolle, D. Vignolles, J. Béard, D. A. Bonn, W. N. Hardy, R. Liang, N. Doiron-Leyraud, Louis Taillefer, and Cyril Proust, *Nature* **531**, 210 EP (2016). ..... on pages 19, 64.

[53] B. Keimer, S. A. Kivelson, M. R. Norman, S. Uchida, and J. Zaanen, *Nature* **518**, 179 (2015). ..... on page 20.

[54] H. Takagi, T. Ido, S. Ishibashi, M. Uota, S. Uchida, and Y. Tokura, *Phys. Rev. B* **40**, 2254 (1989). ..... on page 21, 21.

[55] J. M. Tranquada, A. H. Moudden, A. I. Goldman, P. Zolliker, D. E. Cox, G. Shirane, S. K. Sinha, D. Vaknin, D. C. Johnston, M. S. Alvarez, A. J. Jacobson, J. T. Lewandowski, and J. M. Newsam, *Phys. Rev. B* **38**, 2477 (1988). . on page 21, 21.

[56] Nobuhiko Nishida, Hideaki Miyatake, Daisuke Shimada, Satoshi Okuma, Masayasu Ishikawa, Toshiro Takabatake, Yasuhiro Nakazawa, Yoshitaka Kuno, Rolf Keitel, Jess H. Brewer, Tanya M. Riseman, David Ll. Williams, Yasushi Watanabe, Toshimitsu Yamazaki, Kusuo Nishiyama, Kanetada Nagamine, Eduardo J. Ansaldo, and Eiko Torikai, *Japanese Journal of Applied Physics* **26**, L1856 (1987). . on page 21.

[57] G. Shirane, Y. Endoh, R. J. Birgeneau, M. A. Kastner, Y. Hidaka, M. Oda, M. Suzuki, and T. Murakami, *Phys. Rev. Lett.* **59**, 1613 (1987). ..... on page 21.

[58] D Haug, V Hinkov, Y Sidis, P Bourges, N B Christensen, A Ivanov, T Keller, C T Lin, and B Keimer, *New Journal of Physics* **12**, 105006 (2010). on pages 22, 28, 32, 92.

[59] K. B. Lyons, P. A. Fleury, J. P. Remeika, A. S. Cooper, and T. J. Negran, *Phys. Rev. B* **37**, 2353 (1988). ..... on page 22.

[60] S. Sugai, H. Suzuki, Y. Takayanagi, T. Hosokawa, and N. Hayamizu, *Phys. Rev. B* **68**, 184504 (2003). ..... on page 22.

[61] R. Coldea, S. M. Hayden, G. Aeppli, T. G. Perring, C. D. Frost, T. E. Mason, S.-W. Cheong, and Z. Fisk, *Phys. Rev. Lett.* **86**, 5377 (2001). .....on page 22, 22.

[62] L. Braicovich, J. van den Brink, V. Bisogni, M. Moretti Sala, L. J. P. Ament, N. B. Brookes, G. M. De Luca, M. Salluzzo, T. Schmitt, V. N. Strocov, and G. Ghiringhelli, *Phys. Rev. Lett.* **104**, 077002 (2010). .....on pages 22, 59.

[63] M. Le Tacon, G. Ghiringhelli, J. Chaloupka, M. Moretti Sala, V. Hinkov, M. W. Haverkort, M. Minola, M. Bakr, K. J. Zhou, S. Blanco-Canosa, C. Monney, Y. T. Song, G. L. Sun, C. T. Lin, G. M. De Luca, M. Salluzzo, G. Khaliullin, T. Schmitt, L. Braicovich, and B. Keimer, *Nature Physics* **7**, 725 EP (2011). . on pages 22, 82.

[64] J. Bardeen, L. N. Cooper, and J. R. Schrieffer, *Phys. Rev.* **108**, 1175 (1957). ..on page 23.

[65] W. L. McMillan, *Phys. Rev.* **167**, 331 (1968). .....on page 23.

[66] Yoichi Kamihara, Takumi Watanabe, Masahiro Hirano, and Hideo Hosono, *Journal of the American Chemical Society* **130**, 3296 (2008). .....on page 23.

[67] A. P. Drozdov, M. I. Eremets, I. A. Troyan, V. Ksenofontov, and S. I. Shylin, *Nature* **525**, 73 (2015). .....on page 23.

[68] A. Schilling, M. Cantoni, J. D. Guo, and H. R. Ott, *Nature* **363**, 56 (1993). on page 23.

[69] Michael Tinkham, *Introduction to Superconductivity* (Dover Publications, 2004), second edn. .....on pages 23, 25.

[70] Stefano Giorgini, Lev P. Pitaevskii, and Sandro Stringari, *Rev. Mod. Phys.* **80**, 1215 (2008). ..... on page 24.

[71] C. E. Gough, M. S. Colclough, E. M. Forgan, R. G. Jordan, M. Keene, C. M. Muirhead, A. I. M. Rae, N. Thomas, J. S. Abell, and S. Sutton, *Nature* **326**, 855 (1987). ..... on page 24.

[72] H. Ding, M. R. Norman, J. C. Campuzano, M. Randeria, A. F. Bellman, T. Yokoya, T. Takahashi, T. Mochiku, and K. Kadowaki, *Phys. Rev. B* **54**, R9678 (1996). on pages 25, 26.

[73] D. J. Scalapino, *Physics Reports* **250**, 329 (1995). ..... on page 25.

[74] Yoichi Yanase, Takanobu Jujo, Takuji Nomura, Hiroaki Ikeda, Takashi Hotta, and Kosaku Yamada, *Physics Reports* **387**, 1 (2003). .....on page 25.

[75] Z.-X. Shen, D. S. Dessau, B. O. Wells, D. M. King, W. E. Spicer, A. J. Arko, D. Marshall, L. W. Lombardo, A. Kapitulnik, P. Dickinson, S. Doniach, J. DiCarlo, T. Loeser, and C. H. Park, *Phys. Rev. Lett.* **70**, 1553 (1993). ..... on page 26.

[76] C. C. Tsuei, J. R. Kirtley, C. C. Chi, Lock See Yu-Jahnes, A. Gupta, T. Shaw, J. Z. Sun, and M. B. Ketchen, *Phys. Rev. Lett.* **73**, 593 (1994). ..... on page 26.

[77] Y. Y. Peng, G. Dellea, M. Minola, M. Conni, A. Amorese, D. Di Castro, G. M. De Luca, K. Kummer, M. Salluzzo, X. Sun, X. J. Zhou, G. Balestrino, M. Le Tacon, B. Keimer, L. Braicovich, N. B. Brookes, and G. Ghiringhelli, *Nat Phys* **advance online publication**, (2017). ..... on page 26.

[78] Anderson Philip W., *Science* **316**, 1705 (2007). ..... on page 26.

[79] A. Lanzara, P. V. Bogdanov, X. J. Zhou, S. A. Kellar, D. L. Feng, E. D. Lu, T. Yoshida, H. Eisaki, A. Fujimori, K. Kishio, J. I. Shimoyama, T. Noda, S. Uchida, Z. Hussain, and Z. X. Shen, *Nature* **412**, 510 (2001). ..... on page 26.

[80] D. Reznik, L. Pintschovius, M. Ito, S. Iikubo, M. Sato, H. Goka, M. Fujita, K. Yamada, G. D. Gu, and J. M. Tranquada, *Nature* **440**, 1170 (2006). ..... on page 26.

[81] A. P. Mackenzie, R. K. W. Haselwimmer, A. W. Tyler, G. G. Lonzarich, Y. Mori, S. Nishizaki, and Y. Maeno, *Phys. Rev. Lett.* **80**, 161 (1998). ..... on page 26.

[82] W. W. Warren, R. E. Walstedt, G. F. Brennert, R. J. Cava, R. Tycko, R. F. Bell, and G. Dabbagh, *Phys. Rev. Lett.* **62**, 1193 (1989). ..... on page 26.

[83] H. Alloul, T. Ohno, and P. Mendels, *Phys. Rev. Lett.* **63**, 1700 (1989). on page 26.

[84] V. Hinkov, P. Bourges, S. Pailhès, Y. Sidis, A. Ivanov, C. D. Frost, T. G. Perring, C. T. Lin, D. P. Chen, and B. Keimer, *Nature Physics* **3**, 780 EP (2007). on page 26.

[85] Ch. Renner, B. Revaz, J.-Y. Genoud, K. Kadowaki, and Ø. Fischer, *Phys. Rev. Lett.* **80**, 149 (1998). ..... on page 26.

[86] H. Ding, T. Yokoya, J. C. Campuzano, T. Takahashi, M. Randeria, M. R. Norman, T. Mochiku, K. Kadowaki, and J. Giapintzakis, *Nature* **382**, 51 (1996). on page 26.

[87] M. R. Norman, H. Ding, M. Randeria, J. C. Campuzano, T. Yokoya, T. Takeuchi, T. Takahashi, T. Mochiku, K. Kadowaki, P. Guptasarma, and D. G. Hinks, *Nature* **392**, 157 EP (1998). ..... on page 26.

[88] V. J. Emery and S. A. Kivelson, *Nature* **374**, 434 (1995). ..... on page 27.

[89] M. S. Grbić, N. Barišić, A. Dulčić, I. Kupčić, Y. Li, X. Zhao, G. Yu, M. Dressel, M. Greven, and M. Požek, *Phys. Rev. B* **80**, 094511 (2009). ..... on page 27.

[90] Takeshi Kondo, Rustem Khasanov, Tsunehiro Takeuchi, Jorg Schmalian, and Adam Kaminski, *Nature* **457**, 296 (2009). ..... on page 27.

[91] Tanaka, Kiyohisa and Lee, W. S. and Lu, D. H. and Fujimori, A. and Fujii, T. and Risdiana, and Terasaki, I. and Scalapino, D. J. and Devereaux, T. P. and Hussain, Z. and Shen, Z.-X., *Science* **314**, 1910 (2006). ..... on page 27.

[92] W. S. Lee, I. M. Vishik, K. Tanaka, D. H. Lu, T. Sasagawa, N. Nagaosa, T. P. Devereaux, Z. Hussain, and Z. X. Shen, *Nature* **450**, 81 (2007). ... on page 27, 27.

[93] I. M. Vishik, M. Hashimoto, Rui-Hua He, Wei-Sheng Lee, Felix Schmitt, Donghui Lu, R. G. Moore, C. Zhang, W. Meevasana, T. Sasagawa, S. Uchida, Kazuhiro Fujita, S. Ishida, M. Ishikado, Yoshiyuki Yoshida, Hiroshi Eisaki, Zahid Hussain, Thomas P. Devereaux, and Zhi-Xun Shen, *Proc. Natl. Acad. Sci.* **109**, 18332 (2012). on page 27.

[94] R. Comin, A. Frano, M. M. Yee, Y. Yoshida, H. Eisaki, E. Schierle, E. Weschke, R. Sutarto, F. He, A. Soumyanarayanan, Yang He, M. Le Tacon, I. S. Elfimov, Jennifer E. Hoffman, G. A. Sawatzky, B. Keimer, and A. Damascelli, *Science* **343**, 390 (2014). ..... on pages 27, 32, 92.

[95] Makoto Hashimoto, Inna M. Vishik, Rui-Hua He, Thomas P. Devereaux, and Zhi-Xun Shen, *Nat Phys* **10**, 483 (2014). ..... on page 27.

[96] Yoichi Ando, Kouji Segawa, Seiki Komiya, and A. N. Lavrov, *Phys. Rev. Lett.* **88**, 137005 (2002). ..... on pages 27, 74.

[97] M. J. Lawler, K. Fujita, Jhinhwan Lee, A. R. Schmidt, Y. Kohsaka, Chung Koo Kim, H. Eisaki, S. Uchida, J. C. Davis, J. P. Sethna, and Eun-Ah Kim, *Nature* **466**, 347 (2010). ..... on page 28.

[98] A. Kaminski, S. Rosenkranz, H. M. Fretwell, J. C. Campuzano, Z. Li, H. Raffy, W. G. Cullen, H. You, C. G. Olson, C. M. Varma, and H. Hochst, *Nature* **416**, 610 (2002). ..... on page 28.

[99] S. Nakata, M. Horio, K. Koshiishi, K. Hagiwara, C. Lin, M. Suzuki, S. Ideta, K. Tanaka, D. Song, Y. Yoshida, H. Eisaki, and A. Fujimori, *npj Quantum Materials* **6**, 86 (2021). ..... on page 28.

[100] N. Auvray, B. Loret, S. Benhabib, M. Cazayous, R. D. Zhong, J. Schneeloch, G. D. Gu, A. Forget, D. Colson, I. Paul, A. Sacuto, and Y. Gallais, *Nature Communications* **10**, 5209 (2019). ..... on pages 28, 92.

[101] R. Daou, J. Chang, David LeBoeuf, Olivier Cyr-Choiniere, Francis Laliberte, Nicolas Doiron-Leyraud, B. J. Ramshaw, Ruixing Liang, D. A. Bonn, W. N. Hardy, and Louis Taillefer, *Nature* **463**, 519 (2010). ..... on page 28.

[102] Y. Sato, S. Kasahara, H. Murayama, Y. Kasahara, E. G. Moon, T. Nishizaki, T. Loew, J. Porras, B. Keimer, T. Shibauchi, and Y. Matsuda, *Nature Physics* **13**, 1074 (2017). ..... on pages 28, 92.

[103] H. Murayama, Y. Sato, R. Kurihara, S. Kasahara, Y. Mizukami, Y. Kasahara, H. Uchiyama, A. Yamamoto, E. G. Moon, J. Cai, J. Freyermuth, M. Greven, T. Shibauchi, and Y. Matsuda, *Nat. Commun.* **10**, 3282 (2019). ..... on page 28.

[104] Kousuke Ishida, Suguru Hosoi, Yuki Teramoto, Tomohiro Usui, Yuta Mizukami, Kenji Itaka, Yuji Matsuda, Takao Watanabe, and Takasada Shibauchi, *J. Phys. Soc. Jpn.* **89**, 064707 (2020). ..... on pages 28, 92.

[105] V. Hinkov, D. Haug, B. Fauqué, P. Bourges, Y. Sidis, A. Ivanov, C. Bernhard, C. T. Lin, and B. Keimer, *Science* **319**, 597 (2008). ..... on pages 28, 32, 92.

[106] S. A. Kivelson, E. Fradkin, and V. J. Emery, *Nature* **393**, 550 (1998). on page 28.

[107] S. A. Kivelson, I. P. Bindloss, E. Fradkin, V. Oganesyan, J. M. Tranquada, A. Kapitulnik, and C. Howald, *Rev. Mod. Phys.* **75**, 1201 (2003). ..... on page 28.

[108] Hiroyuki Yamase and Hiroshi Kohno, *JPSJ* **69**, 2151 (2000). ..... on page 28.

[109] Hiroyuki Yamase and Walter Metzner, *Phys. Rev. B* **73**, 214517 (2006). on page 28.

[110] Vadim Oganesyan, Steven A. Kivelson, and Eduardo Fradkin, *Phys. Rev. B* **64**, 195109 (2001). ..... on page 28.

[111] Ying-Jer Kao and Hae-Young Kee, *Phys. Rev. B* **72**, 024502 (2005). .. on page 28.

[112] Christoph J. Halboth and Walter Metzner, *Phys. Rev. Lett.* **85**, 5162 (2000). .. on page 28.

[113] Jing Xia, Elizabeth Schemm, G. Deutscher, S. A. Kivelson, D. A. Bonn, W. N. Hardy, R. Liang, W. Siemons, G. Koster, M. M. Fejer, and A. Kapitulnik, *Phys. Rev. Lett.* **100**, 127002 (2008). ..... on page 28.

[114] S. De Almeida-Didry, Y. Sidis, V. Balédent, F. Giovannelli, I. Monot-Laffez, and P. Bourges, *Phys. Rev. B* **86**, 020504 (2012). ..... on page 28.

[115] Y. Li, V. Baledent, N. Barisic, Y. Cho, B. Fauque, Y. Sidis, G. Yu, X. Zhao, P. Bourges, and M. Greven, *Nature* **455**, 372 (2008). ..... on page 28.

[116] Vivek Aji, Arkady Shekhter, and C. M. Varma, *Phys. Rev. B* **81**, 064515 (2010). on page 28.

[117] Pavan Hosur, A. Kapitulnik, S. A. Kivelson, J. Orenstein, and S. Raghu, *Phys. Rev. B* **87**, 115116 (2013). ..... on page 28.

[118] M. Civelli, M. Capone, S. S. Kancharla, O. Parcollet, and G. Kotliar, *Phys. Rev. Lett.* **95**, 106402 (2005). ..... on page 28.

[119] M. Gurvitch and A. T. Fiory, *Phys. Rev. Lett.* **59**, 1337 (1987). ..... on page 28.

[120] Hussey N. E., K. Takenaka, and H. Takagi, *Philosophical Magazine* **84**, 2847 (2004). on page 28.

[121] C. M. Varma, P. B. Littlewood, S. Schmitt-Rink, E. Abrahams, and A. E. Ruckenstein, *Phys. Rev. Lett.* **63**, 1996 (1989). ..... on page 28.

[122] T. Ito, K. Takenaka, and S. Uchida, *Phys. Rev. Lett.* **70**, 3995 (1993). on pages 28, 63, 65.

[123] Cooper R. A., Wang Y., Vignolle B., Lipscombe O. J., Hayden S. M., Tanabe Y., Adachi T., Koike Y., Nohara M., Takagi H., Proust Cyril, and Hussey N. E., *Science* **323**, 603 (2009). ..... on page 28.

[124] Yoichi Ando, G. S. Boebinger, A. Passner, Tsuyoshi Kimura, and Kohji Kishio, *Phys. Rev. Lett.* **75**, 4662 (1995). ..... on page 28.

[125] R. Daou, Nicolas Doiron-Leyraud, David LeBoeuf, S. Y. Li, Francis Laliberté, Olivier Cyr-Choinière, Y. J. Jo, L. Balicas, J. Q. Yan, J. S. Zhou, J. B. Goodenough, and Louis Taillefer, *Nature Physics* **5**, 31 (2009). ..... on page 28.

[126] A. Legros, S. Benhabib, W. Tabis, F. Laliberté, M. Dion, M. Lizaire, B. Vignolle, D. Vignolles, H. Raffy, Z. Z. Li, P. Auban-Senzier, N. Doiron-Leyraud, P. Fournier, D. Colson, L. Taillefer, and C. Proust, *Nature Physics* **15**, 142 (2019). on page 28.

[127] Gaël Grissonnanche, Yawen Fang, Anaëlle Legros, Simon Verret, Francis Laliberté, Clément Collignon, Jianshi Zhou, David Graf, Paul A. Goddard, Louis Taillefer, and B. J. Ramshaw, *Nature* **595**, 667 (2021). ..... on page 28.

[128] Sean A. Hartnoll and Andrew P. Mackenzie, Planckian dissipation in metals (2021). on page 28.

[129] Edwin W. Huang, Ryan Sheppard, Brian Moritz, and Thomas P. Devereaux, *Science* **366**, 987 (2019). ..... on page 29.

[130] Jan Zaanen and Olle Gunnarsson, *Phys. Rev. B* **40**, 7391 (1989). ..... on page 29.

[131] P. Abbamonte, A. Rusydi, S. Smadici, G. D. Gu, G. A. Sawatzky, and D. L. Feng, *Nat. Phys.* **1**, 155 (2005). ..... on pages 29, 59.

[132] T. Adachi, T. Noji, and Y. Koike, *Phys. Rev. B* **64**, 144524 (2001). ... on page 29.

[133] Y. Nakamura and S. Uchida, *Phys. Rev. B* **46**, 5841 (1992). ..... on page 29.

[134] Valla T., Fedorov A. V., Lee Jinho, Davis J. C., and Gu G. D., *Science* **314**, 1914 (2006). ..... on page 29.

[135] Rui-Hua He, Kiyohisa Tanaka, Sung-Kwan Mo, Takao Sasagawa, Masaki Fujita, Tadashi Adachi, Norman Mannella, Kazuyoshi Yamada, Yoji Koike, Zahid Hussain, and Zhi-Xun Shen, *Nature Physics* **5**, 119 (2009). ..... on page 29.

[136] Tadashi Adachi, Nobuyoshi Kitajima, and Yoji Koike, *Phys. Rev. B* **83**, 060506 (2011). ..... on page 29.

[137] Qing Jie, Su Jung Han, Ivo Dimitrov, J.M. Tranquada, and Qiang Li, *Physica C: Superconductivity* **481**, 46 (2012). Stripes and Electronic Liquid Crystals in Strongly Correlated Materials. ..... on page 30.

[138] John M. Tranquada, Mark P. M. Dean, and Qiang Li, *Journal of the Physical Society of Japan* **90**, 111002 (2021). ..... on page 30.

[139] M. Hücker, M. v. Zimmermann, G. D. Gu, Z. J. Xu, J. S. Wen, Guangyong Xu, H. J. Kang, A. Zheludev, and J. M. Tranquada, *Phys. Rev. B* **83**, 104506 (2011). on page 30.

[140] D. G. Hawthorn, K. M. Shen, J. Geck, D. C. Peets, H. Wadati, J. Okamoto, S.-W. Huang, D. J. Huang, H.-J. Lin, J. D. Denlinger, Ruixing Liang, D. A. Bonn, W. N. Hardy, and G. A. Sawatzky, *Phys. Rev. B* **84**, 075125 (2011). ..... on page 30.

[141] R. Comin, R. Sutarto, E. H. da Silva Neto, L. Chauviere, R. Liang, W. N. Hardy, D. A. Bonn, F. He, G. A. Sawatzky, and A. Damascelli, *Science* **347**, 1335 (2015). on pages 30, 93, 94.

[142] H.-H. Kim, E. Lefrançois, K. Kummer, R. Fumagalli, N. B. Brookes, D. Betto, S. Nakata, M. Tortora, J. Porras, T. Loew, M. E. Barber, L. Braicovich, A. P. Mackenzie, C. W. Hicks, B. Keimer, M. Minola, and M. Le Tacon, *Phys. Rev. Lett.* **126**, 037002 (2021). on pages 30, 33, 34, 39, 68, 68, 75, 76, 76, 76, 76, 79, 81, 82, 82, 84, 88, 90, 90, 93, 95, 100, 102, 116.

[143] M. v Zimmermann, A Vigliante, T Niemöller, N Ichikawa, T Frello, J Madsen, P Wochner, S Uchida, N. H Andersen, J. M Tranquada, D Gibbs, and J. R Schneider, *Europhysics Letters (EPL)* **41**, 629 (1998). ..... on page 30.

[144] A. J. Achkar, R. Sutarto, X. Mao, F. He, A. Frano, S. Blanco-Canosa, M. Le Tacon, G. Ghiringhelli, L. Braicovich, M. Minola, M. Moretti Sala, C. Mazzoli, Ruixing Liang, D. A. Bonn, W. N. Hardy, B. Keimer, G. A. Sawatzky, and D. G. Hawthorn, *Phys. Rev. Lett.* **109**, 167001 (2012). ..... on pages 31, 74, 75, 95.

[145] E. Blackburn, J. Chang, M. Hücker, A. T. Holmes, N. B. Christensen, Ruixing Liang, D. A. Bonn, W. N. Hardy, U. Rütt, O. Gutowski, M. v. Zimmermann, E. M. Forgan, and S. M. Hayden, *Phys. Rev. Lett.* **110**, 137004 (2013). ..... on page 31.

[146] S. Blanco-Canosa, A. Frano, T. Loew, Y. Lu, J. Porras, G. Ghiringhelli, M. Minola, C. Mazzoli, L. Braicovich, E. Schierle, E. Weschke, M. Le Tacon, and B. Keimer, *Phys. Rev. Lett.* **110**, 187001 (2013). ..... on pages 31, 59, 64.

[147] D. Haug, V. Hinkov, A. Suchaneck, D. S. Inosov, N. B. Christensen, Ch. Niedermayer, P. Bourges, Y. Sidis, J. T. Park, A. Ivanov, C. T. Lin, J. Mesot, and B. Keimer, *Phys. Rev. Lett.* **103**, 017001 (2009). ..... on page 32.

[148] Eduardo H. da Silva Neto, Pegor Aynajian, Alex Frano, Riccardo Comin, Enrico Schierle, Eugen Weschke, András Gyenis, Jinsheng Wen, John Schneeloch, Zhijun Xu, Shimpei Ono, Genda Gu, Mathieu Le Tacon, and Ali Yazdani, *Science* **343**, 393 (2014). ..... on pages 32, 92.

[149] W. Tabis, Y. Li, M. Le Tacon, L. Braicovich, A. Kreyssig, M. Minola, G. Dellea, E. Weschke, M. J. Veit, M. Ramazanoglu, A. I. Goldman, T. Schmitt, G. Ghiringhelli, N. Barišić, M. K. Chan, C. J. Dorow, G. Yu, X. Zhao, B. Keimer, and M. Greven, *Nature Communications* **5**, 5875 EP (2014). ..... on pages 32, 92.

[150] Y. Y. Peng, R. Fumagalli, Y. Ding, M. Minola, S. Caprara, D. Betto, M. Bluschke, G. M. De Luca, K. Kummer, E. Lefrançois, M. Salluzzo, H. Suzuki, M. Le Tacon, X. J. Zhou, N. B. Brookes, B. Keimer, L. Braicovich, M. Grilli, and G. Ghiringhelli, *Nature Materials* **17**, 697 (2018). ..... on page 32.

[151] S. Blanco-Canosa, A. Frano, E. Schierle, J. Porras, T. Loew, M. Minola, M. Bluschke, E. Weschke, B. Keimer, and M. Le Tacon, *Phys. Rev. B* **90**, 054513 (2014). ... on pages 32, 32, 48, 65, 68, 84, 90.

[152] T. P. Devereaux, A. M. Shvaika, K. Wu, K. Wohlfeld, C. J. Jia, Y. Wang, B. Moritz, L. Chaix, W.-S. Lee, Z.-X. Shen, G. Ghiringhelli, and L. Braicovich, *Phys. Rev. X* **6**, 041019 (2016). ..... on pages 32, 58, 58.

[153] L. Chaix, G. Ghiringhelli, Y. Y. Peng, M. Hashimoto, B. Moritz, K. Kummer, N. B. Brookes, Y. He, S. Chen, S. Ishida, Y. Yoshida, H. Eisaki, M. Salluzzo, L. Braicovich, Z. X. Shen, T. P. Devereaux, and W. S. Lee, *Nature Physics* **13**, 952 (2017). .. on pages 32, 58, 93.

[154] H. Jang, W.-S. Lee, H. Nojiri, S. Matsuzawa, H. Yasumura, L. Nie, A. V. Maharaj, S. Gerber, Y.-J. Liu, A. Mehta, D. A. Bonn, R. Liang, W. N. Hardy, C. A. Burns, Z. Islam, S. Song, J. Hastings, T. P. Devereaux, Z.-X. Shen, S. A. Kivelson, C.-C. Kao, D. Zhu, and J.-S. Lee, *Proceedings of the National Academy of Sciences* **113**, 14645 (2016). ..... on pages 32, 91.

[155] J. Chang, E. Blackburn, O. Ivashko, A. T. Holmes, N. B. Christensen, M. Hücker, Ruixing Liang, D. A. Bonn, W. N. Hardy, U. Rütt, M. v. Zimmermann, E. M. Forgan, and S M Hayden, *Nat. Commun.* **7**, 11494 EP (2016). on pages 32, 34, 59, 64, 65, 91, 91.

[156] H. Jang, W.-S. Lee, S. Song, H. Nojiri, S. Matsuzawa, H. Yasumura, H. Huang, Y.-J. Liu, J. Porras, M. Minola, B. Keimer, J. Hastings, D. Zhu, T. P. Devereaux, Z.-X. Shen, C.-C. Kao, and J.-S. Lee, *Phys. Rev. B* **97**, 224513 (2018). .on pages 33, 64.

[157] Francis Laliberté, Mehdi Frachet, Siham Benhabib, Benjamin Borgnic, Toshinao Loew, Juan Porras, Mathieu Le Tacon, Bernhard Keimer, Steffen Wiedmann, Cyril Proust, and David LeBoeuf, *npj Quantum Materials* **3**, 11 (2018). on pages 33, 34, 91, 91, 91.

[158] Tao Wu, Hadrien Mayaffre, Steffen Kramer, Mladen Horvatic, Claude Berthier, W. N. Hardy, Ruixing Liang, D. A. Bonn, and Marc-Henri Julien, *Nature* **477**, 191 (2011). ..... on pages 33, 65.

[159] Tao Wu, Hadrien Mayaffre, Steffen Krämer, Mladen Horvatić, Claude Berthier, Philip L. Kuhns, Arneil P. Reyes, Ruixing Liang, W. N. Hardy, D. A. Bonn, and Marc-Henri Julien, *Nat. Commun.* **4**, 2113 (2013). ..... on pages 33, 63.

[160] M. Bluschke, A. Frano, E. Schierle, D. Putzky, F. Ghorbani, R. Ortiz, H. Suzuki, G. Christiani, G. Logvenov, E. Weschke, R. J. Birgeneau, E. H. da Silva Neto, M. Minola, S. Blanco-Canosa, and B. Keimer, *Nature Communications* **9**, 2978 (2018). ..... on pages 33, 59, 82, 88, 91.

[161] David LeBoeuf, Nicolas Doiron-Leyraud, Julien Levallois, R. Daou, J. B. Bonnemaison, N. E. Hussey, L. Balicas, B. J. Ramshaw, Ruixing Liang, D. A. Bonn, W. N. Hardy, S. Adachi, Cyril Proust, and Louis Taillefer, *Nature* **450**, 533 (2007). .. on pages 34, 64, 64, 67, 76.

[162] Suchitra E. Sebastian, N. Harrison, M. M. Altarawneh, C. H. Mielke, Ruixing Liang, D. A. Bonn, and G. G. Lonzarich, *Proc. Natl. Acad. Sci. U.S.A.* **107**, 6175 (2010). on pages 34, 64, 64, 68.

[163] Ryogo Kubo, *Journal of the Physical Society of Japan* **12**, 570 (1957). on pages 35, 50, 53.

[164] Jiun-Haw Chu, James G. Analytis, Kristiaan De Greve, Peter L. McMahon, Zahirul Islam, Yoshihisa Yamamoto, and Ian R. Fisher, *Science* **329**, 824 (2010). on page 35.

[165] M. Shayegan, K. Karrai, Y. P. Shkolnikov, K. Vakili, E. P. De Poortere, and S. Manus, *Applied Physics Letters* **83**, 5235 (2003). ..... on page 36.

[166] Jiun-Haw Chu, Hsueh-Hui Kuo, James G. Analytis, and Ian R. Fisher, *Science* **337**, 710 (2012). ..... on page 36.

[167] Scott C. Riggs, M. C. Shapiro, Akash V Maharaj, S. Raghu, E. D. Bauer, R. E. Baumbach, P. Giraldo-Gallo, Mark Wartenbe, and I. R. Fisher, *Nature Communications* **6**, 6425 (2015). ..... on page 36.

[168] Mark E. Barber, *Uniaxial Stress Technique and Investigations into Correlated Electron Systems* (PhD thesis, University of St Andrews, 2017). .. on pages 36, 37, 48, 54.

[169] Clifford W. Hicks, Mark E. Barber, Stephen D. Edkins, Daniel O. Brodsky, and Andrew P. Mackenzie, *Rev. Sci. Instrum.* **85**, 065003 (2014). . on pages 36, 36, 48.

[170] Alexander Steppke, Lishan Zhao, Mark E. Barber, Thomas Scaffidi, Fabian Jerzembeck, Helge Rosner, Alexandra S. Gibbs, Yoshiteru Maeno, Steven H. Simon, Andrew P. Mackenzie, and Clifford W. Hicks, *Science* **355** (2017). ..... on pages 36, 68.

[171] A. Pustogow, Yongkang Luo, A. Chronister, Y. S. Su, D. A. Sokolov, F. Jerzembeck, A. P. Mackenzie, C. W. Hicks, N. Kikugawa, S. Raghu, E. D. Bauer, and S. E. Brown, *Nature* **574**, 72 (2019). ..... on pages 36, 107.

[172] Teodor M. Atanackovic and Ardéshir Guran, *Theory of Elasticity for Scientists and Engineers* (Springer Nature, 2000). ..... on page 37.

[173] Clifford W. Hicks, Daniel O. Brodsky, Edward A. Yelland, Alexandra S. Gibbs, Jan A. N. Bruin, Mark E. Barber, Stephen D. Edkins, Keigo Nishimura, Shingo Yonezawa, Yoshiteru Maeno, and Andrew P. Mackenzie, *Science* **344**, 283 (2014). on pages 38, 68, 106.

[174] Mark E. Barber, Alexander Steppke, Andrew P. Mackenzie, and Clifford W. Hicks, *Rev. Sci. Instrum.* **90**, 023904 (2019). ..... on pages 40, 41, 92.

[175] C. T. Lin, W. Zhou, W. Y. Liang, E. Schönherr, and H. Bender, *Physica C* **195**, 291 (1992). ..... on page 43.

[176] Daniel Haug, *The Magnetic Phase Diagram of Underdoped $YBa_2Cu_3O_{6+x}$ studied by Neutron Scattering* (PhD thesis, Max-Planck-Institut für Festkörperforschung, 2011). on pages 44, 55.

[177] Andreas Erb, *The Impact Of Crystal Growth , Oxygenation And Microstructure On The Physics Of The Rare Earth (123) Superconductors* (1999). ..... on page 45.

[178] Terrence B. Lindemer, John F. Hunley, Jacques E. Gates, Alfred L. Sutton Jr., Jorulf Brynestad, Camden R. Hubbard, and Patrick K. Gallagher, *J. Am. Ceram. Soc.* **72**, 1775 (1989). ..... on pages 43, 68, 82, 96.

[179] A. Erb, B. Greb, and G. Müller-Vogt, *Physica C: Superconductivity and its Applications* **259**, 83 (1996). ..... on pages 44, 46.

[180] C.T. Lin and A. Kulakov, *Physica C* **408-410**, 27 (2004). on pages 46, 47, 68, 82, 96.

[181] D. R. Wake, F. Slakey, M. V. Klein, J. P. Rice, and D. M. Ginsberg, *Phys. Rev. Lett.* **67**, 3728 (1991). ..... on page 46.

[182] Ruixing Liang, D. A. Bonn, and W. N. Hardy, *Phys. Rev. B* **73**, 180505 (2006). on pages 46, 47, 48, 48, 69.

[183] J. L. Tallon, C. Bernhard, G. V. M. Williams, and J. W. Loram, *Phys. Rev. Lett.* **79**, 5294 (1997). ..... on page 47.

[184] J B Nelson and D P Riley, *Proceedings of the Physical Society* **57**, 160 (1945). .on page 47.

[185] Brad Ramshaw, *Shubnikov-de Haas Measurements and the Spin Magnetic Moment of $YBa_2Cu_3O_{6.59}$* (PhD thesis, The University of British Columbia, 2012). on pages 49, 69, 71.

[186] H. Kamerlingh Onnes, *Leiden Comm. 120b, 122b, 124c* (1911). ..... on page 49.

[187] K. v. Klitzing, G. Dorda, and M. Pepper, *Phys. Rev. Lett.* **45**, 494 (1980). on page 49.

[188] T. Yoshida, X. J. Zhou, H. Yagi, D. H. Lu, K. Tanaka, A. Fujimori, Z. Hussain, Z. X. Shen, T. Kakeshita, H. Eisaki, S. Uchida, Kouji Segawa, A. N. Lavrov, and Yoichi Ando, *Physica B: Condensed Matter* **351**, 250 (2004). ..... on page 52.

[189] Hidetoshi Fukuyama, Hiromichi Ebisawa, and Yasushi Wada, *Progress of Theoretical Physics* **42**, 494 (1969). ..... on page 53.

[190] Takeo Matsubara, *Progress of Theoretical Physics* **14**, 351 (1955). .... on page 53.

[191] Vladimir Hinkov, *In-Plane Anisotropy of the Spin-Excitation Spectrum in Twin-Free* $YBa_2Cu_3O_{6+x}$ (PhD thesis, Max-Planck-Institut für Festkörperforschung, 2007). on page 55.

[192] Riccardo Comin and Andrea Damascelli, *Annual Review of Condensed Matter Physics* **7**, 369 (2016). .....on pages 55, 60.

[193] Thomas P. Devereaux and Rudi Hackl, *Rev. Mod. Phys.* **79**, 175 (2007). on page 57.

[194] E. M. Forgan, E. Blackburn, A. T. Holmes, A. K. R. Briffa, J. Chang, L. Bouchenoire, S. D. Brown, Ruixing Liang, D. Bonn, W. N. Hardy, N. B. Christensen, M. V. Zimmermann, M. Hücker, and S. M. Hayden, *Nature Communications* **6**, 10064 EP (2015). .....on pages 57, 84.

[195] Luuk J. P. Ament, Michel van Veenendaal, Thomas P. Devereaux, John P. Hill, and Jeroen van den Brink, *Rev. Mod. Phys.* **83**, 705 (2011). .....on page 58.

[196] Wei-Sheng Lee, *J. Phys. Soc. Jpn.* **90**, 111004 (2021). .....on pages 58, 64.

[197] L. J. P. Ament, M. van Veenendaal, and J. van den Brink, *EPL (Europhysics Letters)* **95**, 27008 (2011). ..... on page 58.

[198] H. Suzuki, H. Gretarsson, H. Ishikawa, K. Ueda, Z. Yang, H. Liu, H. Kim, D. Kukusta, A. Yaresko, M. Minola, J. A. Sears, S. Francoual, H. C. Wille, J. Nuss, H. Takagi, B. J. Kim, G. Khaliullin, H. Yavaş, and B. Keimer, *Nature Materials* **18**, 563 (2019). on page 59.

[199] da Silva Neto Eduardo H., Comin Riccardo, He Feizhou, Sutarto Ronny, Jiang Yeping, Greene Richard L., Sawatzky George A., and Damascelli Andrea, *Science* **347**, 282 (2015). .....on pages 59, 92.

[200] Jörg Fink, Enrico Schierle, Eugen Weschke, Jochen Geck, David Hawthorn, Viktor Soltwisch, Hiroki Wadati, Hsueh-Hung Wu, Hermann A. Dürr, Nadja Wizent, Bernd Büchner, and George A. Sawatzky, *Phys. Rev. B* **79**, 100502 (2009). ..on page 59.

[201] Jörg Fink, Victor Soltwisch, Jochen Geck, Enrico Schierle, Eugen Weschke, and Bernd Büchner, *Phys. Rev. B* **83**, 092503 (2011). .....on page 59.

[202] J Fink, E Schierle, E Weschke, and J Geck, *Reports on Progress in Physics* **76**, 056502 (2013). .....on pages 60, 82.

[203] Eugen Weschke and Enrico Schierle, *Journal of large-scale research facilities JLSRF* **4** (2018). .....on page 60.

[204] N. B. Brookes, F. Yakhou-Harris, K. Kummer, A. Fondacaro, J. C. Cezar, D. Betto, E. Velez-Fort, A. Amorese, G. Ghiringhelli, L. Braicovich, R. Barrett, G. Berruyer, F. Cianciosi, L. Eybert, P. Marion, P. van der Linden, and L. Zhang, *Nuclear Instruments and Methods in Physics Research Section A: Accelerators, Spectrometers, Detectors and Associated Equipment* **903**, 175 (2018). .....on pages 61, 96.

[205] C. W. Chu, J. M. E. Harper, T. H. Geballe, and R. L. Greene, *Phys. Rev. Lett.* **31**, 1491 (1973). ..... on page 63.

[206] J. Chaussy, P. Haen, J.C. Lasjaunias, P. Monceau, G. Waysand, A. Waintal, A. Meerschaut, P. Molinié, and J. Rouxel, *Solid State Communications* **20**, 759 (1976). on page 63.

[207] Matteo Calandra, I. I. Mazin, and Francesco Mauri, *Phys. Rev. B* **80**, 241108 (2009). on page 63.

[208] Michio Naito and Shoji Tanaka, *J. Phys. Soc. Jpn.* **51**, 219 (1982). ... on page 63.

[209] Xuetao Zhu, Yanwei Cao, Jiandi Zhang, E. W. Plummer, and Jiandong Guo, *Proc. Natl. Acad. Sci. U.S.A.* **112**, 2367 (2015). ..... on pages 63, 92.

[210] Yoichi Ando, Seiki Komiya, Kouji Segawa, S. Ono, and Y. Kurita, *Phys. Rev. Lett.* **93**, 267001 (2004). ..... on pages 63, 65, 71.

[211] Eric Wahlberg, Riccardo Arpaia, Götz Seibold, Matteo Rossi, Roberto Fumagalli, Edoardo Trabaldo, Nicholas B. Brookes, Lucio Braicovich, Sergio Caprara, Ulf Gran, Giacomo Ghiringhelli, Thilo Bauch, and Floriana Lombardi, *Science* **373**, 1506 (2021). ..... on pages 64, 79.

[212] Cyril Proust and Louis Taillefer, *Annu. Rev. Condens. Matter Phys.* **10**, 409 (2019). on pages 64, 68.

[213] N Harrison and S E Sebastian, *New J. Phys.* **14**, 095023 (2012). . on pages 64, 76.

[214] Suchitra E. Sebastian and Cyril Proust, *Annu. Rev. Condens. Matter Phys.* **6**, 411 (2015). ..... on pages 64, 64, 76, 88.

[215] David LeBoeuf, Nicolas Doiron-Leyraud, B. Vignolle, Mike Sutherland, B. J. Ramshaw, J. Levallois, R. Daou, Francis Laliberté, Olivier Cyr-Choinière, Johan Chang, Y. J. Jo, L. Balicas, Ruixing Liang, D. A. Bonn, W. N. Hardy, Cyril Proust, and Louis Taillefer, *Phys. Rev. B* **83**, 054506 (2011). ..... on pages 64, 66, 76, 78.

[216] B. J. Ramshaw, S. E. Sebastian, R. D. McDonald, James Day, B. S. Tan, Z. Zhu, J. B. Betts, Ruixing Liang, D. A. Bonn, W. N. Hardy, and N. Harrison, *Science* **348**, 317 (2015). ..... on page 64.

[217] J. E. Hoffman, K. McElroy, D.-H. Lee, K. M Lang, H. Eisaki, S. Uchida, and J. C. Davis, *Science* **297**, 1148 (2002). ..... on page 64.

[218] C. Howald, H. Eisaki, N. Kaneko, M. Greven, and A. Kapitulnik, *Phys. Rev. B* **67**, 014533 (2003). ..... on page 64.

[219] W. D. Wise, M. C. Boyer, Kamalesh Chatterjee, Takeshi Kondo, T. Takeuchi, H. Ikuta, Yayu Wang, and E. W. Hudson, *Nat. Phys.* **4**, 696 (2008). .. on page 64.

[220] T. P. Croft, C. Lester, M. S. Senn, A. Bombardi, and S. M. Hayden, *Phys. Rev. B* **89**, 224513 (2014). ..... on page 64.

[221] Eduardo H. da Silva Neto, Biqiong Yu, Matteo Minola, Ronny Sutarto, Enrico Schierle, Fabio Boschini, Marta Zonno, Martin Bluschke, Joshua Higgins, Yangmu Li, Guichuan Yu, Eugen Weschke, Feizhou He, Mathieu Le Tacon, Richard L. Greene, Martin Greven, George A. Sawatzky, Bernhard Keimer, and Andrea Damascelli, *Sci. Adv.* **2** (2016). ..... on page 64.

[222] W. Tabis, B. Yu, I. Bialo, M. Bluschke, T. Kolodziej, A. Kozlowski, E. Blackburn, K. Sen, E. M. Forgan, M. v. Zimmermann, Y. Tang, E. Weschke, B. Vignolle, M. Hepting, H. Gretarsson, R. Sutarto, F. He, M. Le Tacon, N. Barišić, G. Yu, and M. Greven, *Phys. Rev. B* **96**, 134510 (2017). ..... on pages 64, 92.

[223] Yuval Gannot, B. J. Ramshaw, and Steven A. Kivelson, *Phys. Rev. B* **100**, 045128 (2019). ..... on pages 65, 65, 66, 76.

[224] Hong Yao, Dung-Hai Lee, and Steven Kivelson, *Phys. Rev. B* **84**, 012507 (2011). on pages 65, 97.

[225] Hiroshi Kontani, Kazuki Kanki, and Kazuo Ueda, *Phys. Rev. B* **59**, 14723 (1999). on page 65.

[226] S. Sadewasser, J. S. Schilling, A. P. Paulikas, and B. W. Veal, *Phys. Rev. B* **61**, 741 (2000). ..... on page 67.

[227] H. Huang, H. Jang, M. Fujita, T. Nishizaki, Y. Lin, J. Wang, J. Ying, J. S. Smith, C. Kenney-Benson, G. Shen, W. L. Mao, C.-C. Kao, Y.-J. Liu, and J.-S. Lee, *Phys. Rev. B* **97**, 174508 (2018). ..... on page 67.

[228] O. Cyr-Choinière, D. LeBoeuf, S. Badoux, S. Dufour-Beauséjour, D. A. Bonn, W. N. Hardy, R. Liang, D. Graf, N. Doiron-Leyraud, and Louis Taillefer, *Phys. Rev. B* **98**, 064513 (2018). ..... on pages 67, 76, 78.

[229] I. Vinograd, R. Zhou, H. Mayaffre, S. Krämer, R. Liang, W. N. Hardy, D. A. Bonn, and M.-H. Julien, *Phys. Rev. B* **100**, 094502 (2019). ..... on pages 67, 78.

[230] M. E. Barber, A. S. Gibbs, Y. Maeno, A. P. Mackenzie, and C. W. Hicks, *Phys. Rev. Lett.* **120**, 076602 (2018). ..... on pages 68, 112.

[231] S. Caprara, C. Di Castro, G. Seibold, and M. Grilli, *Phys. Rev. B* **95**, 224511 (2017). on pages 68, 80.

[232] J. W. Ekin, T. M. Larson, N. F. Bergren, A. J. Nelson, A. B. Swartzlander, L. L. Kazmerski, A. J. Panson, and B. A. Blankenship, *Appl. Phys. Lett.* **52**, 1819 (1988). on page 69, 69, 69.

[233] V. N. Zverev and D. V. Shovkun, *J. Exp. Theor. Phys.* **72**, 73 (2000). on pages 69, 71.

[234] J J Roa, X G Capdevila, M Martínez, F Espiell, and M Segarra, *Nanotechnology* **18**, 385701 (2007). ..... on page 74.

[235] Tao Wu, Hadrien Mayaffre, Steffen Krämer, Mladen Horvatić, Claude Berthier, W. N. Hardy, Ruixing Liang, D. A. Bonn, and Marc-Henri Julien, *Nat. Commun.* **6**, 6438 (2015). ..... on pages 78, 91.

[236] J. M. Harris, N. P. Ong, P. Matl, R. Gagnon, L. Taillefer, T. Kimura, and K. Kitazawa, *Phys. Rev. B* **51**, 12053 (1995). ..... on page 78.

[237] Rufus Boyack, Xiaoyu Wang, Qijin Chen, and K. Levin, *Phys. Rev. B* **99**, 134504 (2019). ..... on page 78.

[238] E. H. da Silva Neto, M. Minola, B. Yu, W. Tabis, M. Bluschke, D. Unruh, H. Suzuki, Y. Li, G. Yu, D. Betto, K. Kummer, F. Yakhou, N. B. Brookes, M. Le Tacon, M. Greven, B. Keimer, and A. Damascelli, *Phys. Rev. B* **98**, 161114 (2018). on page 79.

[239] H. Miao, R. Fumagalli, M. Rossi, J. Lorenzana, G. Seibold, F. Yakhou-Harris, K. Kummer, N. B. Brookes, G. D. Gu, L. Braicovich, G. Ghiringhelli, and M. P. M. Dean, *Phys. Rev. X* **9**, 031042 (2019). ..... on pages 79, 100.

[240] B. Yu, W. Tabis, I. Bialo, F. Yakhou, N. B. Brookes, Z. Anderson, Y. Tang, G. Yu, and M. Greven, *Phys. Rev. X* **10**, 021059 (2020). ..... on page 79.

[241] H. Y. Huang, A. Singh, C. Y. Mou, S. Johnston, A. F. Kemper, J. van den Brink, P. J. Chen, T. K. Lee, J. Okamoto, Y. Y. Chu, J. H. Li, S. Komiya, A. C. Komarek, A. Fujimori, C. T. Chen, and D. J. Huang, *Phys. Rev. X* **11**, 041038 (2021). .. on page 79.

[242] F. Boschini, M. Minola, R. Sutarto, E. Schierle, M. Bluschke, S. Das, Y. Yang, M. Michiardi, Y. C. Shao, X. Feng, S. Ono, R. D. Zhong, J. A. Schneeloch, G. D. Gu, E. Weschke, F. He, Y. D. Chuang, B. Keimer, A. Damascelli, A. Frano, and E. H. da Silva Neto, *Nat. Commun.* **12**, 597 (2021). ..... on pages 79, 94, 97, 100.

[243] J. G. Storey, *Europhys. Lett.* **113**, 27003 (2016). ..... on page 80.

[244] Laimei Nie, Gilles Tarjus, and Steven Allan Kivelson, *Proc. Natl. Acad. Sci. U.S.A.* **111**, 7980 (2014). ..... on pages 81, 94.

[245] B. Keimer, N. Belk, R. J. Birgeneau, A. Cassanho, C. Y. Chen, M. Greven, M. A. Kastner, A. Aharony, Y. Endoh, R. W. Erwin, and G. Shirane, *Phys. Rev. B* **46**, 14034 (1992). ..... on page 90.

[246] T. Wu, R. Zhou, M. Hirata, I. Vinograd, H. Mayaffre, R. Liang, W. N. Hardy, D. A. Bonn, T. Loew, J. Porras, D. Haug, C. T. Lin, V. Hinkov, B. Keimer, and M.-H. Julien, *Phys. Rev. B* **93**, 134518 (2016). ..... on page 91.

[247] Fabian Jerzembeck, Henrik S. Røising, Alexander Steppke, Helge Rosner, Dmitry A. Sokolov, Naoki Kikugawa, Thomas Scaffidi, Steven H. Simon, Andrew P. Mackenzie, and Clifford W. Hicks, The superconductivity of sr2ruo4 under c-axis uniaxial stress (2021). ..... on page 92.

[248] M. D. Johannes, I. I. Mazin, and C. A. Howells, *Phys. Rev. B* **73**, 205102 (2006). on page 92.

[249] S. Raymond, J. Bouchet, G. H. Lander, M. Le Tacon, G. Garbarino, M. Hoesch, J.-P. Rueff, M. Krisch, J. C. Lashley, R. K. Schulze, and R. C. Albers, *Phys. Rev. Lett.* **107**, 136401 (2011). ..... on page 92.

[250] F. Weber, S. Rosenkranz, J.-P. Castellan, R. Osborn, R. Hott, R. Heid, K.-P. Bohnen, T. Egami, A. H. Said, and D. Reznik, *Phys. Rev. Lett.* **107**, 107403 (2011). on page 92.

[251] H. Miao, D. Ishikawa, R. Heid, M. Le Tacon, G. Fabbris, D. Meyers, G. D. Gu, A. Q. R. Baron, and M. P. M. Dean, *Phys. Rev. X* **8**, 011008 (2018). . on page 93.

[252] Jiemin Li, Abhishek Nag, Jonathan Pelliciari, Hannah Robarts, Andrew Walters, Mirian Garcia-Fernandez, Hiroshi Eisaki, Dongjoon Song, Hong Ding, Steven Johnston, Riccardo Comin, and Ke-Jin Zhou, *Proceedings of the National Academy of Sciences* **117**, 16219 (2020). ..... on page 93.

[253] W. S. Lee, Ke-Jin Zhou, M. Hepting, J. Li, A. Nag, A. C. Walters, M. Garcia-Fernandez, H. C. Robarts, M. Hashimoto, H. Lu, B. Nosarzewski, D. Song, H. Eisaki, Z. X. Shen, B. Moritz, J. Zaanen, and T. P. Devereaux, *Nature Physics* **17**, 53 (2021). ..... on page 93.

[254] Sofia-Michaela Souliou, Kaushik Sen, Rolf Heid, Suguru Nakata, Lichen Wang, Hun-ho Kim, Hiroshi Uchiyama, Michael Merz, Matteo Minola, Bernhard Keimer, and Matthieu Le Tacon, *Journal of the Physical Society of Japan* **90**, 111006 (2021). on page 93.

[255] L. Pintschovius, W. Reichardt, M. Kläser, T. Wolf, and H. v. Löhneysen, *Phys. Rev. Lett.* **89**, 037001 (2002). ..... on page 93.

[256] M. Raichle, D. Reznik, D. Lamago, R. Heid, Y. Li, M. Bakr, C. Ulrich, V. Hinkov, K. Hradil, C. T. Lin, and B. Keimer, *Phys. Rev. Lett.* **107**, 177004 (2011). on page 93.

[257] T. J. Boyle, M. Walker, A. Ruiz, E. Schierle, Z. Zhao, F. Boschini, R. Sutarto, T. D. Boyko, W. Moore, N. Tamura, F. He, E. Weschke, A. Gozar, W. Peng, A. C. Komarek, A. Damascelli, C. Schüßler-Langeheine, A. Frano, E. H. da Silva Neto, and S. Blanco-Canosa, *Phys. Rev. Research* **3**, L022004 (2021). ..... on page 93.

[258] Mingu Kang, Jonathan Pelliciari, Alex Frano, Nicholas Breznay, Enrico Schierle, Eugen Weschke, Ronny Sutarto, Feizhou He, Padraic Shafer, Elke Arenholz, Mo Chen, Keto Zhang, Alejandro Ruiz, Zeyu Hao, Sylvia Lewin, James Analytis, Yoshiharu Krockenberger, Hideki Yamamoto, Tanmoy Das, and Riccardo Comin, *Nature Physics* **15**, 335 (2019). ..... on page 94.

[259] A. J. Achkar, X. Mao, Christopher McMahon, R. Sutarto, F. He, Ruixing Liang, D. A. Bonn, W. N. Hardy, and D. G. Hawthorn, *Phys. Rev. Lett.* **113**, 107002 (2014). on page 97.

[260] Wahlberg Eric, Arpaia Riccardo, Seibold Götz, Rossi Matteo, Fumagalli Roberto, Trabaldo Edoardo, Brookes Nicholas B., Braicovich Lucio, Caprara Sergio, Gran Ulf, Ghiringhelli Giacomo, Bauch Thilo, and Lombardi Floriana, *Science* **373**, 1506 (2021). ..... on page 97.

[261] R. Arpaia, S. Caprara, R. Fumagalli, G. De Vecchi, Y. Y. Peng, E. Andersson, D. Betto, G. M. De Luca, N. B. Brookes, F. Lombardi, M. Salluzzo, L. Braicovich, C. Di Castro, M. Grilli, and G. Ghiringhelli, *Science* **365**, 906 (2019). on page 97.

[262] B. Náfrádi, T. Keller, F. Hardy, C. Meingast, A. Erb, and B. Keimer, *Phys. Rev. Lett.* **116**, 047001 (2016). ..... on page 102.

[263] Veronika Sunko, Edgar Abarca Morales, Igor Marković, Mark E. Barber, Dijana Milosavljević, Federico Mazzola, Dmitry A. Sokolov, Naoki Kikugawa, Cephise Cacho, Pavel Dudin, Helge Rosner, Clifford W. Hicks, Philip D. C. King, and Andrew P. Mackenzie, *npj Quantum Materials* **4**, 46 (2019). ..... on page 106.

[264] Vadim Grinenko, Shreenanda Ghosh, Rajib Sarkar, Jean-Christophe Orain, Artem Nikitin, Matthias Elender, Debarchan Das, Zurab Guguchia, Felix Brückner, Mark E. Barber, Joonbum Park, Naoki Kikugawa, Dmitry A. Sokolov, Jake S. Bobowski, Takuto Miyoshi, Yoshiteru Maeno, Andrew P. Mackenzie, Hubertus Luetkens, Clifford W. Hicks, and Hans-Henning Klauss, *Nature Physics* (2021). ..... on page 106.

[265] S. Kasahara, H. J. Shi, K. Hashimoto, S. Tonegawa, Y. Mizukami, T. Shibauchi, K. Sugimoto, T. Fukuda, T. Terashima, Andriy H. Nevidomskyy, and Y. Matsuda, *Nature* **486**, 382 (2012). ..... on page 106.

[266] Jack M. Bartlett, Alexander Steppke, Suguru Hosoi, Hilary Noad, Joonbum Park, Carsten Timm, Takasada Shibauchi, Andrew P. Mackenzie, and Clifford W. Hicks, *Phys. Rev. X* **11**, 021038 (2021). ..... on page 106.

[267] Shingo Yonezawa, Kengo Tajiri, Suguru Nakata, Yuki Nagai, Zhiwei Wang, Kouji Segawa, Yoichi Ando, and Yoshiteru Maeno, *Nat Phys* **13**, 123 (2017). on page 106.

[268] Ivan Kostylev, Shingo Yonezawa, Zhiwei Wang, Yoichi Ando, and Yoshiteru Maeno, *Nature Communications* **11**, 4152 (2020). ..... on page 106.

[269] Danfeng Li, Kyuho Lee, Bai Yang Wang, Motoki Osada, Samuel Crossley, Hye Ryoung Lee, Yi Cui, Yasuyuki Hikita, and Harold Y. Hwang, *Nature* **572**, 624 (2019). on page 106.

[270] Puphal Pascal, Wu Yu-Mi, Fürsich Katrin, Lee Hangoo, Pakdaman Mohammad, Bruin Jan A. N., Nuss Jürgen, Suyolcu Y. Eren, van Aken Peter A., Keimer Bernhard, Isobe Masahiko, and Hepting Matthias, *Science Advances* **7**, eabl8091. on page 106.

[271] Y. Kasahara, T. Ohnishi, Y. Mizukami, O. Tanaka, Sixiao Ma, K. Sugii, N. Kurita, H. Tanaka, J. Nasu, Y. Motome, T. Shibauchi, and Y. Matsuda, *Nature* **559**, 227 (2018). ..... on page 106.

[272] G. Jackeli and G. Khaliullin, *Phys. Rev. Lett.* **102**, 017205 (2009). ...on page 106.

[273] Huimei Liu, Ji ří Chaloupka, and Giniyat Khaliullin, *Phys. Rev. Lett.* **125**, 047201 (2020). .....on page 107.

[274] N.E. Hussey, *Eur. Phys. J. B* **31**, 495 (2003). .....on pages 111, 112.

[275] N E Hussey, *J. Phys.: Condens. Matter* **20**, 123201 (2008). ....on pages 111, 112.

[276] Andrew J. Millis and M. R. Norman, *Phys. Rev. B* **76**, 220503 (2007). on pages 111, 112.

[277] W. A. Harrison, *Electronic structure and the properties of solids* (Freeman, San Francisco, 1980). .....on page 112.

[278] Yawen Fang, Gael Grissonnanche, Anaelle Legros, Simon Verret, Francis Laliberte, Clement Collignon, Amirreza Ataei, Maxime Dion, Jianshi Zhou, David Graf, M. J. Lawler, Paul Goddard, Louis Taillefer, and B. J. Ramshaw, Fermi surface transformation at the pseudogap critical point of a cuprate superconductor (2020). on page 112.

[279] M. C. Shapiro, Patrik Hlobil, A. T. Hristov, Akash V. Maharaj, and I. R. Fisher, *Phys. Rev. B* **92**, 235147 (2015). .....on page 117, 117.